THÈSE

En vue de l'obtention du

DOCTORAT DE L'UNIVERSITÉ DE TOULOUSE

Délivré par : *l'Université Toulouse 3 Paul Sabatier (UT3 Paul Sabatier)*

Présentée et soutenue le *14/09/2020* **par :**

Kanthanakorn NOYSENA

Astronomie multi-messager avec des télescopes à grand champ de vue:

stratégies d'observation, analyse d'images, suivi de candidats, études et implications astrophysiques

---

JURY

Jean	Pierre	Président du Jury
Götz	Diego	Rapporteur
Le Floćh	Emeric	Rapporteur
Komonjinda	Siramas	Examinatrice
Klotz	Alain	Directeur de thése
Boër	Michel	Co-directeur de thése

École doctorale et spécialité :
SDU2E : Astrophysique, Sciences de l'Espace, Planétologie

Unité de Recherche :
Institut de Recherche en Astrophysique et Planétologie (UMR 5277)

Directeur(s) de Thèse :
Alain KLOTZ et *Michel BOËR*

Rapporteurs :
Diego GÖTZ et *Emeric LE FLOĆH*

Multimessenger Astronomy with Large Field of View Telescopes:

Observational strategies, image analysis, candidate follow-up, study and astrophysical implications

Abstract

The detection of gravitational waves (GWs) from LIGO and Virgo interferometers opened a new era for multimessenger observations especially with the coincident detection between GW events and gamma-ray burst (GRB) detection. The first GW event detected by LIGO on the 14^{th} September 2015 (Abbott et al., 2016d) was a binary black hole merger (BBH). Until August 2017 nine other mergers of black holes were detected during runs O1 and O2. But the most interesting object for multimessenger astronomy was the merger of two neutron stars (BNS) detected on 17^{th} August 2017 (Andreoni et al., 2017). This merger was detected in various electromagnetic waves and allowed to confirm the kilonova model.

This research started with the analysis of images recorded by the TAROT telescopes during runs O1, O2 to detect new optical sources associated to black hole mergers. The analysis pipeline was developed to process images and none of optical transient detected but the limiting magnitude of the particular BBH event of 14^{th} August 2017 gave new constraints about the hypothetical link with gamma ray bursts (Noysena et al., 2019). Three GW events; GW150914, GW170104 and GW170814 were observed with TAROT allowing us to constrain $\alpha < 10^{-5}$, the fraction of energy emitted by gravitational waves converted into optical light. An approximately 100% coverage of localization of GW170814 was observed at 0.6 days after GW triggering with no evidence of optical transient and 65% of 147 optical light curves of GRBs known redshift were excluded.

The chance to observe optical transient began when GW interferometers started the run O3 on 1^{st} April 2019 and the campaign ended on 27^{th} March 2020. At the end of run O3, 55 events were detected by LIGO and Virgo and 47 GW events were followed-up by TAROT, thousands of images were searched and analyzed for transient by pipeline using processing techniques described in this manuscript. No new credible optical source associated to GW events was found and 34 GCN circulars reporting optical observations were published to GCN network. The conversion efficiency α for BNS, BBH, and NSBH is at 2×10^{-6}, 3×10^{-7} and 2×10^{-8} respectively. The limiting magnitude and the short delay to start optical observations allow us to reduce severely the hypothesis of the association between GWs and GRBs in case of BBH mergers. However, we have not enough number of cases to exclude definitively the association.

Five binary neutron star mergers were detected before the end of GW observation but none of them was closer than 100 Mpc which is beyond limiting distance where TAROT could detect the associated kilonova. As a consequence, no conclusion to derive any relevant with BNS optical observations.

The optical follow up by TAROT was a pioneering experience with a lot of exciting jobs to adjust event after event to increase the efficiency of the detection pipeline. Joining the GRANDMA group brought more opportunity to detect optical transient during run O3 and result in scientific papers published by Antier et al. (2019, 2020). More GW counterparts and optical observations are needed and we are ready to participate to the optical follow-up of the next GW runs.

Resumé

La détection des ondes gravitationnelles (GWs) par les interféromètres LIGO et Virgo a ouvert une nouvelle ère pour les observations multimessagers, en particulier la détection simultanée d'événements GW et de sursauts gamma (GRB). Le premier événement GW détecté par LIGO le 14 septembre 2015 (Abbott et al., 2016d) était une fusion de trous noirs binaires (BBH). Jusqu'en août 2017, neuf autres fusions de trous noirs ont été détectées lors des campagnes d'observation O1 et O2. Mais l'objet le plus intéressant pour l'astronomie multi messager a été la fusion de deux étoiles à neutrons (BNS) détectée le 17 août 2017 (Andreoni et al., 2017). Cette fusion a été détectée par divers détecteurs d'ondes électromagnétiques et a permis de confirmer l'existence du modèle kilonova.

Mon travail de thèse a commencé par l'analyse d'images enregistrées par les télescopes TAROT lors des campagnes O1, O2 pour essayer de détecter de nouvelles sources optiques associées aux fusions de trous noirs (BBH). J'ai développé la chaîne d'analyse pour traiter les images TAROT. Aucun transitoire optique n'a été détecté, mais la magnitude limite de l'événement BBH du 14 août 2017 a apporté de nouvelles contraintes concernant le lien hypothétique avec les sursauts gamma et a donné lieu à une publication (Noysena et al., 2019). Les trois événements GW150914, GW170104 et GW170814 observés par TAROT nous ont permis de contraindre la valeur $\alpha < 10^{-5}$ de la fraction d'énergie émise par les ondes gravitationnelles convertie en lumière optique. Une couverture d'environ 100% de la localisation de GW170814 a été observée 0,6 jour après l'émission des ondes gravitationnelles sans signe de transitoire optique. Cette limite, comparée à 147 courbes de lumière optiques de GRB de redshift connus, a permis de conclure que 65% des GRBs connus auraient été détectés si GW170814 avait été associé à un GRB.

La possibilité de détecter un transitoire optique a repris lorsque les interféromètres GW ont effectué la campagne O3 entre le 1er avril 2019 et le 27 mars 2020. À la fin de la campagne O3, 55 événements ont été détectées par LIGO et Virgo et 47 événements GW ont été suivi par TAROT. Des milliers d'images ont été enregistrées et analysées pour rechercher les transitoires optiques avec une chaîne logicielle utilisant des techniques de traitement décrites en détail dans ce manuscrit. Aucune nouvelle source optique crédible associée aux événements GW n'a été trouvée. 34 circulaires GCN rapportant les limites de détection des observations optiques ont été publiées dans les circulaires GCN. L'efficacité de conversion α pour BNS, BBH et NSBH est respectivement de 2×10^{-6}, 3×10^{-7} et 2×10^{-8}. La limite de

détection et le court délai pour commencer les observations optiques avec TAROT nous ont permis de réduire fortement l'hypothèse de l'association entre GWs et GRBs en cas de fusion BBH. Cependant, nous n'avons pas suffisamment de cas pour exclure définitivement l'association.

Cinq fusions d'étoiles à neutrons binaires ont été détectées pendant la campagne O3 mais aucune d'entre elles n'était plus proche que 100 Mpc, ce qui est au-delà de la distance limite où TAROT pouvait détecter la kilonova associée. En conséquence, nous ne tirons pas de conclusion sur les observations optiques de BNS.

Le suivi optique par TAROT a été une expérience pionnière, passionnante, et nous avons ajusté la méthodologie événement après événement afin d'augmenter l'efficacité de la chaîne de détection. Le fait d'avoir rejoind le groupe GRANDMA nous a apporté plus d'opportunités pour détecter les transitoires optiques pendant la campagne O3 et a donné lieu à deux articles scientifiques publiés en collaboration (Antier et al., 2019, 2020). Un plus grand nombre de détection d'ondes gravitationnelles et d'observations optiques seront nécessaires dans le futur et nous sommes prêts à participer au suivi optique des prochaines campagnes GW.

Preface

A boy seven years old stood at the yard in the quiet night and he was wondering why there are billions of star in the sky? Why is it still there? To search for the answer, he began a journey. Today he knows that no one knows! To search for the answer, he must not stop a journey.

Thank you to my supervisors; Alain Klotz whom gave me the opportunity and knowledge and treated me as one of his own family which I deeply appreciate very much, Michel Boër whom gave me the path and trust in my success. I would not be here without you both.

To Mom and Dad, all were hard for you to understand what I am doing but the support never ends. You always work hard and I love you very much.

Je suis très contents de cette période d'étude en France et je me suis fait beaucoup d'amis. D'abord Geoffroy De La Vieuville puis Baptiste Klein. La charmante Louise Yu et le génial Edoardo Cucchetti. La très polie Elodie Bourrec et le sympathique Nicolas Longneard. J'ai apprécié l'honèteté de Vincent. Un grand merci à tous ces amis qui m'ont aidé. Vous resterez dans mon coeur.

Contents

List of Tables

List of Figures

Acronyms

BATSE burst and transcient source experiment.

BBH binary black hole.

BH black hole.

BNS binary neutron star.

CBC Compact binary coalescence.

CGRO Compton gamma-ray observatory.

CNES Centre National d'Études Spatiales.

DT-INDU direction technique of Institut National des Sciences de l'Univers.

EM electromagnetic.

FoV field of view.

GCN Gamma-ray Coordinates Network.

GR general relativity.

GRB gamma-ray burst.

GW gravitational wave.

INSU institut national des sciences de l'univers.

IRAP Institut de Recherche en Astrophysique et Planétologie.

LGRB long gamma-ray burst.

LIGO Laser Interferometer Gravitational-Wave Observatory.

MassGap mass gap.

NS neutron star.

NSBH neutron star-black hole.

OHP Observatoire de Haute-Provence.

SGRB short gamma-ray burst.

TAROT Télescope à Action Rapide pour les Objets Transitoires.

TCA TAROT Calern, France.

TCH TAROT la Silla, Chile.

TRE TAROT Les Makes, Reunion island, France.

Chapter 1

Introduction

Gravitational waves (GWs) are space-time deformations predicted by the theory of general relativity (GR) (Einstein, 1915a,b). They are emitted when the mass density of a body evolves under asymmetric geometry. The direct detection of GWs was a challenge during one century due to the high rigidity of the space-time frame leading to very low amplitude effects at the human scale. The strategy was to increase the sensitivity of GW detectors and to choose the most powerful emitters. The most promising emitters were the coalescence of neutron stars (NSs) because these binary systems are massive (higher than 1.4 solar mass) and their binarity gives a natural asymmetry and few of them are known as binary pulsars.

The first detection of GWs occurred in September 2015 (Abbott et al., 2016e) using the Laser Interferometer Gravitational-Wave Observatory (LIGO). This detection was surprising because the masses of the involved objects involved were 29 and 36 solar masses corresponding to binary black holes (BBHs) rather than binary neutron star (BNS). From this discovery and during one year of operations, LIGO discovered two other BBHs but no BNS. No such rate of BBH mergers was expected by stellar evolution theories leading to imagine new theories of formation of BBHs (Zevin et al., 2017). The coalescence of two such massive black holes (BHs) produces a single BH and GWs that bring most of the energy of the lost mass (typically about 10 percent of the initial mass). An electromagnetic (EM) emission could be also produced from this kind of event if either there was matter surrounded the BBH or if BHs themselves were charged (Zhang et al., 2016).

Data from many GW detectors allow to localize the position of GW source in the sky with an accuracy of few hundred square degrees. By this way it is possible to search its EM counterpart. It is important to observe optical

transient from GW source because the EM spectrum brings complementary information about the physics of the GW emitter. The first detection of GWs in September 2015 launched the race to find the EM counterpart. Although 25 teams were involved there was no EM counterpart detected (Abbott et al., 2016c). However, the area on the sky to search was about 1000 square degrees which must be compared to the field of view (FoV) of optical telescopes that cover typically only about one square degree. This provides a very interesting question: Do BBH mergers produce only GWs (so no EM emission) or the technology of EM telescopes can not scan the entire localization boxes efficiently enough?

The gravitational-wave GW170817 was early announced as the first BNS event (Abbott et al., 2017c). Few seconds after the GW event, space telescopes Fermi and INTEGRAL detected a short gamma-ray burst (SGRB) (Abbott et al., 2017a). The link was done between BNSs and GRBs. The triangulation between EM and GW detectors allowed to restrict the sky localization area. By this way, the optical counterpart was found twelve hours after the GW event and the EM source was identified as a kilonova. Kilonovae were predicted (Metzger et al., 2010) but never detected unambiguously before. This event is unique and many questions remain to be answered.

Télescope à Action Rapide pour les Objets Transitoires (TAROT) is a network of three optical telescopes. Initially designed to study the early optical counterparts of GRBs using triggers provided by space telescopes (CGRO-BATSE, Hete-II, Swift, INTEGRAL, Fermi) these telescopes have rapid slewing mounts and optics that cover 3.5 to 17.6 square degrees. The FoV was chosen to encompass the localization error box provided by GRB detectors. In twenty years about 200 GRBs were analysed by TAROTs. Since 2010 the TAROT telescopes are also connected to LIGO and Virgo alerts when a GW is detected. In spite of a large FoV, TAROTs do not cover by themselves the large localization error boxes provided by GW detectors. New strategies have to be found to maximize the counterpart detection.

This thesis starts at the dawn of the multi-messenger area. Many questions are addressed: How to find efficiently optical counterparts of GW sources, what is the nature and the neighborhood of BBHs, what are the first stages of a kilonova? In the first part of this manuscript I present the GWs and the GRBs. The chapter two presents TAROT telescopes. In the chapter three, I analyze the TAROT images taken for the events between 2015 and 2017 (runs O1, O2). In the chapter four, I present new observation strategies and the upgrade of the detection pipeline for the events after 2018 (run O3).

The final chapter is a scientific discussion about the results obtained with TAROTs.

Chapter 2

Scientific background

2.1 Gravitational waves

Gravitational waves are generally defined as the disturbances in the fabric of space-time caused by a merger of massive sources such as a BBH. The first mention of "l'onde gravifique" or gravitational wave is by Henri Poincaré in "Sur la dynamique de l'électron" in July 1905 (Poincaré, 1905). He described that gravity can be transmitted through a wave similar to EM waves. Recall that an EM wave can be generated by oscillations of an electric dipole because it exists positive and negative electric charges. In the case of gravitation we have only positive masses. Nevertheless Poincaré believed of similar principles concerning both wave types.

Later, GWs are subsequently predicted by Albert Einstein in 1916 as he found the linearized weak-field equations that have wave solutions referring to the Equation 2.1 (equation of general relativity):

$$G_{\mu\nu} + \Lambda_{g_{\mu\nu}} = \frac{8\pi G}{c^4} T_{\mu\nu} \tag{2.1}$$

Where G_{uv} is the Einstein tensor which is symmetric and a specific divergence-free combination of the Ricci tensor. T_{uv} is the energy momentum tensor, and g_{uv} is the space-time metric/metric tensor. Other constants are Λ , G, and c which are the cosmological constant, gravitational constant, and speed of light respectively. By this way he suggested the existence of GWs but the amplitude of them would be remarkably small. To detect them we must consider the most massive bodies of the Universe. Amongst them are the BHs. In 1916 Schwarzschild found a solution for the field equation that lead to describe a singularity which will be named "black hole" later. In 1918 Reissner and Nordström studied the case of charged BHs. In 1963, Kerr studied the

rotation of BHs. It is interesting to notice that theories of GWs and BHs were established well before the detection methods become available.

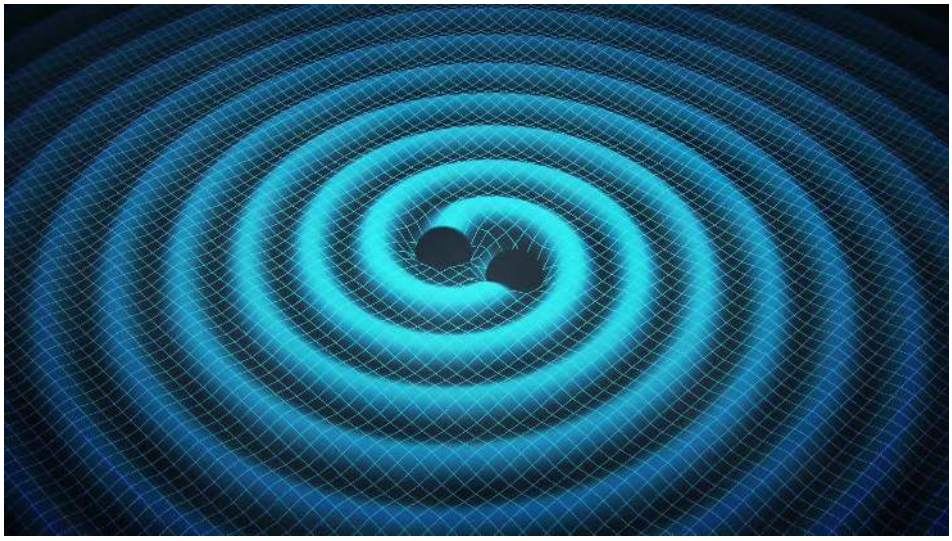

Figure 2.1: The example of perturbed space-time caused by a BBH rotating around each other (Credits: Swinburne Astronomy Productions).

The identification of sources that produce GWs are connected to the temporal behavior (Abbott et al., 2016e). So we can classify GWs into three types:

1. **Stochastic waves** contribute to the gravitational background noise and possibly have their origin in the Big Bang or the background noise caused by the instruments themselves.

2. **Periodic waves** correspond to those whose frequency is more or less constant for long periods of time such as waves caused by a BNS rotating around their center mass which will provide the intensity of the generated waves by the distance from the observer.

3. **Impulsive waves** which are originated from emitting pulses of intense gravitational radiation which could be the creation of BHs in a supernova explosion.

Beginning of GW detectors

Two unsuccessful experiments provide scientists to the edge of GW detection: The Michelson-Morley interferometer and The Weber Bar antenna. The first unforgettable failure experimentation by Albert Michelson and Edward W. Morley in July 1887 intended to study the existence of ether wind by comparing the light speed between parallel and perpendicular directions. The experiment sought for the ether was to detect its drift though the Earth while it was evolving around the sun at speed 30 km/s. The biggest success of that observation was not the positive detection but failed outcome. The geometry of the experiment shown in Figure 2.2 illustrates the phase differences between paths in the case that ether passes through an arm.

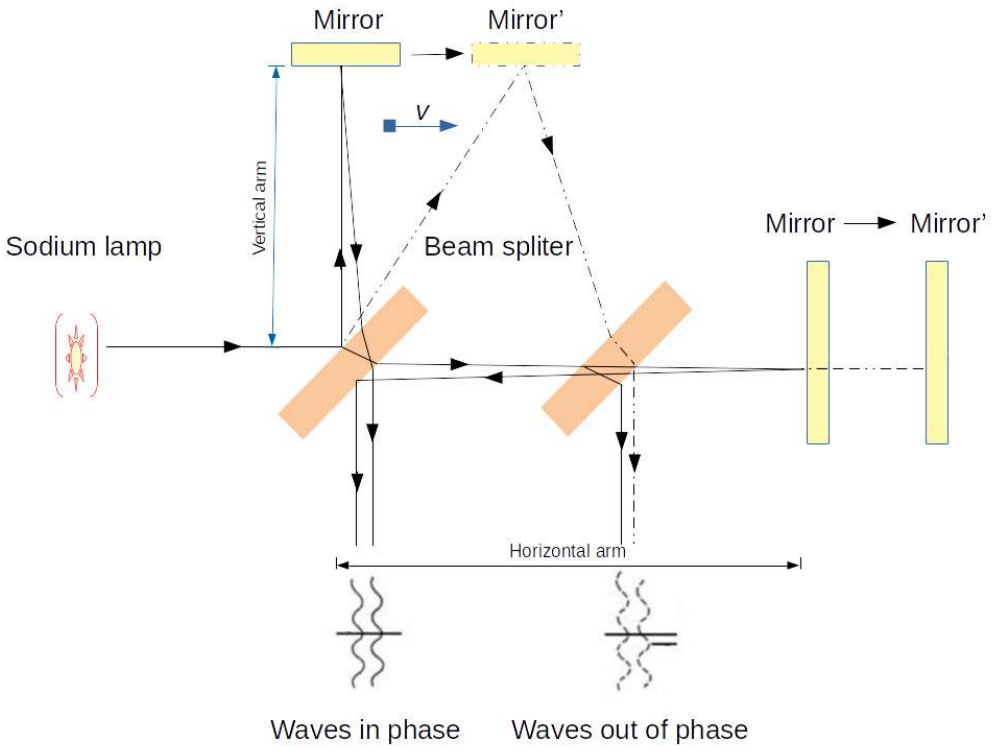

Figure 2.2: The Michelson-Morley experiment in July 1887 to measure the existence of ether.

The second unsuccessful experimentation was lead by Joseph Weber who first attempted to detect GWs with the idea of resonant-mass detector after he attended a General Relativity conference in 1957. Weber started to develop a GW antenna in 1960 to measure electrical signal from piezoelectric crystal caused by the strains in an elastic solid made from a solid cylinder of aluminum at 1.52 m. long and 0.61 m. in diameter, held at ambient temperature and isolated form vibrations in a vacuum chamber. Weber wanted to measure vibrations induced in its mechanical system by resonant vibrations induced in the antenna (Figure 2.3). The early detectors had sensitivity of strain on the order of 10^{-15} $cm.$ and developed up to order of 10^{-17} $cm.$ (Gretz, 2018) while the LIGO detectors have the sensitivity with interferometers better than 1000 times or more (Abbott et al., 2016e). Almost 50 years of failed experiments in attempt to detect GWs with hard work and blunder of operation, Weber and his team provided some disapproved results not officially accepted by scientific community. However, he should be credited and remembered as the first scientist who started to detect the curvature of space-time. Although Joseph Weber had failed in his measurement, his work has since prompted scientists to engage in the search for GWs.

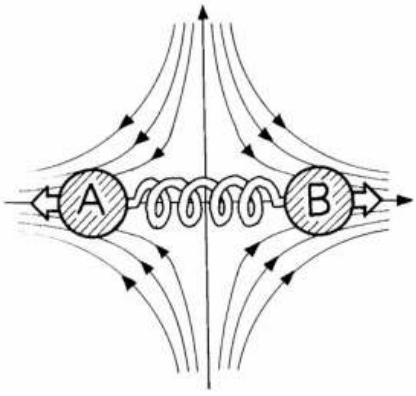

Figure 2.3: The spring will absorb energy from GWs when it passes by the masses A and B which are connected by a spring (Gretz, 2018).

The age of gravitational wave detection

The disappointment reigned among gravity experts and engineer who built the gravitational detectors in the beginning of 1971 soon after those scientists who understood that Joseph Weber proclaimed the spurious detection of GWs (Gretz, 2018). Fortunately in 1974, Joseph Hooten Taylor and Alan Russell Hulse discovered that a binary pulsar PSR 1913 + 16 revealed an accelerated mass radiated gravitational energy (Taylor and Weisberg, 1982). The cumulative shift of periastron time was plotted versus time with the line curve of energy radiated away by GWs from the prediction of General Relativity, show in Figure 2.4. The announcement of this detection was made in 1979 and the result was the awarded the Nobel Prize for Josept Hooten Taylor and Alain Russel Hulse in 1993.

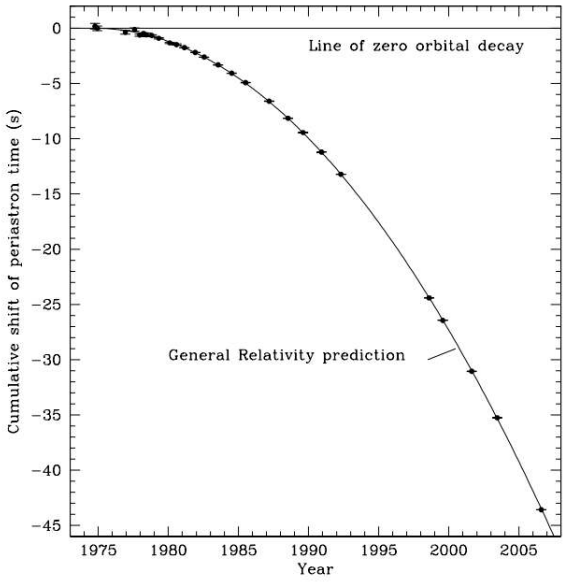

Figure 2.4: The orbital decay of a binary pulsar PSR 1913 + 16 which is caused by the loss of energy by gravitational radiation (Weisberg et al., 2010).

After Tayor and Hulse had revealed that a binary pulsar could emit gravitational energy, they considered detecting a GW. It was unlikely that an experimental observation would be possible because the gravitational constant is really very small to be measured by GW experiments at this time. Before to envisage a technology to detect GWs, it is important to recall that the magnitude of the expected effects of a GW on matter which is almost negligible. The magnitude "h" is introduced for a dimensionless amplitude

and it describes the maximum displacement per unit length that would produce waves on an object. The Figure 2.5 illustrates the stress exerted by a GW perpendicularly on a bar length L and it causes a relative shift between the pair of poles to its length to $\frac{\Delta L}{L} \approx h$. The factor h is influential to consider the design of a realistic GW detector and it depends upon the geometry of the measurement devices, the arrival direction, the event distance, but also the frequency and the polarization of the GW. At the moment of my thesis, an amplitude of $h \approx 10^{-21}$ is achieved using terrestrial interferometers.

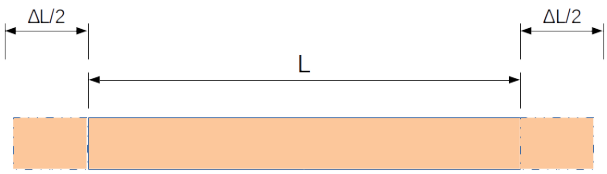

Figure 2.5: The definition of dimensionless amplitude h when GWs pass perpendicularly through it.

The historical experience of the Michelson interferometer was to measure variations in the propagation of the speed of light. The fact that the speed of light is identical in all the directions leads to the idea of using the Michelson interferometer to measure length variations between the two perpendicular arms to detect GWs. This is possible because the GWs are transverse and polarized so they do not act the same manner in the two orthogonal directions of the interferometer arms (Figure 2.6).

The Figure 2.7 shows the main steps of the light path in Michelson interferometer upgraded to allow GW detection. When GWs pass through the interferometer the goal is to observe an intensity change of a recombined laser source. First the beam of monochromatic light, provided by a laser, is shot out to a beam splitter surface. Then the beam will be split to the arms which have a reflecting mirror to reflect the light back to again. Back on the splitter the light from both arms will recombine before reaching the detector. The light intensity of the recombined beam will be affected by arm length variations. These variations can be due to the pass of a GW but also to a lot of noise sources such as earthquakes, mechanical resonances, quantum light noise, etc. After a complex processing to eliminate noises, the amplitude h can be extracted from the signal. Note that a typical GW frequency of 100 Hz (Cervantes-Cota et al., 2016) has a wavelength of few thousand kilome-

ters. It is the utmost importance to have a very long arms to increase the $\Delta L = L \times h$ so the long arms means the possible of a larger scale ΔL.

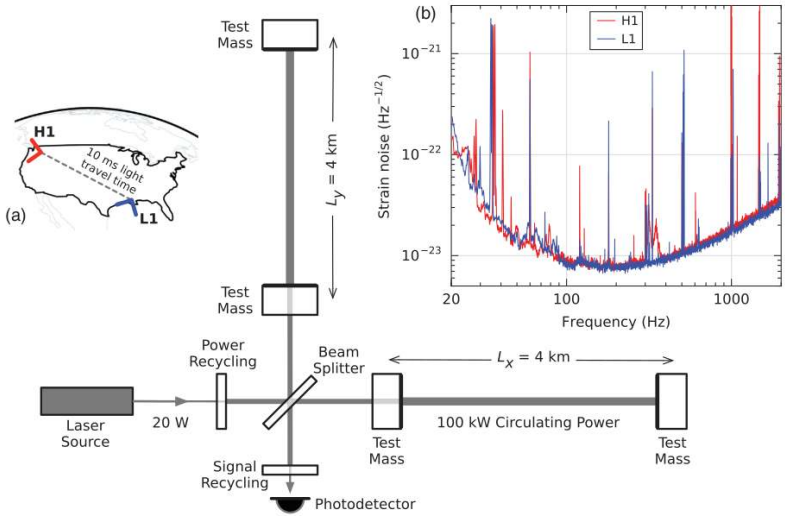

Figure 2.6: Diagram of an Advanced LIGO detector (Abbott et al., 2016d).

Physics of binary mergers from gravitational waves

The discovery of the neutron particle in 1934 was followed by the idea of the existence that some compact stars could be composed by neutrons. The discovery of pulsars in 1967 confirmed the reality of these stars (Hewish et al., 1968). Some of them are known to be binary. The measure of the orbital decay of the binary pulsar PSR 1913 + 16 (Figure 2.4) by Weisberg et al. (2010) lead to expect that the final stage of such a systems is the merging leading to the emission of a huge impulsive GW. This concept is generalized as "binary mergers" including couple of BHs but also to couples formed by a NS with a BH.

The frequency of the GWs emitted by a binary merger is directly linked to the revolution frequency of the couple of stars. As GWs escape from the system the distance between the two object decreases and the revolution frequency increases. The general relativity governs the evolution of the orbital motion leading possible predictions of the GW signal knowing the binary system physical parameters.

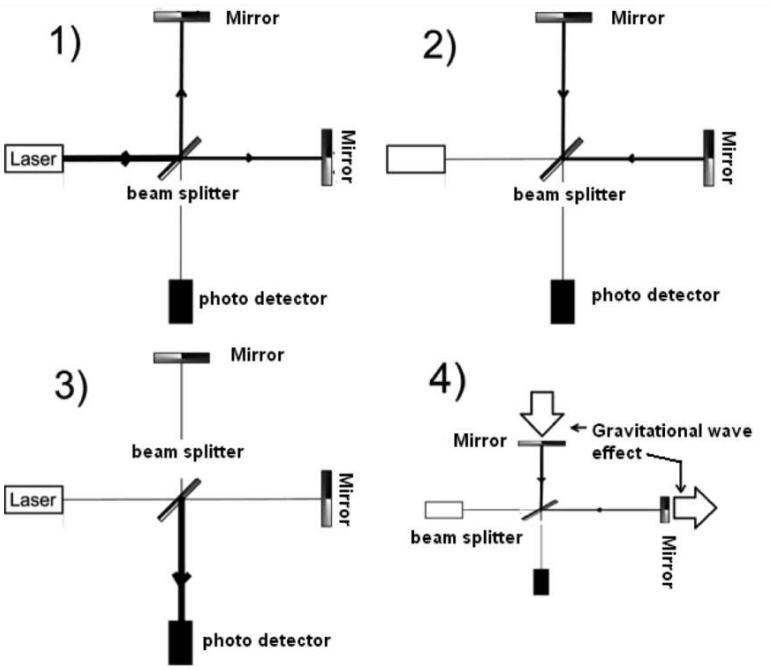

Figure 2.7: A simplified schematic diagram for detecting GWs by interferometre (Cervantes-Cota et al., 2016).

From a simple model involving two masses m_1 and m_2, the frequency f and and its time derivative $\dot{f}$ are linked by the Equation 2.2:

$$\mathcal{M} = \frac{(m_1 m_2)^{3/5}}{(m_1 + m_2)^{1/5}} = \frac{c^3}{G}\left[\frac{5}{96\pi^{-8/3}} f^{-11/3}\dot{f}\right]^{3/5} \tag{2.2}$$

Where G is the gravitational constant, c is speed of light, and $\mathcal{M}$ is called the chirpmass.

GW interferometers monitor frequencies and their time derivative in near real time (Figure 2.8). The detection of a GW due to a binary merger is identified when the observed signal fit the Equation 2.2. The chirpmass is one of the first parameter computed when a GW from binary merger is detected.

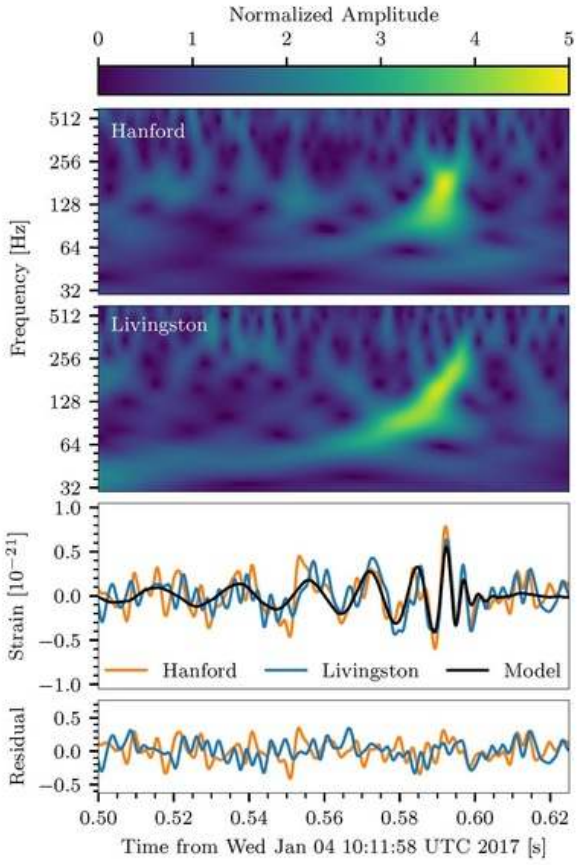

Figure 2.8: Upper colorized images display amplitude of the GW 170104 in a plot frequency versus time. The middle plot showing strain versus time that shows clearly the frequency acceleration until the merging (Abbott et al., 2017b).

The amplitude h_0 of a GW signal from a binary merger allows to derive the distance of the source (Equation 2.3):

$$h_0 = \frac{4\pi^{2/3} G^{5/3}}{c^4} \frac{\mathcal{M}}{(1+z) \times D(z)} [\mathcal{M} f]^{2/3} \tag{2.3}$$

Where z is the redshift and $D(z)$ is the distance luminosity. The amplitude decreases as in inverse of the distance and not by the square of the inverse of the distance as for EM waves. So, GW wave sources can be measured at distances where EM sources are to faint to be detected.

Gravitational Wave Observatories

There are four GW observatories running at the moment, The Laser Interferometer Gravitational-Wave Observatory (LIGO) located at USA (Figure 2.6), one in Handford, Washington and the other in Livingston, Louisiana. Europe also has a GW observatory named Virgo established in Cascina, Italy and the GEO600 project is in Hannover, Germany. Figure 2.9 shows where are located GW detectors.

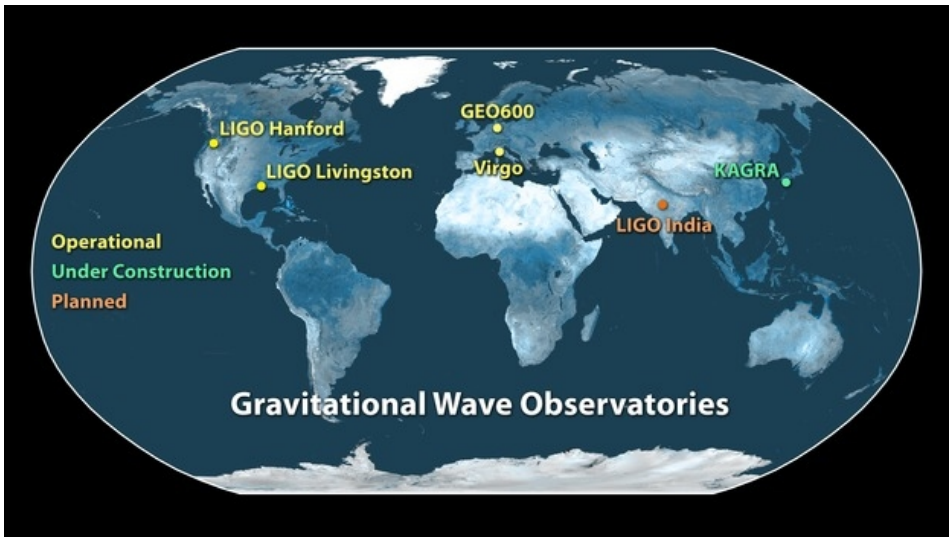

Figure 2.9: Current operating facilities in the global network: LIGO detectors in Hanford, Washington, Livingston, Louisiana, GEO600 in Germany, the Virgo detector in Italy, and the Kamioka GW Detector (KAGRA) in Japan which is undergoing. A sixth observatory is being planned in India. (Credit: LIGO).

To be more specific, it is important to detect GWs in the same time by different interferometers. Runs of scientific observations are defined to coordinate the time of observations (Figure 2.10). Runs O1 and O2 are passed. This thesis occurred during the run O3 and it stops observing on 27^{th} March 2020.

Sky localization of gravitational wave sources

The geometry of the GW interferometers coupled to the polarization of the waves allows to determine the incident direction of the GWs. One interferometer provides a localization as a circle in the sky (orthodrome). The width of the circle is about 8°. The joint localization with more than one interferometer allows to reduce the area to about 100 deg^2. Practically, the on-line

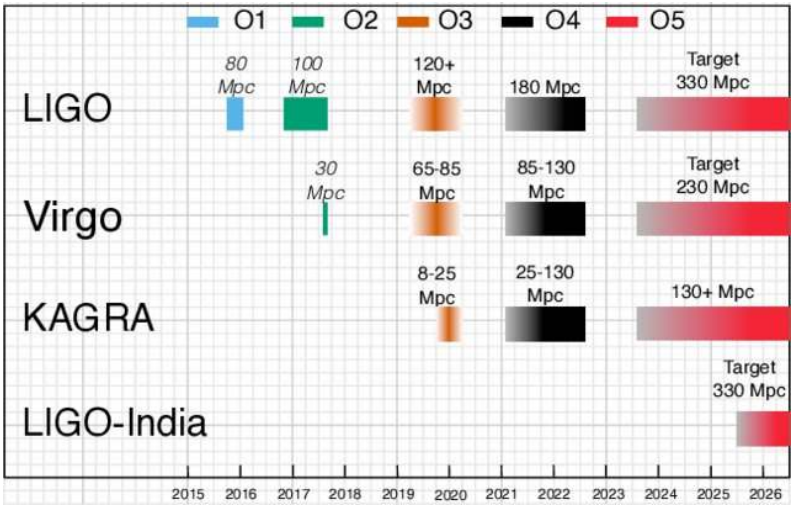

Figure 2.10: LIGO and Virgo collaboration schedule shows the run periods when detectors observe the sky. The distances are the detection limits in case of NS mergers (The LIGO Scientific collaboration, 2019).

pipeline of detection of GW interferometers provides a very large sky area and a few minutes after the GW event. Off-line pipelines allow to combine interferometer signals and reduce the area about half a day after the event (see Figure 2.11). The difficulty to search an optical counterpart is to have a large FoV optical telescope with a high sensitivity.

Bibliography of optical counterpart searches

Many telescope networks are involved in the search optical counterparts. The Table 2.1 summarizes the main results published. The goal is to observe all the sky area in a minimum of time maximizing the detectability. Observing delay, covering area and limiting detection; these three parameters are antagonists and technological compromises must be used. Additional difficulties come from the local visibility of the area to observe.

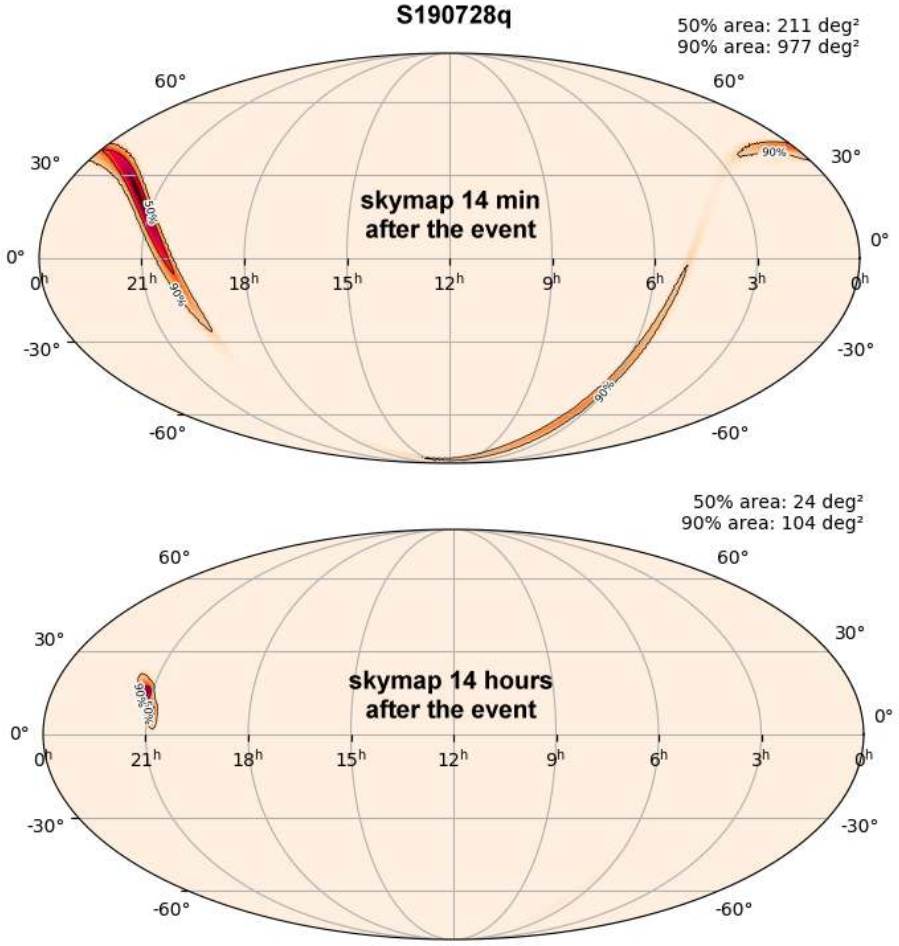

Figure 2.11: The probability skymap is useful to search for the optical counterpart of a GW. The upper skymap is provided few minutes after the GW event. The area to observe is very large, typically about 1000 deg^2. After few hours, combination of LIGO and Virgo detections allows to reduce the searching area to typically 100 deg^2. Adapted from GraceDB https://gracedb.ligo.org/superevents/S190728q/view/.

Table 2.1: Published papers concerning searching optical counterparts of GW events in runs O1 and O2. A symbol > in the detection field means upper limit. In the case of GW170817, we indicate only the reference of the first positive detection.

Telescope	Delay	Area (deg^2)	Area/90% (%)	Detection	Reference
			GW150914		
VST	2.9 - 4 days	90	29	> 21	Brocato et al. (2018)
iPTF	3.0 days	126	45	R > 20.2	Kasliwal et al. (2016)
DECam	4 - 5 days	102	38	i > 22.7	Soares-Santos et al. (2016)
			GW151226		
VST	9 h	72	7	> 21	Brocato et al. (2018)
			GW170104		
Mini-GWAC	2.3 - 12 h	1630	62	> 16	Turpin et al. (2019)
ATLAS	21 - 25 h	1231	43	i > 21.5	Stalder et al. (2017)
			GW170814		
DECam	1 day	87	86	i > 23	Doctor et al. (2019)
			GW170817		
Swope	10.86 h	31	3.0	i = 17.5	Coulter et al. (2017b)

2.2 Gamma-ray bursts

During the cold war era, the United States and the Soviet Union adopted the "Nuclear Test Ban Treaty" in 1963 to limit nuclear bomb tests in the Earth atmosphere and in space. To check the respect of the treaty the United States launched eleven satellites, named Vela, equipped with scintillator sensors sensitive to high energy photons. The signal analysis revealed the existence of GRBs by chance. The first GRB was captured by Vela satellites on 2 July 1967 and its light curve is shown in Figure 2.12. Waiting the detection and analysis of 15 additional events, Klebesadel et al. (1973) published the discovery confirming their cosmic origin. A GRB is the observation of short duration and intense emissions of EM spectrum centered at about 100 keV (Cline et al., 1973). To explain such an amount of energy GRBs were linked to explosions of stars as soon as their discovery (Klebesadel et al., 1973; Woosley et al., 1999). Indeed, the short duration and milliseconds pulses imply a small dimension progenitor as NSs or BHs.

The high energy sensor technology of the years before 1980 did not allow to determine precisely the incident direction of gamma-rays. The question of the direction is important because, if the spatial provenance is concentrated

to the direction of our Galaxy we can conclude the GRB progenitors are located in the Milky Way. Else, the GRBs will be located much more far and perhaps coming from elsewhere in the Universe.

The burst duration is not easy to define because the end of gamma emission has often a shape of an exponential tail. The duration of a GRB is commonly defined by the T90 duration (Kouveliotou et al., 1993). Starting from the light curve, one can compute the instant $t_{5\%}$ when 5% of the flux was emitted and $t_{95\%}$ when 95% of the flux density was emitted. Then T90 = $t_{95\%}$ - $t_{5\%}$. Most of GRBs have T90 lying between few milli-seconds and some hundred of seconds.

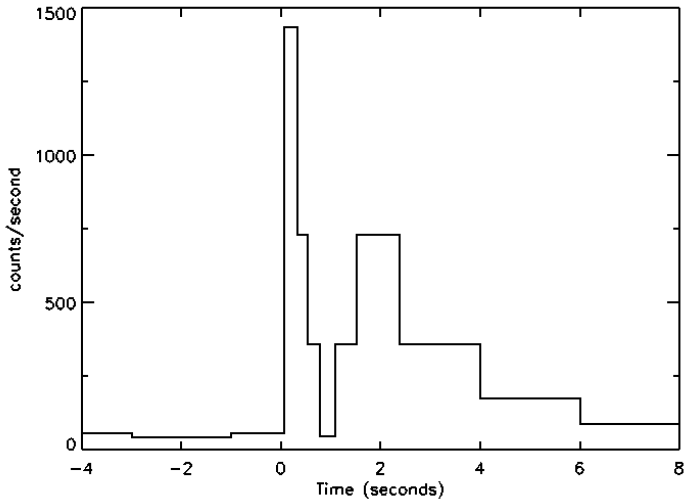

Figure 2.12: The light curve of the first GRB detected by the Vela IVa satellite on 2 July 1967 (Klebesadel et al., 1973).

Note that the flounce, *i.e* integrated energy over the burst duration, is about $10^{-6}\, erg/cm^2$ (with variation of a few orders of magnitude from an event to the other). Converted to a typical galactic distance it corresponds to a source emitting an energy of $E_{ISO} \simeq 10^{43}$ ergs (E_{ISO} stands for an isotropic emission of the energy). Converted to an extra-galactic distance of 1 giga-parsec $E_{ISO} \simeq 10^{50}$ ergs. We must compare these energies with the Solar mass energy (E=mc^2) of $E_{ISO} \simeq 10^{54}$ ergs. The duration of gamma-rays being limited to few seconds, and considering that only a small fraction of the stellar mass can be converted in energy, privilege a galactic origin if the

emission is isotropic. The great debate during the '90 was to discuss about the galactic versus extra-galactic origins (Paczyński, 1991).

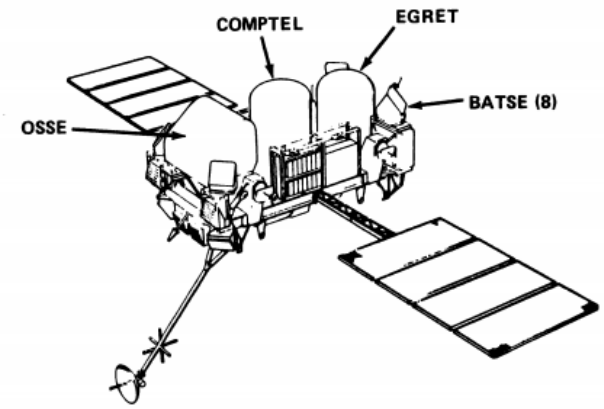

Figure 2.13: The CGRO satellite launched in 1991(Fishman et al., 1982).

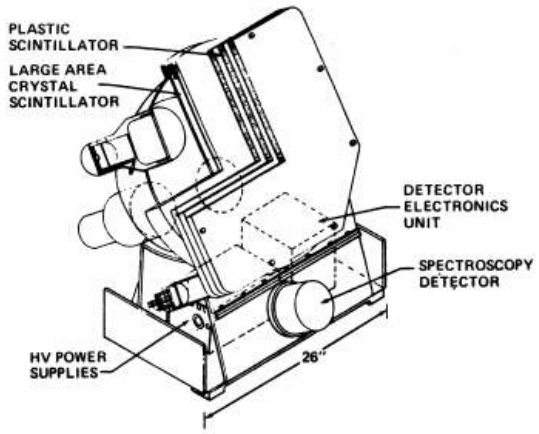

Figure 2.14: One of the height gamma ray detectors BATSE installed aboard the CGRO satellite (Fishman et al., 1982).

The CGRO in operation between 1991 and 2001 was equipped by the experiment BATSE consisting in eight detectors allowing to determine the angular position in sky of about 3000 GRBs (about 1 event per day during 10 years) with a precision of about 5 degrees (Fishman et al., 1982). Despite this low spatial resolution, as soon as 1996, the measures allowed to convince the community that the progenitors of GRBs have an origin outside our Milky Way (Briggs et al., 1996), see Figure 2.15.

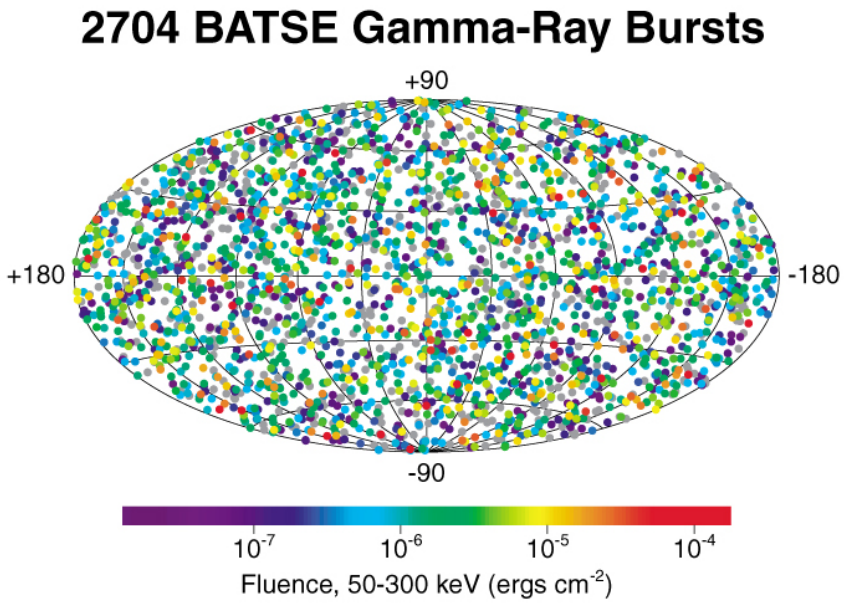

Figure 2.15: Sky has covered with coordinates of 2407 GRBs detected by BATSE (Credit: NASA).

From previously mentioned energetic reasons, it was not probable that an extra-galactic source was emitting its energy isotropically. Then the energy had to be emitted in a narrow beam. In such a beam one is then confronted with the problem of compactness. Indeed, the gamma photons emitted in a compact zone have the property of interacting rapidly by forming electron positron pairs. These electron positron pairs end up annihilating by radiating but no gamma ray emission above energy of 1 MeV should be detected. However, gamma rays above this limit are detected during GRBs. The problem of compactness, however, is circumvented if we add the hypothesis that the ejection of the material into the beam is at ultra-relativistic speeds towards the Earth (Piran, 1999). Under these conditions, the speed (denoted v) is always greater than 99% of that of the light (denoted c) and it is preferable to use the notion of Lorentz factor Γ defined by equation 2.4:

$$\Gamma = \frac{1}{\sqrt{1 - (\frac{v}{c})^2}} \tag{2.4}$$

In this context, the gamma emission would come from the collision of lumps of matter that catch up in the ejected jet. To generate enough energy each lump must travel with a factor $\Gamma > 100$ with small differences from one to the other to generate collisions. The collisions are weak shocks that cause

an X-ray emission that does not suffers from the problem of compactness. The emission of gamma radiation, seen from the Earth, then comes from the Doppler-Fizeau shift by the factor $\Gamma > 100$ towards the blue of the emission X due to shocks inside the jet (Meszaros and Rees, 1993). Finally, the problem of compactness is completely bypassed by the effect of relativistic aberration. Indeed, the light emitted by a particle moving with a relativistic velocity can be observed only in a cone whose principal axis is directed according to the direction of motion of the particle. The opening angle θ of the relativistic aberration cone is given by the relation 2.5:

$$\theta = \frac{1}{\Gamma} \tag{2.5}$$

For a value $\Gamma = 100$, we have $\theta = 0.6$ degrees. Thus, each emitted photon has no interaction with the space outside this narrow cone, which virtually eliminates any absorption of high energy photons.

The principle of the emission of high-energy photons from GRBs results in the synchrotron radiation of electrons in magnetic fields in the jet as large as 10^3 to 10^4 Gauss (Proga et al., 2003). The magnetic field would then be created during collisions in a relatively confined region around the progenitor star and usually referred to as internal shocks (Paczynski and Rhoads, 1993).

The spectral hardness of a burst corresponds to the ratio between the number of photons at high and at low energy. The high / low energy limit is arbitrary and depends mainly on detector technology for each experiment. In the case of BATSE, hardness is defined as the ratio between 100 to 300 keV photons and those emitted between 50 and 100 keV. A hard burst has a spectrum richer in gamma rays than in X-rays. The representation of each burst in the form of a point in a duration / hardness diagram clearly shows two categories: The SGRBs (hard and T90<2s) and long gamma-ray bursts (LGRBs) (soft and T90>2s) (Kouveliotou et al., 1993), see Figure 2.16.

A major breakthrough came with the BeppoSAX satellite (1995-2002). This satellite was equipped with a wide field coded mask camera providing X-ray images with a resolution of a few arcmin (Scarsi, 1984). The satellite was repointed to the bursts detected by BATSE. The burst of February 28, 1997 was detected by BeppoSAX a few hours after the gamma flash in the form of an X-ray source whose brightness was decreasing rapidly (Costa et al., 1997). This event made it possible to distinguish the prompt emission, the gamma flash itself, and the afterglow which lasts for several days after the burst. From the precise position of BeppoSAX, it was possible to point the terres-

trial telescopes towards the X-ray source. At this location, a point source of visible light was detected at the magnitude 20, whose brightness decreased in the same way as the X-ray source.

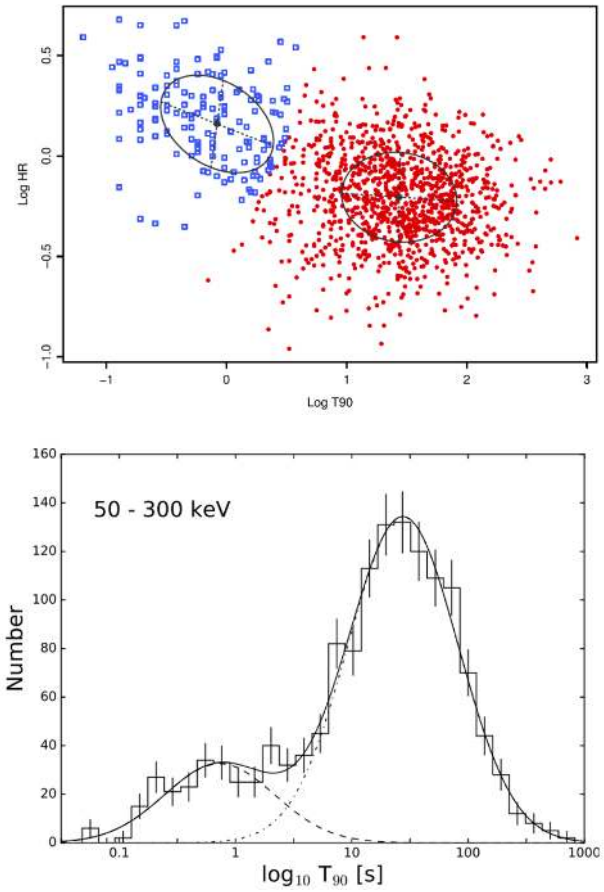

Figure 2.16: Distribution of GRB T_{90} durations in the 50-300keV energy range (top) and classification based on the hardness-duration diagram (bottom). Colors indicated their group membership (red: on average short/hard, blue: on average long/soft). Ellipses show the best fitting multivariate Gaussian models (Bhat et al., 2016).

The interpretation of the afterglow is that the material ejected by the jet meets the gas of the interstellar medium (Piran and Granot, 2001). An external shock occurs, consisting of the slowing of the ejecta that hits the interstellar medium. This shock is much more violent than the internal shocks because it is no longer two layers that catch up but a frontal collision with an initially immobile medium. During external shock, the factor Γ decreases

by a factor of 10 or more. The external shock accelerates the electrons of the interstellar medium and creates strong magnetic fields, which results in the generation of synchrotron radiation observable from X-rays to radiometric waves. The common accepted model of the external shock is the fireball model (Goodman, 1986; Piran, 1999) which will be discussed later.

The afterglow optical emission is important because it acts as a lighthouse in front of which all properties of the matter located between the GRB and the Earth will be able to be measured by absorption spectrometry. The spectrum features are affected by the cosmological redshift which allow to estimate the distance of the GRB progenitor. The LGRBs have an average redshift of ~ 2. Some very far GRBs have a redshift larger than 6.

The first X and optical light curves showed a decay for which the flux decreases as $t^{-\alpha}$ where t is the time that separates the moment of the measure from the beginning of the gamma emission. The light curve is therefore a line in a representation of the magnitude, as a function of the logarithm of t. Generally α is close to 1. This decay index value is important because it means that the afterglow looses a factor 10 in flux between t=2 minutes to t=20 minutes, another factor 10 in flux between t=20 minutes to t=3 hours and so on. The practical consequence is that optical telescopes must start observations as early as possible to maintain the afterglow brighter than the limiting magnitude of the sensors.

For some LGRBs for which the redshift $z < 1$, after the initial afterglow decay, one can find a faint bump of optical light peaked at around 30 days after the gamma-ray emission (Stanek et al., 2003). The spectral analysis of the light in this bump shows that this component is related to type Ib/c supernova (often called hypernova). This late event tends to prove that the progenitors of LGRBs are the end of life of isolated $\geq$35 solar mass stars.

SGRBs progenitors must have very small size expected by the short duration of the gamma-ray emission. The progenitor must be surrounded by matter to allow gamma emission. This excludes BHs that are believed to sweep all the surrounding mater. It remains NSs. However, to explain the reservoir of energy used to create the jet of a GRB, the model of the merging of two NSs is commonly accepted after the discovery and interpretation of GRB 050709 (Hjorth et al., 2005).

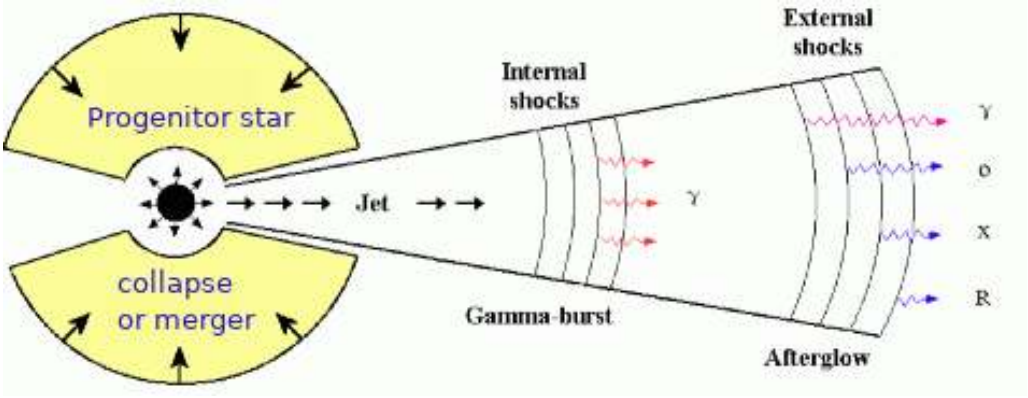

Figure 2.17: Schematic view of a GRB, from a collapsing massive stellar progenitor until the production of gamma-ray and EM waves (Piran, 1999).

Considering the very different progenitor natures of SGRBs and LGRBs one can be surprised by such a common phenomenological consequences that mix them in same designation: GRBs. Regarding the physics, both GRB types start with collapse of matter: External envelope for LGRBs or merging of stars for SGRBs. Then, one can consider a central engine constituted by a massive compact object transforming the falling matter into a beamed ultra-relativistic jet. Many questions remain to answer to explain the efficiency of such a transformation. The later phases, *i.e.* the evolution of the jet and the afterglow, are generally treated by the so-called fireball model.

The fireball model (Goodman, 1986) explains how the kinetic energy of the relativistic flow and some micro physic parameters can explain the spectral energy distribution and its evolution with time (see Figures 2.17 and 2.18). In this way it is possible to fit fireball model parameters to explain the light curve at different wavelengths (Turpin, 2016).

From bibliographic data provided by Damien Turpin (private communication), we are able to plot a collection of optical light curves (Figure 2.19). From these plots we can derive parametric envelopes of light curves using a broken power law (Equation 2.6):

$$F = F_o \cdot \left(\left(\frac{t}{t_o} \right)^{-s \cdot a} + \left(\frac{t}{t_o} \right)^{-s \cdot b} \right)^{(-1/s)} \tag{2.6}$$

The a parameter characterizes the slope of the rise and b is the slope of the decay. The s parameter is the smoothing factor that shapes the break at the time t_0. The Table 2.2 gives the fitted parameters.

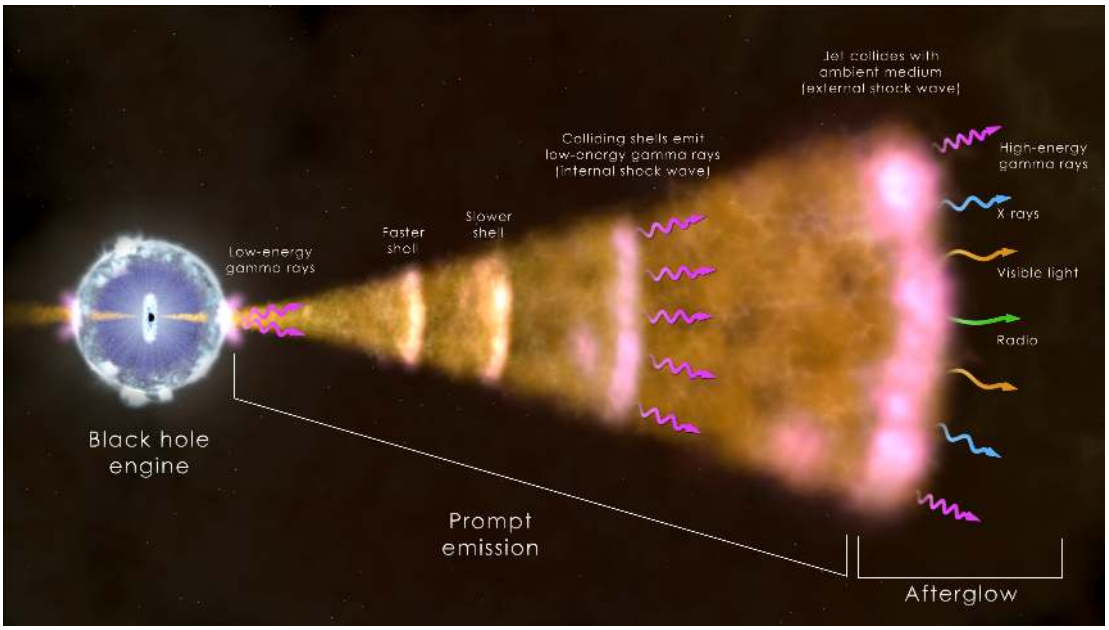

Figure 2.18: Schematic of the Fireball model with the production of the 'prompt' and 'afterglow' emission (Credit: NASA).

Table 2.2: Fit parameters to define light curve envelopes according Equation 2.6 and data from Figure 2.19.

	$F_o(mJy)$	t_o	s	a	b
Short GRBs					
faint	3.0×10^{18}	20s	1.0	2.0	-1.0
bright	3.0×10^{20}	20s	1.0	2.0	-1.0
Long GRBs					
faint	8.0×10^{16}	20s	1.0	2.0	-1.0
bright	3.2×10^{21}	20s	1.0	2.0	-1.0

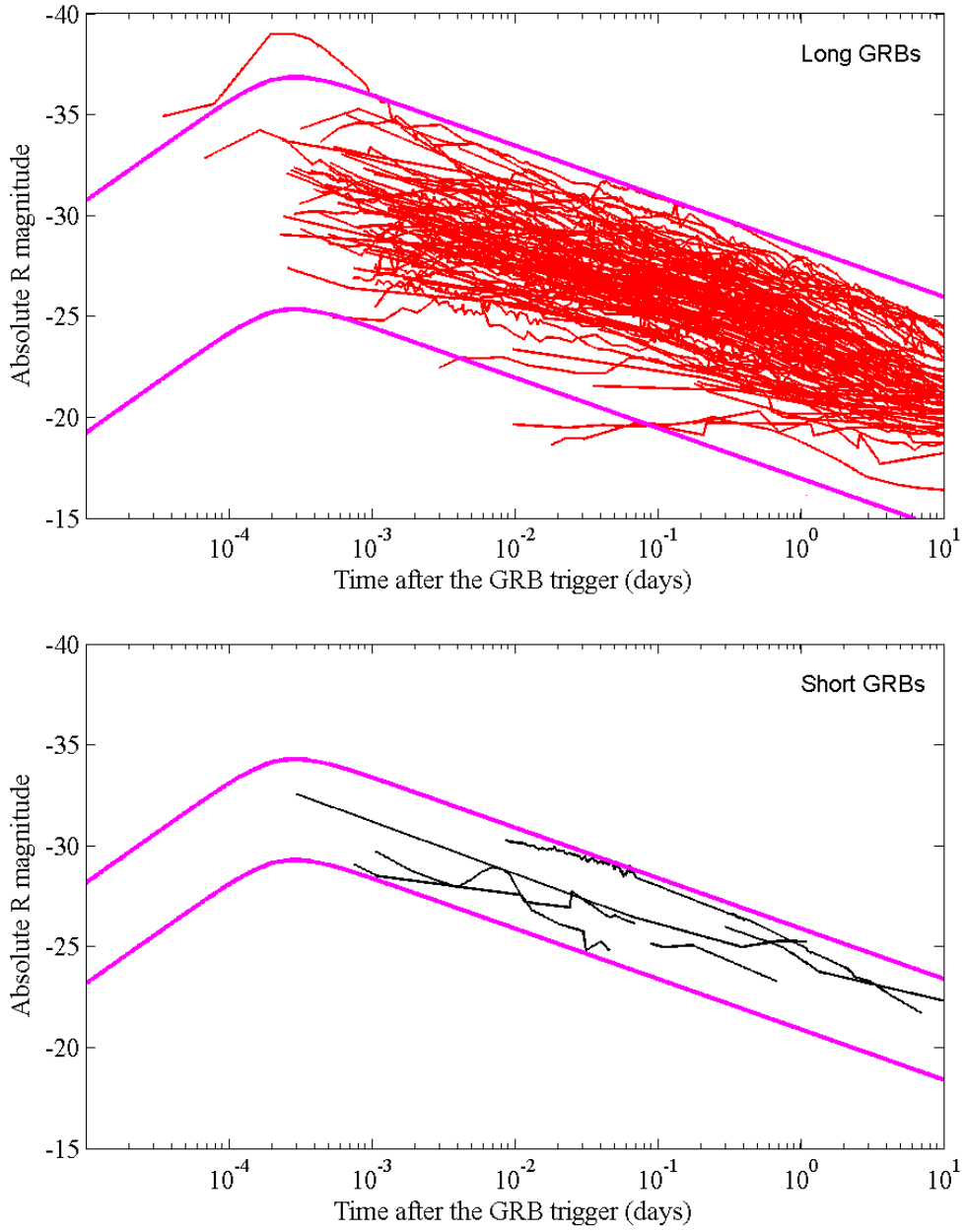

Figure 2.19: Observed light curve of GRBs for which the redshift is known. Top panel: Optical light curves of 141 long GRBs (red lines). Bottom panel: Optical light curves of 6 short GRBs (black lines). We correct the distance to plot magnitude in absolute scale. The pink lines show the brightest and faintest of energy predicted by Equation 2.6.

2.3 Theories of EM emissions from BNSs and the relation between GWs and GRBs

A common object type is invoked for GW and GRB emissions: The BNS merger. The GW emission increases strongly few seconds before the merging and stops few tenths of seconds after. The GRB emission results from internal shocks in a polar jet ejected after the merging occurs. A rapid GW wave form analysis allows to determine the masses of the binary system and also its distance (see formula 2.2 and 2.3). Few minutes after the merging such an event can be classified as BNS, BBH or neutron star-black hole (NSBH).

Theory of kilonova

The merging of BNS or NSBH is expected to eject matter from the NS. Metzger et al. (2010) studied the process which was refined year after year (Metzger, 2017). A huge quantity of neutrons should be blown up in expanding shells and the energy will be released at optical wavelengths many hours later. The theory predicts also a luminosity reaching 1000 times that of a classical nova, giving the name of kilonova for the EM emission. The peak of luminosity depends strongly on the wavelength.

Metzger et al. (2010) predicted that the huge quantity of free neutrons injected in the expanding shells will be absorbed by atomic nuclei creating heavy unstable nuclei (i.e. r-process). Lanthanide nuclei are expected to be created. They induce a high opacity ejecta which gives a unique signature of optical light curves: A blue peak is expected less than one day after the merging followed by a near-infrared peak few days after. This behaviour is very different compared to supernovas associated to LGRB.

Until 2017 only one kilonova was tentatively identified by the late optical light curve of the short GRB 130603B (Tanvir et al., 2013). The discovery of GW170817/GRB170817A confirmed the concept of kilonova.

GW170817

A BNS merger was detected on 17 August 2017 at 12:41 UTC by LIGO/Virgo and was named GW170817 (Abbott et al., 2017a). At about the same time in approximately the same region of the GW event Fermi-GBM and INTEGRAL SPI/ACS detected a GRB called GRB170817A (Abbott et al., 2017c). The merger emitted GWs and SGRB with an afterglow for all EM wavelength

such as visible, X-ray, and radio. This SGRB was detected by Fermi-GBM ~ 2 seconds after the coalescence. The event was suddenly followed up and search for an optical counterpart with many ground-base telescope teams; the coordinates of the event were found after GWs had been detected 11 hours by Coulter et al. (2017a) being $RA : 13^h\ 09^m\ 48^s\ DEC : -23^\circ\ 22'\ 53''$ detected in the host galaxy NGC4993.

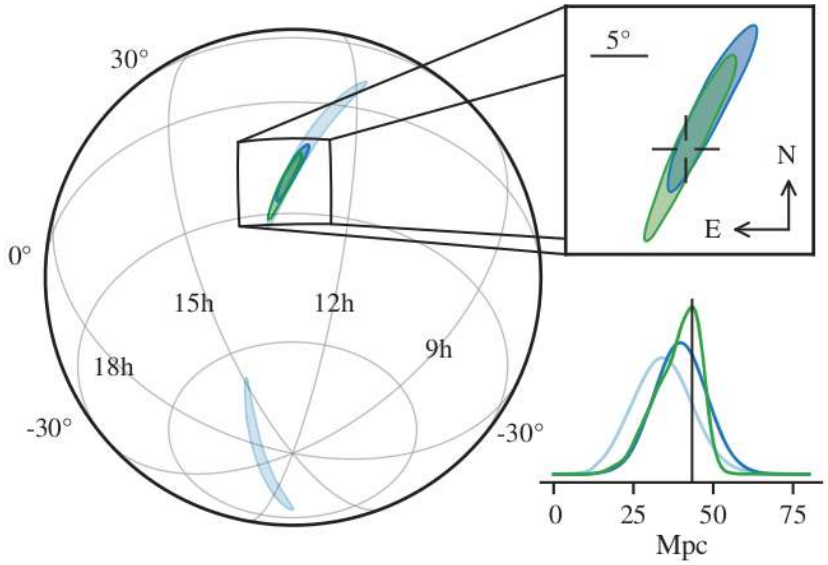

Figure 2.20: GW170817 localizations from Abbott et al. (2017a), light blue illustrates 190 deg^2 of localization and the area is decrease to 31 deg^2 in dark blue and the final reconstructed of localization was small as 29 deg^2 in green.

GW170817 was observed simultaneously between Advanced LIGO and Virgo detectors and this GW signal shows the coalescence between BNS with a combined of signal-to-noise of 32.4 and a false-alarm rate estimate of less than one per 8×10^4 years derived with a matched filter search with post-Newtonian waveform models (Abbott et al., 2017c). The sky location was computed with a rapid localization algorithm from LIGO-Handford and LIGO-Livingston and was large up 190 deg^2 shown in light blue of Figure 2.20 and then the skymap was reduced to 31 deg^2, when Virgo detector was included shown in dark blue contours of Figure 2.20; finally with a higher latency LIGO/Virgo sky location reconstructed error box was as small as 28 deg^2, shown in green of Figure 2.20.

When the GW170817 was detected, the Advanced LIGO detectors and the Advance Virgo detectors were in observing mode with the maximum distant

detection for BNS system by LIGO-Livingston and LIGO-Handford detectors at 218 Mpc and 107 Mpc for a signal-to-noise of 8, and the maximum detection distance for Virgo was 58 Mpc while the maximum detection of GEO600 detector was insufficient ration to detect BNS. We can see a time-frequency plot from all three detectors in Figure 2.21. We note that there is no environmental disturbance observed by LIGO environmental sensors that could account for the GW170817 signal.

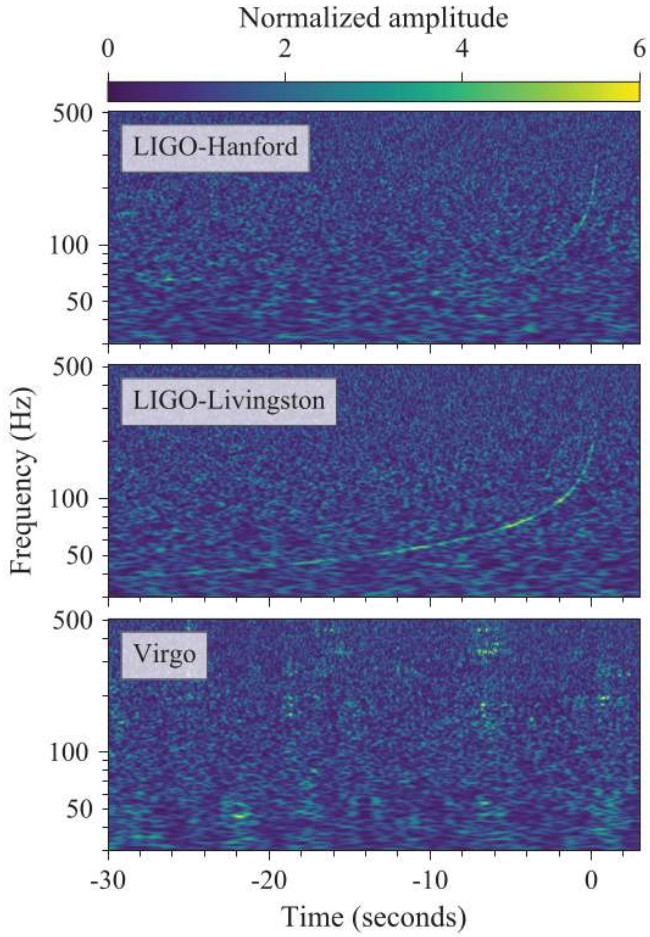

Figure 2.21: The GW event of GW170817 observed by LIGO/Virgo shown in time-frequency plot on 17 August 2017 12:41:04 UTC from Abbott et al. (2017a).

The derived source properties of GW170817 in Table 2.3 for the inspiral and coalescence of two compact objects were predicted by General relativity in either case NSs or BHs. These properties of the GW source are inferred by matching the data with predicted waveforms. The inspiral of objects was calculated from the chirp mass, $M = (m_1 m_2)^{3/5}(m_1 + m_2)^{1-/5}$, using Post-Newtonian. This GW event was observable as the orbit shrinks to merger at above $f_{gw} \simeq 600Hz$, the merger only be calculated using numerical relativity. The ring down was calculated using BH perturbation theory.

Table 2.3: Source properties for GW170817 were derived from predicted waveform models.

Source properties	
Primary mass m_1	$1.46^{+0.12}_{-0.10}M_\odot$
Secondary mass m_2	$1.27^{+0.09}_{-0.09}M_\odot$
Final mass	$2.8M_\odot$
Chirp mass $\mathcal{M}$	$1.186^{+0.001}_{-0.001}M_\odot$
Radiated energy E_{rad}	$> 0.04M_\odot c^2$
Luminosity distance D_L	40^{+10}_{-10}

GRB170817A

GRB170817A was announced by a GCN Notice 14 seconds after the burst was detected by Fermi-GBM and was on 17 August 2017 12:41:06.47 UTC, with a time delay after GW event at nearly 2 seconds (Andreoni et al., 2017). The event was consistent and after 11 hours optical transient was detected, in the 90% probability region of coincident GW event, as AT 2017gfo (Andreoni et al., 2017) in the host galaxy NGC4993 at luminosity distance around $40Mpc$, see Figure 2.22. Significant confirmation was provided by number of observing team with multi-wavelength detectors. Subsequent observations by ultraviolet that revealed a blue transient fading withing 48 hours (Abbott et al., 2017c). Optical transient showed a red ward evolution during period of about 10 days whereas X-ray and radio were not discovery in early observation but it appeared at day 9 and 16 for X-ray and radio respectively whereas ultra high energy gamma-ray and neutrino were not detected (Abbott et al., 2017c).

The SGRB, GRB170817A and an optical transient AT 2017agfo located in the host galaxy NGC 4993 was detected over all the EM spectrum; X-rays,

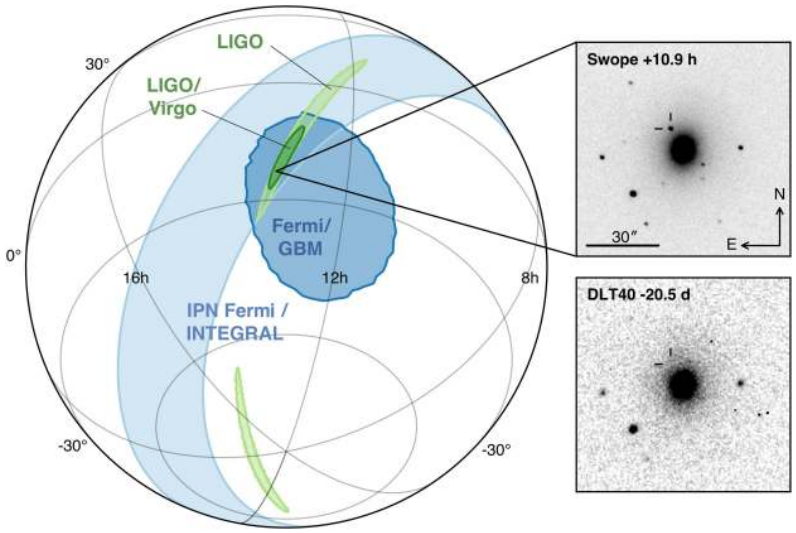

Figure 2.22: Localization of the GW, GRB, and optical signals, on the left panel shows 190 deg^2 in light green for the projection of the 90% credible regions from LIGO, and in the dark green is at 31 deg^2 from LIGO/Virgo localization, and in the dark blue is the IPN triangulation from the time delay between Fermi and INTEGRAL, and top right is the image from Swope optical discovery image at 10.9 hours after GW event comparing with DLT40 early discovery image form 20.5 days before merging (Abbott et al., 2017c).

ultraviolet, optical, infrared, and radio bands over period of hours, days, and weeks (Abbott et al., 2017c). The figure 2.23 illustrates the timeline of the discovery by optical telescopes.

The source was not associated with a supernova so that this event support the merger between NS which followed by SGRB and kilonova powered by the radioactive decay of r-process nuclei synthesized in the ejecta.
The optical light curve of GW170817 is the first and unique case of a well sampled set of data that describes the evolution of the optical brightness of a kilonova. In the perspective of using the GW170817 optical light curve as a template to search for optical transients compatible with a kilonova in this study we fit known optical data as shown in Figure 2.24.

The broken power law in Equation 2.6 can be used to explain the GW170817 kilonova by fitting t_0, rising, and decaying parameters in the Table 2.4 with the soft energy $1.0 \times 10^{16}\ mJy$ and the hard energy $2.5 \times 10^{17}\ mJy$.

The bright curve and the faint curve envelope all the light curves of the

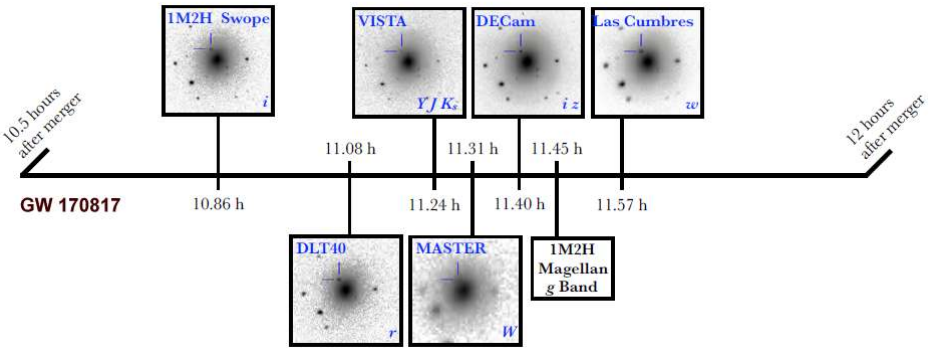

Figure 2.23: GW170817 time line of the optical counterpart discovery. Adapted from Abbott et al. (2017c).

GW70817 kilonova obtained from various observatories (Andreoni et al., 2017; Drout et al., 2017; Lipunov et al., 2017; Tanvir et al., 2017) which provided the energy range emitting between 10^{16} mJy and 10^{17} mJy that the kilonova takes from GW radiated energy (E_{rad}) $0.025 M_{\odot} c^2$.

Table 2.4: Fit parameters to define light curve envelopes the BNS's kilonova.

	$F_o(mJy)$	t_0 (day)	s	a	b
Kilonova GW170817					
faint	1.0×10^{16}	0.16	0.07	8.0	-2.85
bright	2.5×10^{17}	0.25	0.07	4.0	-2.90

2.4 Theories of EM emissions from BBHs

As shown in the Table 2.1, no optical counterpart was found after observing area of GWs due to BBHs. A BBH is usually believed to be almost free of surrounding matter, preventing detectable EM emission (Díaz et al., 2016). EM waves are closely coupled to matter thus they provide significant information about the environment of the progenitor system, e.g. an accretion disk, and the physical process at work during and after the coalescence (Burns et al., 2019; Zhang et al., 2016).

BBHs can be produced either by the evolution of massive stars (Belczyn-

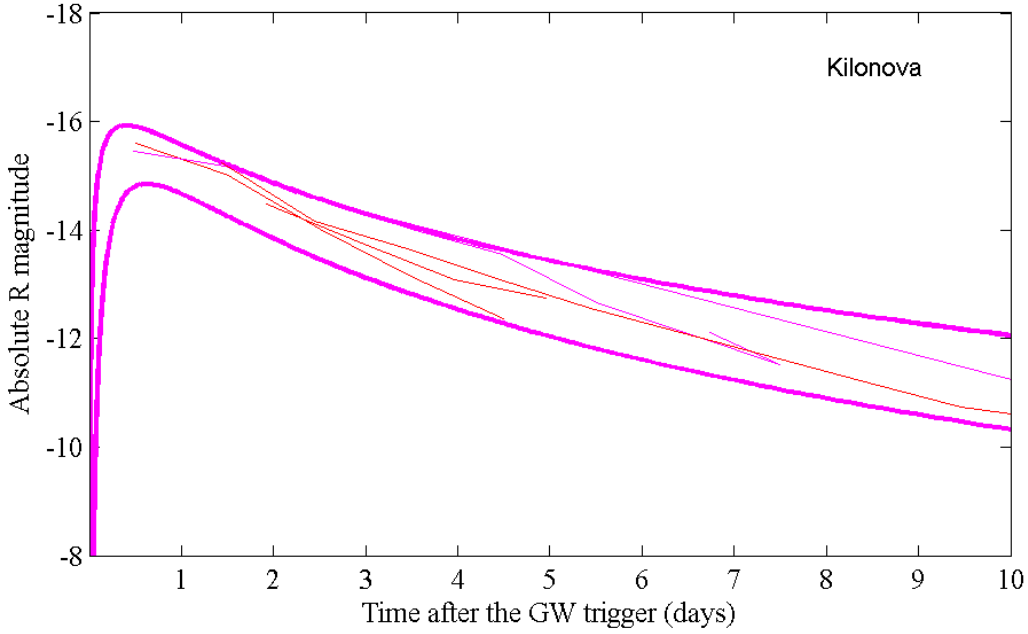

Figure 2.24: Observed light curve in absolute magnitude (red lines) of the GW170817 kilonova observed by various observatories (Andreoni et al., 2017; Drout et al., 2017; Lipunov et al., 2017; Tanvir et al., 2017). The pink lines show the brightest and faintest of energy predicted by Equation 2.6.

ski et al., 2016) in a binary system or by dynamical formation in globular clusters (Rodriguez et al., 2016). The relative importance of both routes remains debated.

It has been proposed that if at least one of two BHs has enough quantity of charge retained by a rotating magnetosphere then a rapid merger's evolution could drives a Poynting flux to power a SGRB or an optical transient that would be detectable (Zhang, 2016).

Another process invoked by Stone et al. (2017) is based on BBH formation in the self-gravitating disks of active galactic nuclei (AGN). The authors proposed that these conditions can favor an EM counterpart due to super-Eddington accretion onto the BH following the merger.

The detection of an EM counterpart of a BBH event, or the limits we can derive from the absence of such detection, would contribute to the understand-

ing of BBH merger processes and it would provide clues on its localization and history, e.g. evolution from a field binary system or dynamic evolution in a globular cluster.

Chapter 3

The TAROT telescopes

TAROT (Télescope à Action Rapide pour les Objets Transitoires – Rapid Action Telescope for Transient Objects) is an automated telescope network (Boër et al., 2017; Klotz et al., 2008) located at three sites around the world observing automatically without user interaction. The TAROT design was set in 1995 to record early optical emission of GRBs (Klotz et al., 2009). It is important to mention at that time no optical counterpart had been found. Nobody was able to estimate the optical brightness of the counterpart of a GRB.

In 1995, GRB triggers were provided by CGRO-BATSE having an error box of position with a mean radius of 3 degrees. For that reason, TAROTs privileged a large FoV. The ideal telescope would have a FoV of $6° \times 6°$ with the possibility to detect a new source at magnitude 18 in less than 1 minute (typical duration of long GRBs). To reduce costs, it was decided to use a single CCD with 2048 $\times$ 2048 pixels (27.6 mm side). All these points were used to size the TAROT telescopes.

To reach a FoV of $6° \times 6°$ using a CCD of 27.6 mm side one must have a spatial sampling of 11 arcsec/pixel, not compatible with the goal to detect magnitude 18 objects due to the sky brightness contribution and spatial confusion. So it was decided to adapt the FoV fixing the CCD size and the spatial sampling at 3.3 arcsec/pixel to avoid spatial confusion and to remain at a sky brightness level allowing to make exposures longer than 2 minutes. In this way the FoV is $1.8° \times 1.8°$, corresponding to a focal length of f=85 cm. The aperture diameter D of the telescope is limited by the optical technologies limiting the ratio f/D to values upper than 3. This limits the aperture diameter to 28 cm. Finally an aperture of 25 cm was chosen.

Since 1995 the TAROT project is lead by Michel Boër CNRS researcher at the Institut de Recherche en Astrophysique et Planétologie (IRAP) at that time. Initial Funds were brought by the IRAP director, three engineers (mechanics, electronic, software) were provided by the direction technique of Institut National des Sciences de l'Univers (DT-INDU). In 2005, engineers of DT-INDU were replaced by those of Observatoire de Haute-Provence (OHP). From 2005 recurrent funds are brought by the Centre National d'Études Spatiales (CNES) allowing the installation of two more telescopes in 2006 and 2016.

Since 2008, TAROTs are also used to react to high energetic neutrino triggers provided by the Antares experiment (Adrián-Martínez et al., 2016) thanks to their large FoV. Outside the time of GRB or neutrino events, routine scientific programs are performed: A survey of the Blazhko effect of RRLyr variable stars (Le Borgne et al., 2012), discovery of 1175 new variable stars (Damerdji et al., 2007), stellar occultations by minor planets (Braga-Ribas et al., 2013), quasars for GAIA calibration (Taris et al., 2018), supernovae discoveries (Contreras et al., 2018) and artificial satellite tracking. The know-how acquired with GRB observations allowed TAROT to participate in 2010 to the first prompt search for gravitational-wave transient electromagnetic counterparts organized by the LIGO and Virgo teams (LIGO Scientific Collaboration et al., 2012). This pioneering work represented a general rehearsal waiting for the run O1 of GW interferometers in 2015.

3.1 Anatomy of the telescopes

Three TAROTs are operated at the moment, TAROT Calern, France (TCA), TAROT la Silla, Chile (TCH), TAROT Les Makes, Reunion island, France (TRE). Hardware is funded by CNRS and CNES. TCA was build in 1998 and is installed at Calern observatory, Observatoire de la Cote d'Azur, France. After some years of tuning the telescope was fully operational for GRB observations in 2003. TCH was designed as a twin of TCA and was installed in 2006 at La Silla ESO observatory, Chile. TRE was designed in 2012 taking account for new GW searching specifications. As a consequence, the FoV was increased by a factor 5 leading to a loss of sensitivity by a factor 3. The innovative concept of TRE is described in Klotz and Thierry (2019). The telescope is installed at Les Makes Observatory, Reunion island, France. All characteristics can be found in Table 3.1.

TAROT telescopes are autonomous. This implies no human interaction during observations. One or two maintenance visits are planed every year to upgrade the hardware. The software is based on AudeLA (Klotz et al., 2012). Tcl scripts are managing the robotic mode from the alert reception to the image calibrations (ROS scripts). Time consuming operations (image processing, celestial mechanics) are written in C as Tcl extensions. A new observing schedule is re-computed when there is a new observing submission within 3 seconds of computing delay. The planning is then flexible and allows to insert acquisition on alerts at any time. When an image is acquired, it is immediately calibrated (dark, flat, WCS) and made available typically less than one minute after the end of acquisition. In this way the archive of FITS processed images can be used to make a rapid analysis.

Table 3.1: TAROT main characteristics.

Name	TAROT Calern (TCA)	TAROT Chile (TCH)	TAROT Reunion (TRE)
Longitude (deg)	6.92 E	70.73 W	55.41 E
Latitude (deg)	43.75 N	29.26 S	21.20 S
Altitude (m)	1320	2398	991
Optical system	Newtonian	Newtonian	Newtonian
Aperture (cm)	25	25	18
Focal ration	f/3.2	f/3.2	f/2.8
Pointing precision (arcmin)	5	5	0.5
Filters	Sloan: g', r', i', z', clear	Sloan: g', r', i', z', clear	No filter
Camera	ANDOR IKON L936 BEX2-DD	ANDOR IKON DW 436N-BV	FLI PL16803
Field of View (deg^2)	1.8 × 1.8	1.8 × 1.8	4.2 × 4.2
Spatial sampling (arcsec/pixel)	3.35	3.35	3.73
Pixel number	2048 × 2048	2048 × 2048	4096 × 4096
Detectivity at SNR= 3 in 2 min (R_{mag})	18	18	17

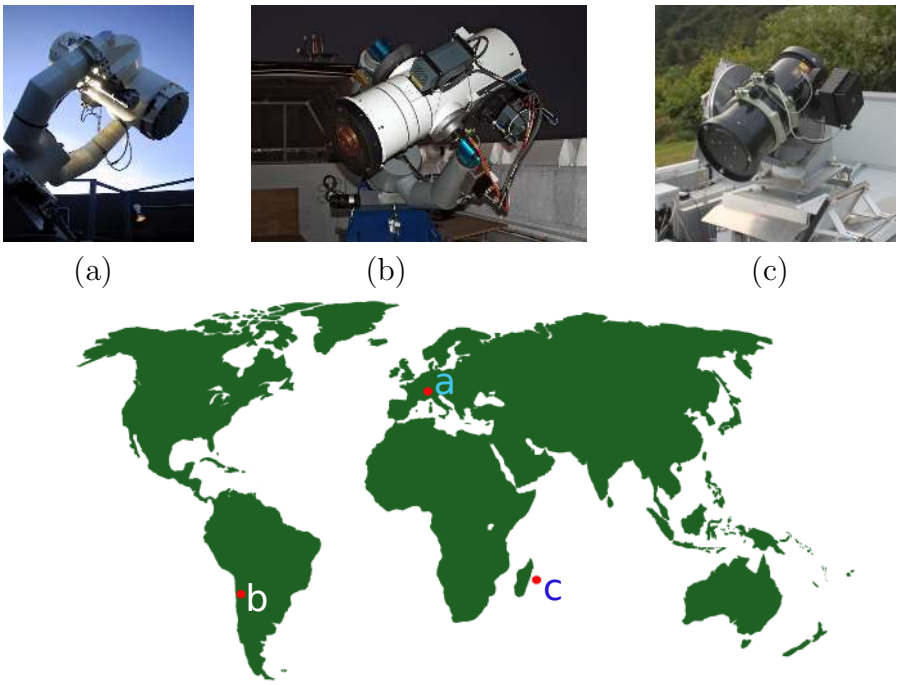

(a) (b) (c)

(d)

Figure 3.1: (a) TCA at Calern observatory, France. (b) TCH at La Silla ESO observatory, Chile. (c) TRE at Réunion island, France. (d) TAROTs on the world map.

Figure 3.2: TRE at Réunion island, Les Makes observatory.

3.2 Historical GRB observations with TAROT

The internet transport protocol service of GRB alerts is provided by the Gama-ray Coordinate Network (GCN) which makes the link between space satellites and ground telescopes (Barthelmy et al., 1995). The first light of TCA was achieved in 1998 and the year after it was tested and prepared for GRB observations (Boër et al., 1999). GRB triggers were provided by the CGRO-BATSE experiment and its large error box obliged TCA to cover the area by a mosaic of individual pointings. Between 1999 and 2000, 21 GRBs were recorded by TCA (Boër et al., 2001) confirming the ability of TAROT in early GRB observations. Unfortunately, no detection of the early afterglow phase was made with 20 seconds of exposures within R magnitude 15^{th}. The CGRO-BATSE experiment was stopped in 2000.

New experiments HETE-II (NASA, 2020) and INTEGRAL (ESA, 2020) started to provide smaller GRB error boxes than the FoV of TCA. Since 2004 the Swift-BAT experiment (NASA, 2012) has provided GRB triggers with small error boxes of $6' \times 6'$ corresponding to 110×110 pixels in a TCA image. In these conditions a simple eye examination of the TCA cropped image allows to detect the optical counterpart. Until now more than 90 percent of the GRBs triggers observed by TAROTs are provided by Swift. In 2019, TCA had observed 108 alerts, TCH had observed 77 alerts and TRE 3 alerts.

3.2.1 GRB 050525A

GRB 050525A showed an optical counterpart bright enough to allow TCA to record its first light curve of a GRB. With these observations, initial goals of TAROT were overtaken. The light curve of TAROT was useful because it was obtained during the Earth occultation of Swift avoiding the experiment UVOT to observe. An optical flux was explained by the TAROT the light curve (Klotz et al., 2005) showing a re-brightening event (see Figure 3.3).

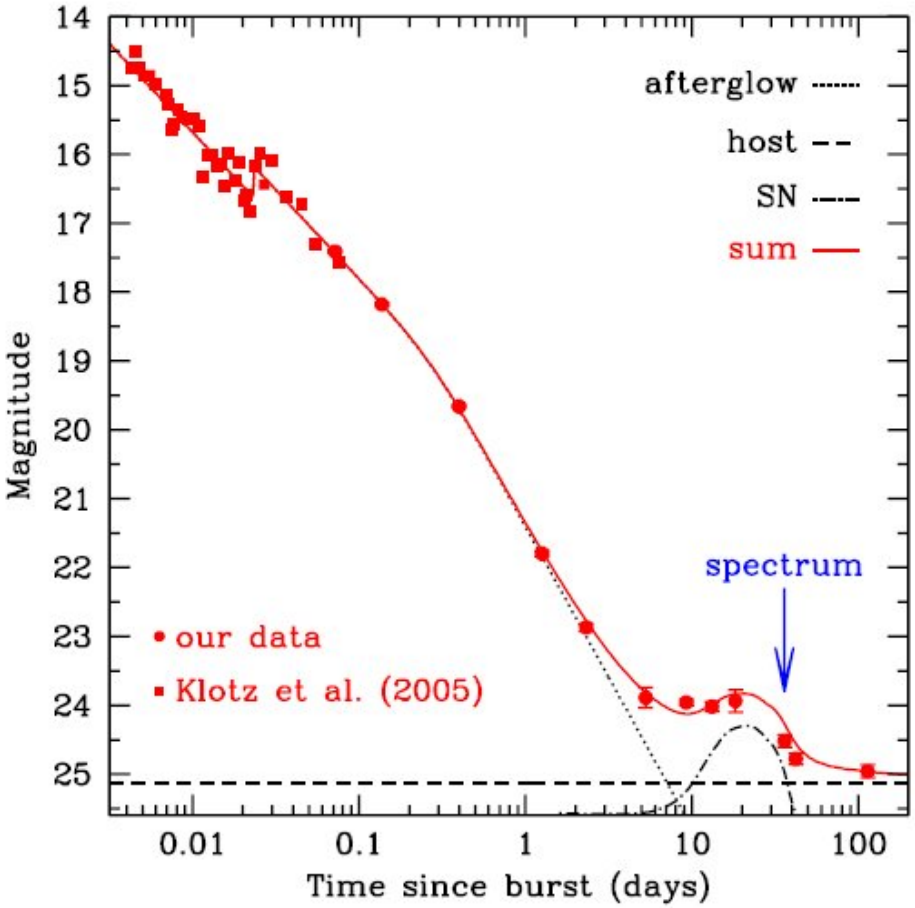

Figure 3.3: Light curve of GRB 050525A published by Della Valle et al. (2006) using early measures from TAROT and late measures from TNG and VLT telescopes. The rebrightening occured at about 0.02 days after the trigger.

3.2.2 GRB 050904

GRB 050904 is exceptional because it was the farthest GRB known at the redshift 6.29 opening the field of cosmology studies with GRBs (Boër et al., 2006). The Swift-BAT experiment detected it using the image trigger mode, optimized when the flux is not intense but the emission remains active for a long time as it is expected for a high redshifted GRB. TCA started observations 86 seconds after the trigger the GRB which was still active (T90=225 s). A peak in optical was temporally correlated with a X-ray flare (Boër et al., 2006) during the prompt emission (see Figure 3.4).

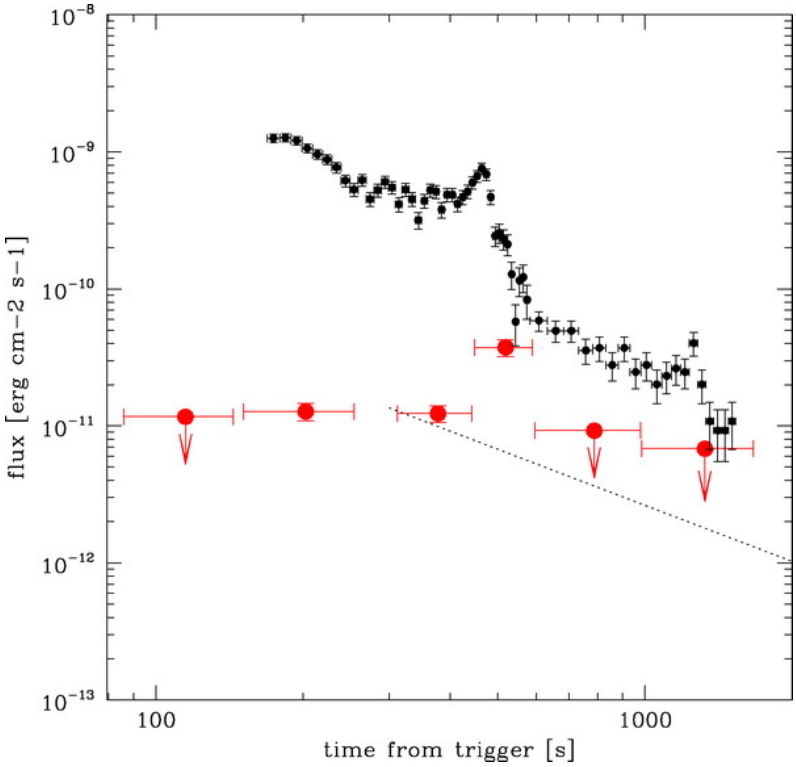

Figure 3.4: Optical (I-band, red) and X-ray (0.5-10 keV, black) light curves of GRB 050904 published by Boër et al. (2006) showing the end of the prompt emission and the transition to the afterglow. The optical emission was measured with TAROT from 86 seconds to 28 minutes after trigger. The X-ray light curve (0.5-10 keV, black) was measured with the XRT from 160s to 33 minutes after the trigger (2). The dotted line shows the extrapolation of the late afterglow (measured 3 hours after the trigger).

3.2.3 GRB 060111B

After the success of the GRB 050904 observations it was decided to change the TCA observation strategy. One of the problem inherent to CCD sensors is the readout time (5 seconds with the TAROT CCD) during which it is impossible to record any information. Applied to the prompt emission of a GRB it means that we are not able to record short temporal optical flux variations. The problem is that GRBs are known to exhibit short duration emission peaks in gamma-rays. It is important to check if during gamma-ray activity the optical emission recorded by TAROT is temporally correlated or not leading to different interpretations. To do that the idea was to let the CCD shutter open, integrate flux during one minute and set the telescope motion to obtain stars as continuous trails over 10 pixels. By this method the stars appear as trails in the one minute image. If one star has flux variations, it is recorded with no dead time due to CCD readout and no lost of sensitivity. The only limitation comes from the density of stars that can overlap each over. GRB 060111B was the first GRB recorded by this method and it was evident there is no correlation between optical and gamma emission (see Figure 3.5). In this case, the decay of the optical emission lead to conclude that TAROT observed a reverse shock event (Klotz et al., 2006).

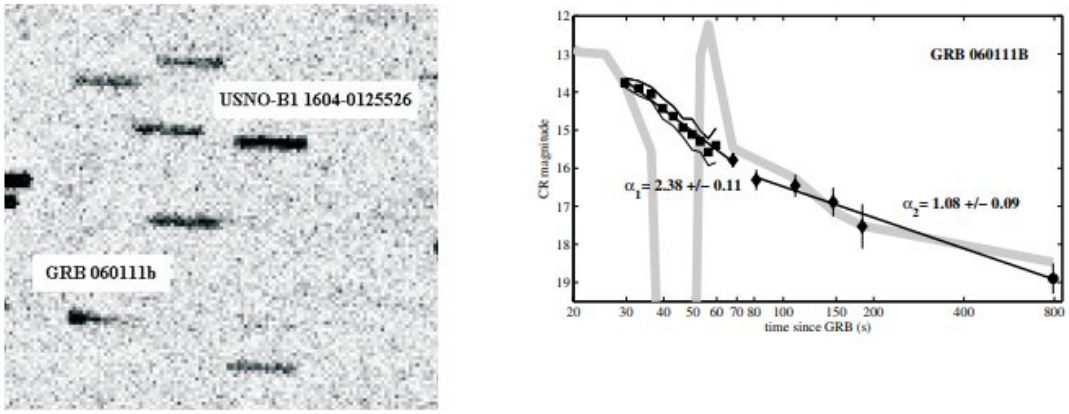

Figure 3.5: Left: Image of 1 minute exposure showing the trailed stars due to the modification of the drift motion in order to spread photometric measures according time along horizontal axis. Right, The corresponding light curve (black for TAROT data) published by Klotz et al. (2006) showing no correlation with Swift-XRT data (grey light curve).

3.2.4 GRB 110205A

Even if gamma emission and afterglow emissions have not the same origin, the relativistic time contraction leads generally to entangle the prompt and afterglow lightcuves. It is possible to separate clearly the two phases if the rise of the afterglow is very slow. It was the case for GRB 110205A. Even if this LGRB remained active during 257 seconds, the afterglow rose progressively to reach a maximum flux 1000 seconds after the trigger. By this way it was simple to analyze the afterglow in the frame of the fireball model (Gendre et al., 2012). Moreover the trail mode used during the first minute allowed to observe the optical flux correlated to the gamma-ray emission (see Figure 3.6 bin 1 to bin 5).

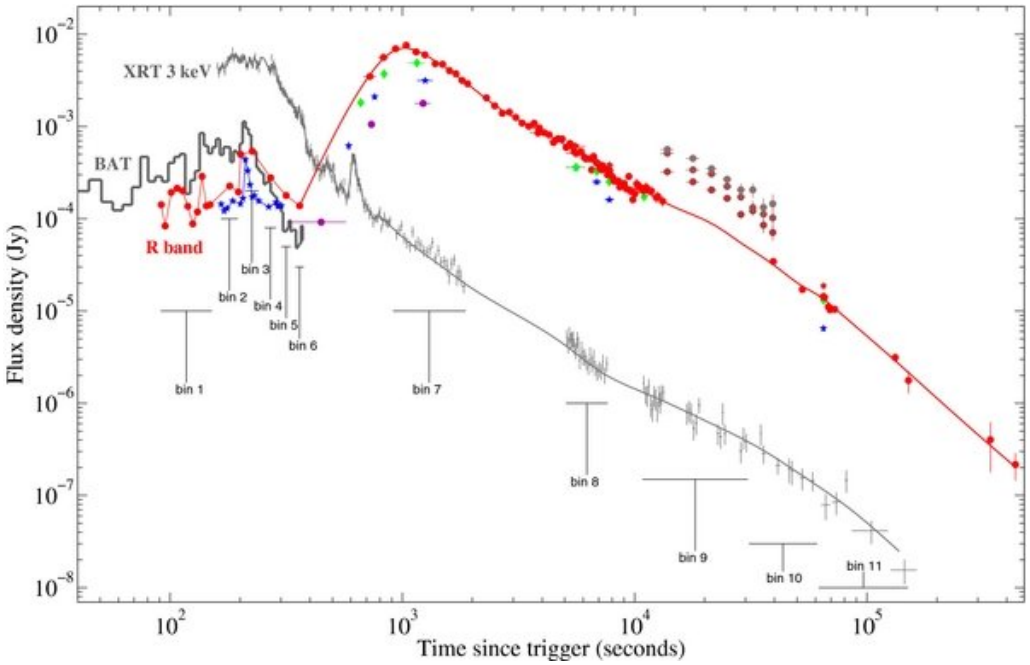

Figure 3.6: Panchromatic light curve of GRB 110205A from Gendre et al. (2012). The BAT data are indicated as a light gray continuous line. The XRT data are indicated by small plus symbols (with errors). The optical data are indicated by purple circles (U band), blue stars (B band), green diamonds (V band), red circles (R band), and red stars (I band). The JHK data during bin 9 are indicated as brown circles. The red (optical) and dark gray (X-ray) lines are the best-fit decay laws.

3.2.5 GRB 111209A

GRB 111209A is the prototype of rare cases where the gamma-ray emission lasts a very long time. In that case T90=6 hours! The TAROT observations are correlated with the gamma-ray ones (see Figure 3.7). This ultra long GRB is interpreted as the collapse of a blue supergiant star (Gendre et al., 2013). Other interpretations were proposed (Kann et al., 2018; Moriya et al., 2020; Stratta et al., 2013).

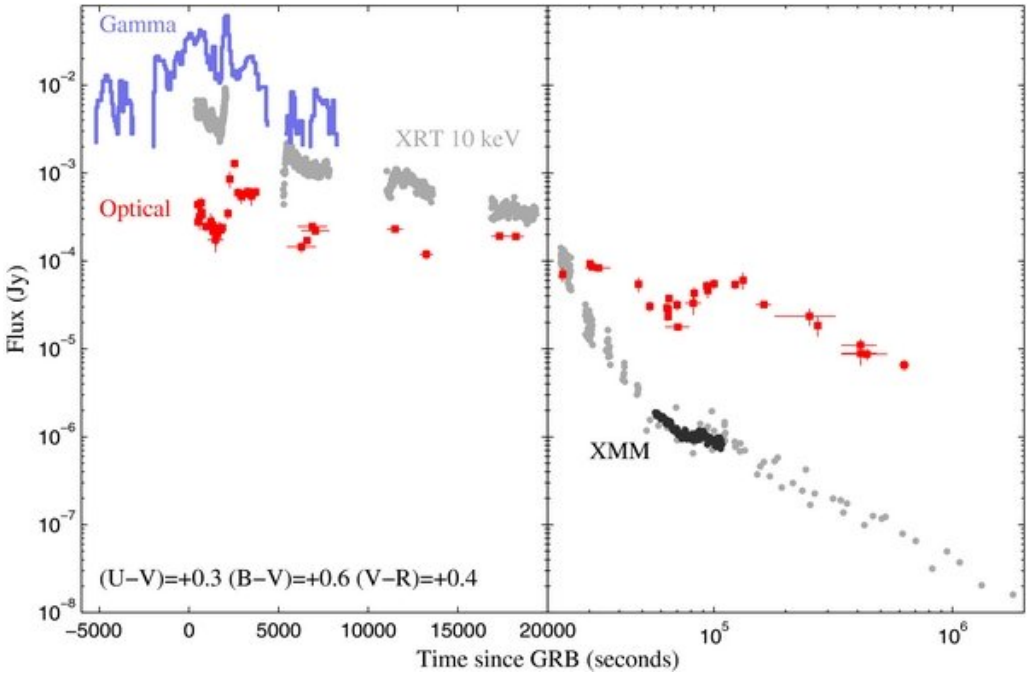

Figure 3.7: Light curve of GRB 111209A, presented with a temporal axis which is linear in the left panel (the prompt emission) and logarithmic in the right panel (the afterglow emission) from Gendre et al. (2013). X-ray data are in gray (XRT) and black (XMM-Newton). The Konus-Wind data (blue solid line) has been scaled to the X-ray data for comparison. The R-band light curve is constructed from TAROT and Swift/UVOT data (color indices are indicated on the plot).

3.2.6 GRB 180418A

Data from TAROT and RATIR telescopes were merged to study the optical light curve of GRB 180418A. The observed T90 = 2.6 seconds lies in the range where one cannot clearly distinguish short from long GRBs. The redshift was not measured. Anyway GRB 180418A remains a good short GRB candidate. The TAROT data indicate that the early decay is compatible with a reverse shock (see Figure 3.8). It is the first case where a reverse shock is detected at optical wavelengths in a short GRB (Becerra et al., 2019).

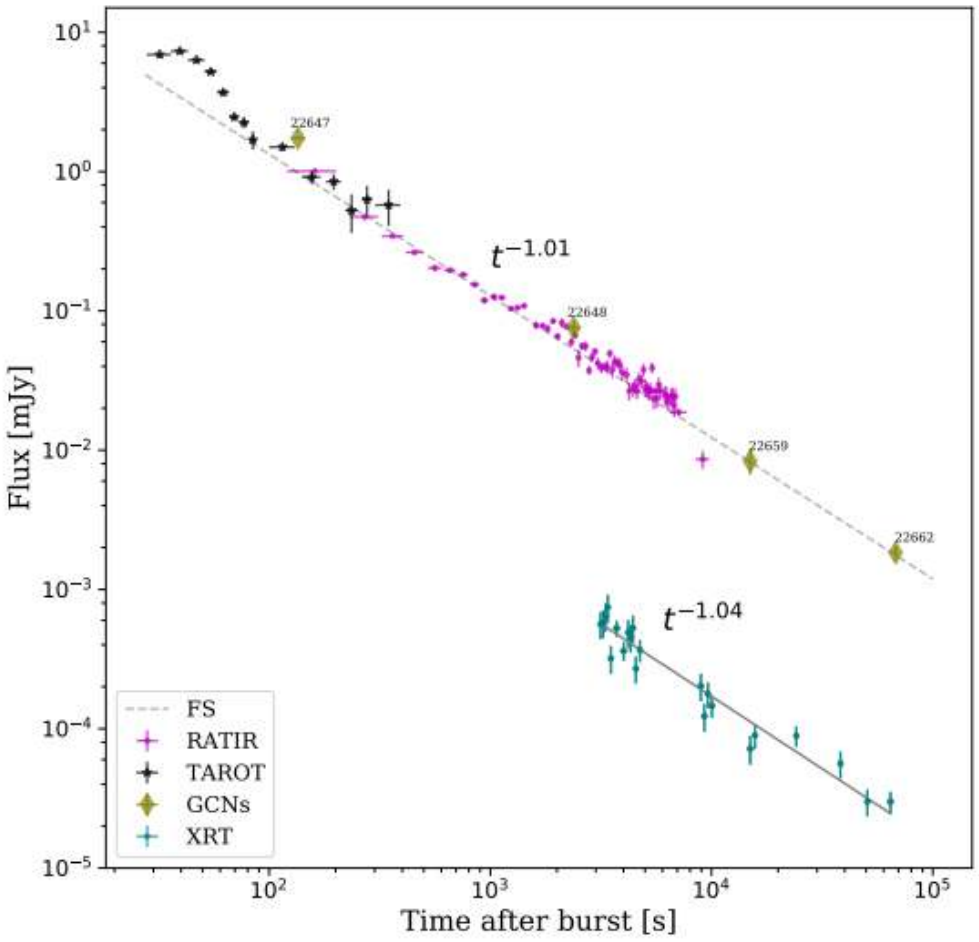

Figure 3.8: Light curve of GRB 180418A, showing a flux excess before 100 seconds revealing a reverse shock emission in this short GRB candidate (Becerra et al., 2019).

3.3 Conclusions on GRB observations with TAROT

Even with a small aperture diameter, TAROT telescopes proved it is possible to perform scientific discoveries even for objects located at cosmological distances. TAROTs also are able to react very quickly to a signal from a satellite or Gamma-ray Coordinates Network (GCN) indicating that a GRB is in progress and can provide fast and accurate positions of transient events within seconds as TAROTs are designed to follow counterparts of GRBs.

The GRB experience opens the doors of new topics to multimessenger astronomy. TAROTs have started to search for optical transients coming from GW events since 2015 and the TAROT team worked on the challenge for search strategy and candidate identification ever since.

Chapter 4

Optical transient search during runs O1 and O2

Advanced LIGO detectors H1 at Hanford, Washington, and L1 at Livingston, Louisiana, performed science run O1 (see Figure 2.10) from 12 September 2015 0:00 UTC to 19 January 2016 16:00 UTC. Detectors were locked together to obtain simultaneous observations during 49 days. Three events were detected: GW150914 (Abbott et al., 2016e), GW151012 (Abbott et al., 2016a) and GW151226 (Abbott et al., 2016b). The identifier of a GW is composed by the two last digits of the year, two digits of the month and two digits of the day of the trigger. If a second GW is detected in the same day the letter B is added at the end of the identifier, and so on. During run O1, the instrumental setup to detect a GW with a signal-to-noise above 8 was a strain sensitivity of $10^{-23}/\sqrt{Hz}$ for frequency around 100Hz. Considering this setup it was expected to detect a BBH mergers of mass around $30M_{\odot}$ and $30M_{\odot}$ within a distance range of 1.3 Gpc, and to detect a BNS mergers of mass around $1.4M_{\odot}$ and $1.4M_{\odot}$ to a distance smaller than 75 Mpc (Abbott et al., 2016f).

The second observing run (run O2) was better in sensitivity and Advanced Virgo joined LIGO on August 1st, 2017. The BNS detection range for LIGO was 80 Mpc in the early phase and larger than 100 Mpc by the run's end, but for Virgo the detection range was limited to around 25 Mpc (Abbott et al., 2019). Run O2 occured from 30 November 2016 16:00 UTC to 25 August 2017 22:00 UTC. Detectors were locked simultaneously during 117 days. Eight events were detected (The LIGO Scientific Collaboration et al., 2019): GW170104, GW170608, GW170729, GW170809, GW170814, GW170817, GW170818 and GW170823. The only BNS detection was GW170817 (Abbott et al., 2017c) and a SGRB followed by an afterglow were detected soon

after the event (see Section 2.3 for details).

4.1 GW detections by interferometers during runs O1 and O2

A total of 11 GW mergers were reported, including a binary neutron collision (reported in Table 4.1). The GW credible region ($\Delta\Omega$) is very large, up to thousands square degrees in the run O1 and down to hundreds of square degrees in the run O2. It is due to the fact the GW signals were better localized once Virgo came online and joined LIGO in August 2017. Figures 4.1 and 4.2 show the sky localizations of 11 GWs.

Table 4.1: GWs detected by LIGO and Virgo during runs O1 and O2. Before merging the masses of the bodies are m_1 and m_2. The chirp mass is $\mathcal{M}$ and the final mass after merging is M_f. d_L is the luminosity distance, E_{rad} the radiated gravitational energy and z the redshift. $\Delta\Omega$ is the location area at including 90% of probability.

Event	m_1 ($M_\odot$)	m_2 ($M_\odot$)	$\mathcal{M}$ ($M_\odot$)	M_f ($M_\odot$)	d_L (Mpc)	E_{rad} ($M_\odot c^2$)	z	$\Delta\Omega$ deg^2
GW150914	$35.6^{+4.8}_{-3.0}$	$30.6^{+3.0}_{-4.4}$	$28.6^{+1.6}_{-1.5}$	$63.1^{+3.3}_{-3.0}$	$430.0^{+150.0}_{-170.0}$	$3.1^{+0.4}_{-0.4}$	$0.09^{+0.03}_{-0.03}$	179
GW151012	$23.3^{+14.0}_{-5.5}$	$13.6^{+4.1}_{-4.8}$	$15.2^{+2.0}_{-1.1}$	$35.7^{+9.9}_{-3.8}$	$1060.0^{+540.0}_{-480.0}$	$1.5^{+0.5}_{-0.5}$	$0.21^{+0.09}_{-0.09}$	1555
GW151226	$13.7^{+8.8}_{-3.2}$	$7.7^{+2.2}_{-2.6}$	$8.9^{+0.3}_{-0.3}$	$20.5^{+6.4}_{-1.5}$	$440.0^{+180.0}_{-190.0}$	$1.0^{+0.1}_{-0.2}$	$0.09^{+0.04}_{-0.04}$	1033
GW170104	$31.0^{+7.2}_{-5.6}$	$20.1^{+4.9}_{-4.5}$	$21.5^{+2.1}_{-1.7}$	$49.1^{+5.2}_{-3.9}$	$960.0^{+430.0}_{-410.0}$	$2.2^{+0.5}_{-0.5}$	$0.19^{+0.07}_{-0.08}$	924
GW170608	$10.9^{+5.3}_{-1.7}$	$7.6^{+1.3}_{-2.1}$	$7.9^{+0.2}_{-0.2}$	$17.8^{+3.2}_{-0.7}$	$320.0^{+120.0}_{-110.0}$	$0.9^{+0.0}_{-0.1}$	$0.07^{+0.02}_{-0.02}$	396
GW170729	$50.6^{+16.6}_{-10.2}$	$34.3^{+9.1}_{-10.1}$	$35.7^{+6.5}_{-4.7}$	$80.3^{+14.6}_{-10.2}$	$2750.0^{+1350.0}_{-1320.0}$	$4.8^{+1.7}_{-1.7}$	$0.48^{+0.19}_{-0.2}$	1033
GW170809	$35.2^{+8.3}_{-6.0}$	$23.8^{+5.2}_{-5.1}$	$25.0^{+2.1}_{-1.6}$	$56.4^{+5.2}_{-3.7}$	$990.0^{+320.0}_{-380.0}$	$2.7^{+0.6}_{-0.6}$	$0.2^{+0.05}_{-0.07}$	340
GW170814	$30.7^{+5.7}_{-3.0}$	$25.3^{+2.9}_{-4.1}$	$24.2^{+1.4}_{-1.1}$	$53.4^{+3.2}_{-2.4}$	$580.0^{+160.0}_{-210.0}$	$2.7^{+0.4}_{-0.3}$	$0.1^{+0.03}_{-0.04}$	87
GW170817	$1.46^{+0.12}_{-0.10}$	$1.27^{+0.09}_{-0.09}$	$1.186^{+0.001}_{-0.001}$	$\leqslant 2.8$	$40.0^{+10.0}_{-10.0}$	$\geqslant 0.04$	$0.01^{+0.0}_{-0.0}$	16
GW170818	$35.5^{+7.5}_{-4.7}$	$26.8^{+4.3}_{-5.2}$	$26.7^{+2.1}_{-1.7}$	$59.8^{+4.8}_{-3.8}$	$1020.0^{+430.0}_{-360.0}$	$2.7^{+0.5}_{-0.5}$	$0.2^{+0.07}_{-0.07}$	39
GW170823	$39.6^{+10.0}_{-6.6}$	$29.4^{+6.3}_{-7.1}$	$29.3^{+4.2}_{-3.2}$	$65.6^{+9.4}_{-6.6}$	$1850.0^{+840.0}_{-840.0}$	$3.3^{+0.9}_{-0.8}$	$0.34^{+0.13}_{-0.14}$	1651

The occurrence of a GW event is not predictable and ground telescopes can react only after the publication of the localization skymap. The delivery of the skymap took about three days after the event for the first GW and typically fell to a few hours at the end of the run O2 due to LIGO/Virgo improvement of the detection pipeline.

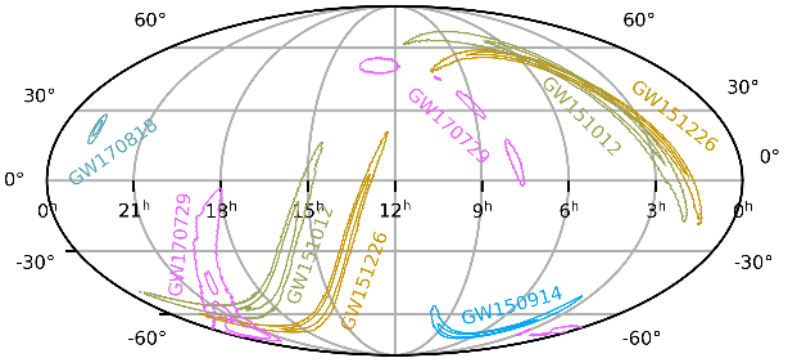

Figure 4.1: Skymaps of O1 events, GW150914, GW151226, GW151012 are detected and sent to GCN network for EM counterpart, along with O2 events GW170729, GW170818 which are not previously released for EM counterpart (The LIGO Scientific Collaboration et al., 2019).

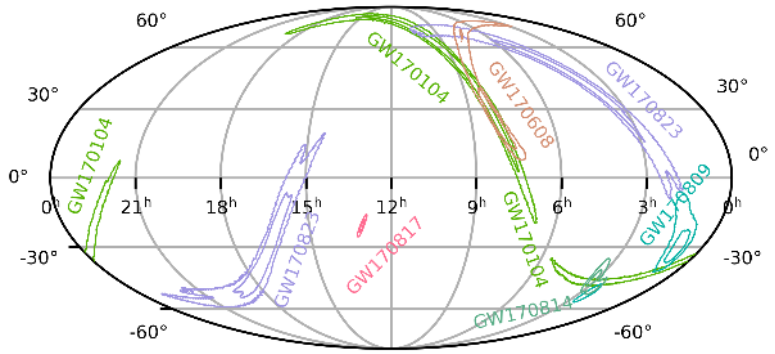

Figure 4.2: Skymaps of O2 events, GW170817, GW170104, GW170823, GW170608, GW170809, GW170814 are confidently detected and sent to GCN network for EM counterpart (The LIGO Scientific Collaboration et al., 2019).

4.2 TAROT observations

The TAROT observations were triggered by the arrival of the VOEvent message from LIGO/Virgo which contains the skymap. During runs O1 and O2 the delay between the GW event and the delivery of the skymap was of the order of hours and the pioneer optical observations were based on the best effort of the community. The TAROT network took the advantage of the robotic operation mode. Note that the delivery of alerts and skymaps during runs O1 and O2 were restricted to some selected observatories. TAROT signed a Memorandum of Understanding (MoU) by Michel Boër and was authorized for the observations of GW events. This implied a publication embargo imposed by the LIGO/Virgo collaboration.

The observation strategy is governed by the identification of candidates as new optical sources and by the photometry follow-up to characterize the candidate types. Known optical transients associated with BHs are usually coming from the interaction of the environment, typically an accretion disk. Intensity and duration of the EM emission depends on the disk content and the magnetic fields. BBH events do not involve such a disk. So the associated optical source nature is difficult to predict because of the lack of a unique theory (see Section 2.4). In the framework of this thesis we are searching first for the brightest optical transients known, i.e. GRBs. We search transients compatible with GRB light curves. During runs O1 and O2, the delay of few hours between the GW event and the reception of the skymap by optical telescopes lead us to consider that the photometry follow-up must be focused only on the decay of the GRB afterglows, i.e. $F \propto t^{-1}$ (see Table 2.2 and Figure 2.19).

When TAROT received a VOEvent, the skymap was downloaded and ten pointing coordinates at the center of error region were computed for each TAROT. We restrict to ten the number of pointings to let time to cover the GW credible region as much as possible. To eliminate the CCD false detections (mainly cosmics and artificial satellites) each image is composed by three frames of 120 seconds. We decided to analyze the three frames separately to eliminate the false detections only after analysis. By this way it is always possible to keep discoveries of very rapid events. After the first visit of the ten pointings, further visits are planed every hour until at least three days after the GW event.

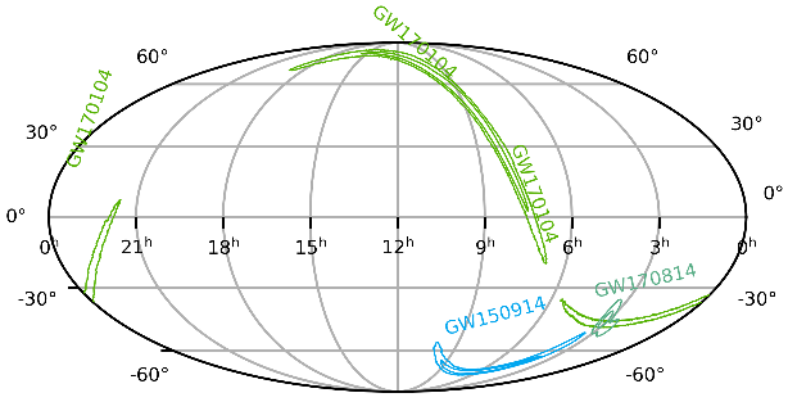

Figure 4.3: Three GW events were observed and followed-up for optical transient by TAROT network.

Three GW events related to BBH mergers were observed by the TAROT network: GW150914, GW170104, and GW170814. As the FoV of the TAROT is small compared to the size of the error boxes, then we divided into tiles covering the area of probability levels above 10%. The tiles were chosen in order to observe them at least three times during the night to avoid fake detections and to get comparison images (Table 4.3).

The GW150914 error box was observed by TCA and TCH from three days after the event, until 2015 September 30. A total of 8 tiles were observed as shown in Figure 4.4. As a result we obtained 400 frames.

The error box of GW170104 was observed by TCA, TCH, and TRE within 30 hours after the GW detection until 2017 January 10. As shown in Figure 4.5, tiles were observed repeatedly. A total of 337 images was produced.

The GW170814 error box was observed by TCA, and TRE within 10 hours after GW detection until 2017 August 18. As shown, 13 pointing were repeated (Figure 4.6), resulting in a total of 333 images.

The exposure time for each observation was 120 seconds and clear filter was used. The limiting magnitude was measured to be $\sim$ 18. We applied the procedure described above to all images.

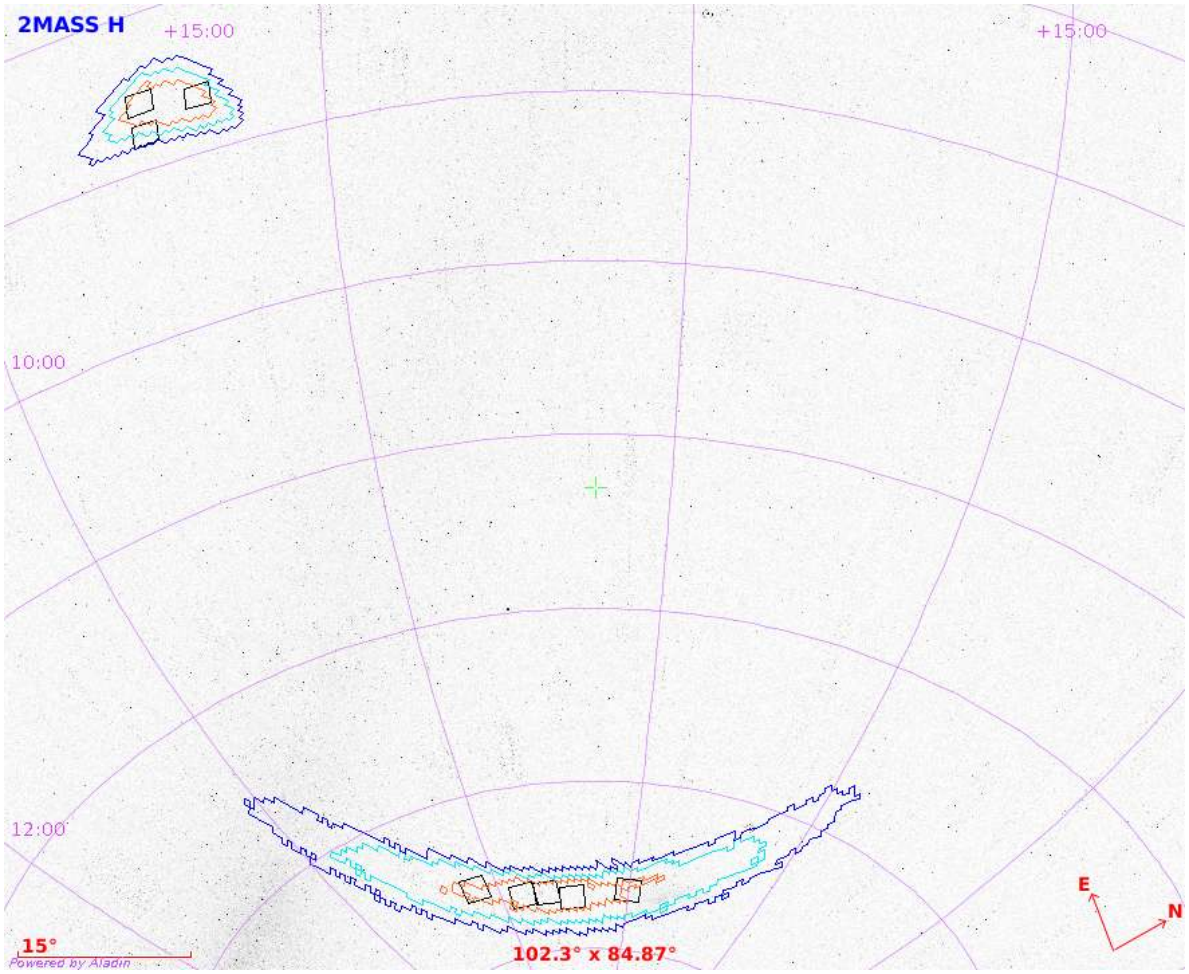

Figure 4.4: Tiles observed by TAROT are displayed over the contours of the initial distributed localization of GW150914. Each square represents an FoV of 3.24 deg^2. The lines represent the enclosed 90%, 70%, and 30% probability contour levels. TAROT observed ∼8% of the GW initial error box.

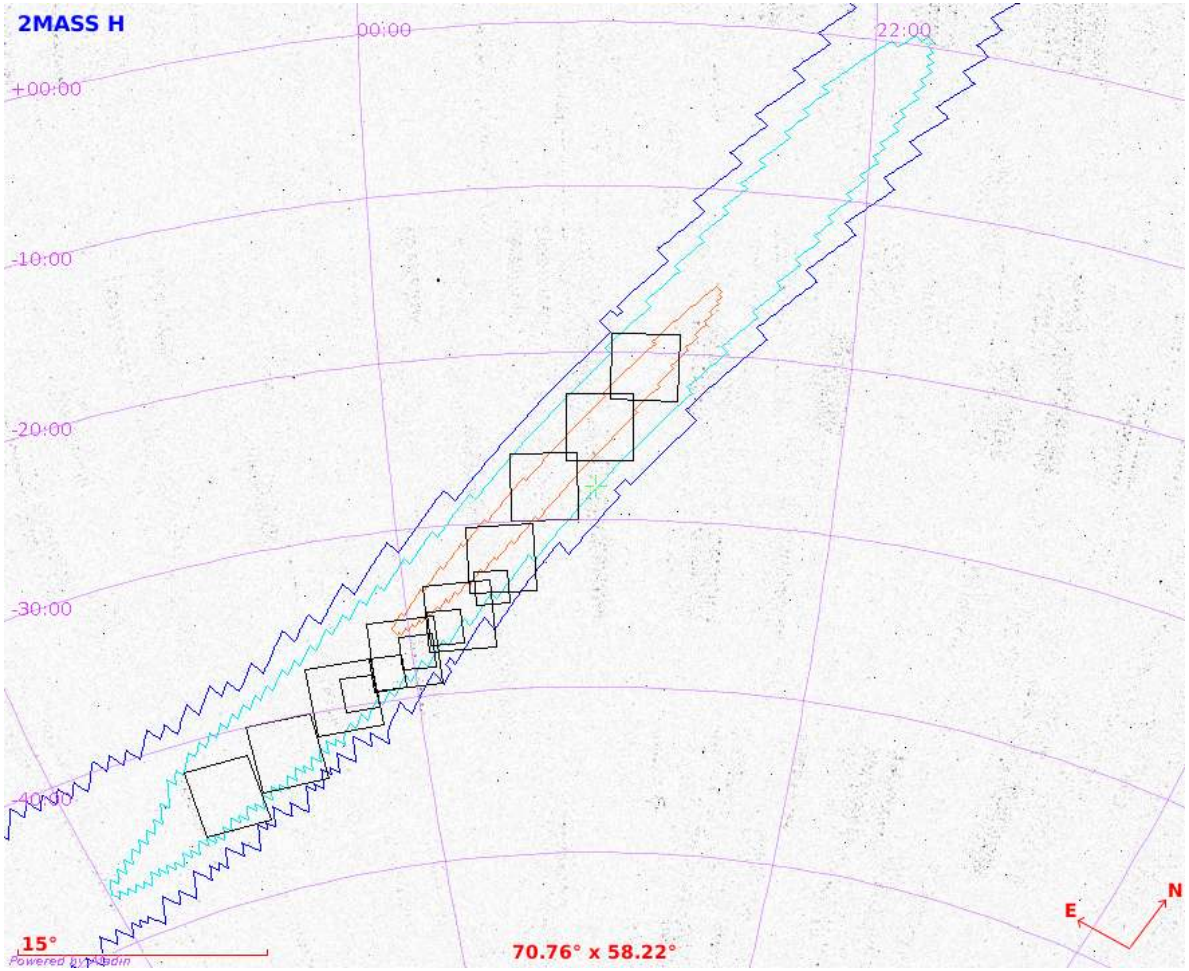

Figure 4.5: Tiles observed by TCA and TCH (3.24 deg^2), and TRE (17.64 deg^2), are displayed over the contours of the localization of GW170104. The lines represent the enclosed 90%, 70%, and 30% probability contour levels of the initial BAYESTAR localization. Two-thirds of the 70% error box were observed by TAROT.

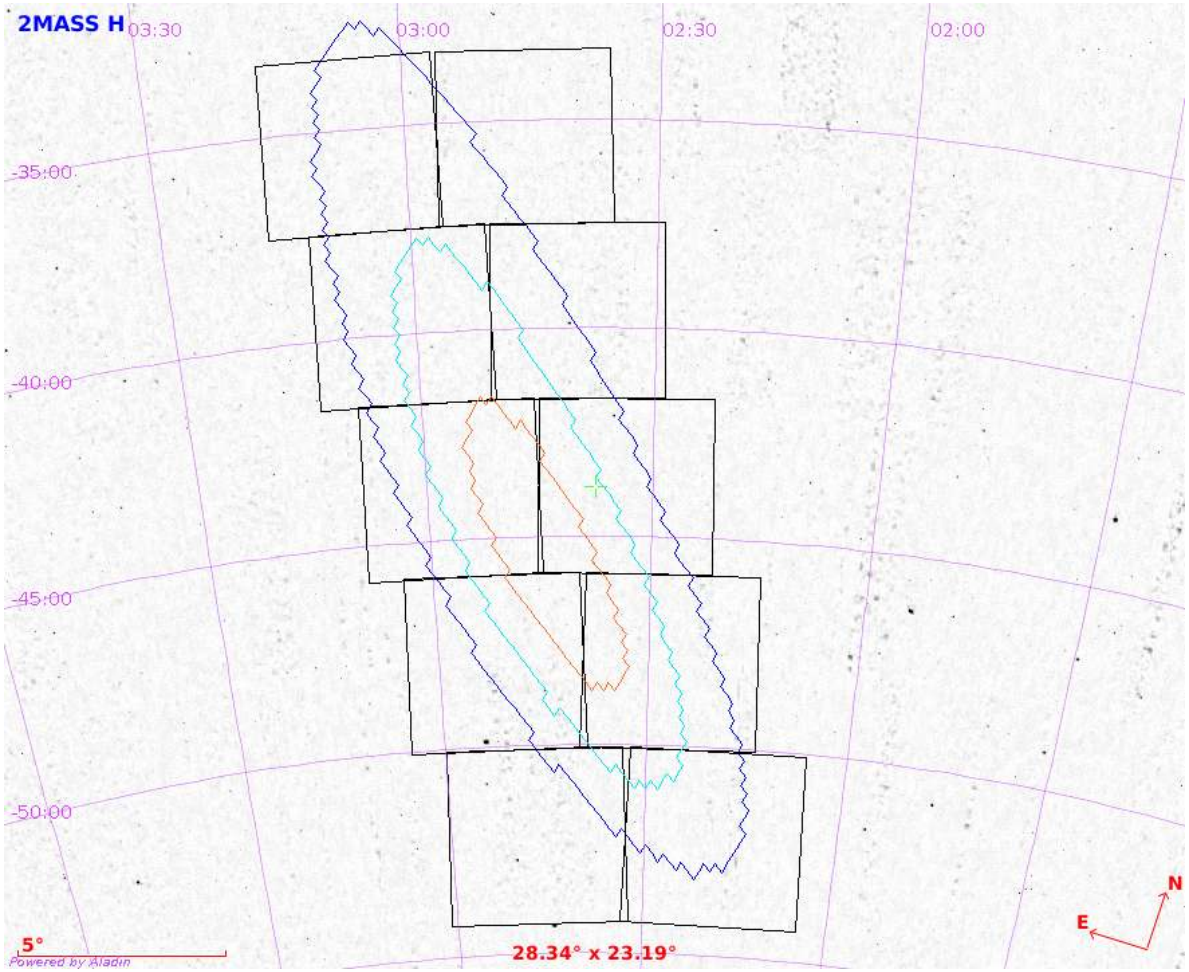

Figure 4.6: Tiles observed by TRE (17.64 deg^2) are displayed over the contours of the localization of GW170814. The lines represent the enclosed 90%, 70%, and 30% probability contour levels of the initial BAYESTAR localization. Almost the entire 90% error box was observed by TRE.

4.3 The image analysis method

In this section we call image a raw frame corrected by dark and flat frames and archived automatically by the standard processing software of TAROT. The standard processing software of TAROT also performs a fit of pure Gnomonic projection in each image and the WCS coefficients are stored in the header of the FITS file. However the large FoV of TAROT implies that images are subject to optical distortions and the pure Gnomonic description gives errors of about 15 arcsec in the corners of the images. This problem is solved in the following procedure.

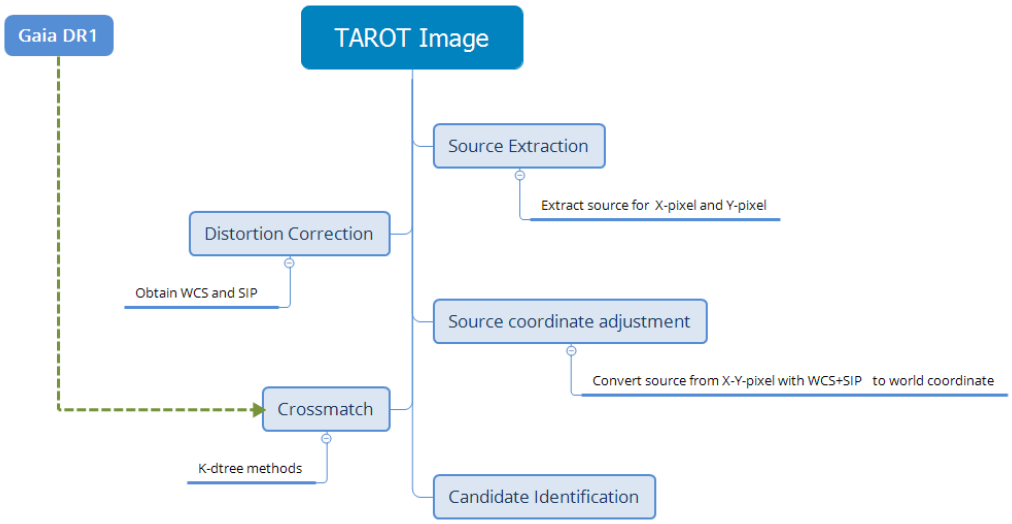

Figure 4.7: Image processing method for a TAROT image.

The principle of image analysis shown in 4.7 is to compare the sources that are found with the entries from the *Gaia* Catalogue Data Release 1 (DR1; Lindegren et al. 2016). To speed up the process, we implemented the catalogue in a local machine. The traditional approach is to crossmatch the presence of the possible objects in a catalog within a given error region that depends on the instrument, acquisition conditions and of a catalog (Egret et al., 1992). Another approach is to cluster the objects hierarchically in a dendrogram before comparison: the hierarchical clustering methods that are either of the "agglomerate type," such as single-linkage (Budavári and Lubow, 2012), or of the "divisive type," such as the k dimensional tree (a K-d tree) by Bentley (1975), are often used in computationally data to illustrate the clustering of samples. A k-d tree is a data structure for storing a finite set of points

from a k-dimensional space. It works by dividing data set in half (left, right or up, down), know as half-spaces. All the points in the 'left' subspace are represented by the left subtree, and the points in the 'right' subspace are represented by the right subtree. To find a closest point to a given query point, we can start at the root and recursively search in both subtrees.

In this work, we used the K-d tree algorithm as it saves computing time. Saving time is important because in the context of run O3, we shall need to send our results timely for the follow-up and confirming our candidates by large aperture telescopes. Moreover, the lower complexity of the K-d tree algorithm requires less memory. This algorithm performs also a quick search for the nearest neighbors for any data coordinate. The algorithm is available in scipy.spatial.KDTree (Maneewongvatana and Mount, 1999) and it has been implemented in *math_coordinates_sky* function of the *Astropy* package by Astropy Collaboration et al. (2013).

Our procedure is summarized in Figure 4.8; it is based on the following five steps:

1. After acquisition, the image is calibrated for non-uniformity and distortions using the *Astrometry.net* package (Lang et al., 2010); we use index files from the Tycho-2 and the Two Micron All-Sky Survey (2MASS) catalogs; this algorithm compares the shape of sets of four stars with the shape of reference stars in the index files and it computes the World Coordinate System (WCS) coefficients with the Simple Imaging Polynomial (SIP) convention (Calabretta et al., 2004). The optical distortions are shown as the residues of angular separations between WCS and the astrometric catalog coordinates in Figure 4.17(a) and (b). The color code shows the angular separation from dark blue (exact match) to red, the redder the higher. To correct distortion, we then apply a distortion correction with the SIP at the fifth order (SIP5; Shupe et al. 2005) in FITS WCS. The result is displayed in Figure 4.17(c), showing a much more homogeneous residue map than that of Figure 4.17(a); nevertheless, this is not satisfactory because the median residue is still at $4.10''$ in Figure 4.17(b), which is higher than the pixel scale of TAROT: $3.35''$/pixel for TCA and TCH and $3.73''$/pixel for TRE (Boër et al., 2017). This is due to the blind matching, which dissociates some sources from the objects in the catalog. In the next section we explain how we refine this result to the ultimate sub-pixel precision for TAROT.

2. The SExtractor package developed by Bertin and Arnouts (1996) has

been used to extract sources in TAROT images; This algorithm works by determining the background and whether pixels belong to the background or objects before it separates objects from background. Extracted sources with pixel coordinates, pixel size, and flux are used for further analysis.

3. The pixel coordinates of the sources are converted to equatorial coordinates using the tools available in the *Astropy.wcs* package from Astropy Collaboration et al. (2013) and the WCS and SIP coefficients obtained from the second step.

4. We use the K-d tree algorithm to match each source with the *Gaia* DR1 available in a local server. The catalog coordinates in the FoV are used as training data by recursively partitioning to the data set: we look for source coordinates in the same FoV through the data set at the nearest neighbor point. The median of the angular separation and the vector of the direction of match are computed and applied to shift the image before matching again until the median of angular separation are minimized. If a source has an angular separation higher than the median, then it is considered as a mismatch and classified as an unknown source.

5. We then flag this *Gaia* unknown source as a possible candidate if it is not present in the USNO-B1.0 catalog, after retrieval of the the updated position from the online VizieR database (Ochsenbein et al., 2000). We apply eventually the photometric measure.

4.4 The transient search algorithm

The algorithm problems have two main objectives which are (1) how to search for possible candidates that do not match any sources in the catalogue, and (2) that are of real astrophysical origin. The Transient Search algorithm locates an unknown source appearing in the image by using K-d tree algorithm with a updated star catalogue as the training data. We copied the *Gaia* DR1 catalogue on a local machine for fast retrieval. Because of its precision at $\sim$ 10 milliarcsecond (mas) (Lindegren et al., 2016) and completeness considered in relation with the TAROT sensitivity of Rmag 17-18 to *Gaia* DR1 of Gmag $\geq$ 20.7, then *Gaia* DR1 is appropriate to train the machine. The mismatches and duplicate matches constitute the preliminary list of candidate transient sources. Duplicate matches occurred when there are more standard stars obtained from catalog. This problem had happened

at the beginning of research (runs O1 and O2) but it was solved by setting the limiting magnitude for star catalog.

We iterate the matching procedure by computing the median of angular separation from first matching between data and catalog, then data coordinate was shifted, see Algorithm 1 in Appendix B, in order to get the smallest possible angular separations, and to reach the ultimate, sub-pixel, precision for TAROT. As a result the median separation got much smaller, as shown in 4.17e and 4.17f. We then decided that a source does not match a known catalog source if its angular separation is above the 3σ median separation. We check for the possible presence of the source in other catalogues using the VizieR database with a small search radius of $10''$. These results in a refined list of possible candidate transient sources.

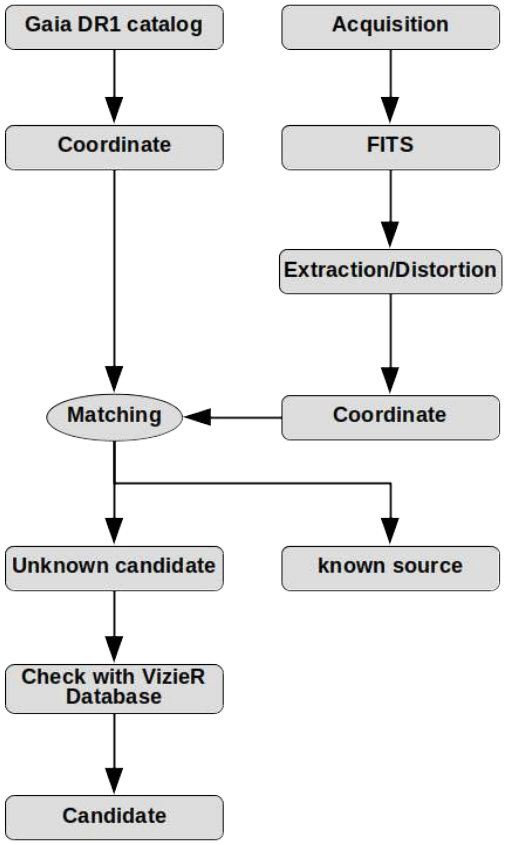

Figure 4.8: Schematics of the processing.

In the final selection of candidates and final confirmation by photometric comparison with standard catalog, we check the list of possible transient sources against the USNO-B1.0 catalog (Monet et al., 2003) with a search radius of $10''$. If the source is not present in this catalogue then a possible candidate is identified. We, then, perform aperture photometry of the candidate to get its magnitude, and whenever possible its light-curve. If it fits with a transient (i.e. non periodic, variable) event, then we validate the source as a possible counterpart candidate. Of course, at this stage, it is not possible to conclude definitively on the nature of the object, as it can be real, i.e. of astrophysical origin, but not related to the GW or GRB transient itself, or an artefact mimicking an astrophysical source. However this careful procedure ensures that the list of possible candidates that has to be observed for later confirmation contains only plausible sources.

To validate the transient search algorithm, we injected simulated sources into several images and we ran the algorithm. The injected sources were spread over the image. As long as the injected sources had high angular separations with respect to the catalogue, they were all detected and correctly flagged as candidates. This applies also to duplicate matches. However fake sources which were at a distance smaller than $10''$ from a catalog source were logically not detected.

4.5 Image analysis and results

TAROT, the network of robotic telescopes, has two types of FoVs $1.8° \times 1.8°$ for TCA and TCH and $4.2° \times 4.2°$ for TRE, but each telescope has the different characteristic which affects to source extraction. We used Sextractor with appropriate configurations for each telescope and sensor combination, and with similar output parameters. The threshold of extraction was set at 3σ and the minimum number of pixels above threshold was set to 5. The value of the seeing was obtained directly from the FITS header (it is a part of the initial calibration procedure of TAROT) and used to discriminate star-like objects from extended sources.

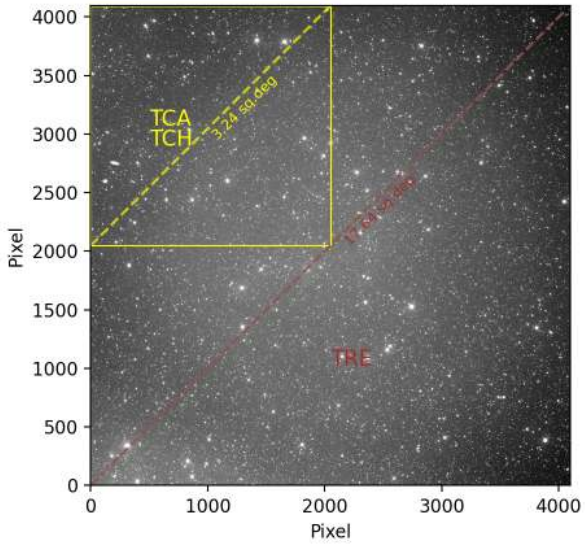

Figure 4.9: TRE has FoV four times larger than the one of TCA but its limiting magnitude is smaller than the one of TCA and TCH. However the large FoV of TRE could cover the sky area much more than TCA and TCH with the same observing duration.

All TAROT images are automatically produced for data reduction with the direct Gnomonic projection which is the fastest method to reduce distortion and the least time consuming. However, the distortion exists and source coordinates are not precise enough for an excellent crossmatch with Gaia DR1 catalog. A better residual distortion will give a better crossmatching. As shown in Figure 4.10 distortion is still present after the first matching

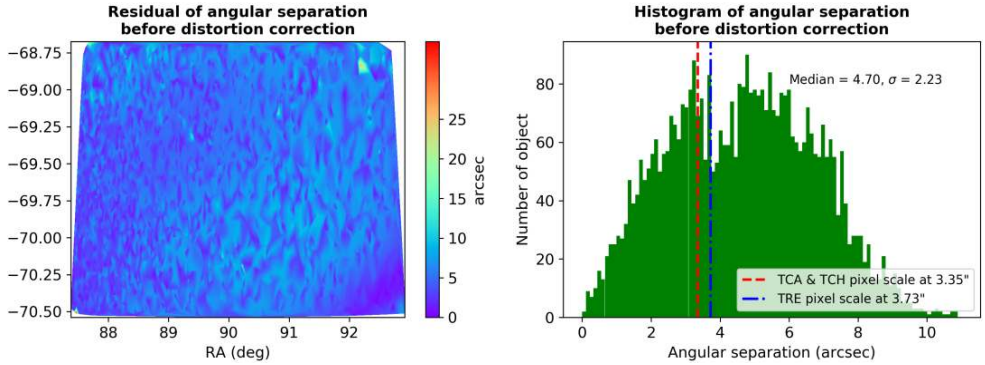

Figure 4.10: Distortions in TAROT images obtained from the comparison with the *Gaia* DR1 catalogue. Left image shows the distortion after the first direct Gnomonic projection and right image is the histogram of the angular separation.

step. We used the Tycho-2 and 2MASS catalogs to map the shape of the bright stars in the image. All TAROT telescopes were considered as having a large FoV and we were able to use the same configuration and index files in range 22′ to 60′ for both Tycho-2 and 2MASS.

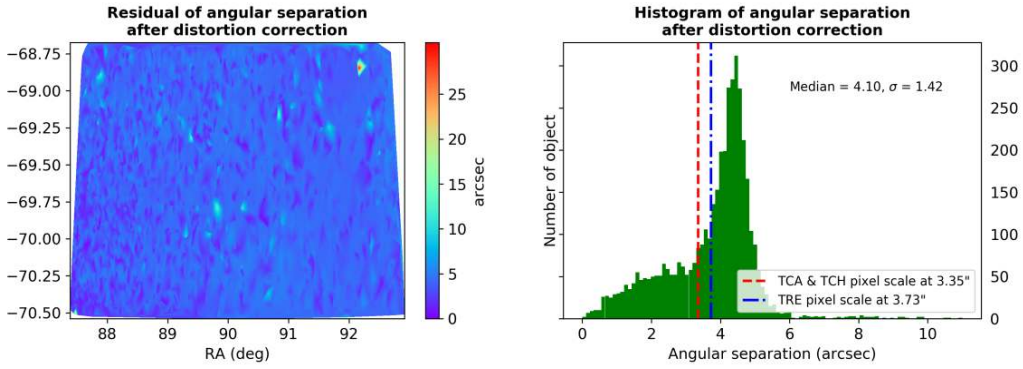

Figure 4.11: Distortions in TAROT images that shows the distortion after the correction computed using the SIP5 algorithm and the corresponding histogram in the right image.

The median of angular separation are compared with TAROT pixel scale as shown in Figure 4.11, but the median of angular separation is still larger than the TAROT pixel scale and catalog-source's matching are acceptable but less accurate. In order to get the smallest angular separations and to reach the

ultimate sub-pixel precision for TAROT, we iterated the matching procedure. As a result the median separation was reduced, as shown in Figure 4.12.

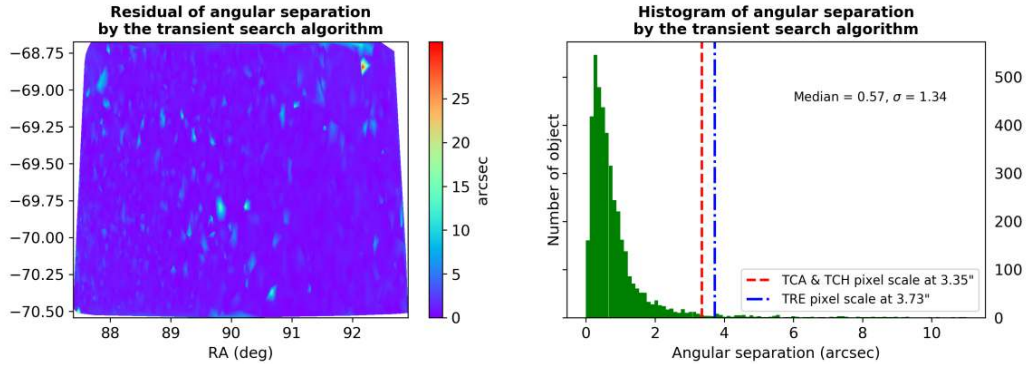

Figure 4.12: Distortions in TAROT images after correction by the transient search algorithm and the histogram shows that we reached a sub-pixel accuracy.

As TAROT has a large FoV, images are subject to optical distortions which are shown in the residues of angular separations between WCS and the astrometric catalog coordinates in Figures 4.10. The color code shows the angular separation from dark blue (exact match) to red. However, a distortion can be corrected by applying the SIP convention (Calabretta et al., 2004) at the fifth order (SIP5) in FITS WCS, and the result is displayed in Figure 4.11 that shows a much more homogeneous residue map than that of Figure 4.10; nevertheless, the median residue is still at $4''.10$ in Figure 4.11, which is higher than the pixel scale of TAROT. we applied the transient search algorithm to get the smallest angular separations shown in Figure 4.12. The transient search algorithm was performed for each image before the search for a candidate and this method gave us the reliable crossmatch.

The possible candidates that were stars and galaxies were automatically rejected by comparing with standard catalogs by a search radius of $10''$. For every candidate we looked for a possible association in a catalog from the VizieR database. Asteroids and artificial objects were eliminated by human vetting, if it was not in standard catalogs. For each candidate, photometry was performed and a light curve was computed. None of the candidates appeared to be a credible optical counterpart of the GW event among the 13 objects reported in Table 4.2.

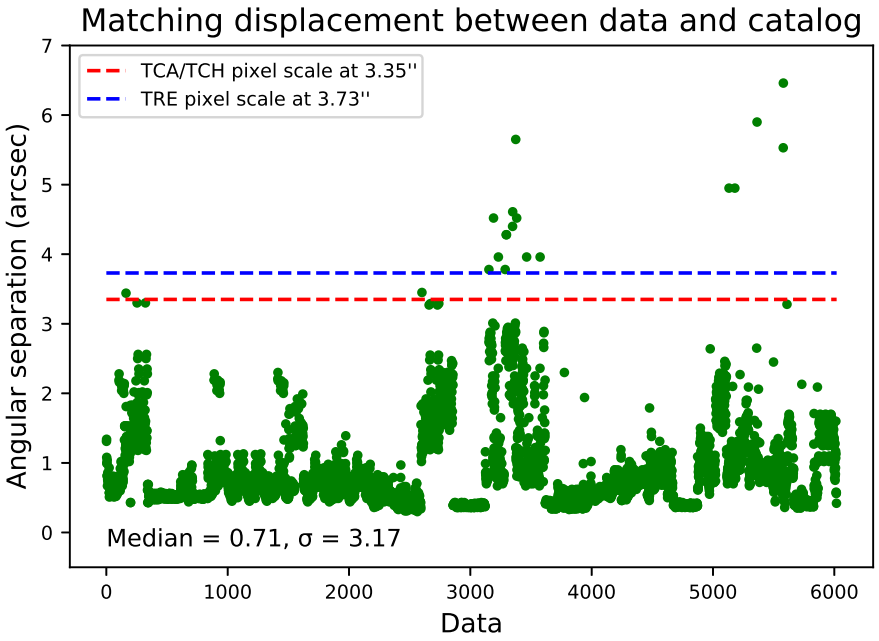

Figure 4.13: The median of matching displacement compared to the TAROT pixel scale in red and blue dashed lines. The efficient matching by search algorithm can be seen that most of the sources are smaller than the size of pixel scale, however, some of them have larger angular distance and will be treated as a mismatch.

After the transient search algorithm, we had to filter the candidates among artificial objects or cosmic-ray hits and the candidate identification depends on these conditions:

- Prompt particle events distributed across an image were rejected as they failed to meet the starlike point spread function criterion of SExtractor with appropriate parameters. Even though some cosmic-rays were still left in the image, they were rejected after applying the photometric test.

- It was possible that some candidates were accidentally eliminated if they were closer than $10''$ to a known source. However a human screening was made at the end of the procedure.

- The algorithm ran poorly on dense star regions, such as the center of Milky Way or clusters. The failure of the algorithm came from the

detection of faint sources that have a magnitude above 18 spread over the entire image considering the pixel scale and FoV of telescopes. For TCA and TCH, the process failed when the number of sources exceeds 15,000 and TRE was around 65,000. In that case it is not possible to run the algorithm, and the processing stops.

- Highly distorted image was ignored by the algorithm.

In total, 13 candidates during runs O1 and O2 where provided this procedure. They are listed in Table 4.2. Figures 4.14, 4.15 and 4.16 show Limiting magnitude, background and α value that we converted from the fraction of the energy released during the coalescence of GW event.

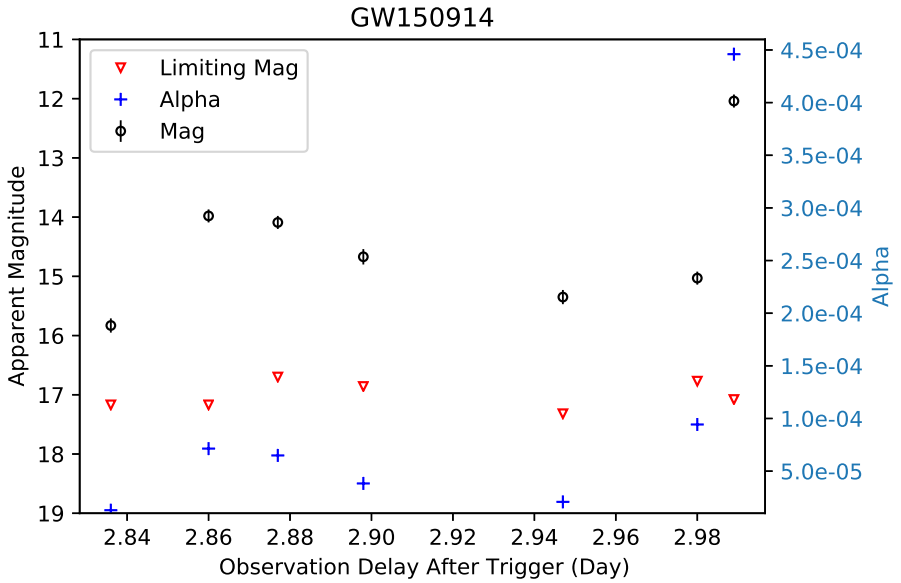

Figure 4.14: The magnitude and limiting magnitude of candidates detected in GW150914 plotted against observation delay with indication of alpha factor. Noted: the last candidate is shifted -6.95 days from actual delay.

There are 7 candidates which are identified from GW150914 (see Figure 4.14), the first candidate was detected in 2.836 days after the event. The limiting magnitude is at around ~ 17 and the α value distributes from 10^{-4} to 10^{-5}, excluding the last candidate which was detected in nearly 10 days after the event which it provided the high α value. This is the first GW detection and TAROT spent a long observation searching for optical transient as we

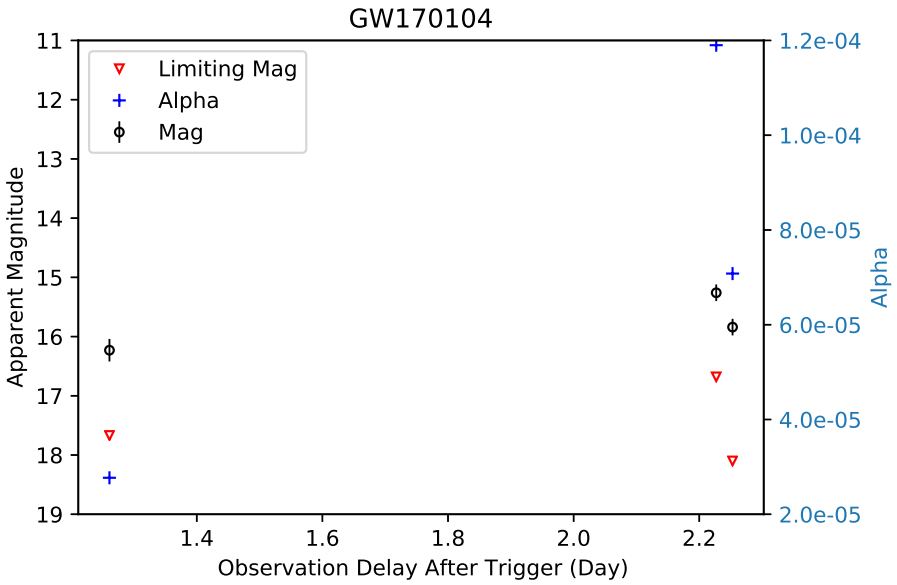

Figure 4.15: The magnitude and limiting magnitude of candidates detected in GW170104 plotted against observation delay with indication of alpha factor.

do not have any knowledge about the connection between optical transient and GWs.

There are 3 candidates which are identified from GW170104 (see Figure 4.15), the first candidate was detected in 1.261 days after the event. The limiting magnitude is at around ~ 17 and the α value distributes from 10^{-4} to 10^{-6}. The gap of candidate detection was nearly a day. We can see that the α value is high with the late detection.

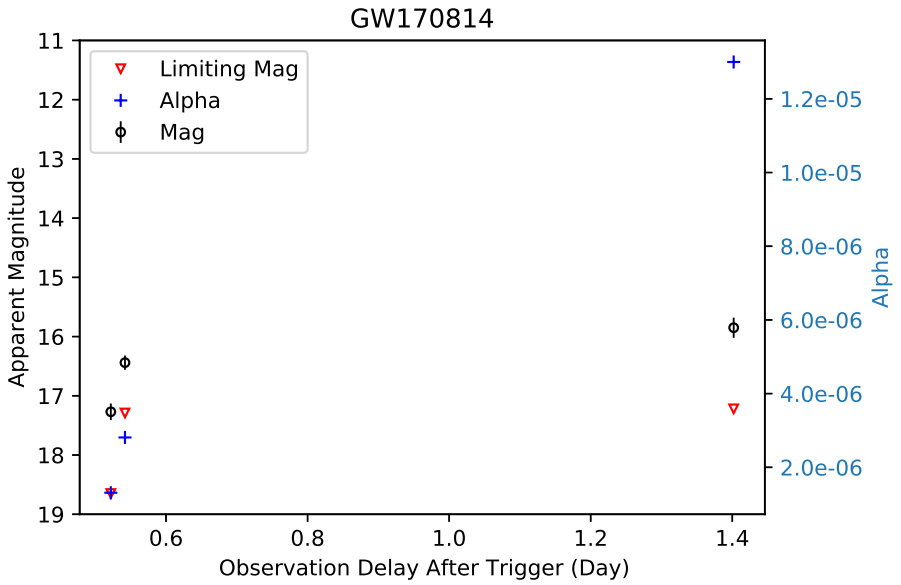

Figure 4.16: The magnitude and limiting magnitude of candidates detected in GW170814 plotted against observation delay with indication of alpha factor. Noted: the second candidate is shifted +0.02 days from actual delay.

There are 3 candidates which are identified from GW170814 (see Figure 4.16), the first candidate was detected in 0.522 days after the event. The limiting magnitude is at around ~ 17 and the α value distributes from 10^{-5} to 10^{-6}. The next candidate was detected around 21 hours after the first one.

If we consider that the flux is proportional to $t^{-\alpha_{opt}}$, as it is the case of decays of GRB afterglows, we can compute the decay parameter, α_{opt}, using Equation 4.1 for the candidates that have measured magnitudes m_1 and m_2 at two epochs t_1 and t_2.

$$\alpha_{opt} = \frac{m_1 - m_2}{2.5 \times log\left(\frac{t_1 - t_{trig}}{t_2 - t_{trig}}\right)} \tag{4.1}$$

where t_{trig} is the trigger time of GW event. We considered that GRBs have decays $0.5 < \alpha_{opt} < 2.5$. All candidates that do not satisfy this criterion are rejected. Unfortunately, all candidates detected in runs O1 and O2 do not have any connection with a GRB or the GW event concerning Equation 4.1.

Table 4.2: The candidates found by the procedure during O1 and O2 explained in this work.

GW Event	Observation Delay After Trigger(day)	R.A. ($J2000$) (h:m:s)	Decl. ($J2000$) (d:m:s)	Mag ($Rmag$)	Limit Mag ($Rmag$)	α (10^{-5})
GW150914	2.836	$07:24:21.00$	$-68:59:05.90$	15.83 ± 0.02	17.17	1.29
LV trigger: G184098	2.857	$07:33:06.29$	$-70:24:57.80$	13.98 ± 0.01	17.17	7.14
2015-09-14 09:50:45	2.877	$07:33:47.07$	$-69:31:16.10$	14.09 ± 0.01	16.70	6.49
$\Delta E = 3.1 M_{\odot}$	2.898	$07:33:22.89$	$-70:27:40.10$	14.67 ± 0.03	16.86	3.83
Luminosity distance = 430 Mpc	2.989	$07:33:45.71$	$-69:33:21.10$	12.04 ± 0.01	17.08	44.6
	2.947	$07:25:16.73$	$-68:50:05.30$	15.35 ± 0.02	17.32	2.08
	9.930	$07:34:56.33$	$-70:03:24.70$	15.03 ± 0.01	16.77	9.43
GW170104	1.261	$23:52:17.83$	$-37:52:45.08$	16.23 ± 0.09	17.67	2.77
LV trigger: G268556	2.253	$23:09:18.14$	$-26:36:52.50$	15.26 ± 0.04	16.69	7.08
2017-01-04 10:11:59	2.227	$00:58:21.95$	$-45:30:20.36$	15.84 ± 0.04	18.10	11.94
$\Delta E = 2.2 M_{\odot}$						
Luminosity distance = 960 Mpc						
GW170814	0.522	$02:41:02.41$	$-49:42:41.28$	17.27 ± 0.04	18.65	0.13
LV trigger: G297595	0.522	$02:40:46.12$	$-49:25:40.31$	16.44 ± 0.02	17.29	0.28
2017-08-14 10:30:43	1.402	$02:45:11.30$	$-49:21:27.00$	15.85 ± 0.07	17.22	1.30
$\Delta E = 2.7 M_{\odot}$						
Luminosity distance = 580 Mpc						

The α parameter represents the efficiency of conversion of GW into EM radiation (see Chapter 6).

Table 4.3: The log of the observations of the tiles derived from the GW error boxes by the TAROT network for GW150914, GW170104, and GW170814.

1	2	3	4	5	6	7	8
Tile #	Instrument	FoV	R.A.	Decl.	Δt	Limiting Magnitude	Conversion Efficiency
		(deg^2)	(J2000)	(J2000)	(day)	(R)	($\times 10^{-6}$)
GW150914							
1	TCH	3.24	090.20	-69.60	2.798	17.16	3.75
2	TCH	3.24	103.50	-70.30	2.805	16.10	9.99
3	TCH	3.24	109.50	-69.70	2.812	19.00	0.69
4	TCH	3.24	115.00	-69.60	2.854	18.62	0.99
5	TCH	3.24	125.00	-68.00	2.937	18.60	1.04
6	TCA	3.24	130.10	+05.30	3.736	17.01	5.72
7	TCA	3.24	134.50	+03.30	3.743	17.09	5.34
8	TCA	3.24	134.70	+06.30	3.749	17.13	5.15
GW170104							
1	TRE	17.64	343.07	-20.85	1.255	17.33	11.03
2	TRE	17.64	000.58	-37.34	1.260	16.88	15.20
3	TRE	17.64	011.15	-42.02	1.265	18.24	4.34
4	TRE	17.64	352.89	-32.19	1.273	16.75	17.29
5	TRE	17.64	345.98	-24.51	1.277	16.82	16.22
6	TRE	17.64	356.19	-35.47	1.284	17.50	8.77
7	TRE	17.64	005.70	-39.44	1.290	17.70	7.29
8	TRE	17.64	016.93	-43.67	1.296	18.49	3.54
9	TRE	17.64	349.71	-28.01	1.301	16.54	21.36
10	TCA	3.24	132.80	+47.98	1.304	16.78	17.18
11	TCA	3.24	130.86	+46.04	1.307	17.01	13.99
12	TCA	3.24	136.38	+52.02	1.326	16.70	18.86
13	TCA	3.24	134.20	+49.89	1.346	17.28	11.19
14	TCH	3.24	353.66	-33.89	1.617	18.78	3.39
15	TCH	3.24	357.32	-36.05	1.621	17.34	12.74
16	TCH	3.24	002.04	-38.37	1.631	19.10	2.54
17	TCH	3.24	004.45	-39.33	1.633	16.80	21.28
18	TCH	3.24	359.62	-37.32	1.667	18.83	3.34
GW170814							
1	TRE	17.64	034.83	-52.29	0.399	16.60	1.86
2	TRE	17.64	046.61	-35.47	0.499	14.83	11.85
3	TRE	17.64	041.46	-35.48	0.503	16.95	1.70
4	TRE	17.64	044.01	-43.84	0.511	18.00	0.66
5	TRE	17.64	038.36	-43.89	0.516	15.93	4.43
6	TRE	17.64	042.96	-48.08	0.521	15.41	7.22
7	TRE	17.64	036.68	-48.09	0.525	17.11	1.52
8	TRE	17.64	045.38	-39.68	0.578	15.58	6.91
9	TRE	17.64	039.92	-39.68	0.583	16.07	4.42
10	TRE	17.64	041.65	-52.29	0.587	16.29	3.63
11	TCA	3.24	034.14	+48.15	3.373	16.16	23.53
12	TCA	3.24	033.10	+44.43	3.378	16.14	24.00
13	TCA	3.24	036.93	+48.15	3.384	16.94	11.49

The first column is the ID number of the tile; column 2 is the telescope name;column 3 is the corresponding FoV; columns 4 and 5 are the centre of the tile; column 6 is the time of the first acquisition with respect of the GW event time; column 7 is the limiting magnitude; column 8 is the conversion efficiency from GW to EM, as defined by the α factor in Equation 6.1.

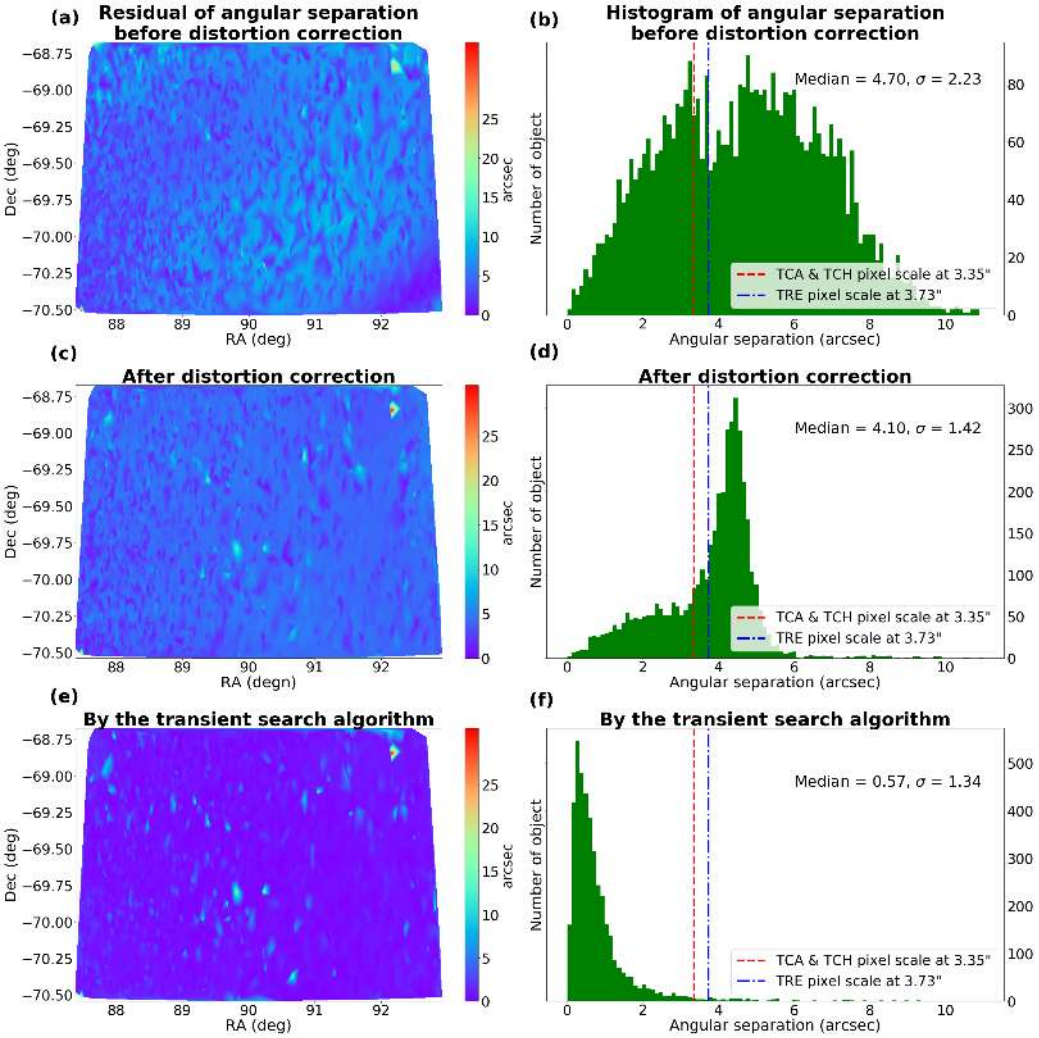

Figure 4.17: Distortions in TAROT images obtained from the comparison with the *Gaia* DR1 catalogue. (a) The distortion after the first direct Gnomonic projection and (b) the histogram of the angular separation; (c) the distortion after the correction computed using the SIP5 algorithm and (d) the corresponding histogram; (e) After correction by the transient search algorithm, (f) the histogram shows that the precision reached is at sub-pixel level. The red dashed line and blue dash-dotted line is the pixel size of TCA and TCH, the blue dash-dotted line is the pixel size of TRE. On the left the color code is from red (high separation) to dark blue (exact matching).

Chapter 5

Optical transient search during run O3

The Gravitational-wave Observatories, LIGO and Virgo, started the third observing run (*i.e.* run O3) on April 2019, 1^{st} and ended on March 2020, 27^{th} as a nearly year long observation. Initially the run was supposed to end on April 2020, 30^{th} but the observation were stopped earlier due to the Corona virus outbreak. More precisely the run O3 was split into a first run O3a from April 2019, 1^{st} to September 2019, 30^{th} and a second run O3b from November 2019, 1^{st} to March 2020, 27^{th}. For NS-related mergers, the expected detection rate was 1 event per month within the range 110 - 130 Mpc for masses of $1.4M_{\odot} + 1.4M_{\odot}$ (The LIGO Scientific Collaboration et al., 2013).

The GW identifiers evolved for the run O3. A GW event is now designed by the form prefix-date-suffix. The prefix S stands for "superevent". Many test events are also injected every day and the prefix is then MS. The date is composed by 6 digits as GRBs. For example 190504. The suffix is a mix of low case letters. The alphabetic order is incremental from a to z and then aa to zz to distinguish every event occurred in the same day.

Note that the delivery of alerts and skymaps during run O3 was public with no need to sign an MoU with LIGO/Virgo as it was the case for runs 01 and O2. As a consequence we have no access to the detailed GW analysis such as the estimated m_1, m_2 values. Public values are mainly the classification of the merger, the estimated distance and the skymap.

For the run O3, the TAROT team decided to join the GRANDMA group (Global Rapid Advanced Network Devoted to the Multi-messenger Addicts).

GRANDMA is a network of robotic telescopes connected all over the world for Time-domain Astronomy. Information is available at `https://grandma.lal.in2p3.fr`. The Figure 5.1 shows the data flow from the alert until the candidates found. In that context, the candidates from the image analysis described in this chapter are published in the GRANDMA papers.

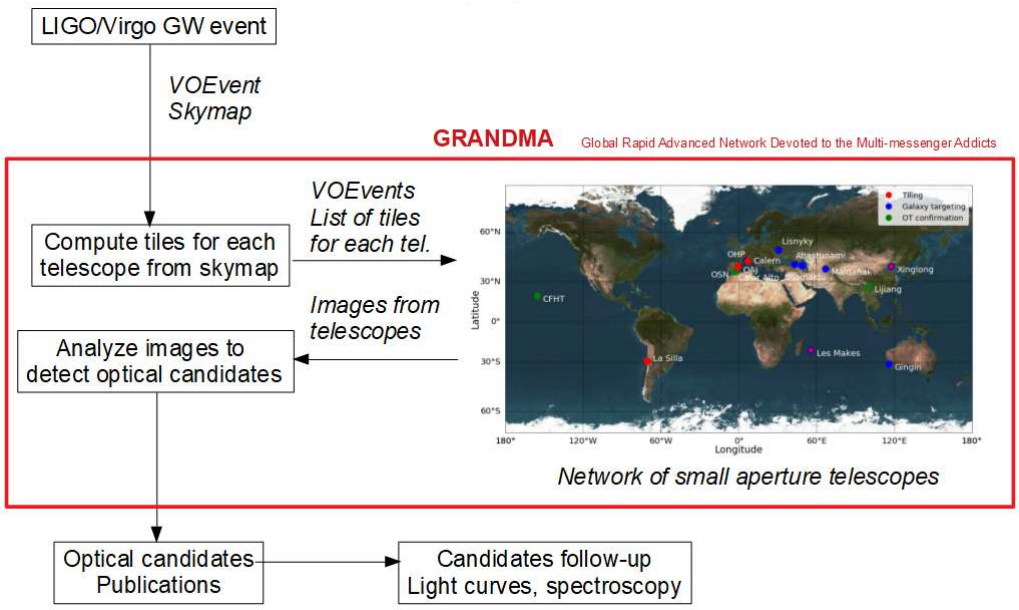

Figure 5.1: Data flow of the GRANDMA network. For a given GW event, TAROT receive a list of tiles selected by the GRANDMA strategy. The Analysis of the produced images are the subject of the chapter of thesis.

5.1 GW detections by interferometers during run O3

During the run O3, the first VOEvent notice of GW candidate events was generally sent within few minutes from the GW detection. Further VOEvnt notices are received according refinements of the event. In GCN VOEvent notices, the tag AlertType is used to indicate the classification level of a GW event. Values of AlertType can be Preliminary, Initial, Update corresponding to an increase of the accuracy of parameters (distance, skymap, classification). Sometimes, AlertType becomes Retractation which corresponds to a vetting decision taken after human inspection for data quality, noise problems from detectors and pipeline behavior. The diagram in Figure 5.2 shows

the sequence of LIGO/Virgo alerts for a single event that distributes through the GCN via notices and circulars.

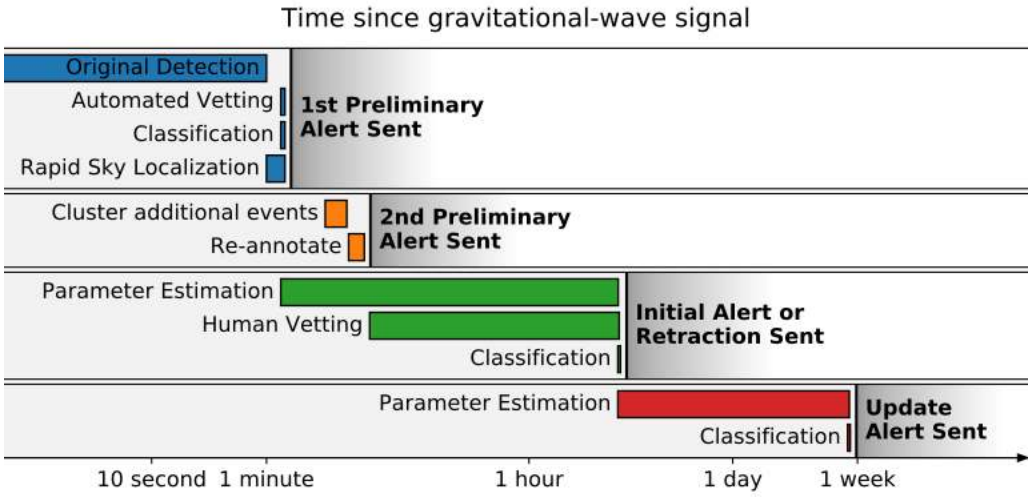

Figure 5.2: Timeline for a single event distributed through the Gamma-ray Coordinates Network (Credit: LIGO/Virgo).

LIGO/Virgo search pipelines run in a low latency mode using two different search methods named modeled and unmodeled. The first method is the modeled of Compact Binary Coalescence (CBC) searches. It uses matched-filtering method pipelines to identify compact binary merges events rapidly, such as GstLAL, MBTA, PyCBC Live and SPIIR. The CBC will look for signals from compact binary mergers of NSs and BHs such as BNS, NSBH, and BBH systems. The second method is the unmodeled (Burst) searches. It has the capability to detect signals from a wide variety of astrophysical sources included compact binary mergers but also core-collapse of massive stars, magnetar star-quakes, and more speculative sources such as intersecting cosmic strings or unknown GW sources. Further informations can be read online from `https://emfollow.docs.ligo.org/userguide`. However the detection methods and classification are beyond scope of this study. We take these information "as is" in this thesis.

Run O3 provides *Classification* for the merger events of that the source belongs to: BNS, NSBH, BBH, mass gap (MassGap) and Terrestrial:

1. BNS is the merger of binary neutron stars. The two masses are lower than $3M_{\odot}$.

2. NSBH is the merger of neutron star and black hole. One mass is higher than $5M_{\odot}$, the other is lower than $3M_{\odot}$.

3. BBH is binary black hole collision. The two masses are higher than $5M_{\odot}$.

4. MassGap is a compact binary systems with one of the masses between NSs and BHs *i.e.* in the range $3M_{\odot} - 5M_{\odot}$.

5. Terrestrial means that the triggered signal is due to statistical noise fluctuations, glitches in detectors, and environmental motion. Therefore Terrestrial signals are not of astrophysical origin.

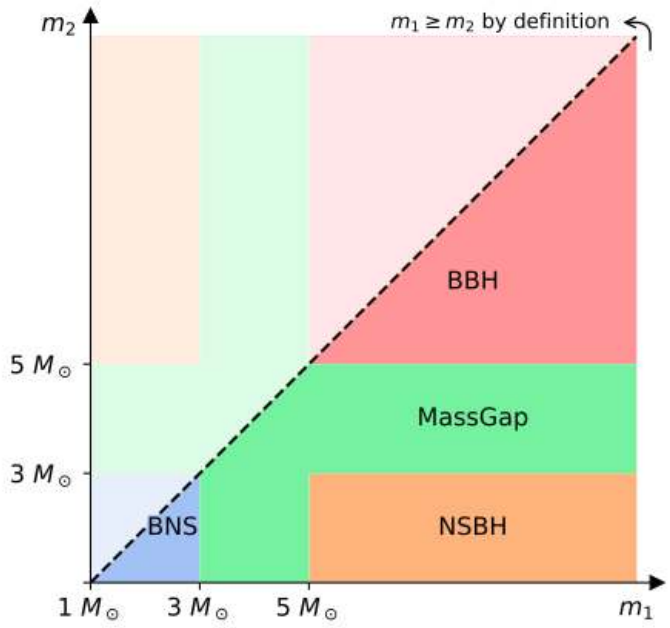

Figure 5.3: The extent of the three astrophysical categories (BNS, NSBH, and BBH) in terms of the component masses m_1 and m_2 (Credit: LIGO/Virgo).

The Figure 5.3 shows the astrophysical categories provided by the Compact Binary Coalescence (CBC) searches. The component masses are defined such that $m_1 \geq m_2$, this gives the primary compact object in the binary more massive than the secondary compact. In the same figure, the upper diagonal region defines such that $m_1 < m_2$, it is lightly shaded color in order to indicate that the definitions of four mass classes (BNS, NSBH, BBH, and

MassGap) are symmetric in m_1 and m_2.

Unfortunately, the alerts do not contain quantitative estimates of the intrinsic properties: masses, spins, GW strain and reconstructed waveforms. These intrinsic properties for run O3 will be available at `www.gw-openscience.org` therefore the computation and estimation by theory of this research are different between runs O1, O2 and run O3.

The total of the detected GW candidates since run O1 is 67 event which is shown in Figure 5.4. There are 3 events detected in run O1 and 8 events in run O2. Significantly run O3 detected 55 GW candidates; 5 BNS events, 5 NSBH events, 36 BBH events, 5 MassGap events and 4 events are classified as Terrestrial. The unmodeled GW burst candidate was detection only one time and it does not list in any category of GW type. All the events are listed in Table 5.1 and 5.2. The skymaps and tiles covered by TAROT for follow-up are shown in Appendix A.2.

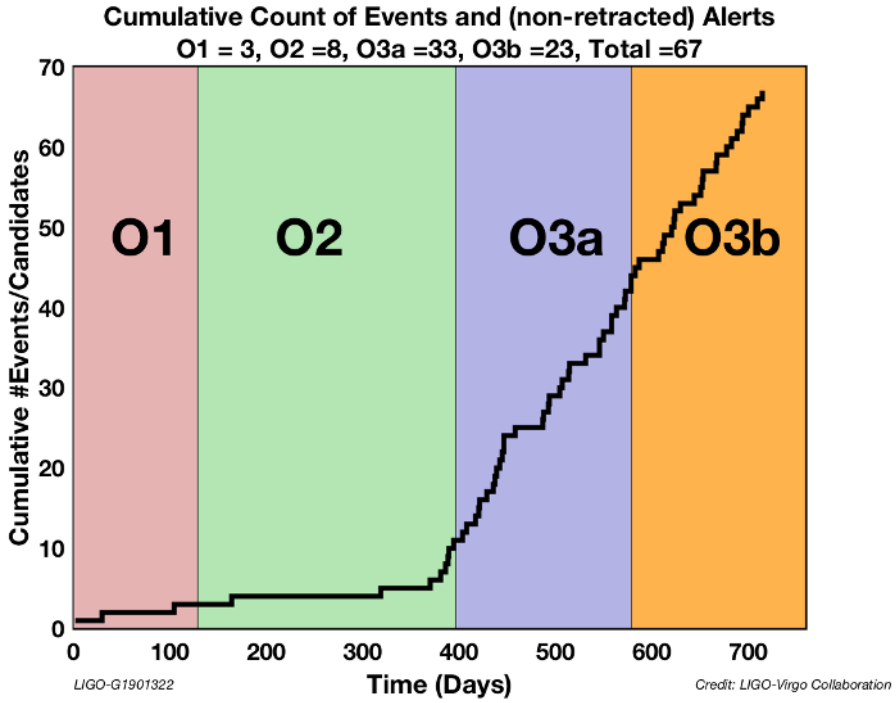

Figure 5.4: A grand total of 55 GW detection candidates was reported since beginning of run O3 on 1st April 2019 and the plot shows the total of GW detection includeing runs O1, O2 and O3 is 67 events (Credit: LIGO/Virgo Collaboration).

Table 5.1: Gravitational wave candidate sources detected by LIGO and Virgo after commissioning break on October 2019 (run O3b).

Event		Initial Analysis				Final Analysis				Classification				
ID	Date	Delay Min	$\Omega^{\circ}_{50\%}$	$\Omega^{\circ}_{90\%}$	Distance Mpc	Delay Min	$\Omega^{\circ}_{50\%}$	$\Omega^{\circ}_{90\%}$	Distance Mpc	BNS %	NSBH %	BBH %	MassGap %	Terrestrial %
S200316bj	2020-03-16 21:57:56	3.17	206	1117	1222 ± 340	1144	21	508	1178 ± 283	0	0	0	100	0
S200311bg	2020-03-11 11:58:53	2.98	15	52	924 ± 188	187	10	34	1115 ± 175	0	0	100	0	0
S200302c	2020-03-02 01:58:11	1.95	1870	6704	1737 ± 500	1429	1368	5656	1820 ± 536	0	0	89	0	11
S200225q	2020-02-25 06:04:21	3.53	205	823	1167 ± 331	865	3	22	995 ± 188	0	0	96	0	4
S200224ca	2020-02-24 22:22:34	3.90	17	69	1476 ± 309	1181	13	72	1575 ± 322	0	0	100	0	0
S200219ac	2020-02-19 09:44:15	148.70	318	1251	1510 ± 405	806	163	781	3533 ± 1031	0	0	96	0	4
S200213t	2020-02-13 04:10:40	2.08	150	2587	224 ± 90	1336	129	2326	201 ± 80	63	0	0	0	37
S200208q	2020-02-08 13:01:17	3.62	128	1120	2900 ± 960	1070	7	26	2142 ± 459	0	0	99	0	1
S200129m	2020-01-29 06:54:58	4.73	10	53	908 ± 202	33	8	41	755 ± 194	0	0	100	0	0
S200128d	2020-01-28 02:20:11	3.70	712	2521	4031 ± 1241	20	625	2293	3702 ± 1265	0	0	97	0	3
S200115j	2020-01-15 04:23:09	6.27	164	920	333 ± 100	818	153	765	340 ± 79	0	0	0	100	0
S200114f	2020-01-14 02:08:18	5.47	37	403	0 ± 0	40	37	403	0 ± 0	0	0	0	0	0
S200112r	2020-01-12 15:58:38	2.92	1540	6199	1136 ± 320	16	611	4004	1125 ± 289	0	0	100	0	0
S200105ae	2020-01-05 16:24:26	194.68	1187	7719	265 ± 71	88	1728	7373	283 ± 74	0	3	0	0	97
S191222n	2019-12-22 03:35:37	3.98	600	2324	868 ± 265	198	449	1850	2518 ± 679	0	0	99	1	0
S191216ap	2019-12-16 21:33:38	16.52	85	300	324 ± 78	1221	68	253	376 ± 70	0	0	99	0	0
S191215w	2019-12-15 22:30:52	7.52	250	923	2216 ± 590	1041	52	361	1770 ± 455	0	0	100	0	0
S191213g	2019-12-13 04:34:08	5.37	259	1393	195 ± 59	1281	852	4480	201 ± 81	77	0	0	0	23
S191205ah	2019-12-05 21:52:08	2.85	692	6378	385 ± 164	34	692	6378	385 ± 164	0	93	0	0	7
S191204r	2019-12-04 17:15:26	42.98	103	433	589 ± 159	64	12	103	678 ± 149	0	0	100	0	0
S191129u	2019-11-29 13:40:29	42.10	263	1011	763 ± 200	474	176	852	742 ± 180	0	0	100	0	0
S191109d	2019-11-09 01:07:17	9.27	448	1487	1810 ± 604	27	448	1487	1810 ± 604	0	0	100	0	0
S191105e	2019-11-05 14:35:21	206.68	249	1253	1185 ± 332	468	65	643	1168 ± 330	0	0	95	0	5

Table 5.2: Gravitational wave candidate sources detected by LIGO and Virgo during run O3a, 1 April 2019 to 30 September 2019.

Event		Initial Analysis				Final Analysis				Classification				
ID	Date	Delay Min	$\Omega^{\circ}_{50\%}$	$\Omega^{\circ}_{90\%}$	Distance Mpc	Delay Min	$\Omega^{\circ}_{50\%}$	$\Omega^{\circ}_{90\%}$	Distance Mpc	BSN %	NSBH %	BBH %	MassGap %	Terrestrial %
S190930t	2019-09-30 14:34:07	6.65	8061	24220	108 ± 38	14	8061	24220	108 ± 38	0	74	0	0	26
S190930s	2019-09-30 13:35:41	7.22	706	1998	752 ± 224	1136	536	1748	709 ± 191	0	0	0	95	5
S190924h	2019-09-24 02:18:46	6.55	144	515	514 ± 132	982	81	303	548 ± 112	0	0	0	100	0
S190923y	2019-09-23 12:55:59	6.05	534	2107	438 ± 133	36	534	2107	438 ± 133	0	68	0	0	32
S190915ak	2019-09-15 23:57:02	6.78	153	528	1557 ± 381	1163	70	318	1584 ± 381	0	0	99	0	1
S190910h	2019-09-10 08:29:58	6.58	8066	24226	241 ± 89	91	8040	24264	230 ± 88	61	0	0	0	39
S190910d	2019-09-10 01:26:19	6.12	1033	3829	606 ± 197	1396	643	2482	632 ± 186	0	98	0	0	2
S190901ap	2019-09-01 23:31:01	5.80	4176	13613	242 ± 81	742	3472	14753	241 ± 79	86	0	0	0	14
S190828l	2019-08-28 06:55:09	22.53	202	948	1609 ± 426	439	108	359	1528 ± 387	0	0	100	0	0
S190828j	2019-08-28 06:34:05	16.08	155	587	1803 ± 423	93	32	228	1946 ± 388	0	0	100	0	0
S190814bv	2019-08-14 21:10:39	21.00	133	772	236 ± 53	165	5	23	267 ± 52	0	100	0	0	0
S190728q	2019-07-28 06:45:10	14.27	211	977	786 ± 212	824	24	104	874 ± 171	0	14	34	52	0
S190727h	2019-07-27 06:03:33	8.40	289	1357	1104 ± 289	662	19	151	2839 ± 655	0	0	92	3	5
S190720a	2019-07-20 00:08:36	2.70	523	1599	1159 ± 364	1105	11	443	869 ± 283	0	0	99	0	1
S190718y	2019-07-18 14:35:12	27.90	79	7246	227 ± 165	65	79	7246	227 ± 165	2	0	0	0	98
S190707q	2019-07-07 09:33:26	39.87	396	1375	810 ± 234	259	310	921	781 ± 211	0	0	100	0	0
S190706ai	2019-07-06 22:26:41	17.77	281	1100	5725 ± 1446	1311	196	826	5263 ± 1402	0	0	99	0	1
S190701ah	2019-07-01 20:33:06	4.92	19	67	1045 ± 234	268	14	49	1849 ± 446	0	0	93	0	7
S190630ag	2019-06-30 18:52:05	3.63	1936	8493	1059 ± 307	65	217	1483	926 ± 259	0	1	94	5	0
S190602aq	2019-06-02 17:59:27	6.47	286	1172	797 ± 238	30	286	1172	797 ± 238	0	0	99	0	1
S190521r	2019-05-21 07:43:59	6.32	162	488	1136 ± 279	33	162	488	1136 ± 279	0	0	100	0	0
S190521g	2019-05-21 03:02:29	6.23	281	1163	663 ± 156	645	144	765	3931 ± 953	0	0	97	0	3
S190519bj	2019-05-19 15:35:44	59.00	169	967	3154 ± 791	84	169	967	3154 ± 791	0	0	96	0	4
S190517h	2019-05-17 05:51:01	35.70	152	939	2950 ± 1038	40	152	939	2950 ± 1038	0	0	98	2	0
S190513bm	2019-05-13 20:54:28	27.28	134	691	1987 ± 501	27	134	691	1987 ± 501	0	1	94	5	0
S190512at	2019-05-12 18:07:14	51.68	79	399	1331 ± 341	1312	44	252	1388 ± 322	0	0	99	0	1
S190510g	2019-05-10 02:59:39	145.32	575	3462	269 ± 108	443	31	1166	227 ± 92	42	0	0	0	58
S190503bf	2019-05-03 18:54:04	36.10	104	448	421 ± 105	45	104	448	421 ± 105	0	0	96	3	0
S190426c	2019-04-26 15:21:55	25.17	472	1932	423 ± 128	66	214	1131	377 ± 100	24	6	0	12	58
S190425z	2019-04-25 08:18:05	42.75	2806	10183	155 ± 45	393	1378	7461	156 ± 41	100	0	0	0	0
S190421ar	2019-04-21 21:38:56	1127.37	447	1917	2281 ± 697	1072	399	1444	1628 ± 535	0	0	97	0	3
S190412m	2019-04-12 05:30:44	60.83	37	156	812 ± 194	115	37	156	812 ± 194	0	0	100	0	0
S190408an	2019-04-08 18:18:02	34.47	82	387	1473 ± 358	123	82	387	1473 ± 358	0	0	100	0	0

5.2 GRANDMA-TAROT observations

GRANDMA aims to locate the optical transients of GW alerts with a network of 18 observatories (24 telescopes) spread around the world which shows in Figure 5.5. The three TAROT telescopes were used in the GRANDMA collaboration during the run O3. GRANDMA telescopes are very different. Some of them can record only images to find optical counterpart candidates, other telescopes can perform spectrometry to characterize the candidates. When a GW trigger is received by GRANDMA, the observation strategy depends on the GW classification. In case of BNS events, GRANDMA activates the small FoV telescopes to record images of selected galaxies located in the skymap. Large FoV telescopes are used for any kind of GW events with a strategy based on the skymap divided into tiles. Data and observational results from this research were used by GRANDMA published papers (Antier et al., 2019; Antier et al., 2020). TAROT researchers involved in GRANDMA are K. Noysena, A. Klotz, and M. Boër appearing as co-authors in the published papers.

Table 5.3: GRANDMA-TAROT telescopes and and their photometric performance from Antier et al. (2019).

Telescope Name	Location	Aperture (m)	FoV (deg)	Filters	$3-\sigma$ limit (AB mag)	Maximum Night slot (UTC)
TAROT/TCH	La Silla Obs.	0.25	1.85×1.85	Clear, $g'r'i'$	18.0 in 60s (Clear)	00h-10h
FRAM-Auger	Pierre Auger Obs.	0.30	1.0×1.0	BVR$_C$I$_C$, *Clear*	17.0 in 120s (R$_C$)	00h-10h
VIRT	Etelman Obs.	0.50	0.27×0.27	$UBVRI$, *Clear*	19.0 in 120s (Clear)	22h-04h
CFHT/WIRCAM	CFH Obs.	3.60	0.35×0.35	JH	22.0 in 200s (J)	10h-16h
CFHT/MEGACAM	CFH Obs.	3.60	1.00×1.00	$g'r'i'z'$	23.0 in 200s (r')	10h-16h
Zadko	Gingin Obs.	1.00	0.17×0.12	Clear, $g'r'i'I_C$	20.5 in 40s (Clear)	12h-22h
TNT	Xinglong Obs.	0.80	0.19×0.19	$BVg'r'i'$	19.0 in 300s (R_C)	12h-22h
Xinglong-2.16	Xinglong Obs.	2.16	0.15×0.15	$BVRI$	21.0 in 100s (R_C)	12h-22h
GMG-2.4	Lijiang Obs.	2.40	0.17×0.17	$BVRI$	22.0 in 100s (R_C)	12h-22h
Thai/TNT	Thai National Obs.	2.40	0.13×0.13	Clear, $u'g'r'i'z'$	22.3 in 3s (g')	11h-23h
UBAI/NT-60	Maidanak Obs.	0.60	0.18×0.18	BVR_CI_C	18.0 in 180s (R_C)	14h-00h
UBAI/ST-60	Maidanak Obs.	0.60	0.11×0.11	BVR_CI_C	18.0 in 180s (R_C)	14h-00h
TAROT/TRE	La Reunion	0.18	4.20×4.20	Clear	16.0 in 60s (Clear)	15h-01h
Les Makes/T60	La Reunion	0.60	0.30×0.30	Clear, BVR_C	19.0 in 180s (R_C)	15h-01h
Abastumani/T70	Abastumani Obs.	0.70	0.50×0.50	BVR_CI_C	18.2 in 60s (R_C)	17h-03h
Abastumani/T48	Abastumani Obs.	0.48	0.33×0.33	$UBVR_CI_C$	15.0 in 60s (R_C)	17h-03h
ShAO/T60	Shamakhy Obs.	0.60	0.28×0.28	BVR_CI_C	19.0 in 300s (R_C)	17h-03h
Lisnyky/AZT-8	Kyiv Obs.	0.70	0.38×0.38	$UBVR_CI_C$	20.0 in 300s(R_C)	17h-03h
TAROT/TCA	Calern Obs.	0.25	1.85×1.85	Clear, $g'r'i'$	18.0 in 60s (Clear)	20h-06h
IRIS	OHP	0.50	0.40×0.40	Clear,$u'g'r'i'z'$	18.5 in 60s (r')	20h-06h
T120	OHP	1.20	0.30×0.30	$BVRI$	20.0 in 60s (R)	20h-06h
OAJ/T80	Javalambre Obs.	0.80	1.40×1.40	r'	21.0 in 180s (r')	20h-06h
OSN/T150	Sierra Nevada Obs.	1.50	0.30×0.22	BVR_CI_C	21.5 in 180s (R_C)	20h-06h
CAHA/2.2m	Calar Alto Obs.	2.20	0.27∅	$u'g'r'i'z'$	23.7 in 100s (r')	20h-06h

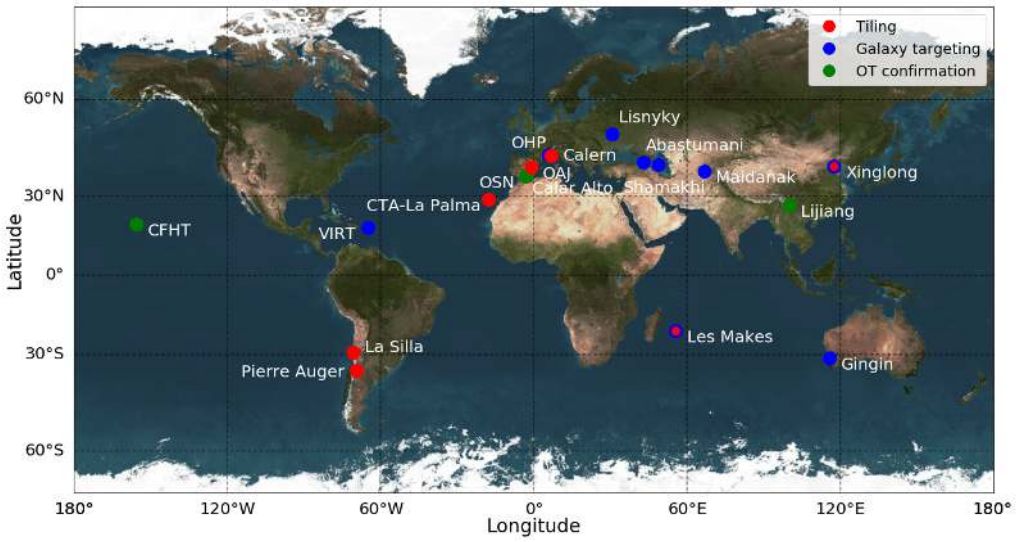

Figure 5.5: GRANDMA-TAROT network are the connection of 18 observatories. TCA, TCH and TRE are shown on the map as Calern, La Silla and Les Makes respectively. The colour encodes the observation strategy followed by telescopes at a given observatory: red for tiling, blue for targeting galaxies, green for following-up candidates (Antier et al., 2019).

The observational strategy is different between runs O1, O2 and run O3. In the first two observing runs, TAROT telescopes focused at the high probability of localization region and attempted to cover skymaps along with the attention of repeated observation for each tile to be able to produce the light curve of unknown object. For example, A 100% coverage of GW170814 with small skymaps was done with the revisiting of all tiles. However, the run O3 observation strategy was optimized for optical follow-up of gravitational-wave skymaps based on Gravitational-wave Electromagnetic Optimization (GWEMOPT) `https://github.com/mcoughlin/gwemopt`. GWEMOPT accounts for tiling that telescopes could observe for both location in skymaps probability and hours available in sky. Tiles issued by GRANDMA were included galaxy-targeting method using the GLADE catalog (Coughlin et al., 2019).

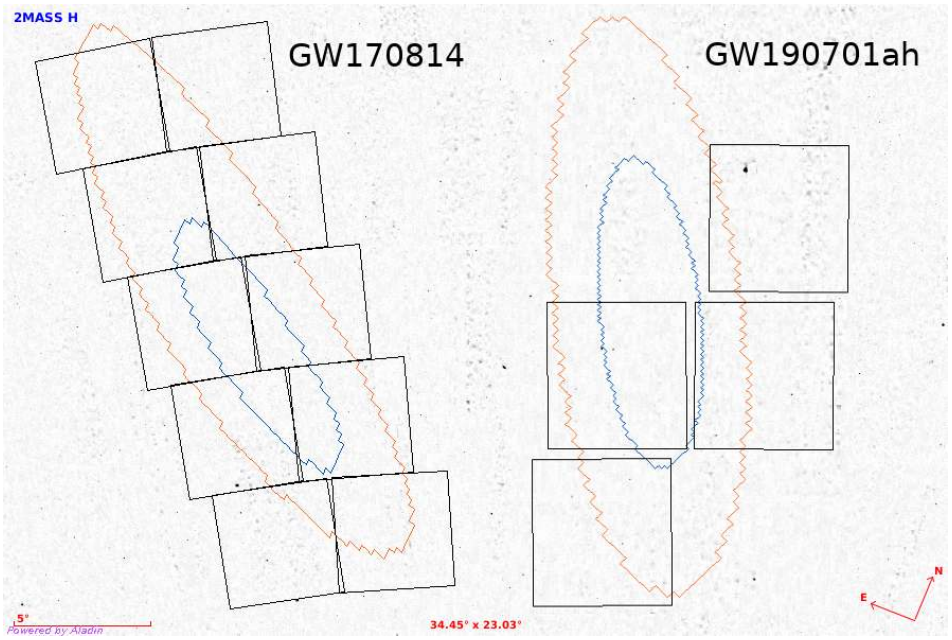

Figure 5.6: TAROT has changed the observational strategy. TAROT attempted to cover 100% of 90% probability of localization in runs O1 and O2 (left) but in the run O3, TAROT observed tiles with optimization for optical follow-up GWs issued by GRANDMA (right).

The summary of TAROT observations performed during run O3 for BBH, NSBH, BNS, MassGap is shown in Table 5.4, 5.5 and 5.6. The 90% c.r. corresponds to the 90 % credible region of the latest sky localisation area sent by LIGO/Virgo. $\delta\, t$ is the delay of observation start with respect to the GW trigger, Δ T is the duration of the observations, Prob (%), Area deg^2 to the coverage of GRANDMA observations compared to the latest revision of the sky localisation area in percentage and in squares degrees. There are some events not observed by TAROT due to maintenance, poor weather conditions, constraint of Moon or Sun.

Table 5.4: GRANDMA-TAROT observations during run O3a for BBH.

Alert	Time (UTC)	Type	Dist (Mpc)	90% c.r. (deg^2)	Telescope	δt (h)	Δ T (h)	Lim. mag	Prob (%)	Area (deg^2)
S190412m	05:30:44	BBH (100%)	812 ± 194	156	TCA	14.1	8.2	18	36.3	24
					TCH					
					TRE	10.1	7.7	17	73.4	123
S190421ar	21:38:56	BBH (97%)	1628 ± 535	1444	TCA					
					TCH					
					TRE	19.7	8.2	17	18.0	124
S190503bf	18:54:04	BBH (96%)	421 ± 105	448	TCA					
					TCH	4.3	4.7	18	17.1	24
					TRE					
S190512at	18:07:14	BBH (99%)	1388 ± 322	252	TCA	25.5	5.8	18	7.2	22
					TCH	13.8	18.1	18	24	24
					TRE					
S190513bm	20:54:28	BBH (94%)	1987 ± 501	691	TCA	0.7	5.6	18	7.0	24
					TCH	6.0	7.5	18	16.7	21
					TRE					
S190517h	05:51:01	BBH (98%)	2950 ± 1038	939	TCA					
					TCH	4.2	17.3	18	8.9	11
					TRE					
S190630ag	18:52:05	BBH (94%)	926 ± 259	1483	TCA	4.7	3.0	18	8.9	21
					TCH					
					TRE	21.0	2.5	17	2.5	71
S190701ah	20:33:06	BBH (93%)	1849 ± 446	49	TCA					
					TCH					
					TRE	2.7	2.9	17	41.7	71
S190706ai	22:26:41	BBH (99%)	5263 ± 1402	826	TCA	0.6	22.7	18	0.27	22
					TCH	0.5	9.1	18	3.9	24
					TRE	3.2	2.0	17	11.8	121
S190707q	09:33:26	BBH (99%)	781 ± 211	921	TCA	10.7	6.1	18	2.4	21
					TCH	13.4	6.3	18	4.0	25
					TRE	5.7	4.8	17	9.5	88
S190720a	00:08:36	BBH (99%)	869 ± 283	443	TCA	0.6	26.8	18	5.0	60
					TCH	1.7	29.4	18	4.0	50
					TRE	0.3	22.7	17	4.0	71
S190727h	06:03:33	BBH (92%)	2839 ± 655	151	TCA					
					TCH	1.6	163.8	18	48.4	68
					TRE	16.7	17.2	17	0.7	70
S190728q	06:45:10	MassGap (52%)	874 ± 171	104	TCA	13.2	29.6	18	18.8	26
					TCH	0.5	50.2	18	23.2	56
					TRE	10.5	22.6	17	83.3	121
S190828j	06:34:05	BBH (99%)	1946 ± 388	228	TCA	12.5	31.3	18	2.7	67
					TCH	0.5	47.6	18	0.04	21
					TRE	15.6	23.4	17	3.4	122
S190828l	06:55:09	BBH (99%)	1528 ± 387	359	TCA	12.6	31.2	18	0.3	67
					TCH	1.2	49.7	18	11.5	69
					TRE	14.2	23.7	17	0.8	157
S190915ak	23:57:02	BBH (99%)	1584 ± 381	318	TCA	0.3	50.7	18	36.1	80
					TCH					
					TRE					
S190930s	13:35:41	MassGap (95%)	709 ± 191	1748	TCA	4.4	55.2	18	5.1	68
					TCH	12.7	46.0	18	3.0	38
					TRE	1.9	31.4	17	18.0	242

Table 5.5: GRANDMA-TAROT observations during run O3b for BBH.

Alert	Time (UTC)	Type	Dist (Mpc)	90% c.r. (deg^2)	Telescope	δt (h)	Δ T (h)	Lim. mag	Prob (%)	Area (deg^2)
S191105e	14:35:21	BBH (95%)	1183 ± 281	643	TCA	56.1	6.4	18	1.1	25
					TCH	57.4	7.9	18	33.6	46
					TRE	49.0	8.47	17	57.3	242
S191109d	01:07:17	BBH (>99%)	1810 ± 604	1487	TCA	1.0	26.0	18	2.1	43
					TCH	29.5	2.2	18	1.0	11
					TRE	20.2	2.5	17	12.3	191
S191129u	13:40:29	BBH (100%)	742 ± 180	852	TCA	10.6	5.5	18	4.6	63
					TCH	10.7	49.0	18	21.9	63
					TRE					
S191204r	17:15:26	BBH (100%)	678 ± 149	103	TCA	0.9	57.1	18	0.8	68
					TCH	7.5	30.4	18	18.2	68
					TRE	1.0	47.8	17	72.9	417
S191215w	22:30:52	BBH (>99%)	1770 ± 455	361	TCA	42.6	5.1	18	18.6	25
					TCH	2.2	54.7	18	13.0	36
					TRE	0.6	47.3	17	8.6	226
S191216ap	21:33:38	BBH (99%)	376 ± 70	253	TCA	19.4	146.4	18	40.1	67
					TCH	27.6	122	18	0.7	11
					TRE					
S191222n	03:35:37	BBH (>99%)	2518 ± 679	1850	TCA	0.7	1.2	18	3.6	71
					TCH	3.0	48.5	18	8.8	56
					TRE	12.5	30.5	17	10.0	157
S200112r	15:58:38	BBH (>99%)	1125 ± 289	4004	TCA	1.5	48.8	18	5.8	71
					TCH	8.6	50.5	18	2.4	63
					TRE	0.3	47.9	17	8.7	379
S200115j	04:23:09	MassGap (>99%)	340 ± 79	765	TCA	12.9	153.8	18	3.8	71
					TCH	0.3	164.9	18	6.5	68
					TRE	11.7	28.8	17	7.4	174
S200128d	02:20:11	BBH (97%)	3702 ± 1265	2293	TCA	19.1	3.2	18	1.5	22
					TCH	2.6	52.5	18	8.7	67
					TRE					
S200208q	13:01:17	BBH (>99%)	2142 ± 459	26	TCA	7.6	104.0	18	0.1	69
					TCH	11.4	56.5	18	43.6	69
					TRE	27.0	8.9	17	91.1	364
S200219ac	09:44:15	BBH (96%)	3533 ± 1031	781	TCA	8.5	50.7	18	8.6	70
					TCH	14.6	27.6	18	11.2	63
					TRE	6.1	31.9	17	23.8	277
S200224ca	22:22:34	BBH (>99%)	1575 ± 322	72	TCA	0.3	99.3	18	1.4	26
					TCH	5.0	52.9	18	20.9	32
					TRE	0.8	98.2	17	90.6	139
S200225q	06:04:21	BBH (96%)	995 ± 188	22	TCA	12.0	58.1	18	0.4	81
					TCH	18.4	51.8	18	< 0.1	74
					TRE	11.9	26.7	17	< 0.1	106
S200302c	01:58:11	BBH (89%)	1820 ± 536	5656	TCA	17.5	54.9	18	6.3	92
					TCH					
					TRE	17.0	28.7	17	10.9	349
S200316bj	21:57:26	MassGap (>99%)	1178 ± 283	508	TCA	0.3	52.5	18	68.0	69
					TCH					
					TRE	41.7	6.4	17	4.9	244

Table 5.6: GRANDMA-TAROT observations during run O3a and O3b for NSBH and BNS.

Alert	Time (UTC)	Type	Dist (Mpc)	90% c.r. (deg^2)	Telescope	δt (h)	Δ T (h)	Lim. mag	Prob (%)	Area (deg^2)
Run O3a										
S190425z	08:18:05	BNS (99%)	156 ± 41	7461	TCA	38.1	29.1	18	0.9	18
					TCH	22.4	47.7	18	1.0	25
					TRE	6.7	33.6	17	2.4	124
S190426c	15:21:55	BNS (24%)	377 ± 100	1131	TCA	7.4	52.9	18	9.7	23
					TCH	15.4	51.4	18	4.3	25
					TRE	7.4	50.9	17	14.0	105
S190510g	02:59:39	BNS (42%)	227 ± 92	1166	TCA	16.7	54.7	18	0.3	24
					TCH	2.1	68.3	18	44.7	31
					TRE					
S190718y	14:35:12	BNS (2%)	227 ± 165	7246	TCA					
					TCH					
					TRE	7.4	51.1	17	48.8	120
S190814bv	21:10:39	NSBH (99%)	267 ± 52	23	TCA	0.6	13.5	18	21.9	32
					TRE					
					TRE	0.5	22.2	17	89.0	139
S190901ap	23:31:01	BNS (86%)	241 ± 79	14753	TCA	1.2	57.4	18	2.5	100
					TCH	4.5	46.6	18	3.0	112
					TRE	0.4	48.6	17	7.2	279
S190910d	01:26:19	NSBH (98%)	632 ± 186	2482	TCA	1.0	67.6	18	4.0	103
					TCH	3.5	52.6	18	11.0	158
					TRE	18.3	44.2	17	32.0	360
S190910h	08:29:58	BNS (61%)	230 ± 88	24264	TCA	10.5	129.1	18	0.5	175
					TCH	25.0	113.1	18	0.6	161
					TRE					
S190923y	12:55:59	NSBH (68%)	438 ± 133	2107	TCA	5.5	46.3	18	2.2	64
					TCH	10.7	32.7	18	3.5	64
					TRE	3.6	55.6	17	20.0	312
S190930t	14:34:07	NSBH (74%)	108 ± 38	24220	TCA	3.5	80.0	18	0.7	135
					TCH	11.9	71.5	18	0.6	110
					TRE	1.0	80.5	17	0.4	94
Run O3b										
S191205ah	21:52:08	NSBH (93%)	385 ± 164	378	TCA	18.9	133.2	18	3.0	71
					TCH	2.9	151.6	18	1.2	68
					TRE					
S191213g	04:34:08	BNS (77%)	201 ± 81	4480	TCA	47.6	73.3	18	0.5	42
					TCH					
					TRE					
S200105ae	16:24:26	NSBH (3%)	282 ± 74	7373	TCA	27.5	118.2	18	3.2	70
					TCH	59.0	98.7	18	3.3	70
					TRE	48.0	7.6	17	9.9	295
S200213t	04:10:40	BNS (63%)	201 ± 80	2326	TCA	0.4	163.3	18	30.4	70
					TCH	45.1	120.1	18	< 0.1	4
					TRE	12.0	31.0	17	0.8	193

5.3 The transient search pipeline

The search for unknown sources from runs O1 and O2 were based on python2 scripts and a lot of human intervention to extract candidates and their photometry was done by hand. The Python script started with the Source extraction and then calibration for extract coordinate by correcting for distortion, then the crossmatch between sources and the Gaia DR1 was performed with the search nearby method and the unknown sources were identified by the angular matching distance. However Asteroids and comets were checked manually with the asteroid's database and comet's database. The light curve of unknown object was compared to the temporal profile of optical transients then the candidates were identified afterwards and user vetting was needed eventually. The experience from runs O1 and O2 has been used to code the detection pipeline for TAROT telescopes in the run O3.

The transient search pipeline shown in Figure 5.7 for run O3 is designed by including an aggregate of scripts from data analysis of runs O1 and O2 with autonomous improvement and is based on Python3 and the Gaia DR2 catalog is used for crossmatching.

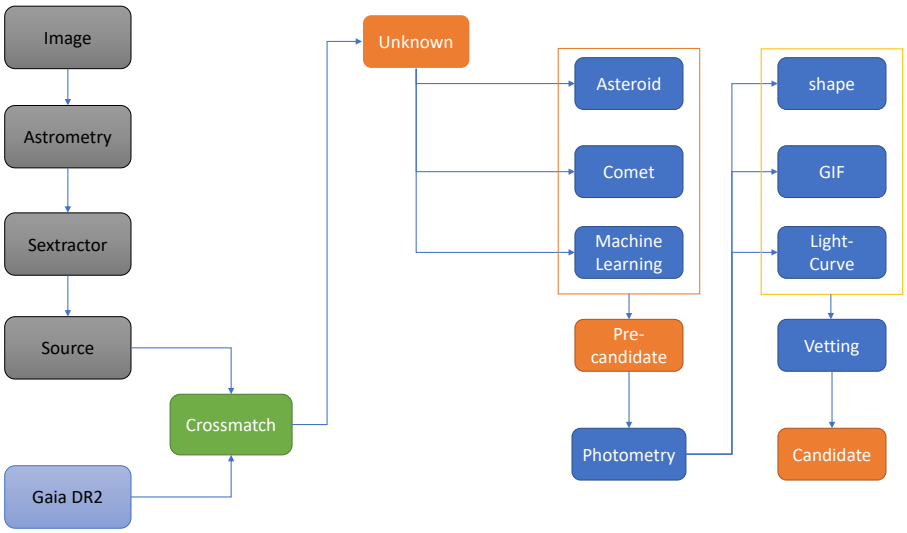

Figure 5.7: There are two parts in the detection pipeline. The unknown source identification (left) and the candidate identification (right). The pipeline is to identify unknown sources in TAROT images and then to classify the objects by machine learning before human vetting.

TAROT produces images as soon as it starts to follow-up GW event issued tiles by GRANDMA network, however TCA, TCH and TRE will begin observing only the suitable sky condition. Images are archived in CADOR and later retrieved to pipeline, see Figure 5.8. Each image is processed differently which depends on the the condition of image, mainly for source extraction such as seeing, pixel size, and threshold. More details of configuration of source extraction and distortion calibration are explained in chapter 4.3.

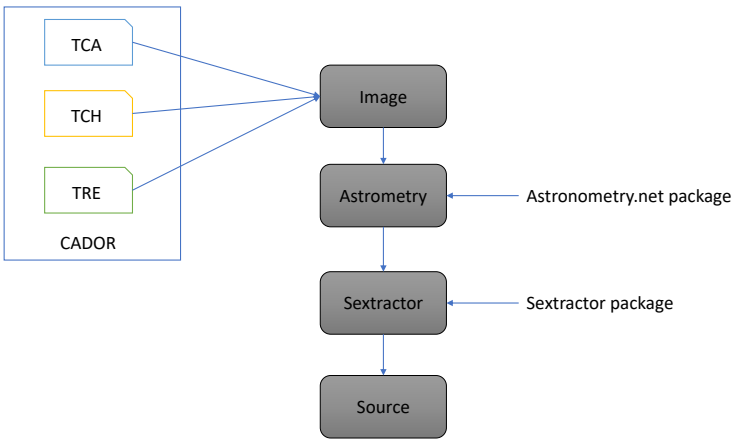

Figure 5.8: Images are retrieved from different telescopes and each image is treated different, by depending on the astronomical conditions.

The first result of identification by the pipeline is an unknown (see Figure 5.9) source by the definition of mismatching, again more detail in chapter 4.3. Each unknown source has to be checked for solar system objects such as asteroids, planets, natural satellites and comets or any objects in solar system. Sky Body Tracker (SkyBoT) provided by Institut de Mécanique Céleste et de Calcul des Éphémérides (IMCCE) Services (Berthier et al., 2006) is the tool for seeking and identifying solar system objects located in a time-stamped FoV of TAROT images by quickly computing the ephemeris of any solar system objects at a observational date implemented in the header. The SkyBoT database is updated daily including lately discovered bodies and the ephemerides of bodies (mainly asteroids) of which orbits were improved.

If the source is non-existent in the SkyBoT database , the interesting source will be passed through for source classification; a cosmic or a source. source

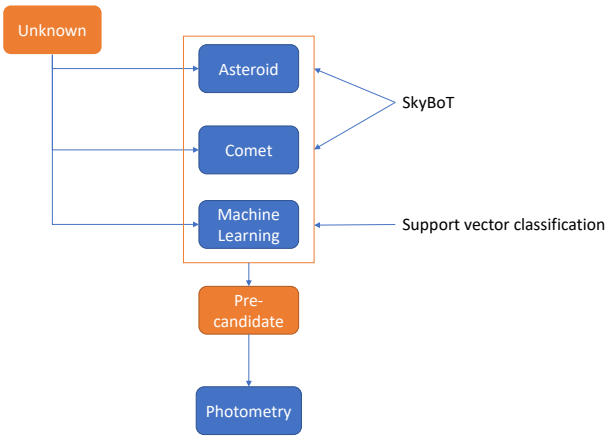

Figure 5.9: The unknown sources are checked against existence of the asteroids and comets nearby with IMCCE Services. If it is not the same position with solar system object, then the source is compared for the actual source or cosmic-ray with the machine learning.

is classified by Support Vector Machines (SVMs) which are a set of supervised learning methods, which means that it needs to learn from training data before put in authentic classification as Support Vector Classification (SVC).

Thousand of images with size of 20×20 pixels are prepared for training the machine and it is very important to prepare few thousands of training datasets for source classification for TCA and TRE image; fortunately TCA and TCH have the same properties as they are the same telescope size (both diameter and focal length) and also CCD, however the training dataset is different for TRE as it has different pixel size and image scale but the same size of training image at 20×20 pixels that is applied for machine learning.

In general, sources can be classified in 5 types before photometry as star, cosmic, unresolved objects, saturated source, poor quality image. Then we label these five models for a machine to learn and to recognize, mainly tell them to understand what is a favourable source and unfavourable source with a simple label in number from 0 to 4 shown in Figure 5.10. The number '0' is for a very faint source, a look alike cosmic-ray, or some noise; these sources will not be picked up for photometry, even if it is genuine source, because it is a faint source which is just beyond limiting magnitude of TAROT. Number

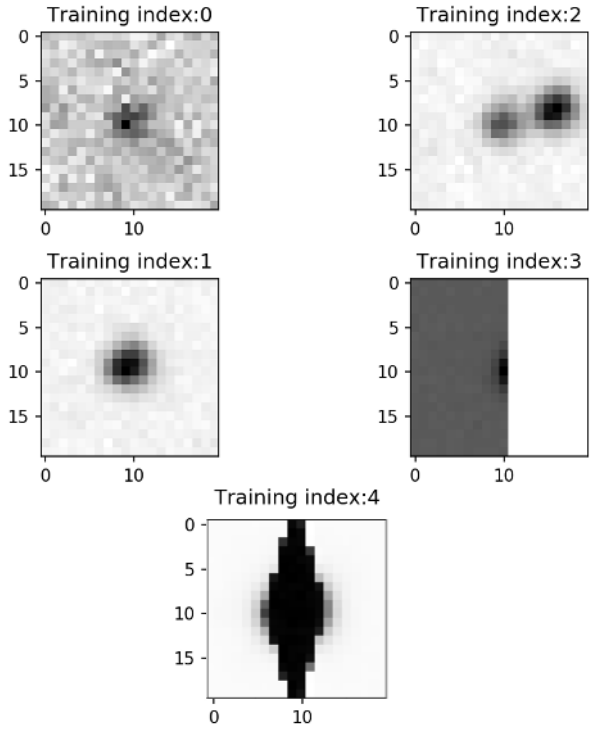

Figure 5.10: Five models of dataset are for train the machine, 0 = cosmic-ray, 1 = source, 2 = double source, 3 = poor quality image, 4 = saturated.

'1' is marked for a source answering positively to star-shape criteria. Number '2' is for unresolved objects or dual sources that are close to each other or those stars are in the frame of training image size 20×20 pixels. Number '3' is for "unpromising" image, either poor quality or bad image. Number '4' is a label for saturated image which comes from bright stars, planes, artificial objects. There are 2,339 training images in total for TCA and TCH and for TRE is 10,015. After learning, the software can classify the sources by model '0' to '4' at 50%, 93%, 52%, 49%, and 94% respectively and the precision of prediction shows in Table 5.7. The results of some predictions are illustrated in Figure 5.11 in actual label (model) and prediction.

Table 5.7: The software learns for source classification based on five models. The training datasets, called support, are used for training and the effective prediction indicates by precision, sensitivity (recall), and accuracy (F-score).

	precision	recall	f1-score	support
0 (Cosmic)	0.50	0.81	0.62	560
1 (Source)	0.93	0.66	0.77	1374
2 (Double)	0.52	0.51	0.52	276
3 (Poor quality)	0.49	0.77	0.60	111
4 (Saturated)	0.94	0.94	0.94	18
accuracy			0.69	2339
macro avg	0.68	0.74	0.69	2339
weighted avg	0.76	0.69	0.70	2339

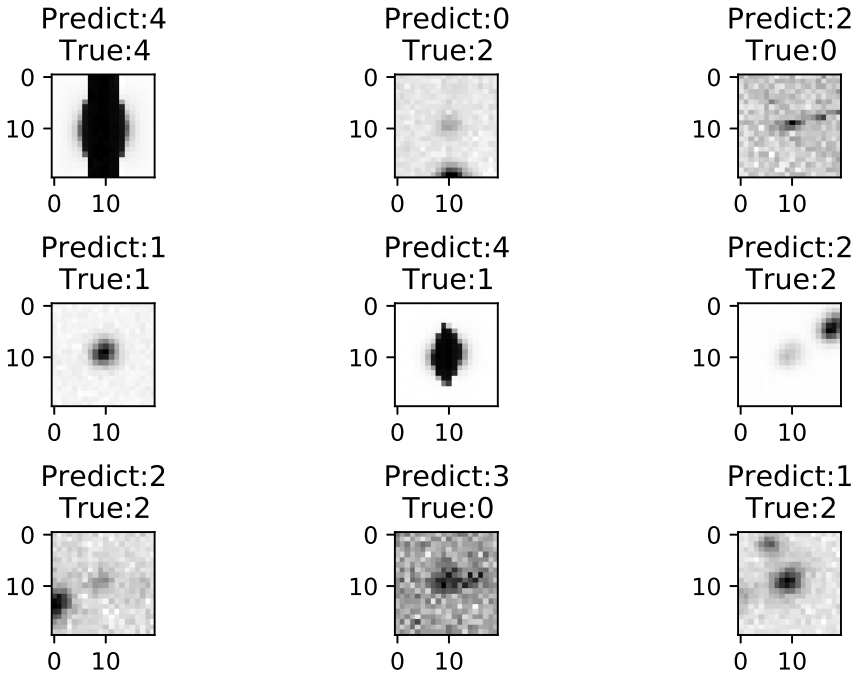

Figure 5.11: The result of prediction in high percentage provided a satisfactory for filter a general poor quality and it reduced the number of candidate before doing photometry.

The pre-candidate that passes through the prediction as a star-like source and it is not in the catalog of solar system object will be sent for photometry. The robust photometry extracts flux from pre-candidate and reference star before converting to apparent magnitude and then light curve is constructed from series of images that observes in different time. The Limiting magnitude, background flux and zero magnitude are displayed for classified judgement. Animation improvises for human consideration comparing with reference star, see Figure 5.12. Flux of candidate and background are plotted over observing time and apparent magnitude is displayed along with limiting magnitude in Figure 5.13.

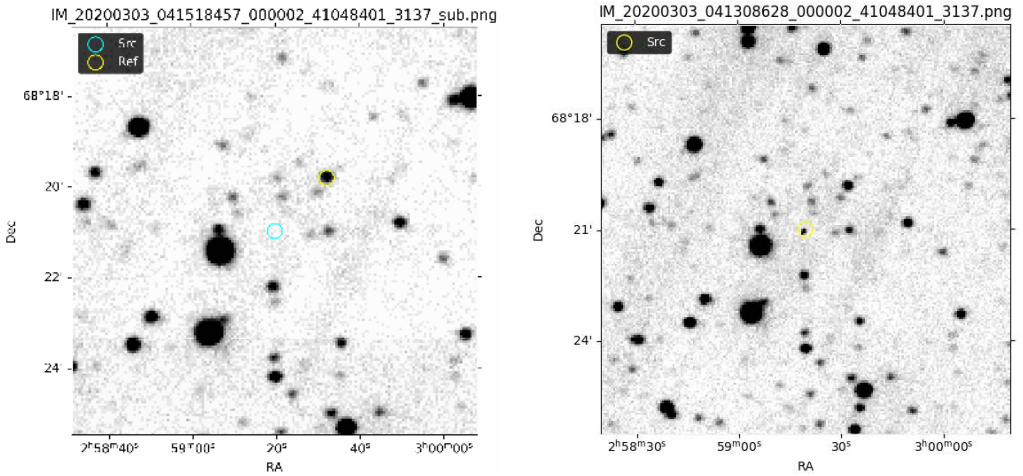

Figure 5.12: Pre-candidate detected in S200302c event, source is located in the center image RA: 44.831 and Dec: 68.350 (left) before it appears (right). Shape and brightness were examined and later classified as a cosmic.

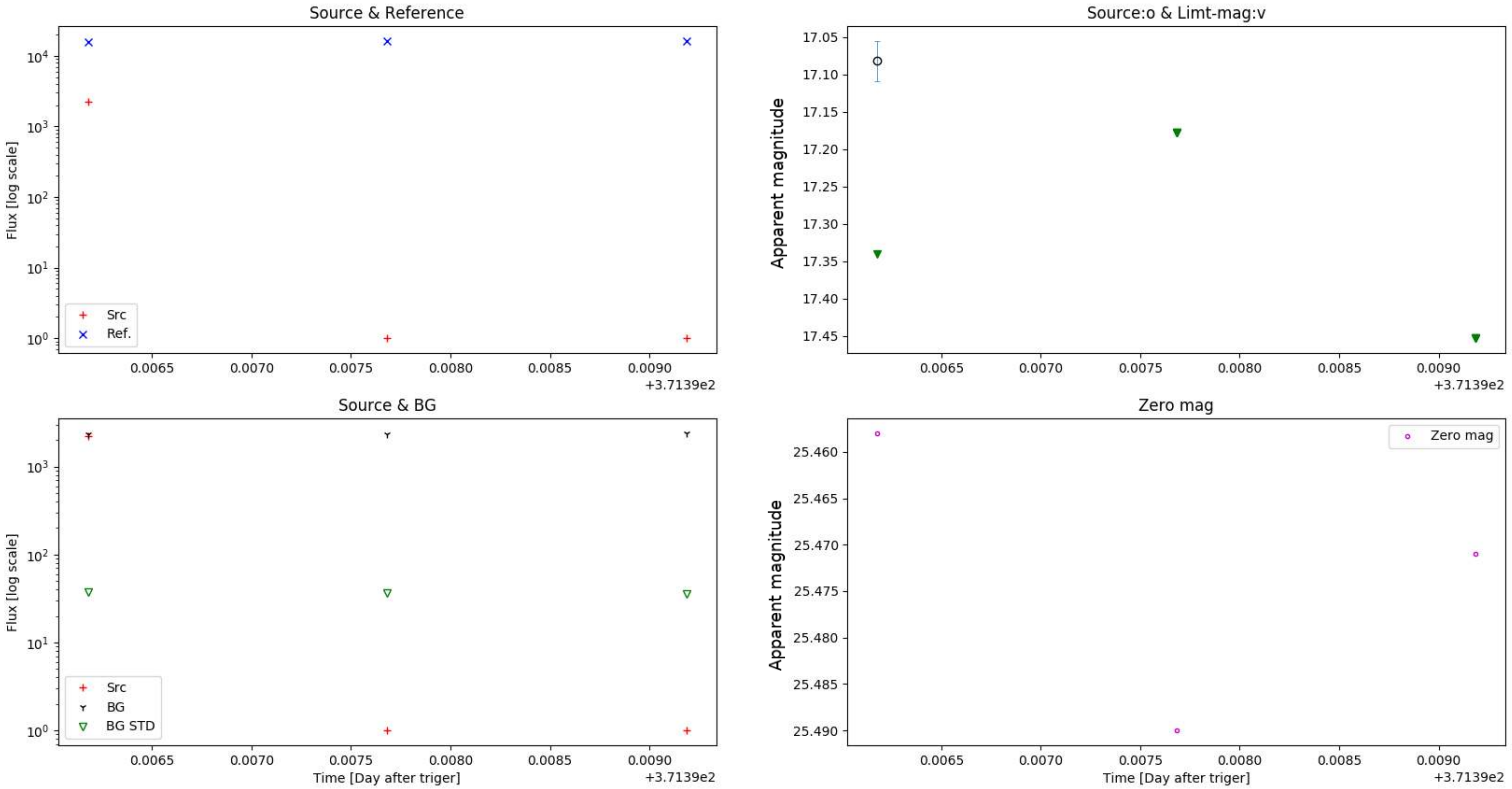

Figure 5.13: Flux of pre-candidate and reference star are for comparison and light curve of apparent magnitude is gained with limiting magnitude. The collation of background and source flux is plotted to assist human decision.

5.4 Detection results

TAROT telescope has search for counterparts of 47 GW events in run O3 and covered skymaps for 11,015 square degrees, less than 10% of total skymaps issued by LIGO/Virgo. The search pipeline was used to detect unknown sources in a wide field image of TAROT and candidates are extracted using the detection method described in the previous section. Each GW event has an individual map and its location in sky is affected by number of unknown sources such as near the center of our galaxy.

The amount of unknown sources detected by the pipeline were compared to observed region which provided the number of source detection per area. From all GW candidates followed-up by TAROT, there were an average of 32 unknown sources per square degree. However, the pre-candidate that passed for human vetting was just < 2 sources per square degree.

Table 5.8: The number of sources detected by the pipeline in average per square degree.

	TCA	TCH	TRE
Observed area (deg^2)	2362	1986	6667
Unknown sources (deg^{-2})	29	53	15
Pre-candidates (deg^{-2})	1	3	< 1

TRE has the largest FoV among TAROT network, TRE FoV is 5 times larger than TCA/TCH. From Table 5.8, TRE alone covered skymaps at 6,667 square degrees follow by TCA which had a coverage of 2362 square degrees and TCH just overlaid only 1986 square degrees.

Interestingly, TRE has the largest sky coverage observation in a large covering area of skymaps but the number of identification is the lowest follow by TCA and TCH. A low level of detection in TRE is due to the limiting magnitude of the telescope itself, approximately 17 in clear filter, and so the low limiting magnitude means it detects only the brightest object and its results for uncomplicated identification by the algorithm and poor quality sources can be filtered out simply. TCA and TCH, on the another hand, have the same image properties but TCH has a higher number of unknown sources than TCA, by about 2 times despite TCH covered smaller area than TCA. The number of individual detections can be seen in Figure 5.14 and 5.15. The exact number over each telescope in each GW event shows in Appendix C.

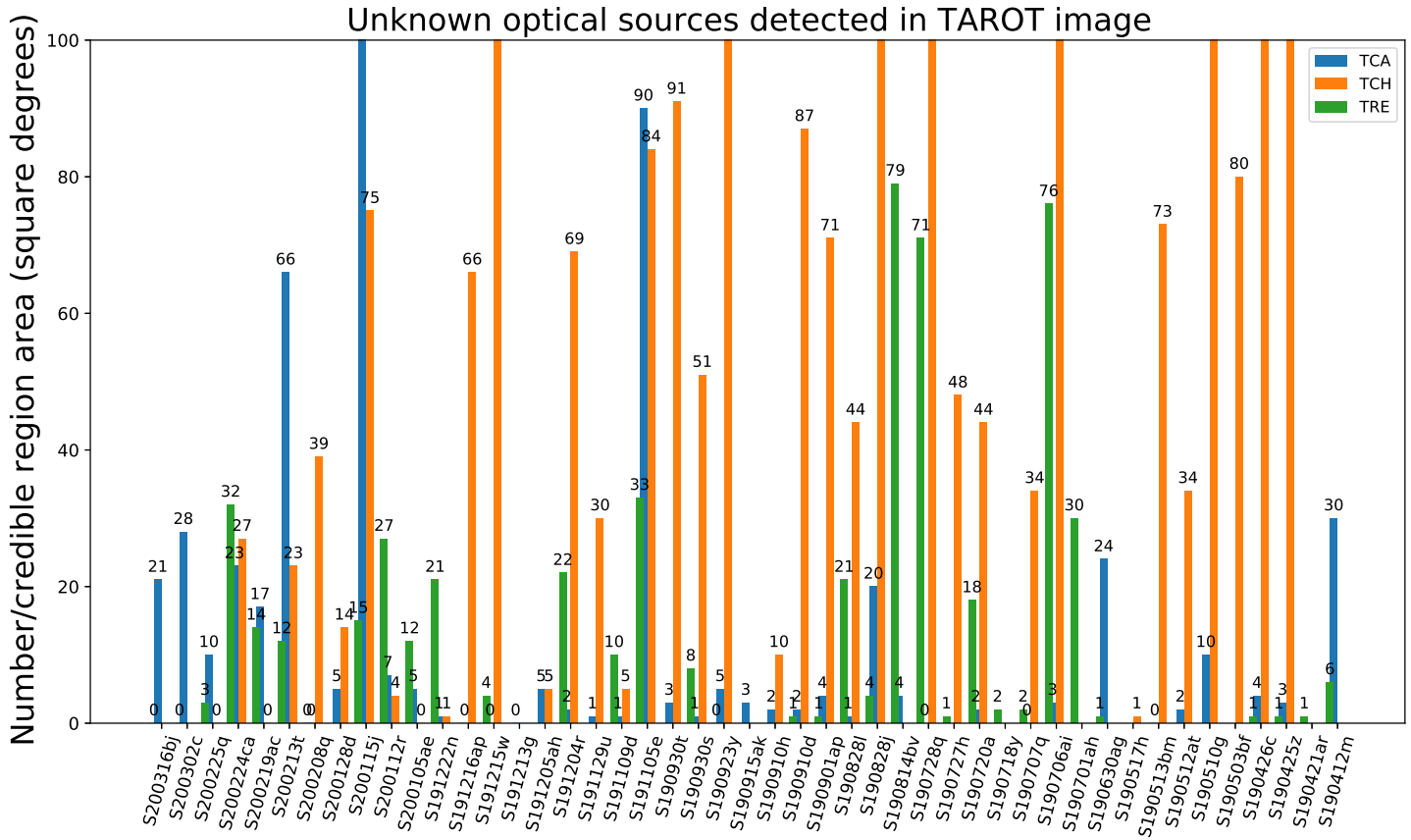

Figure 5.14: Unknown source identified by the pipeline indicated above each bar and there are nine events that pipeline found $>$ 100 source per square degree.

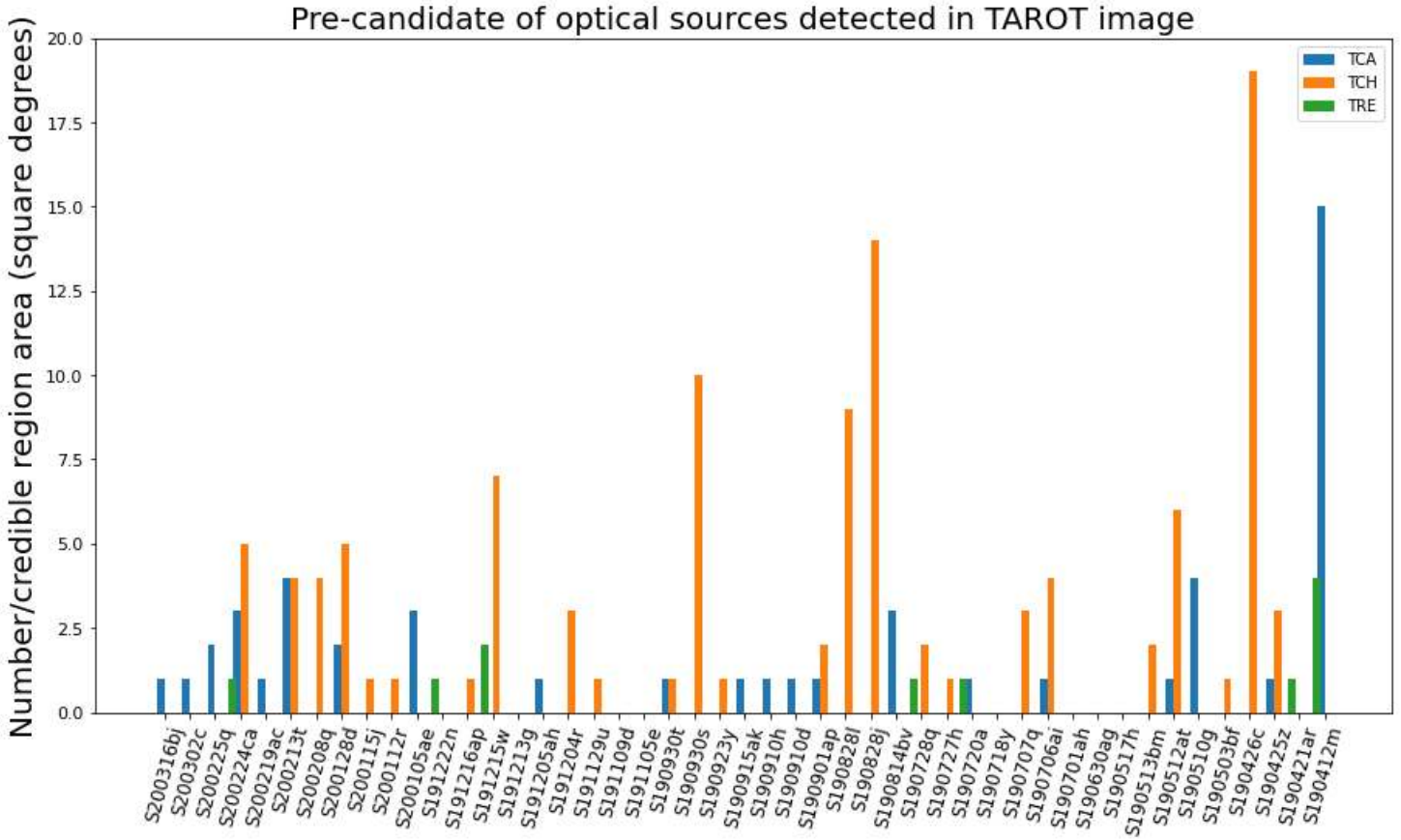

Figure 5.15: Pre-candidate is the unknown source which is classified by pipeline before human vetting. The low numbers of pre-candidate in each GW event were feasible for human intervention before taking it as the significant candidate.

Chapter 6

Astrophysical implication discussion of TAROT and GRANDMA observations

Except the case of the unmodeled event S200114f (LIGO Scientific Collaboration and Virgo Collaboration, 2020) all the objects detected during runs O1, O2 and O3 are mergers of highly dense and compact objects. This chapter deals with implications of EM observations about their natures.

The BNS merger case involves the presence of gas in a disk or in an envelope surrounding the couple of stars. When the merging occurs a quantity of matter is ejected implying EM emission as SGRB and kilonova (see Section 2.3). In that case, the optical signal after few hours is a light curve such as presented in Figures 2.19 and 2.24. Any merger involving a NS could in principle produce such optical light curves depending on the viewing angle.

The BBH case involves bodies who swept the matter around them. As a consequence, the merging does not involve any gas and no EM is expected by the interaction of the gas with BHs. In Section 2.4 we presented some theories that can explain an EM emission involving other processes.

The MassGap cases are the less known systems. We consider MassGap cases in the same category as BBHs.

The optical detection of a GW counterpart is very important because, optical spectra allow to measure the redshift, so the distance, and bring useful information about the host galaxy and the nature of the emission processes. Before using a spectrograph, the optical counterpart must be found scanning

the large area of credible regions provided by skymaps of LIGO/Virgo. This step is the role of TAROT during the runs O1, O2. During the run O3, the TAROT collaboration in GRANDMA (described in chapter 5 and observations reported in Section 5.2) allows to include some other telescopes. A large part of the science discussed in this chapter is published in Antier et al. (2019, 2020); Noysena et al. (2019).

6.1 Summary of GW detections by LIGO/Virgo

The detectivity (*i.e* the limiting magnitude) of GRANDMA telescopes involved to search the optical counterparts of GW mergers detected by LIGO/Virgo is limited to magnitudes 17 or 18 depending on the instruments. Before discussing the science to derive from GRANDMA measures we must have a look on the physical characteristics of GW events. The detection of GW by interferometers allows to know the distance and the location of the credible region in the sky.

From data provided in the Tables 5.1 and 5.2 we plotted the Figure 6.1. The distance of GW170817 was believed to be characteristic of the BNS which were expected to be found during the run O3. Unfortunately, the reality shows that GW170817 is exceptionally close compared to the BNS found by LIGO/Virgo during the run O3.

The Figure 6.2 gives the cumulative probability to get a BNS or a BBH event according on the distance distribution of the Figure 6.1. For a given event, we consider the distance as a Gaussian probability with a standard deviation as the width provided by upper and lower limits of distance in LIGO/Virgo data. The Figure 6.2 is the addition of Gaussians of all events, normalized to unit. The median distance for BNS is 200 Mpc. At such a distance a kilonova should peak at magnitude 20.5 which is too faint for GRANDMA detections. However, if a SGRB afterglow occurs, the optical emission should be about magnitude 14.5 two hours after the trigger, which is well detectable with GRANDMA telescopes.

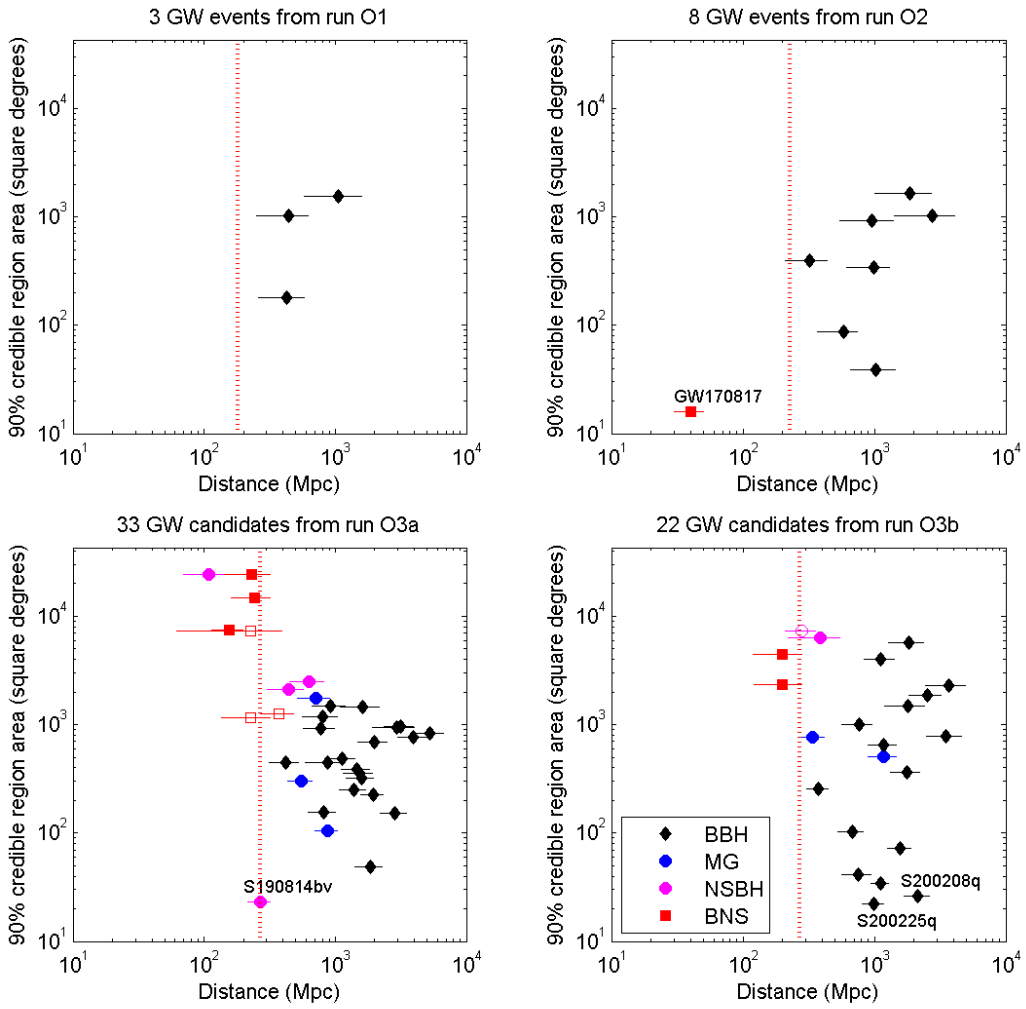

Figure 6.1: The 90% credible region area ($\Omega_{90\%}$) versus the luminosity distance (posterior mean distance and posterior standard deviation of distance) for all LIGO/Virgo GW events/candidates of runs O1, O2, O3a and O3b. Vertical red dotted lines are the expected limiting distances to detect binary neutron star mergers (BNS) by the LIGO/Virgo detectors. BBH (binary black hole mergers), MG (mass gap mergers), NSBH (neutron star - black hole mergers), and BNS are represented in different colours. Four candidates for run O3 are indicated by open symbols corresponding to a predominantly terrestrial classification (above 50%) and the classification indicated in these plots is the second most likely.

The Figure 6.2 provided the TAROT limits for a BBH and a kilonova detection. TAROT, a 0.25 m. diameter telescope, is able to detect a BBH optical source at probability of 90% at apparent magnitude of 17 however a kilonova is beyond TAROT limits. TAROT telescopes have possibility only 20% to detect at the same magnitude. Nevertheless, we can increase the probability of the detection from 20% to 50% by increasing the telescope diameter to 0.8 meters but the FoV should decrease. Another is to employ many robotic telescopes pointing the same area and take an exposure at the exact moment and combine them later.

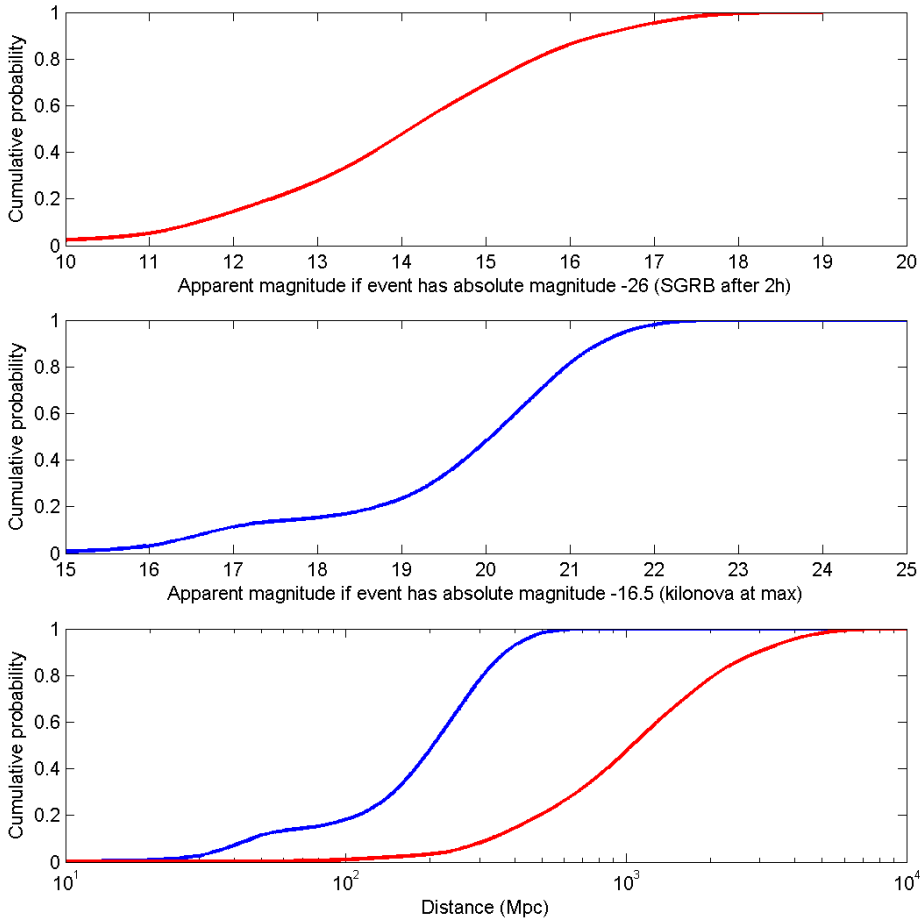

Figure 6.2: Cumulative probability to find an event according on the limiting magnitude of the distance. The red line shows the apparent magnitude for SGRB for absolute magnitude at -26 (top), the blue line shows the apparent magnitude for kilonova for absolute magnitude at -16.5 (middle), and both SGRB and kilonova are compared in distance (bottom).

6.2 Spatial completion of optical observations

The credible region to locate the GW sources at a level of 90% (hereafter $\Omega_{90\%}$) covers hundreds of square degrees. The goal is to record images to cover the entier area of the $\Omega_{90\%}$. Knowing their distance of the GW provided by LIGO/Virgo notices we can convert the apparent limiting magnitude of the GRANDMA telescopes to absolute magnitudes. Figure 6.3 shows the absolute limiting magnitude of the GRANDMA observations versus the GRANDMA coverage relative to the $\Omega_{90\%}$. We can see 11 GWs covered more than 80%. On the plot we indicated their names and the types. Clearly these 11 GW constitute the sample of the GRANDMA analysis which is statistically relevant.

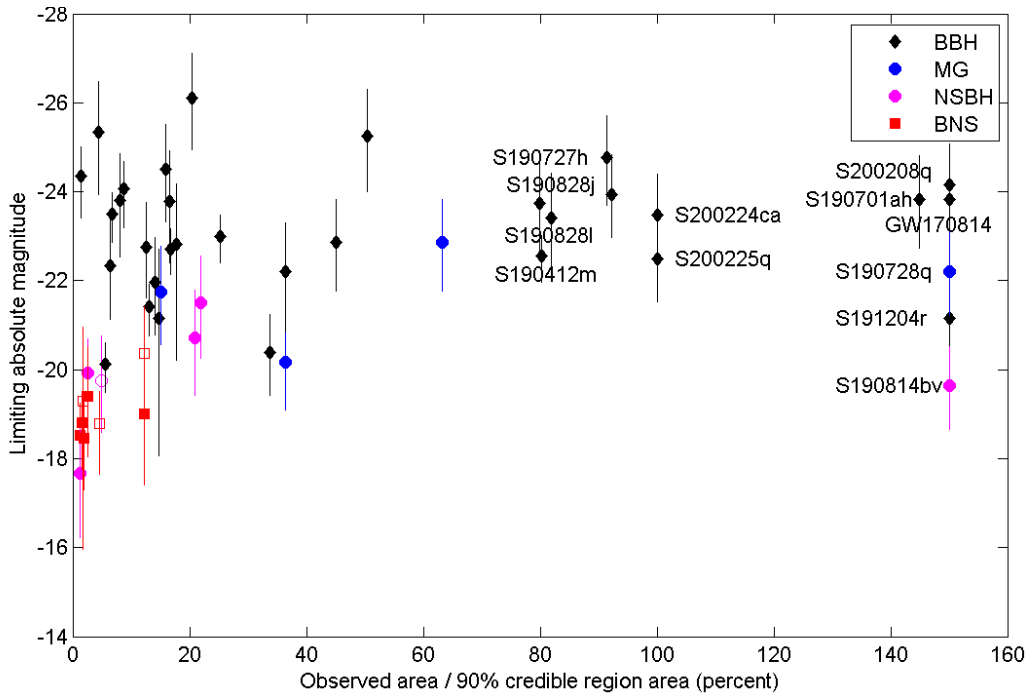

Figure 6.3: All LIGO/Virgo GW events observed by GRANDMA telescopes are plotted as limiting absolute magnitude versus the percentage of the 90% credible region that was observed. When an event has a percentage of the 90% credible region greater than 150% we plot it at 150% for clarity.

6.3 Energy constraints from optical observations

In absence of ever detected optical transient associated to BBHs, one can compute the upper limit of energy converted into visible light associated to the BBH events. The LIGO signal analysis showed that an energy of $\Delta E = 3.0^{+0.5}_{-0.4} M_{\odot}$ was released during the coalescence of GW150914. In absence of a unique theory detailing an EM emission process we can consider that only a very small fraction of ΔE can be converted into EM radiation. The corresponding luminosity L is given by Equation 6.1:

$$L = \frac{\alpha \Delta E}{\Delta t} \tag{6.1}$$

where α is the fraction of the ΔE energy converted into EM radiation ($0 < \alpha \ll 1$) and Δt is the emission duration. We must spread the EM energy over the EM spectrum. There are mainly two kinds of energy distribution: Synchrotron or black body radiation. A synchrotron spectrum is composed by flat segments separated by spectral breaks. Spectral breaks are governed by the electron energy distribution and by the magnetic fields. This implies to use a model but we have no precise good description of a theory to explain such an EM emission by BBHs for now. The black body approach is easy to apply because the only assumption is to consider the optical transient as an opaque sphere. This view is probably not realistic but allows to compare the amount of EM energy of different BBHs.

A rough estimation of the optical luminosity is made considering, for example, a constant solar black body emission from the date of the trigger until the date of the observation. Knowing the Sun luminosity $L_{\odot} = 4 \times 10^{26}$W and distance $D_{\odot} = 1.5 \times 10^{11}$m, we can estimate the optical magnitude from Equation 6.2:

$$m_{candidate} = -16.12 - 2.5 log \frac{L}{D^2} \tag{6.2}$$

where D is the luminosity distance of the GW source (430 Mpc in case of GW 150914). If we suppose that the optical counterpart has a magnitude of 14 during 20 minutes, then $\alpha = 3 \times 10^{-7}$; If the emission lasts 2 days, then the parameter α will become 5×10^{-5}. This calculation shows that small aperture telescopes as TAROT are adequate for the detection and follow-up of a possible optical transient event because they can probe values of $\alpha \ll 1$ as it is expected.

The α factor can be constrained by optical observations even if the nature of the emission process is not known. If there is no optical detection we derive an upper value of the α factor constraining the upper limit amount of energy converted into EM emission. Mixing the formula 6.1 and 6.2 we obtain a more general formula (Equation 6.3) to compute α from observed parameters expressed in their common units as:

$$\alpha = 0.32 \cdot \frac{\Delta t_{min} \times D_{Mpc}^2 \times 10^{-0.4 \cdot (m_{candidate} + 16.12)}}{\Delta E_{M_\odot}} \tag{6.3}$$

The counterpart optical detection of the BNS GW170817 gives $\alpha \sim 2 \times 10^{-6}$. For run O3 we do not have the ΔE values but we can take reasonably form results of run O1, O2 (Table 4.1) 0.2 for BNS, 1.5 for MG, 1 for NSBH and 2 for BBH. Figure 6.4 plots the limits of α for all the GW observed by GRANDMA. For BBH events, S191204r gives the deeper limit $\alpha = 3 \times 10^{-7}$. For NSBH events, S190814bv gives the deeper limit $\alpha = 2 \times 10^{-8}$.

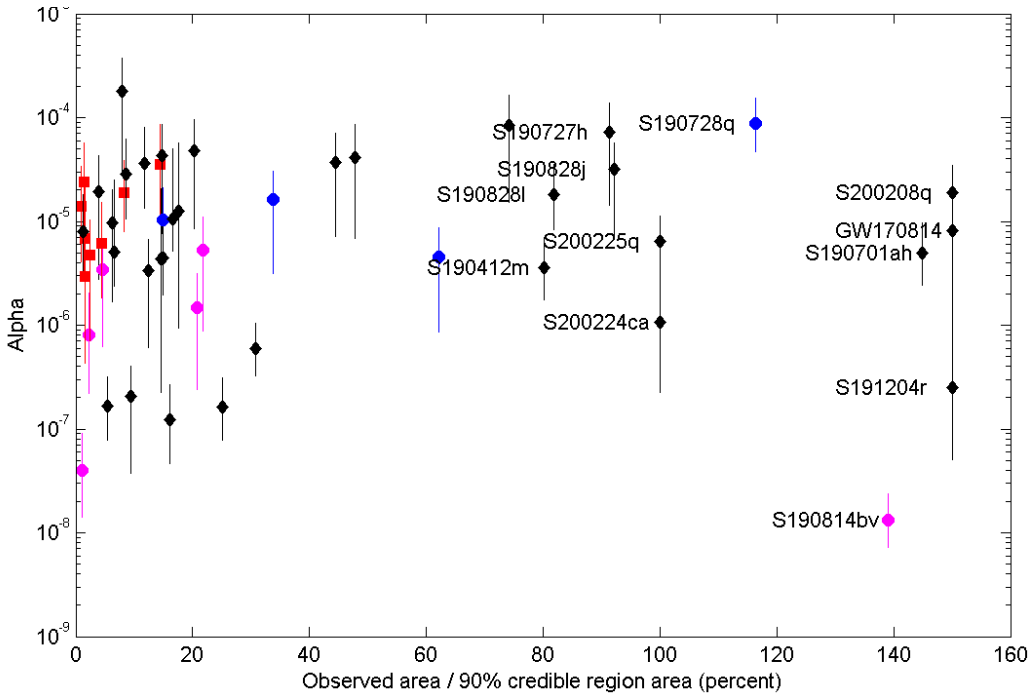

Figure 6.4: Alpha derived from limits of TAROT observations versus the TAROT coverage relative to the $\Omega_{90\%}$. Colors are the same than for the Figure 6.3, Red square are BNS, magenta disks are NSBH, blue disks are MG and black diamonds are BNS events.

6.4 Analysis of BBH events observed by TAROT during runs O1 and O2

None of the three GW events observed by TAROT during the runs O1 and O2 exhibits an optical counterpart (see Section 4.5). The best constraint is a limiting magnitude of R=15.0 at 0.6 day after the GW170814 coalescence (conservative values), for which TAROT observed almost the entire 90% probability contour area. At the distance of the GW event (D_{GW} = 580 Mpc) (The LIGO Scientific Collaboration et al., 2019) the absolute limiting magnitude from TAROT is M_R = -23.8. In a context of a collaborative work with Damien Turpin, he provided us 141 optical light curves of LGRBs and 6 light curves of SGRBs for which the redshifts are known and we converted them in absolute R magnitude (Figure 6.5). 65% of them are brighter than M_R = -23.8 at the equivalent time of the TAROT observations for GW170814

(i.e. 0.6 day). As a consequence our observations exclude at 65% an association of GW170814 with a GRB optical counterpart. These limits are not constraining for a kilonova or supernova event possibly associated with the GW event (albeit this is not expected in the case of the coalescence of two BHs).

As presented in the introduction section some theories predict an EM emission from BBH mergers. For example, the emission process proposed by Zhang (2016) depends on the parameter $\hat{q}$ which is the fraction of the characteristic charge of the BHs. However to constrain these theories we computed the α parameter defined in the Equation 6.1. The link between α and the Zhang's $\hat{q}$ parameter requires a theoretical work beyond the scope of this thesis. Values are given in the Tables 4.2 and 4.3. Conservative values are $\alpha < 1 \times 10^{-5}$, $\alpha < 2 \times 10^{-5}$ and $\alpha < 1 \times 10^{-5}$ for GW150914, GW170104 and GW170814 respectively. The GW170814 gives the most constraining value of α due mainly to the short delay of the observations after the trigger. Moreover only the error box of GW170814 was fully covered by the TAROT observations.

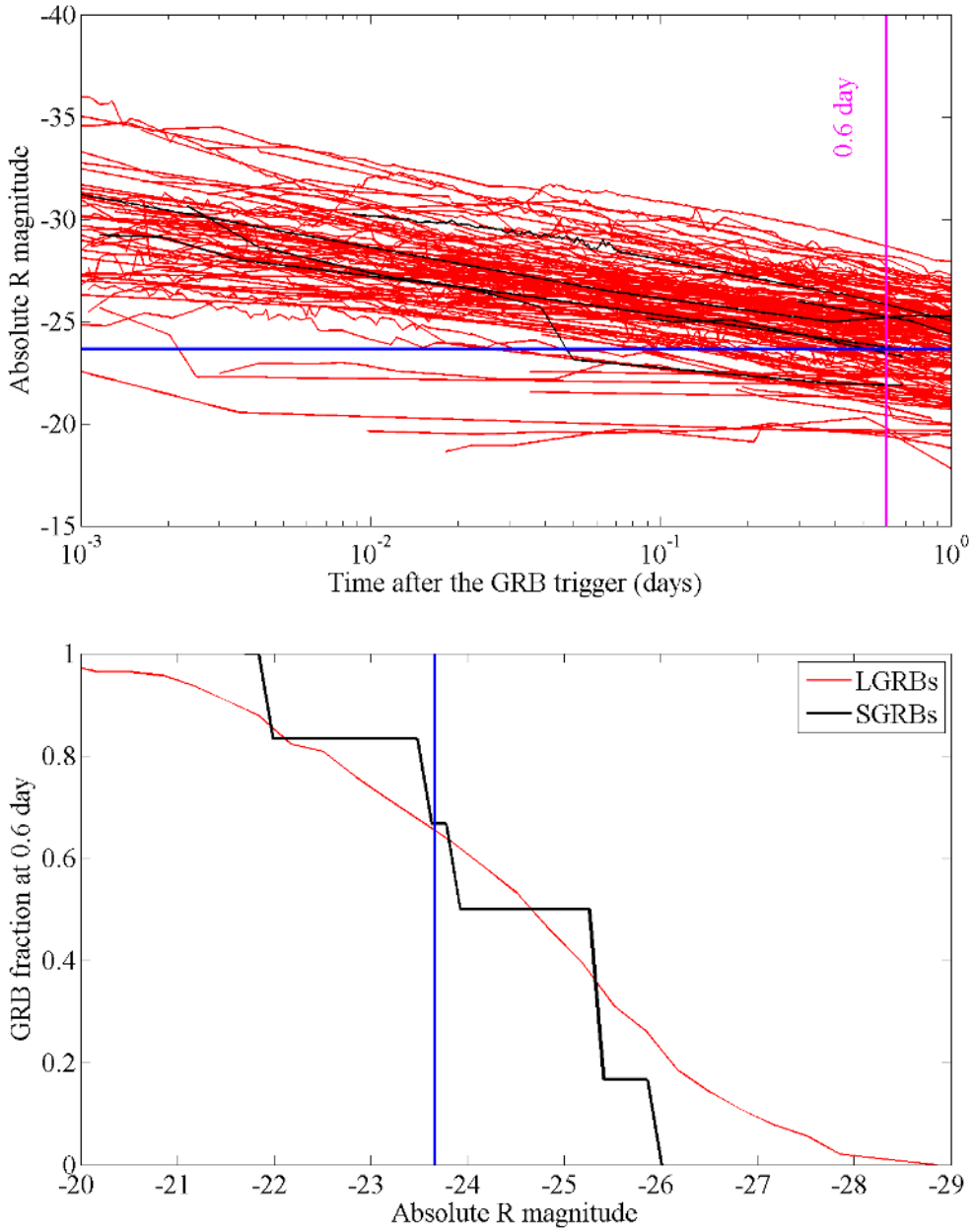

Figure 6.5: Top panel: Optical light curves of 141 long GRBs (red) and 6 of short GRBs (black) observed at 0.6 day after their events and with known redshifts. GRB data (light curves and GRB distances) are provided by Damien Turpin private communication. The TAROT observation time is 0.6 day (pink line) and the TAROT limiting magnitude is the blue line. Bottom panel: Cumulative fraction of GRBs at 0.6 day derived from the data used for the upper plot.

6.5 Comparison of optical limits of GW events observed by GRANDMA with GRB and kilonova light curves

In the Section 6.4 we presented in detail the limiting magnitude of the BBH GW170814 in the context of the GRB light curves. At the end of the run O3 it is possible to make the same analysis considering all types of GW events and optical light curves of LGRB, SGRB and kilonova. The Figure 6.6 summarizes the results.

The improvement of LIGO/Virgo pipeline to build the credible region skymap and the GRANDMA infrastructure of GRANDMA helped to start optical observations earlier than for the runs O1, O2. As a consequence, even if the limiting magnitude remains about the same during the run O3, the fact to start observations only few minutes after the trigger is important regarding the decay of GRB light curves.

The Figure 6.6 shows that 11 BBH events (including the mass gap event S190728q as a BBH) could be optically detected by GRANDMA if GRBs were associated and their jet directed to the Earth. If we consider the 11 GRBs were not detected just because the jet was not oriented toward the Earth we can give a constraint of the maximum opening angle of the jets of $4\pi/11$ steradian. Applying the formula $2\pi \cdot (1 - \cos\theta)$ we obtain $\theta = 35°$. This value must be compared to typical measured opening angles $\theta \simeq 4°$ of GRBs (Frail et al., 2001). Anyway, our deep and early detection limits gives new constraints in the GRB associations to BBH but we are not able to exclude them definitively. To reach the $\theta = 4°$ value, hundreds of GW events must be observed during the next GW runs. If we want to be rigorous, we must consider only the three GW candidates S200224ca, S190728q and S191204r which are located near the 100% of excluding region of GRBs. We can see here the huge efforts to maintain during the next years in this topic.

Concerning BNS, the GRANDMA limiting magnitude is too bright to constrain anything regarding the kilonova models. The use of larger aperture telescopes or a close BNS event by chance will allow to detect the kilonova.

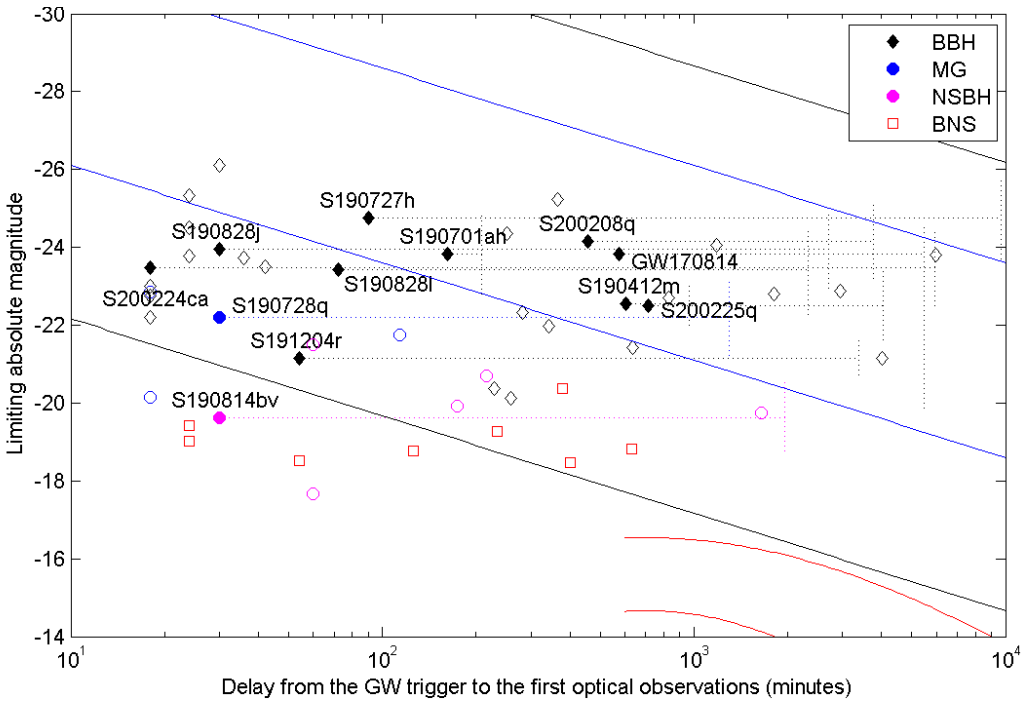

Figure 6.6: All LIGO/Virgo GW events observed by GRANDMA telescopes are plotted as limiting absolute magnitude versus the delay between the GW trigger and the first GRANDMA observations. Filled symbols are used for events for which more than 80% of the 90% credible region have been observed. The black lines are the typical limits of LGRB light curves, blue lines for SGRBs (from Table 2.2) and red lines for the GW 170817 kilonova (from Table 2.4).

Chapter 7

Conclusions

The thesis objective was to identify optical sources associated to gravitational wave events detected by LIGO/Virgo interferometers to improve the knowledge of the nature of the GW sources. We used images recorded by the optical TAROT telescopes implied in the GRANDMA network.

We have developed an image analysing pipeline based on procedures tested and applied to the observations performed in response to 50 GW triggers during the runs O1, O2 and O3. Thousand images were analyzed, hundreds of candidates were checked but no new credible optical source was found associated to GW events. Results are published in Antier et al. (2019, 2020); Noysena et al. (2019) and in 34 GCN circulars.

The limiting magnitude and the short delay to start optical observations allow us to derive energetic and statistical constraints. If we consider an electromagnetic transient associated to a BBH event emitting isotropic optical light, our observations exclude such a source to be brighter than the absolute magnitude M_R=-25 one hour after the event.

We studied also the association of BBH mergers with GRBs as optical transients. GRBs do not emit isotropic light because energy is concentrated in the direction of a jet. TAROT observed three events early enough to be sure that the optical detection should have been positive if the jet was oriented toward the telescope. TAROT observed eight other events with a statistical detection better than 50%. If we make the hypothesis there is always a GRB associated to BBH mergers, we can derive a constraint of $\theta = 35^\circ$ on the opening angle of the ultra relativistic jets of the GRBs. Although, our deep and early detection limits reduce the possibility in the GRB associations with BBH mergers we are not able to exclude the association definitively.

Concerning BNS, we were disappointed not to have events from LIGO/Virgo closer than 100 Mpc during the run O3. As a consequence the GRANDMA limiting magnitude is too bright to constrain anything regarding the kilonova models. The use of larger aperture telescopes during the next runs are the only way to detect the kilonova if no new BNS event occurs closer than 100 Mpc.

This thesis learned us that the success of the optical detection of BNS mergers during the next GW runs must imply: *(i)* The help of new GW interferometers to reduce the credible region to less than 100 square degrees, *(ii)* to keep large field of view as TAROT ($2^\circ \times 2^\circ$ or more),*(iii)* improve the detectivity by the use of larger aperture optical telescopes. Typically, to reach the limiting magnitude to detect the kilonova associated to a BNS at 200 Mpc, we must use a telescope with an aperture larger than 0.8 meter. The technological problem is to keep a large field of view which implies expensive optics and a mosaic of detectors at the focus plane. Another solution is to use optical tubes as for TRE, preserving the field of $4^\circ \times 4^\circ$ recording the same sky field in the same time and to combine the images later. This last solution has the advantage to eliminate cosmics and cosmetic detector defects which are the main source of false detections.

Conclusions

L'objectif de la thèse était d'identifier des sources optiques associées aux événements d'ondes gravitationnelles détectés par les interféromètres LIGO/ Virgo pour améliorer la connaissance de la nature des sources GW. Nous avons utilisé des images enregistrées par les télescopes optiques TAROT en collaboration avec le réseau GRANDMA.

Nous avons développé une chaîne d'analyse d'images basée sur des procédures testées et appliquées aux observations effectuées en réponse à 50 événements GW lors des campagnes O1, O2 et O3. Des milliers d'images ont été analysées, des centaines de candidates ont été vérifiées mais aucune nouvelle source optique crédible, associée aux événements GW, n'a été trouvée . La conclusion scientifique de ces résultats a été publiée dans Antier et al. (2019, 2020); Noysena et al. (2019) et dans 34 circulaires GCN.

La limite de détection et le court délai pour commencer les observations optiques avec TAROT nous permettent d'en déduire des contraintes énergétiques et statistiques. Si nous considérons un transitoire électromagnétique associé à un événement BBH émettant une lumière optique isotrope, nos observations excluent qu'une telle source soit plus lumineuse que la magnitude absolue M_R=-25 une heure après l'événement.

Nous avons également étudié l'association de fusions BBH avec des GRBs en tant que transitoires optiques. Les GRBs n'émettent pas de lumière isotrope car l'énergie est concentrée dans un jet dirigé vers la Terre. TAROT a observé trois événements suffisamment tôt pour être certain que la détection optique aurait dû être positive si le jet avait été orienté vers le télescope. TAROT a observé neuf autres événements avec une détection statistique meilleure que 50%. Si nous faisons l'hypothèse qu'il y a toujours un GRB associé aux fusions BBH, nous pouvons en déduire une contrainte de $\theta = 35°$ sur l'angle d'ouverture des jets ultra relativistes des GRBs. Bien que la profondeur de nos limites de détection précoce réduisent la possibilité d'association de GRB

avec des fusions BBH, nous ne sommes pas en mesure d'exclure définitivement une telle association.

Concernant les fusions d'étoiles à neutrons (BNS), il a été décevant de ne pas avoir d'événements LIGO/Virgo inférieurs à 100 Mpc lors de la campagne O3. En conséquence, la magnitude limite GRANDMA est trop brillante pour contraindre quoi que ce soit concernant les modèles kilonova. L'utilisation de télescopes de plus grand diamètre lors des prochaines exécutions est le seul moyen de détecter le kilonova si aucun nouvel événement BNS ne se produit à moins de 100 Mpc.

Cette thèse nous a appris que le succès de la détection optique des fusions BNS lors des prochaines campagnes GW doit impliquer: *(i)* l'aide de nouveaux interféromètres GW pour réduire la région de recherche à moins de 100 degrés carrés, *(ii)* de conserver un grand champ de vision comme TAROT ($2^\circ \times 2^\circ$ ou plus), *(iii)* améliorer la détectivité en utilisant des télescopes optiques de plus grand diamètre. Typiquement, pour atteindre la magnitude limite afin de détecter la kilonova associée à un BNS à 200 Mpc, il faut utiliser un télescope avec une ouverture supérieure à 0,8 mètre. Le problème technologique est de conserver un large champ de vue qui implique des optiques coûteuses et une mosaïque de détecteurs au niveau du plan image. Une autre solution est d'utiliser des tubes optiques comme pour TRE, en préservant le champ de $4^\circ \times 4^\circ$ enregistrant le même champ de ciel au même moment et de combiner les images plus tard. Cette dernière solution présente l'avantage d'éliminer les défauts cosmiques et cosmétiques des détecteurs qui sont la principale source des fausses détections.

Appendix A

TAROT observations

A.1 TAROT tiles over localization of runs O1 and O2

TAROT prompted after the first GW detection and follow-up event as soon as skymaps and tiles were ready. GW150914 was followed-up for 14 days as we do not understand the nature of GW event and the astrophysical origin that may or may not provide optical transient or other EM wavelengths. However, the search for transient was reduced to a few days in the last two GW events. Here images were illustrated the TAROT tiles over localization at 50% and 90% probability respectively.

The Table A.1 shows all the GW follow-up performed by TAROT telescopes during runs O1 and O2. The first column is the GW event; the second column is the GW classification into BNS (binary neutron star mergers), NSBH (neutron star - black hole mergers), BBH (binary black hole mergers), MG (mass gap mergers) and Terr (terrestrial events). The third column is burst time in UTC. The forth column is number of scientific image that had been observed by TAROT telescopes: TAROT-TCA, TAROT-TCH and TAROT-TRE.

Table A.1: TAROT observations during run O1 and O2.

	Classification						No. scientific image		
Event	BNS	NSBH	BBH	MG	Terr	Date	TCA	TCH	TRE
GW150914	0	0	100	0	0	2015-09-14 09:50:45	400	0	0
GW170104	0	0	100	0	0	2020-01-04 10:11:58	167	122	48
GW170814	0	0	100	0	0	2020-08-14 10:30:43	0	0	333

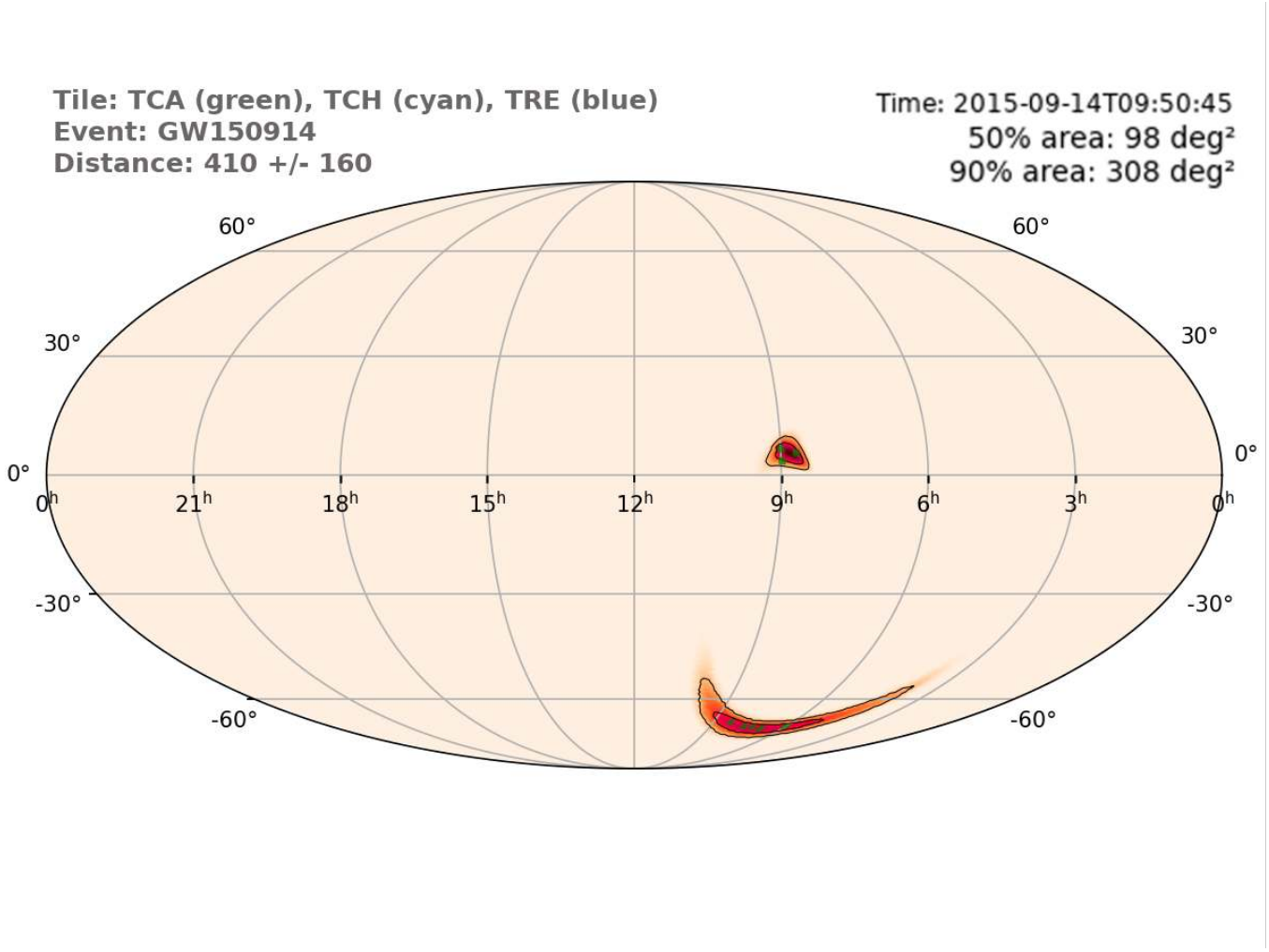

Figure A.1: TAROT tiles are displayed over the contours of the localization of GW150914.

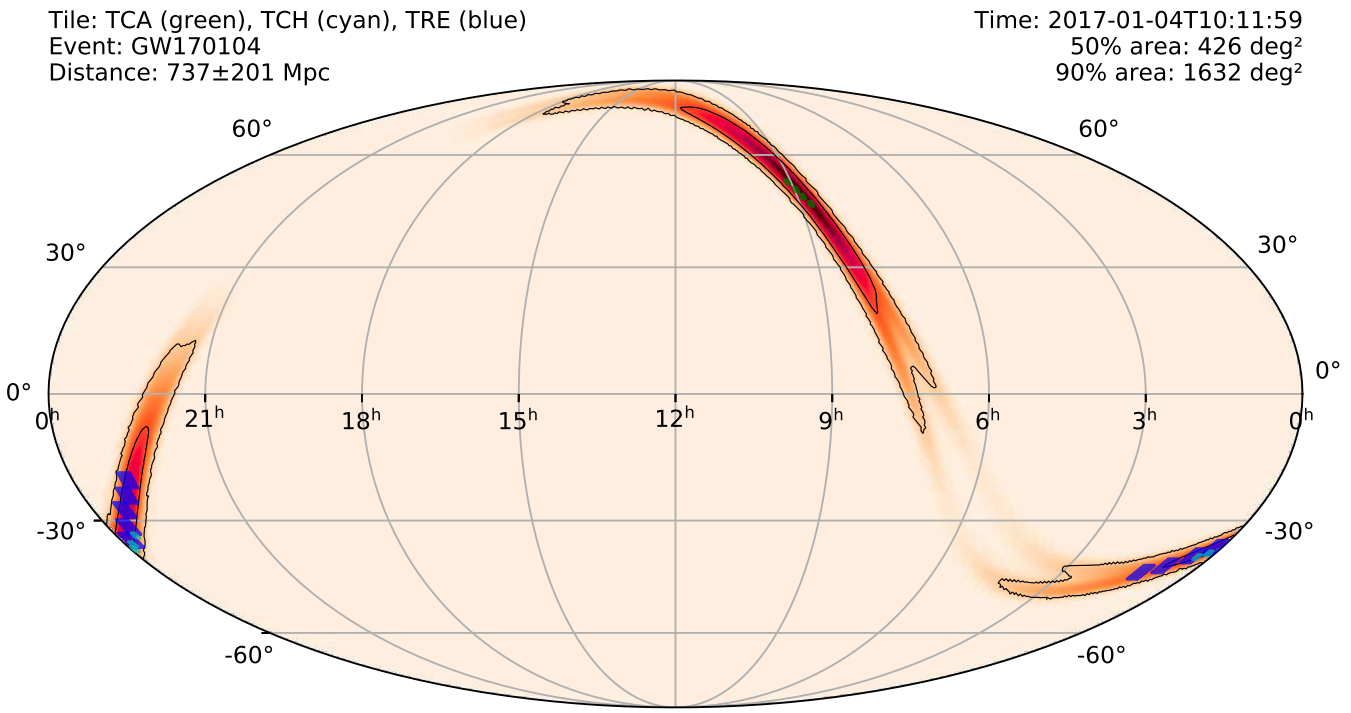

Figure A.2: TTAROT tiles are displayed over the contours of the localization of GW170104.

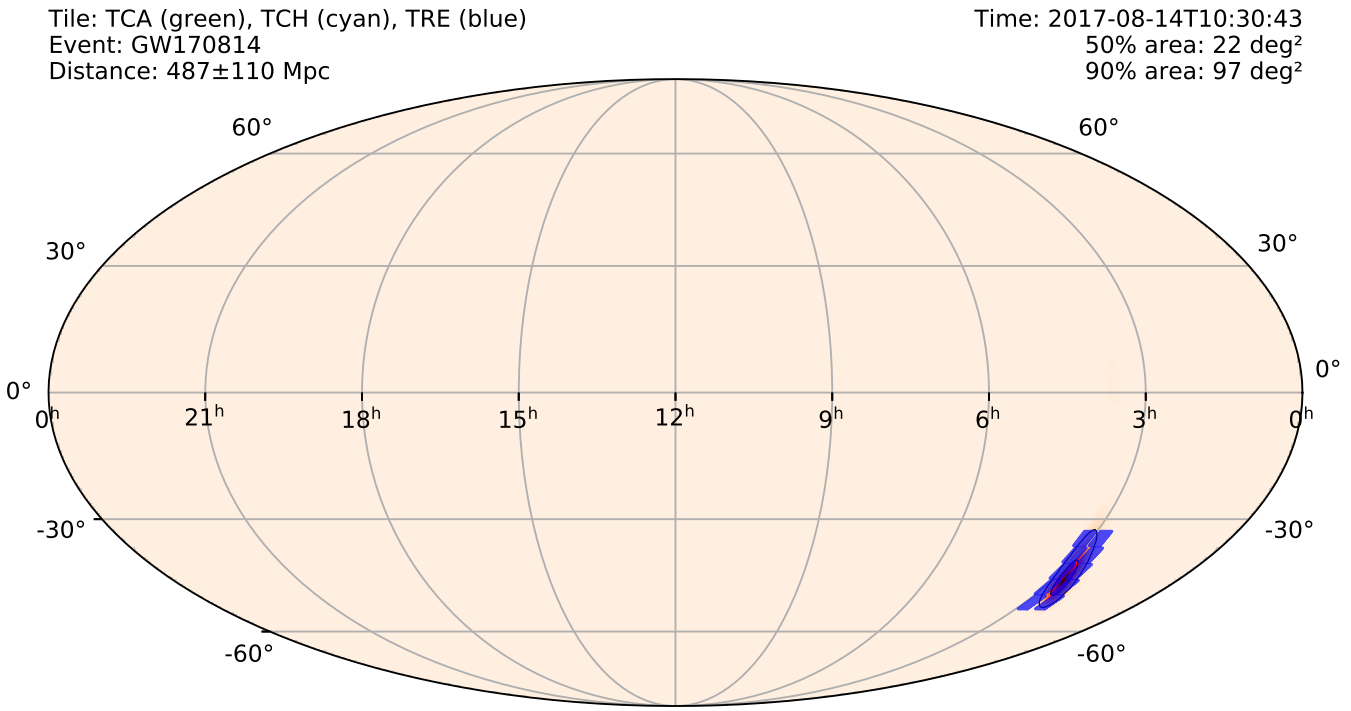

Figure A.3: TAROT tiles are displayed over the contours of the localization of GW170814.

A.2 TAROT tiles over localization of run O3

TAROT telescopes prepared for GW follow-up in the run O3. The Experience form the last two GW observing runs provided us the method to follow-up including the cooperation with GRANDMA network. Telescope tiles were optimized by GRANDMA and the follow-up was reduced to a few days. A search strategy and image analysis were based on the crossmatch method described in chapter 4. Results were shared in public in the Gamma-ray Coordinates Network (GCN) where it is the public archive system. GCN distributes locations of GRBs and other transients called 'the Notices' detected by spacecraft and also GCN reports the follow-up observations called 'the Circulars' made by ground- and space-based optical, radio, X-ray, TeV and other particle observations. TAROT telescopes stand by for the Notices from GW alert and GRB alert. TAROT reports back the Circulars after GW counterparts. TAROT reported in total of 34 Circulars to the GCN. The link to the Circulars is given under each image. Each Figure has TAROT tiles over 50% and 90% probability respectively.

The Table A.2 shows all the GW follow-up performed by TAROT telescopes during run O3. The first column is the GW event; the second column is the GW classification into BNS (binary neutron star mergers), NSBH (neutron star - black hole mergers), BBH (binary black hole mergers), MG (mass gap mergers) and Terr (terrestrial events). The third column is burst time in UTC. The forth column is number of scientific image that had been observed by TAROT telescopes: TAROT-TCA, TAROT-TCH and TAROT-TRE.

Table A.2: TAROT observations during run O3.

	Classification					Date	No. scientific image		
Event	BNS	NSBH	BBH	MG	Terr	UTC	TCA	TCH	TRE
S200316bj	0	0	0	100	0	2020-03-16 21:57:56	692	0	90
S200302c	0	0	89	0	11	2020-03-02 01:58:11	579	0	97
S200225q	0	0	96	0	4	2020-02-25 06:04:21	349	197	39
S200224ca	0	0	100	0	0	2020-02-24 22:22:34	206	396	151
S200219ac	0	0	96	0	4	2020-02-19 09:44:15	425	118	93
S200213t	63	0	0	0	37	2020-02-13 04:10:40	852	15	66
S200208q	0	0	99	0	1	2020-02-08 13:01:17	332	238	21
S200128d	0	0	97	0	3	2020-01-28 02:20:11	39	186	0
S200115j	0	0	0	94	6	2020-01-15 04:23:09	921	334	60
S200112r	0	0	100	0	0	2020-01-12 15:58:38	209	264	114
S200105ae	0	3	0	0	97	2020-01-05 16:24:26	563	381	75
S191222n	0	0	100	0	0	2019-12-22 03:35:37	322	129	33
S191216ap	0	0	0	100	0	2019-12-16 21:33:38	247	18	0
S191215w	0	0	100	0	0	2019-12-15 22:30:52	93	91	81
S191213g	77	0	0	0	23	2019-12-13 04:34:08	66	0	0
S191205ah	0	93	0	0	7	2019-12-05 21:52:08	612	354	72
S191204r	0	0	100	0	0	2019-12-04 17:15:26	278	327	111
S191129u	0	0	100	0	0	2019-11-29 13:40:29	96	219	0
S191109d	0	0	100	0	0	2019-11-09 01:07:17	126	9	62
S191105e	0	0	95	0	5	2019-11-05 14:35:21	307	366	227
S190930t	0	74	0	0	26	2019-09-30 14:34:07	643	764	0
S190930s	0	0	0	95	5	2019-09-30 13:35:41	286	61	135
S190923y	0	68	0	0	32	2019-09-23 12:55:59	589	596	490
S190915ak	0	0	99	0	1	2019-09-15 23:57:02	410	0	0
S190910h	61	0	0	0	39	2019-09-10 08:29:58	562	312	0
S190910d	0	98	0	0	2	2019-09-10 01:26:19	602	881	273
S190901ap	86	0	0	0	14	2019-09-01 23:31:01	364	531	251
S190828l	0	0	100	0	0	2019-08-28 06:55:09	136	204	30
S190828j	0	0	100	0	0	2019-08-28 06:34:05	136	72	30
S190814bv	0	0	0	100	0	2019-08-14 21:10:39	88	445	142
S190728q	0	0	100	0	0	2019-07-28 06:45:10	114	285	141
S190727h	0	0	1	0	99	2019-07-27 06:03:33	300	449	12
S190720a	0	0	99	0	1	2019-07-20 00:08:36	231	304	21
S190718y	2	0	0	0	98	2019-07-18 14:35:12	0	0	188
S190707q	0	0	100	0	0	2019-07-07 09:33:26	169	183	102
S190706ai	0	0	99	0	1	2019-07-06 22:26:41	129	274	102
S190701ah	0	0	93	0	7	2019-07-01 20:33:06	0	0	39
S190630ag	0	1	94	5	0	2019-06-30 18:52:05	54	0	20
S190517h	0	0	98	2	0	2019-05-17 05:51:01	21	119	0
S190513bm	0	1	94	5	0	2019-05-13 20:54:28	69	150	0
S190512at	0	0	99	0	1	2019-05-12 18:07:14	72	102	0
S190510g	98	0	0	0	2	2019-05-10 02:59:39	380	222	0
S190503bf	0	0	96	3	0	2019-05-03 18:54:04	0	90	2
S190426c	49	13	0	24	14	2019-04-26 15:21:55	255	162	73
S190425z	100	0	0	0	0	2019-04-25 08:18:05	128	264	243
S190421ar	0	0	4	0	96	2019-04-21 21:38:56	0	0	72
S190412m	0	0	100	0	0	2019-04-12 05:30:44	149	0	100

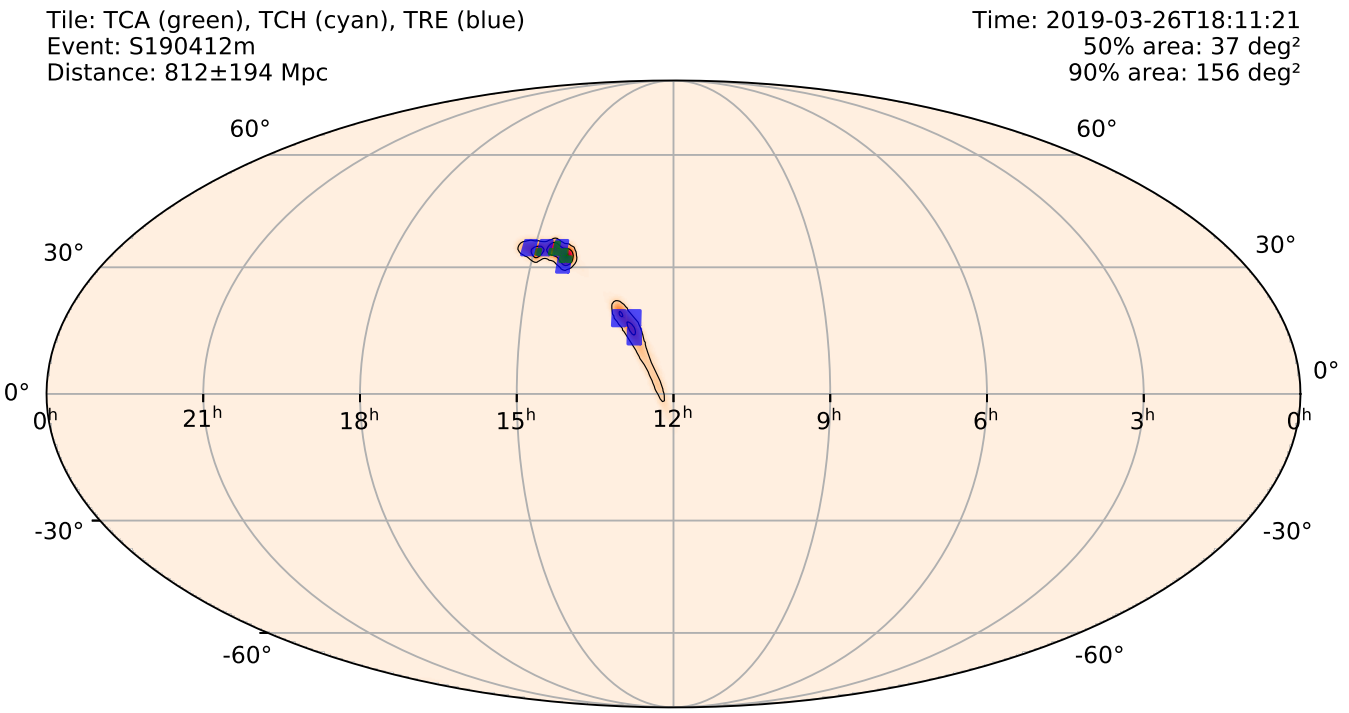

Figure A.4: TAROT tiles are displayed over the contours of the localization of S190412m. See the Circular report `https://gcn.gsfc.nasa.gov/gcn3/24126.gcn3`.

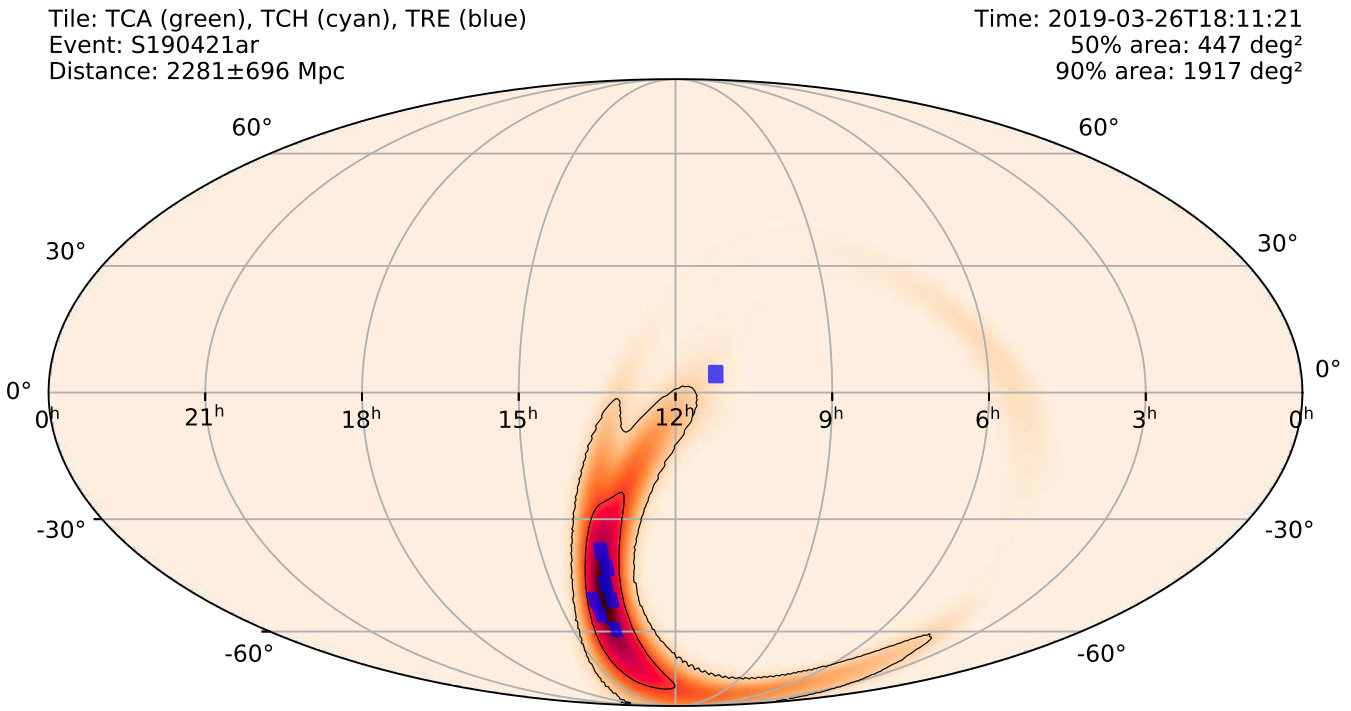

Figure A.5: TAROT tiles are displayed over the contours of the localization of S190421ar. See the Circular report `https://gcn.gsfc.nasa.gov/gcn3/24162.gcn3`.

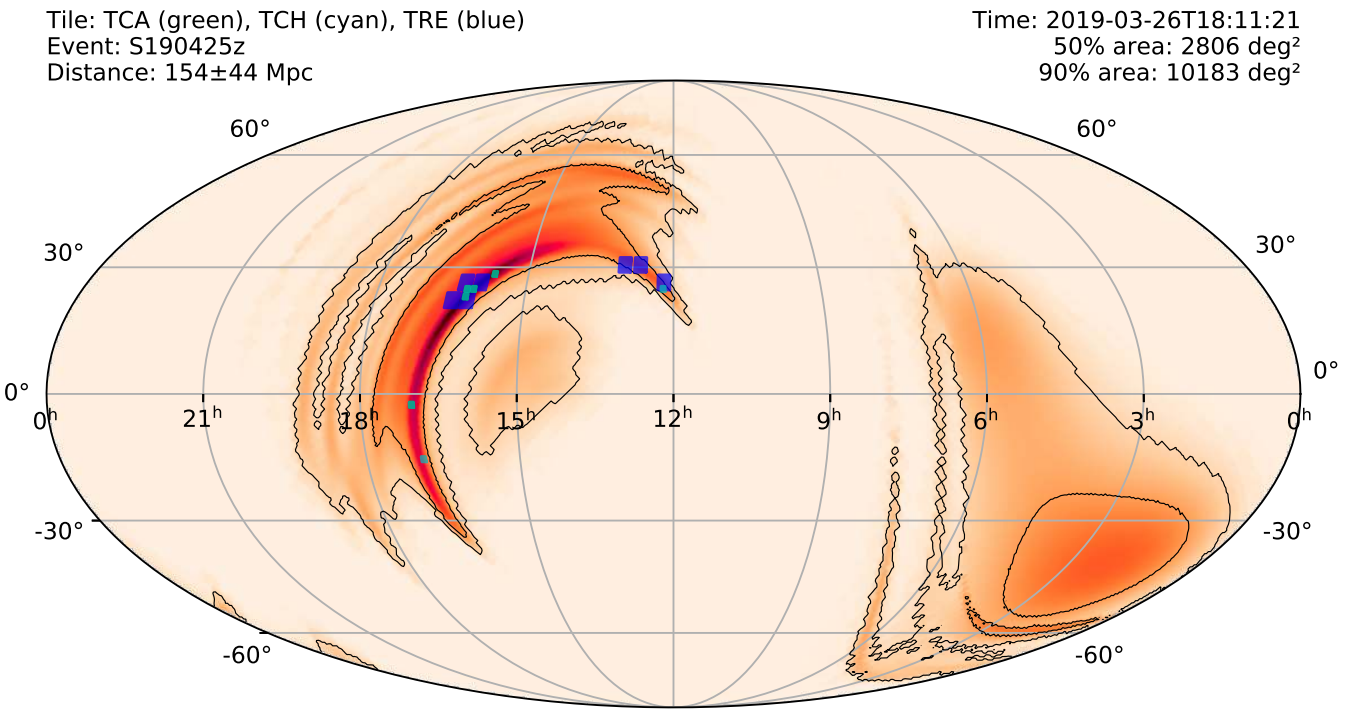

Figure A.6: TAROT tiles are displayed over the contours of the localization of S190425z. See the Circular report `https://gcn.gsfc.nasa.gov/gcn3/24227.gcn3`.

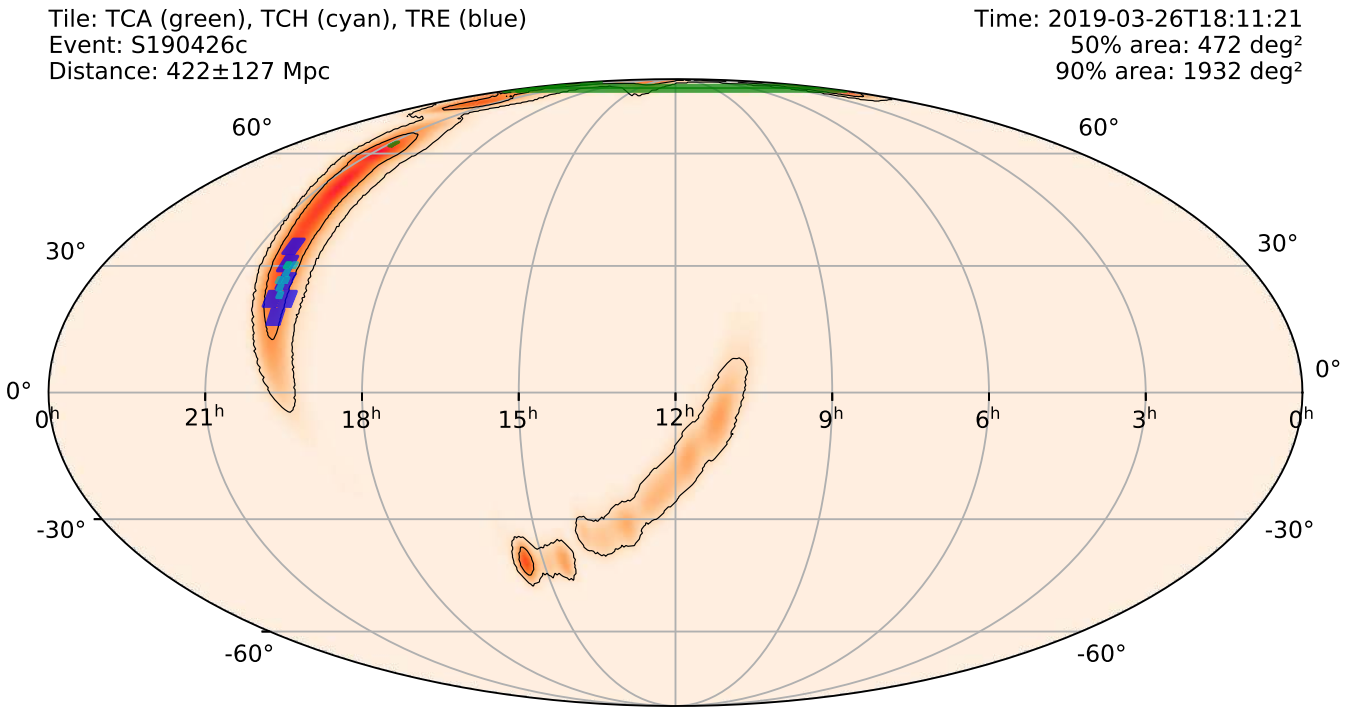

Figure A.7: TAROT tiles are displayed over the contours of the localization of S190426c.

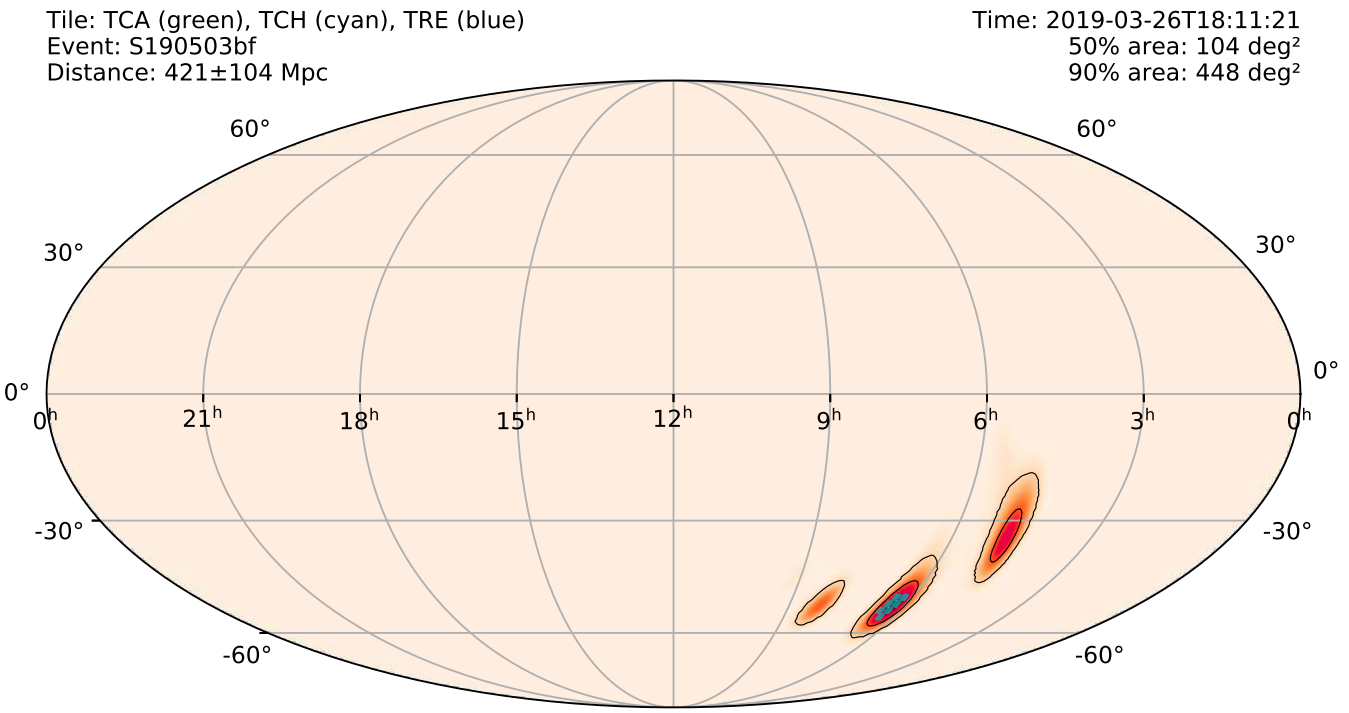

Figure A.8: TAROT tiles are displayed over the contours of the localization of S190503bf. See the Circular report `https://gcn.gsfc.nasa.gov/gcn3/24431.gcn3`.

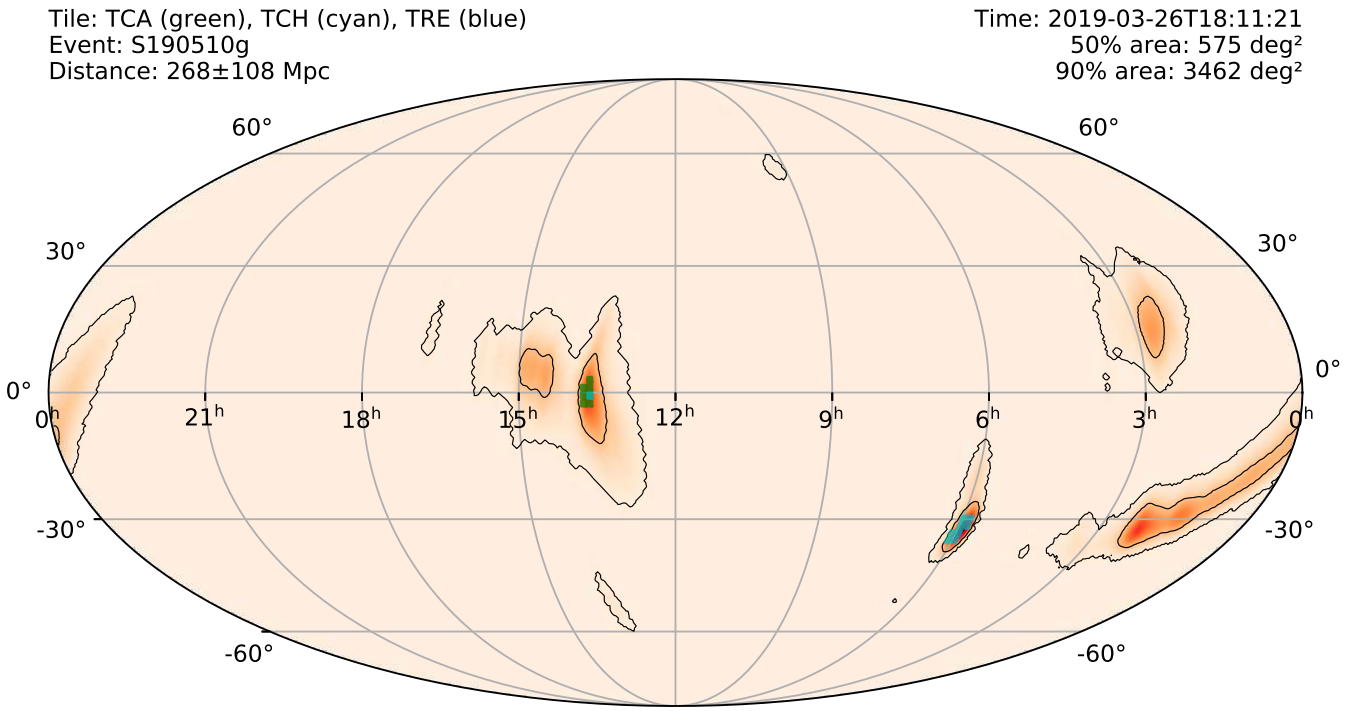

Figure A.9: TAROT tiles are displayed over the contours of the localization of S190510g.

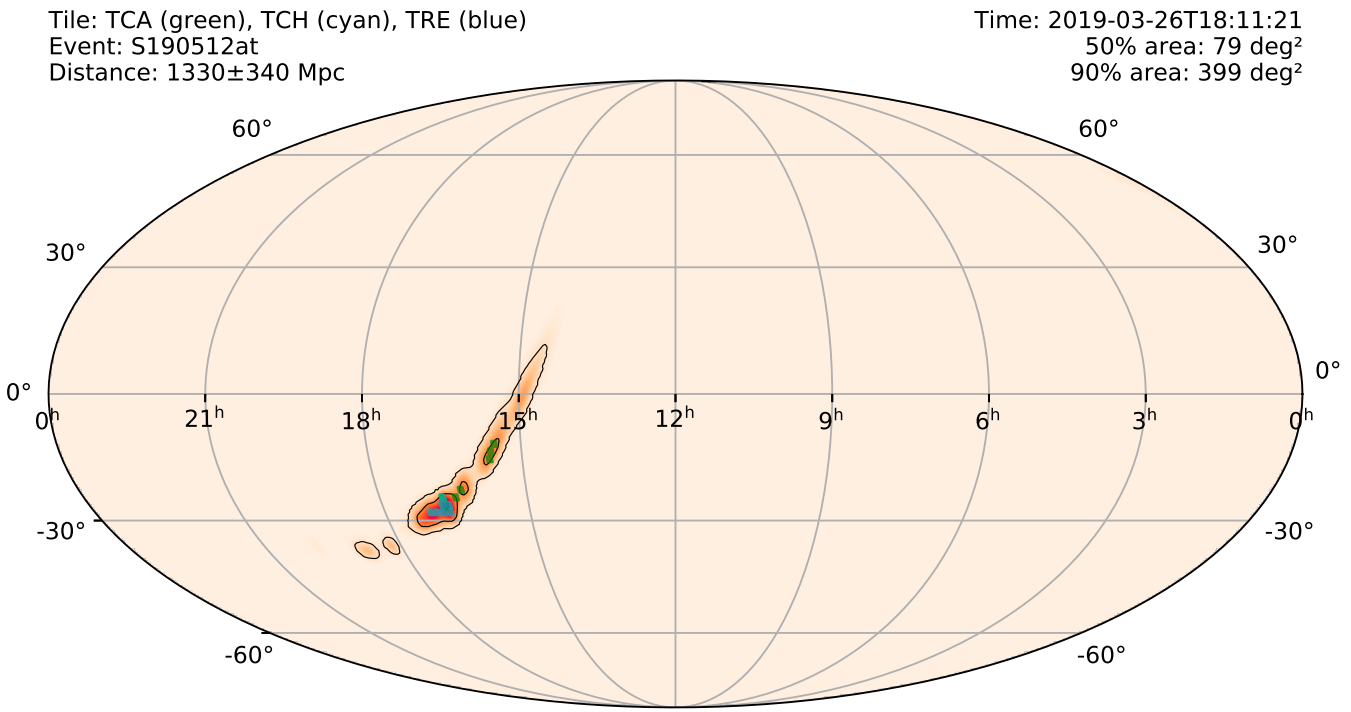

Figure A.10: TAROT tiles are displayed over the contours of the localization of S190512at.

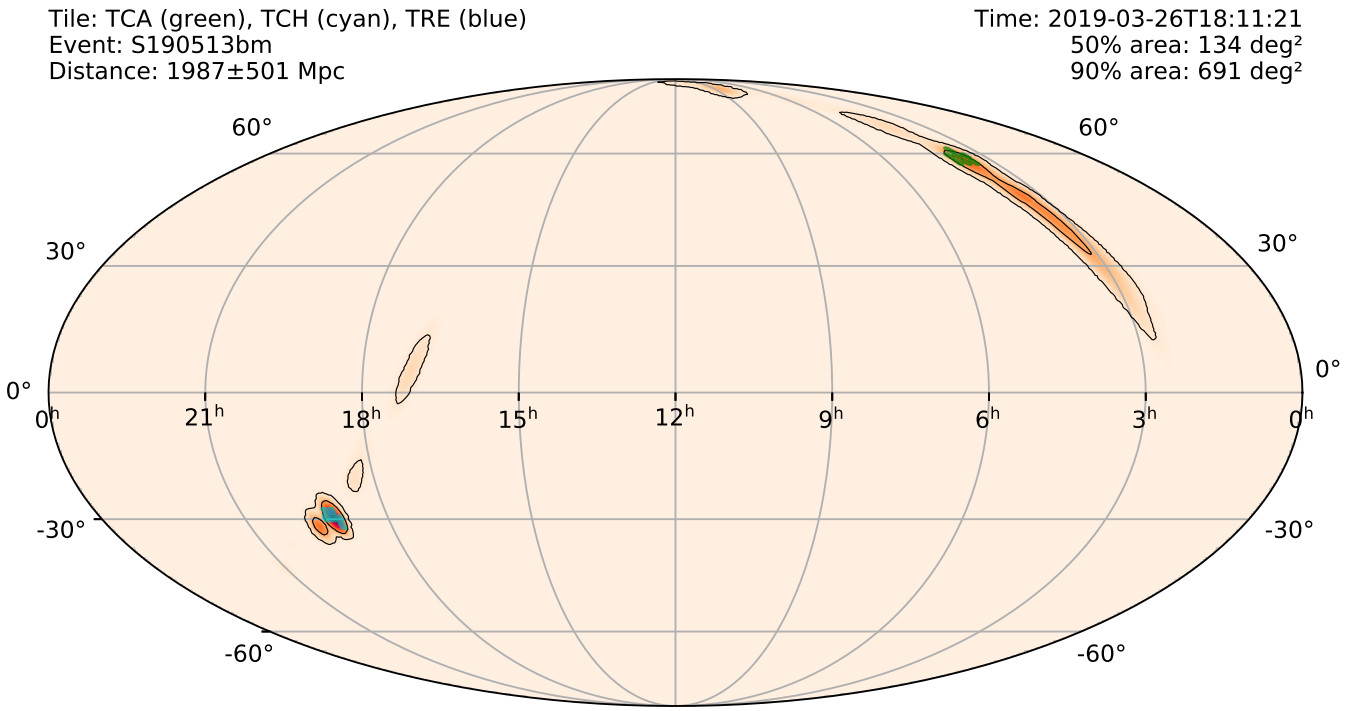

Figure A.11: TAROT tiles are displayed over the contours of the localization of S190513bm. See the Circular report `https://gcn.gsfc.nasa.gov/gcn3/24549.gcn3`.

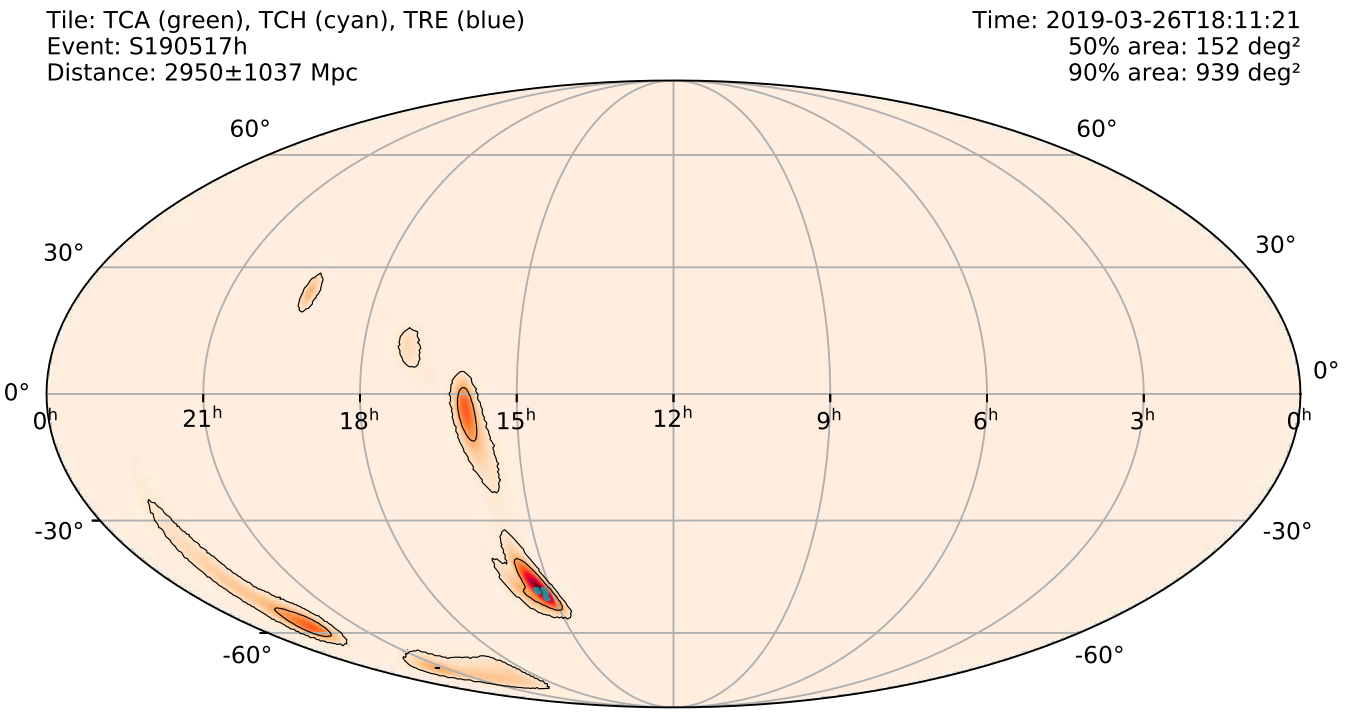

Figure A.12: TAROT tiles are displayed over the contours of the localization of S190517h. See the Circular report `https://gcn.gsfc.nasa.gov/gcn3/24631.gcn3`.

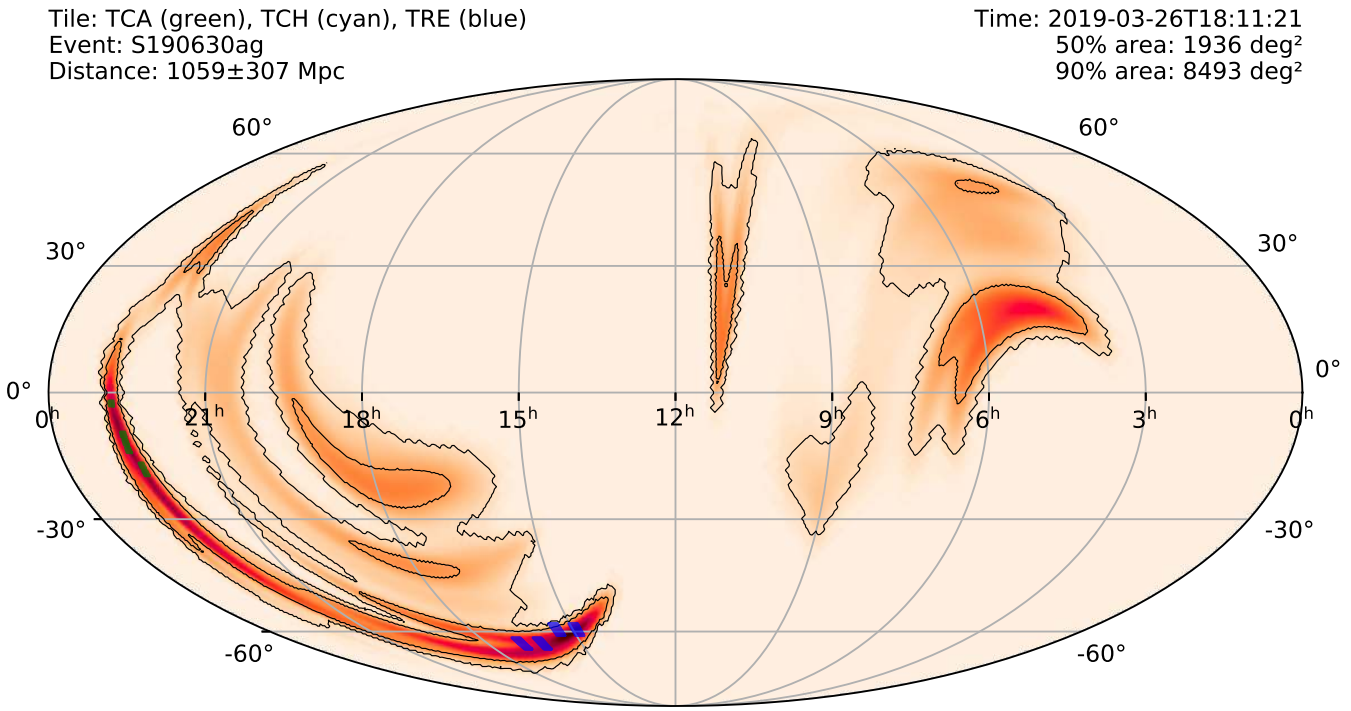

Figure A.13: TAROT tiles are displayed over the contours of the localization of S190630ag.

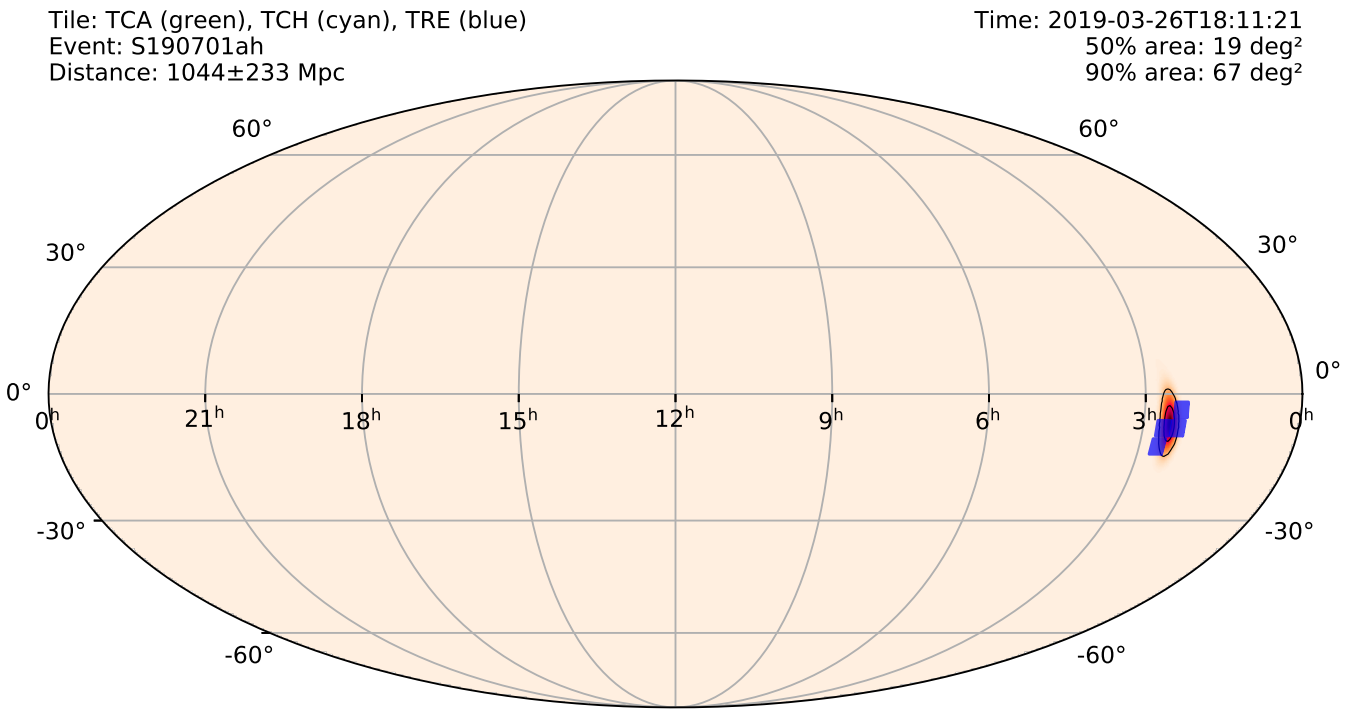

Figure A.14: TAROT tiles are displayed over the contours of the localization of S190701ah.

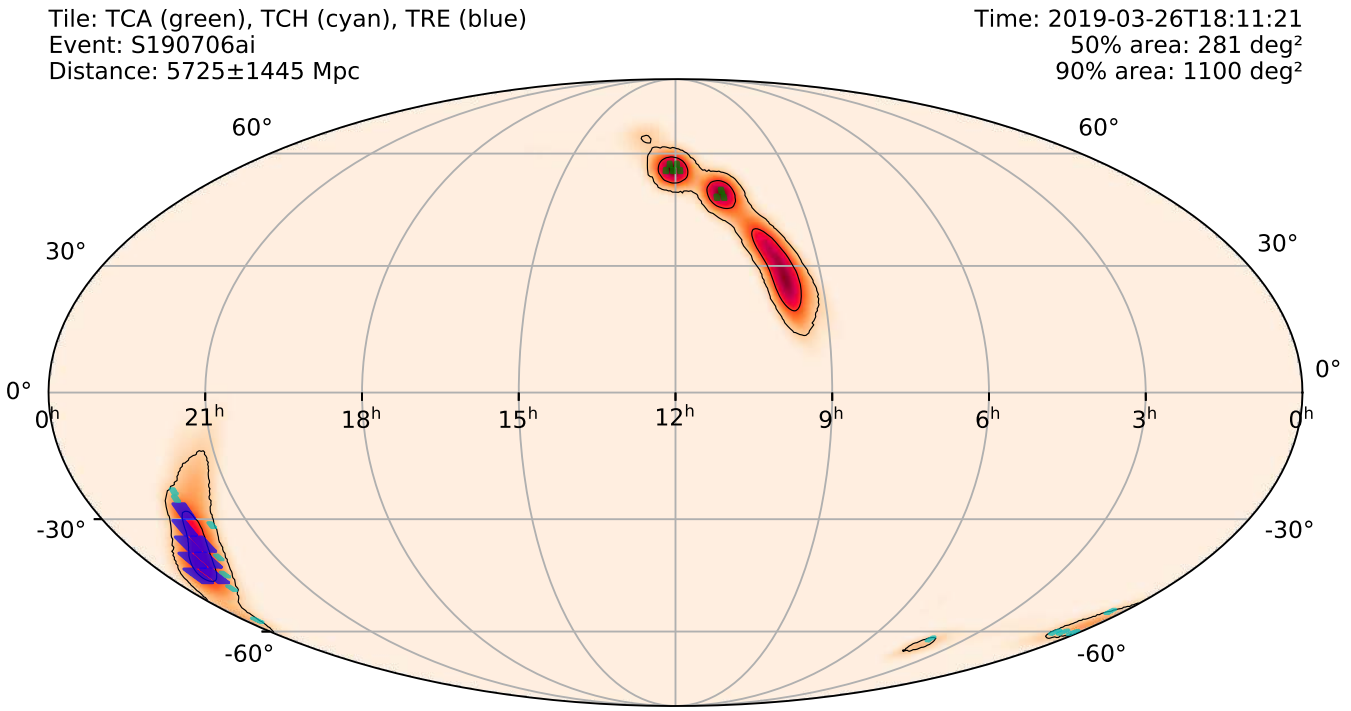

Figure A.15: TAROT tiles are displayed over the contours of the localization of S190706ai.

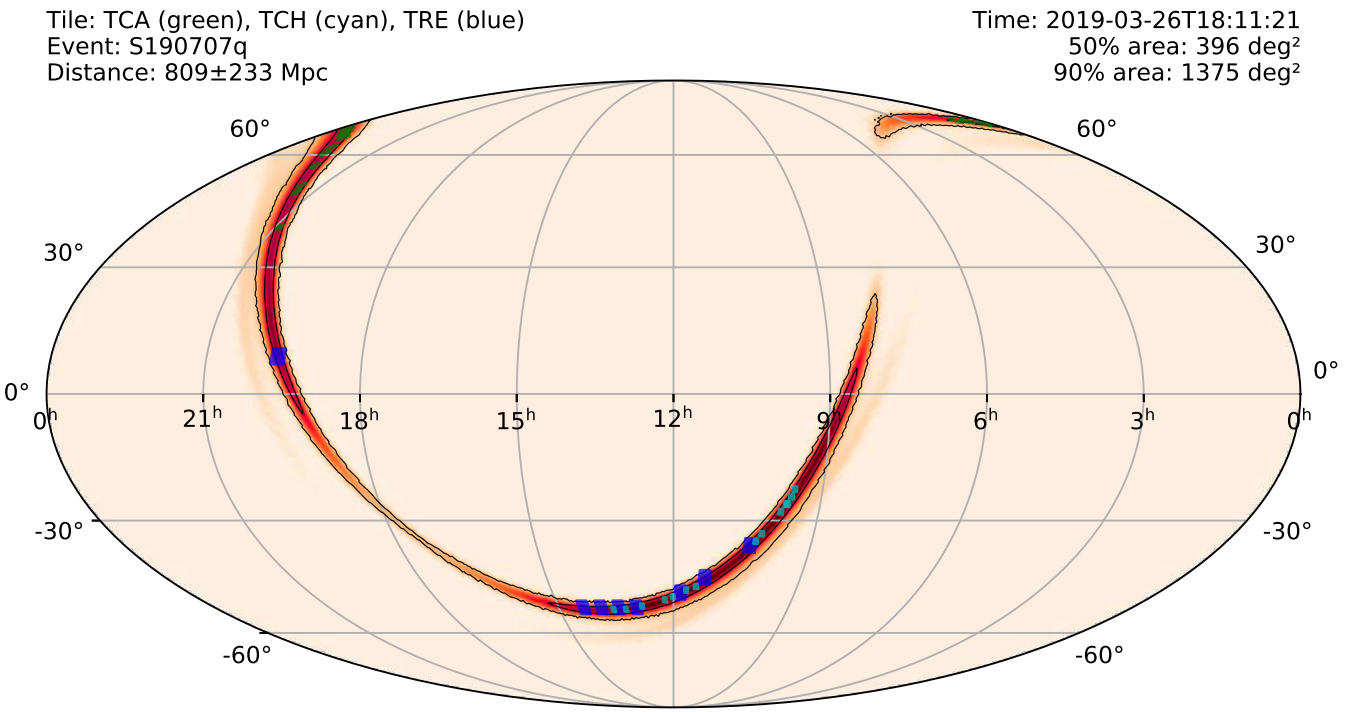

Figure A.16: TAROT tiles are displayed over the contours of the localization of S190707q.

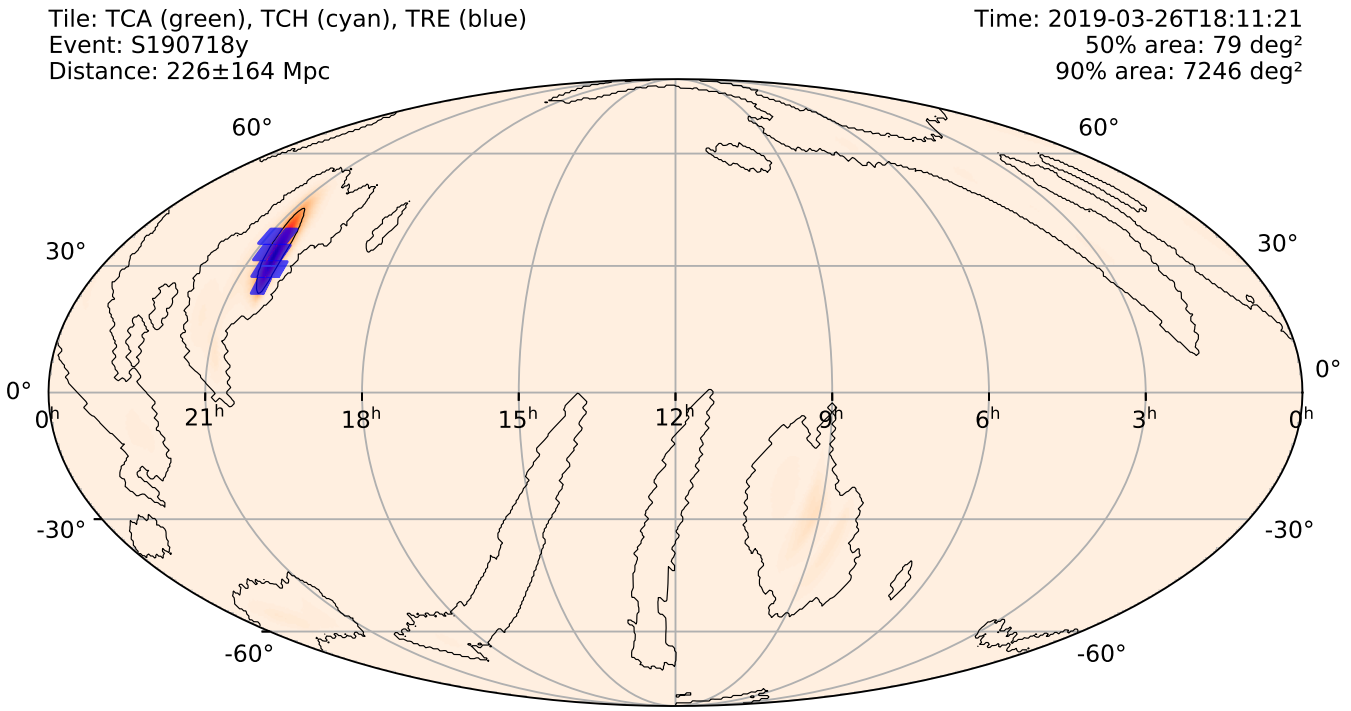

Figure A.17: TAROT tiles are displayed over the contours of the localization of S190718y.

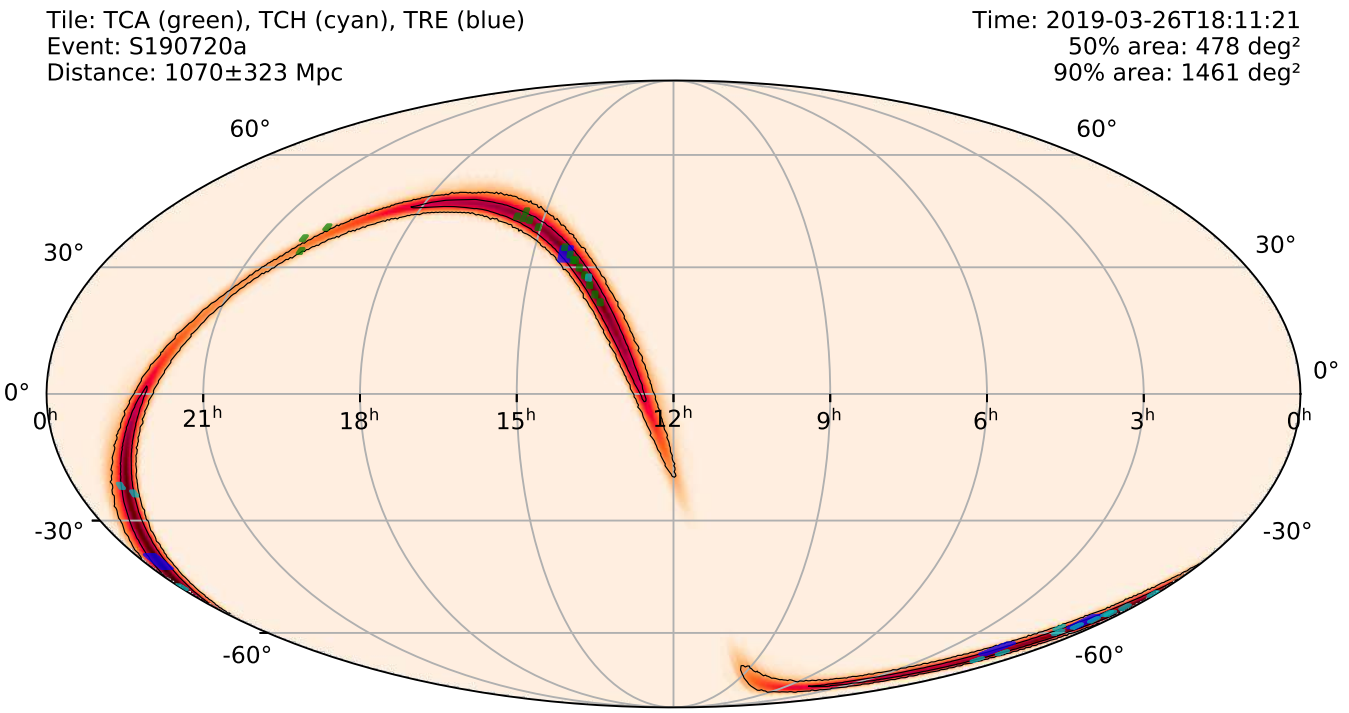

Figure A.18: TAROT tiles are displayed over the contours of the localization of S190720a.

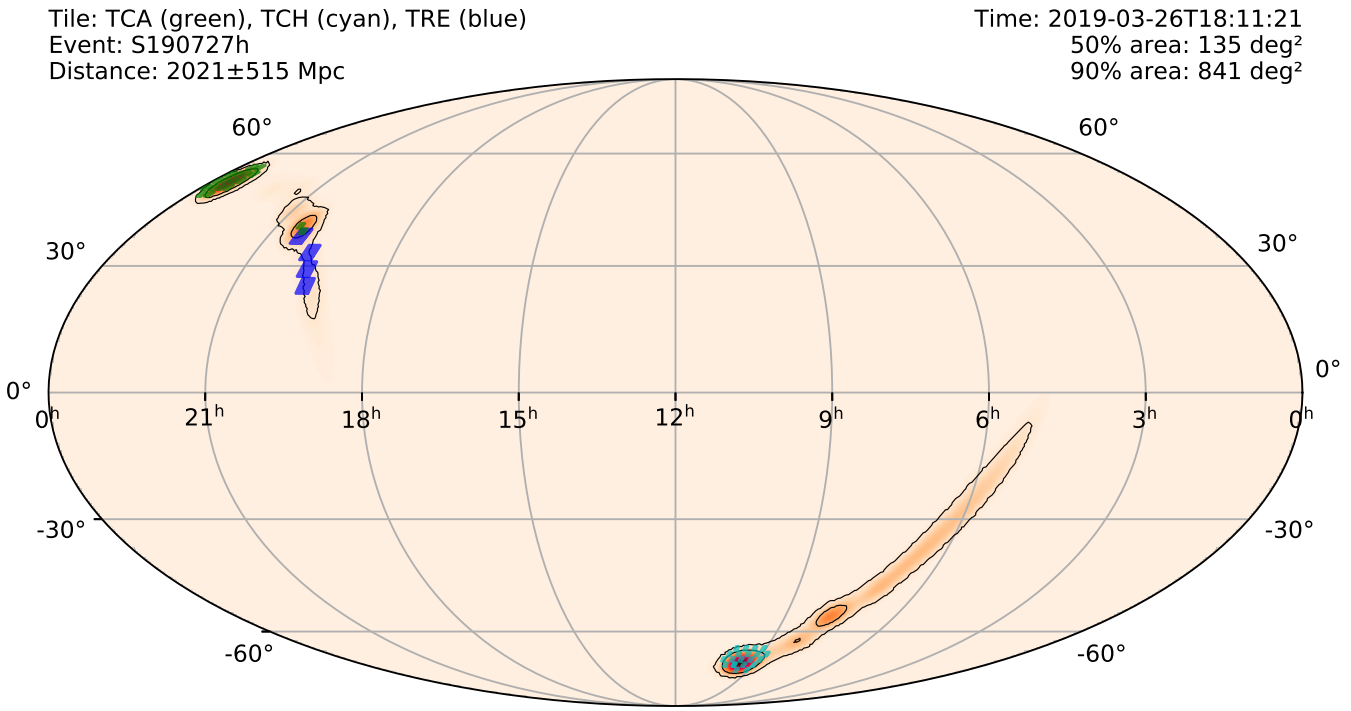

Figure A.19: TAROT tiles are displayed over the contours of the localization of S190727h.

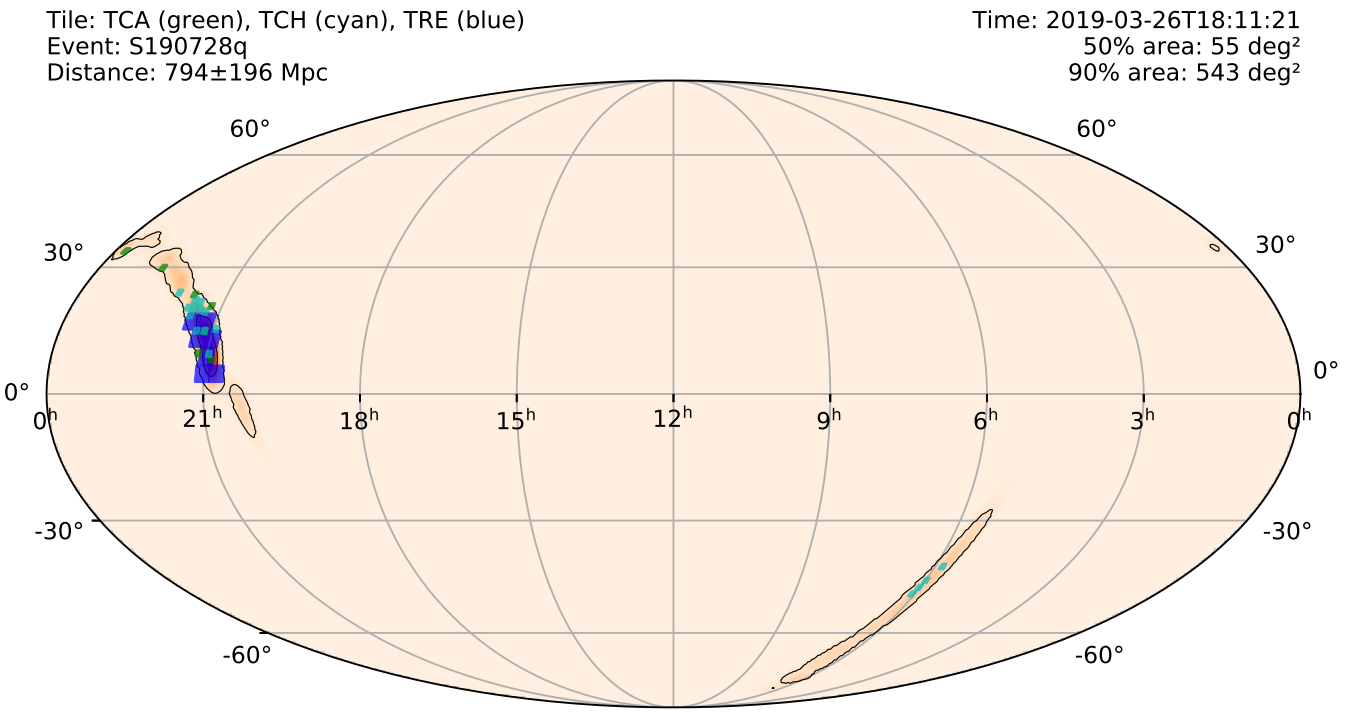

Figure A.20: TAROT tiles are displayed over the contours of the localization of S190728q.

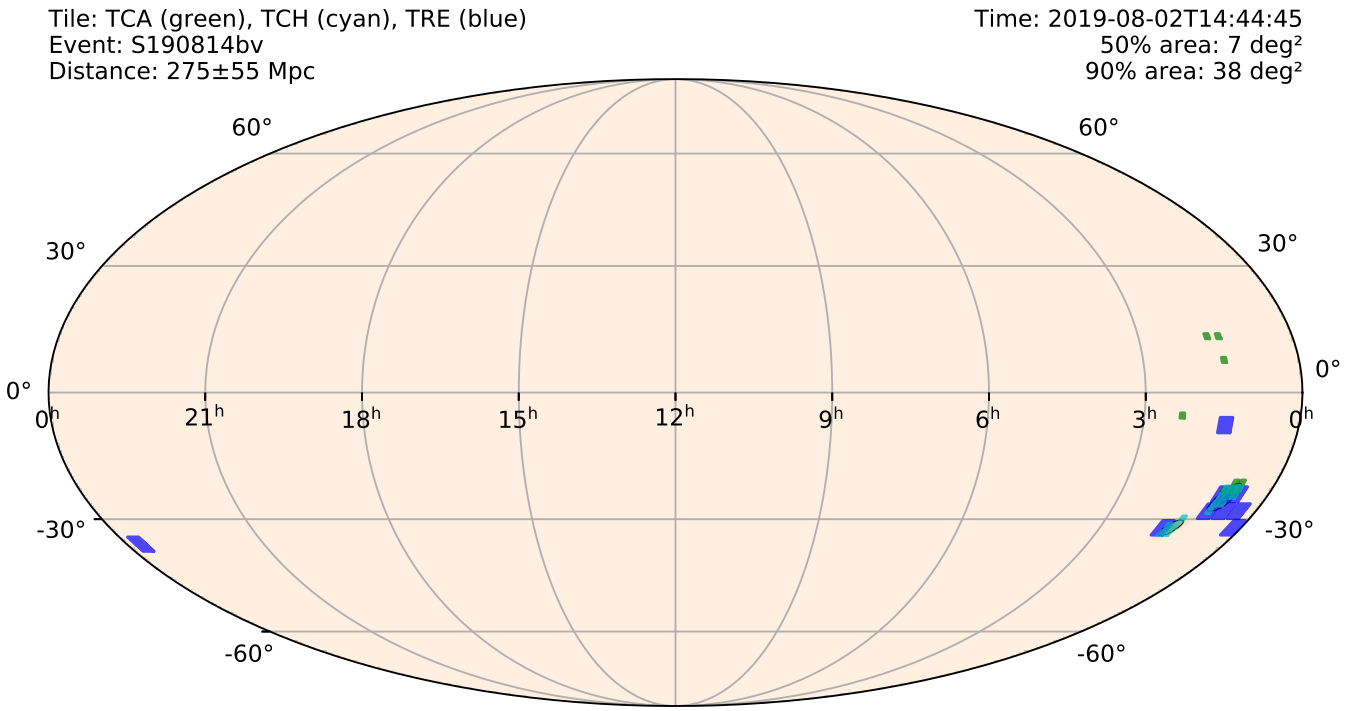

Figure A.21: TAROT tiles are displayed over the contours of the localization of S190814bv. See the Circular report `https://gcn.gsfc.nasa.gov/gcn3/25599.gcn3`.

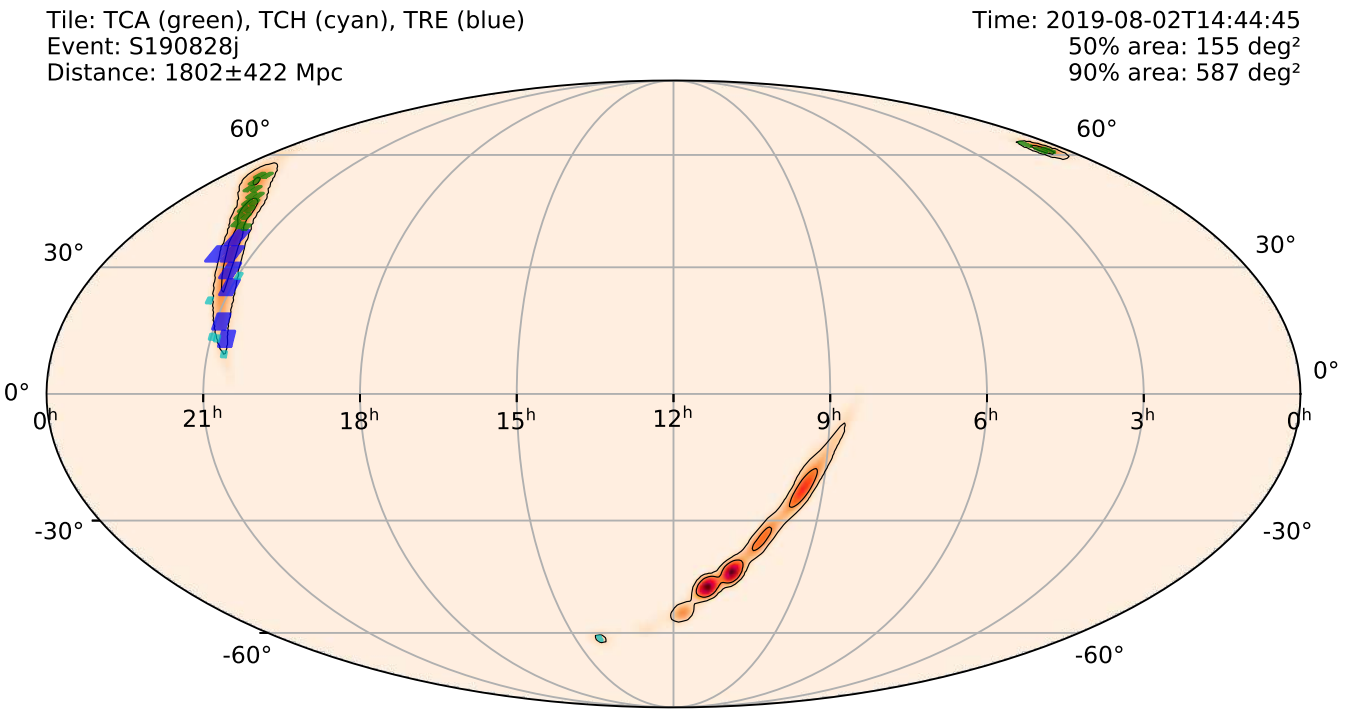

Figure A.22: TAROT tiles are displayed over the contours of the localization of S190828j. See the Circular report `https://gcn.gsfc.nasa.gov/gcn3/25594.gcn3`.

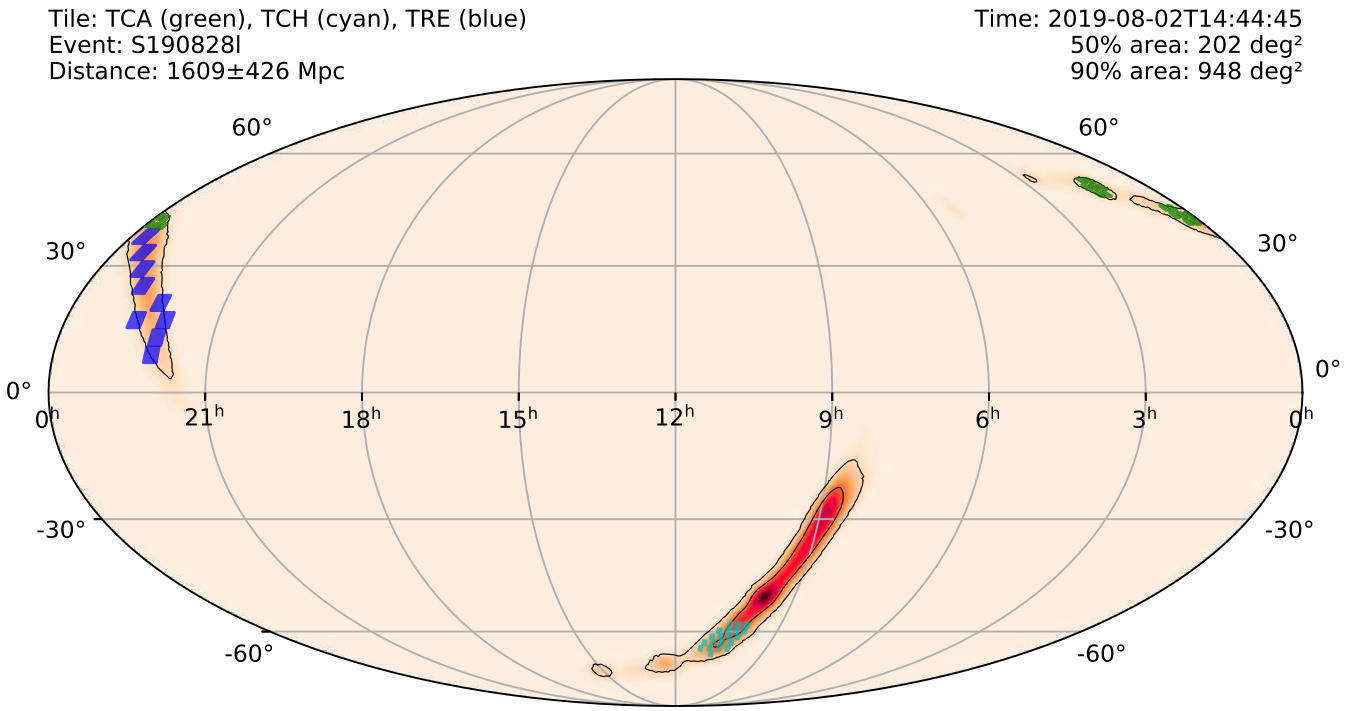

Figure A.23: TAROT tiles are displayed over the contours of the localization of S190828l. See the Circular report `https://gcn.gsfc.nasa.gov/gcn3/25593.gcn3`.

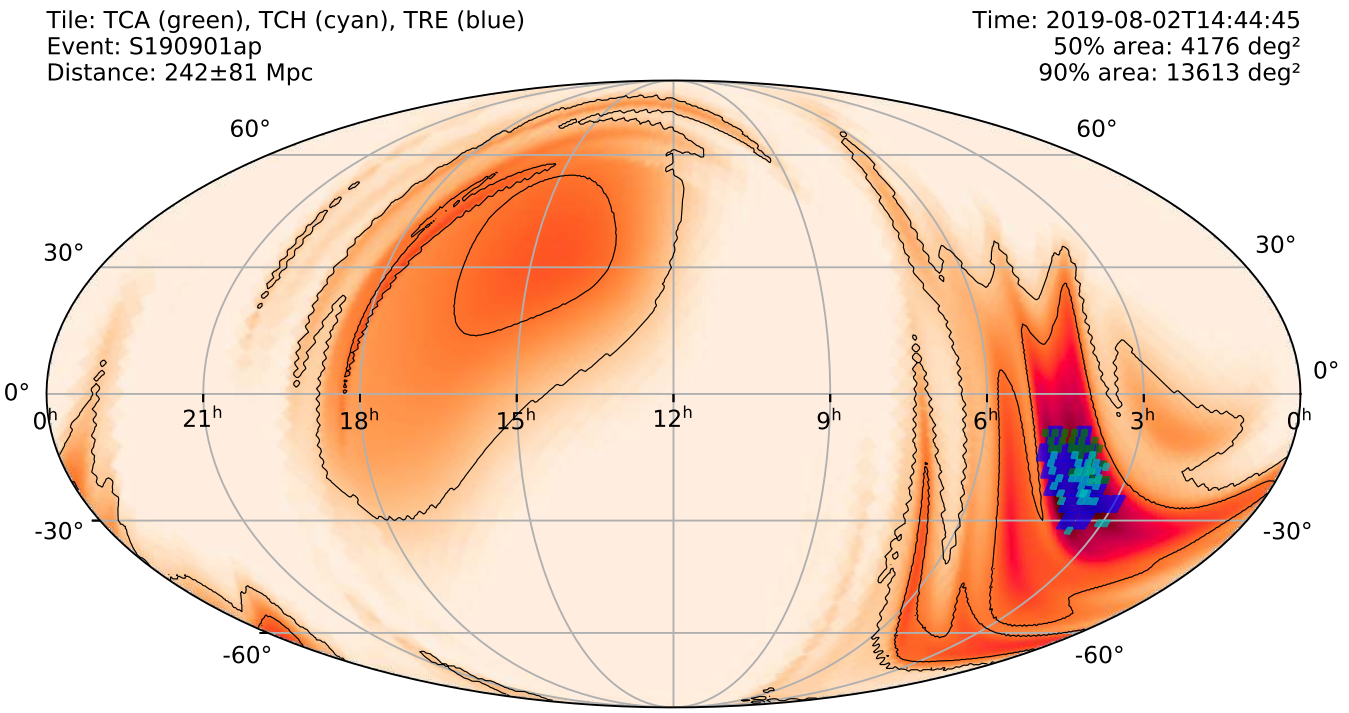

Figure A.24: TAROT tiles are displayed over the contours of the localization of S190901ap. See the Circular report `https://gcn.gsfc.nasa.gov/gcn3/25666.gcn3`.

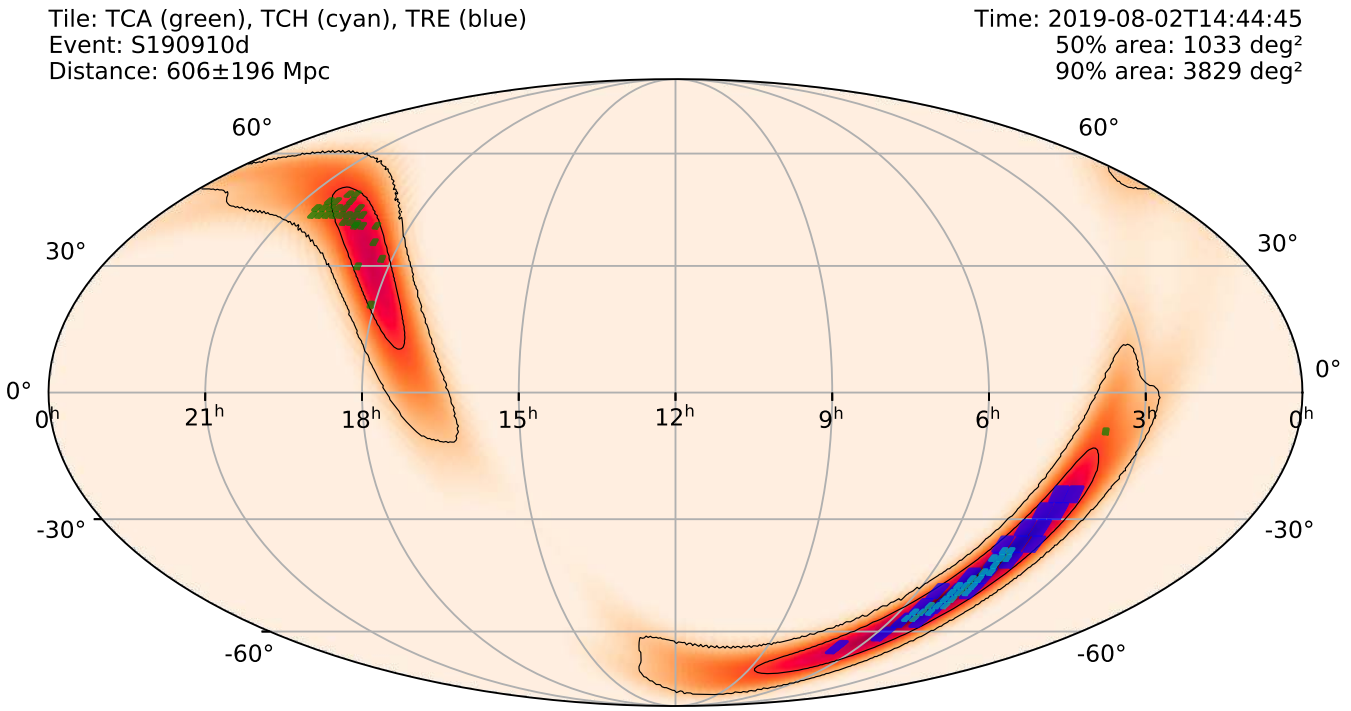

Figure A.25: TAROT tiles are displayed over the contours of the localization of S190910d. See the Circular report `https://gcn.gsfc.nasa.gov/gcn3/25749.gcn3`.

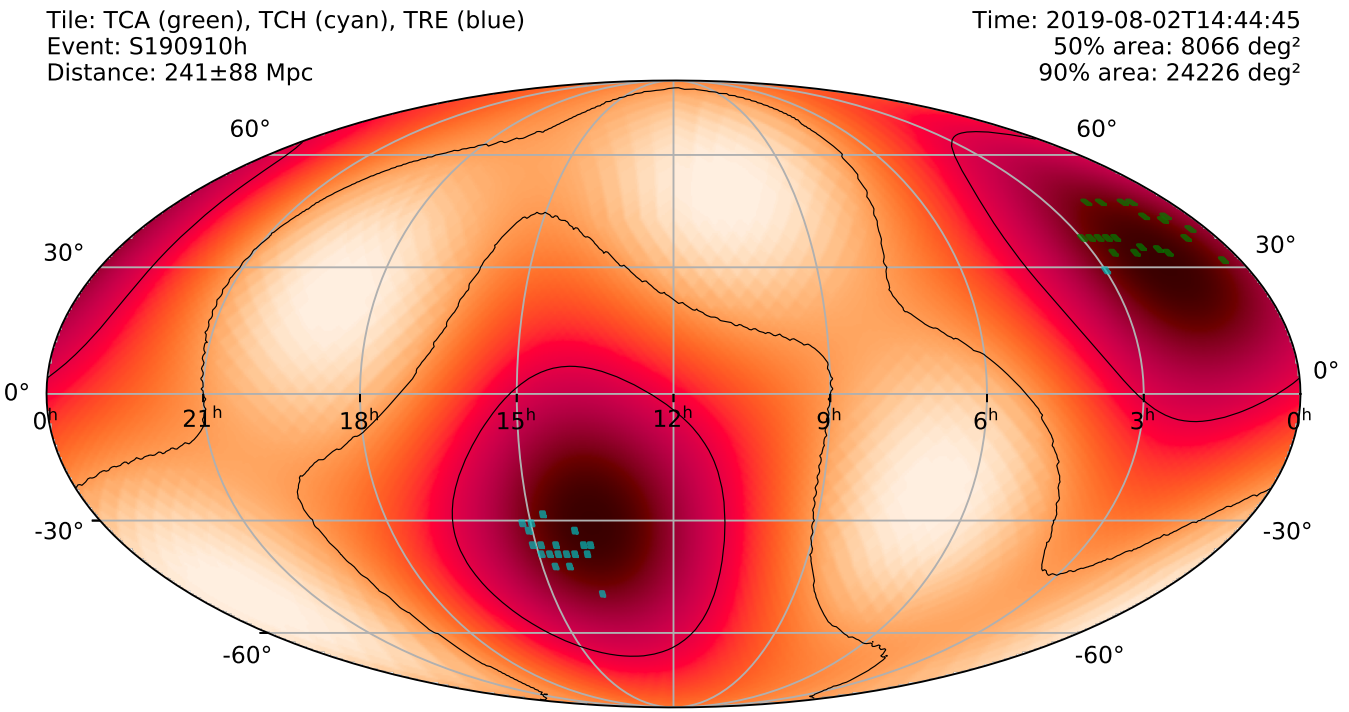

Figure A.26: TAROT tiles are displayed over the contours of the localization of S190910h. See the Circular report `https://gcn.gsfc.nasa.gov/gcn3/25780.gcn3`.

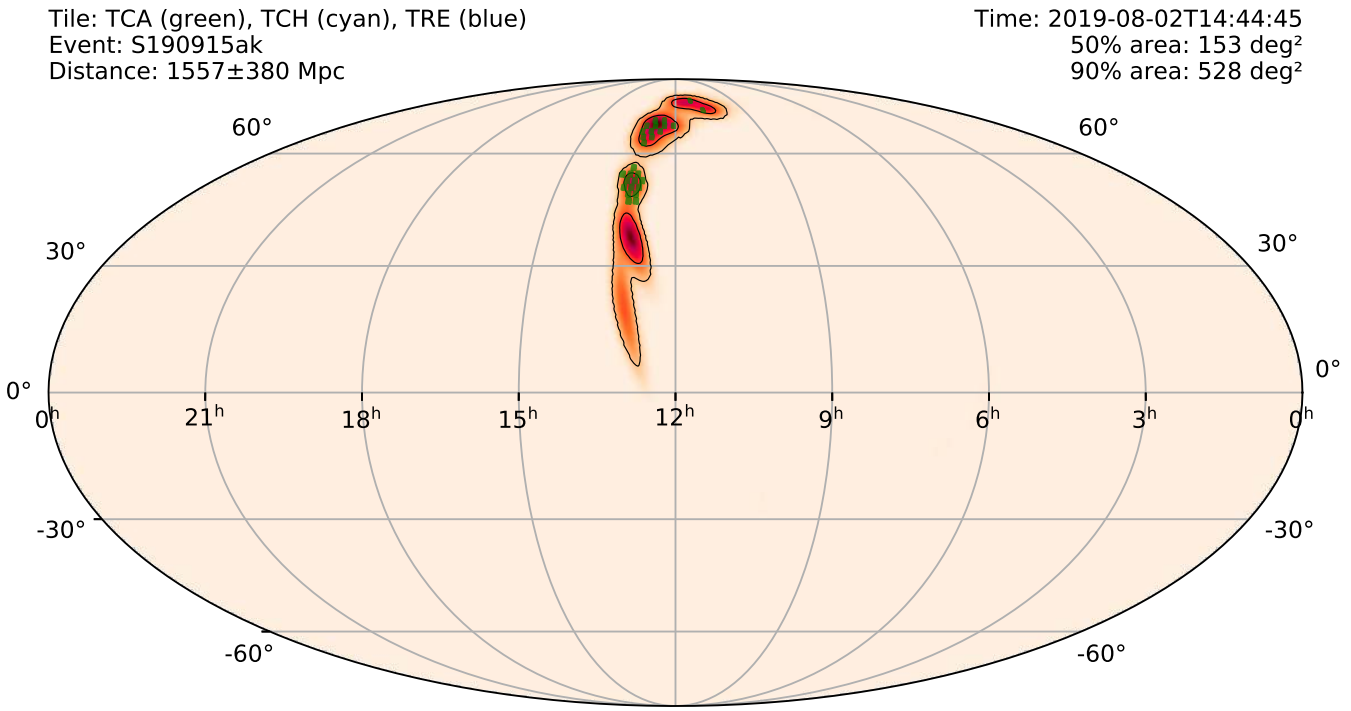

Figure A.27: TAROT tiles are displayed over the contours of the localization of S190915ak. See the Circular report `https://gcn.gsfc.nasa.gov/gcn3/25781.gcn3`.

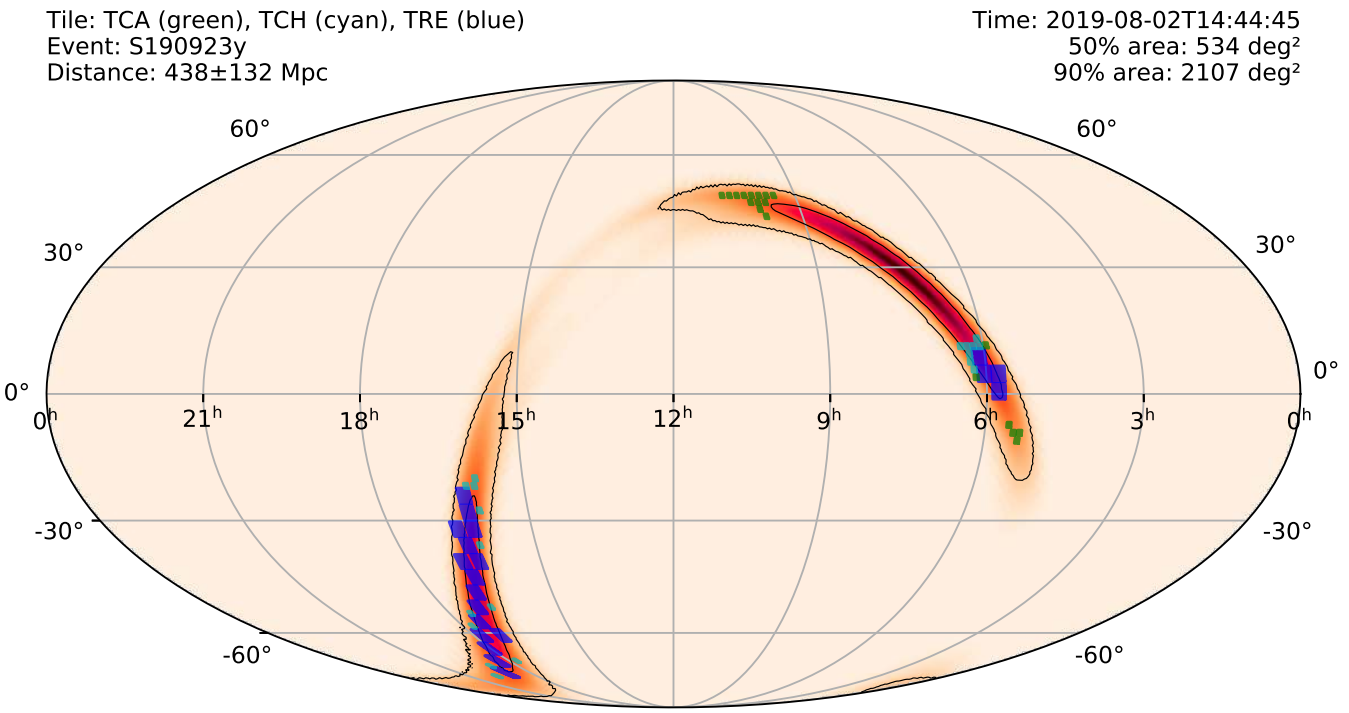

Figure A.28: TAROT tiles are displayed over the contours of the localization of S190923y. See the Circular report `https://gcn.gsfc.nasa.gov/gcn3/25847.gcn3`.

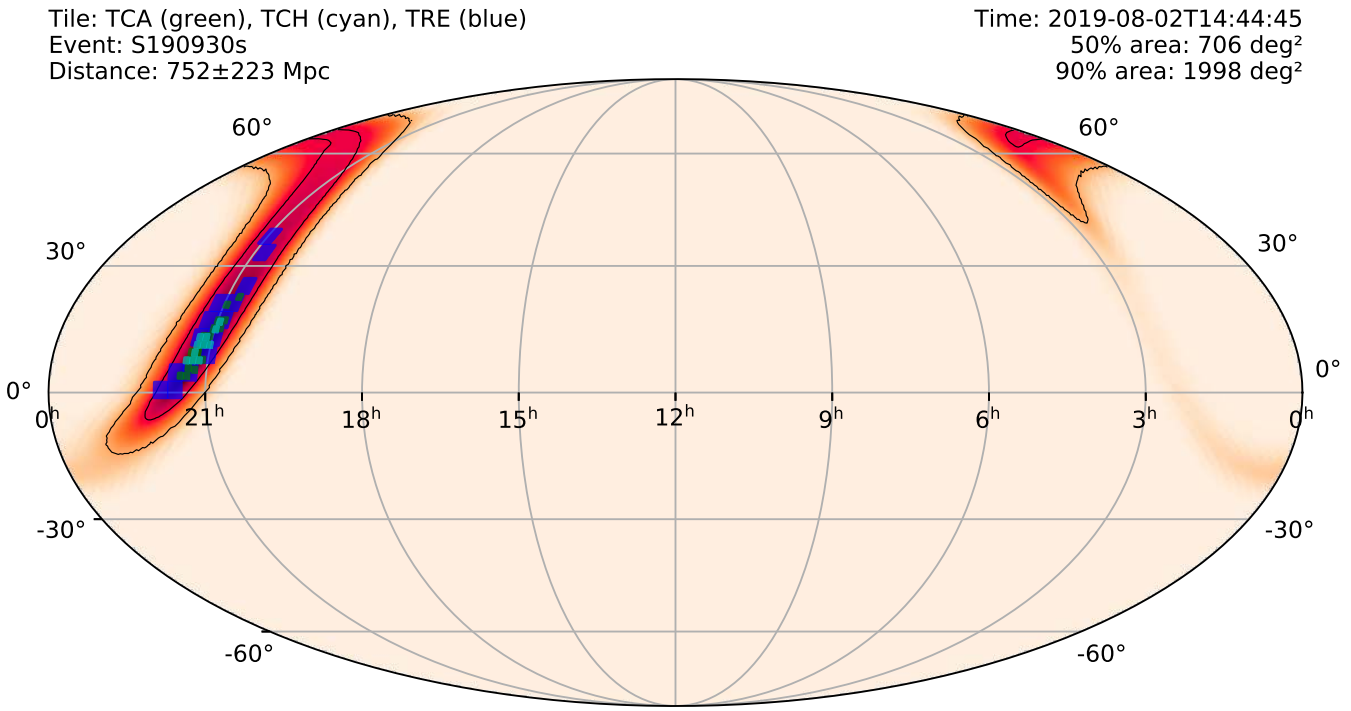

Figure A.29: TAROT tiles are displayed over the contours of the localization of S190930s.

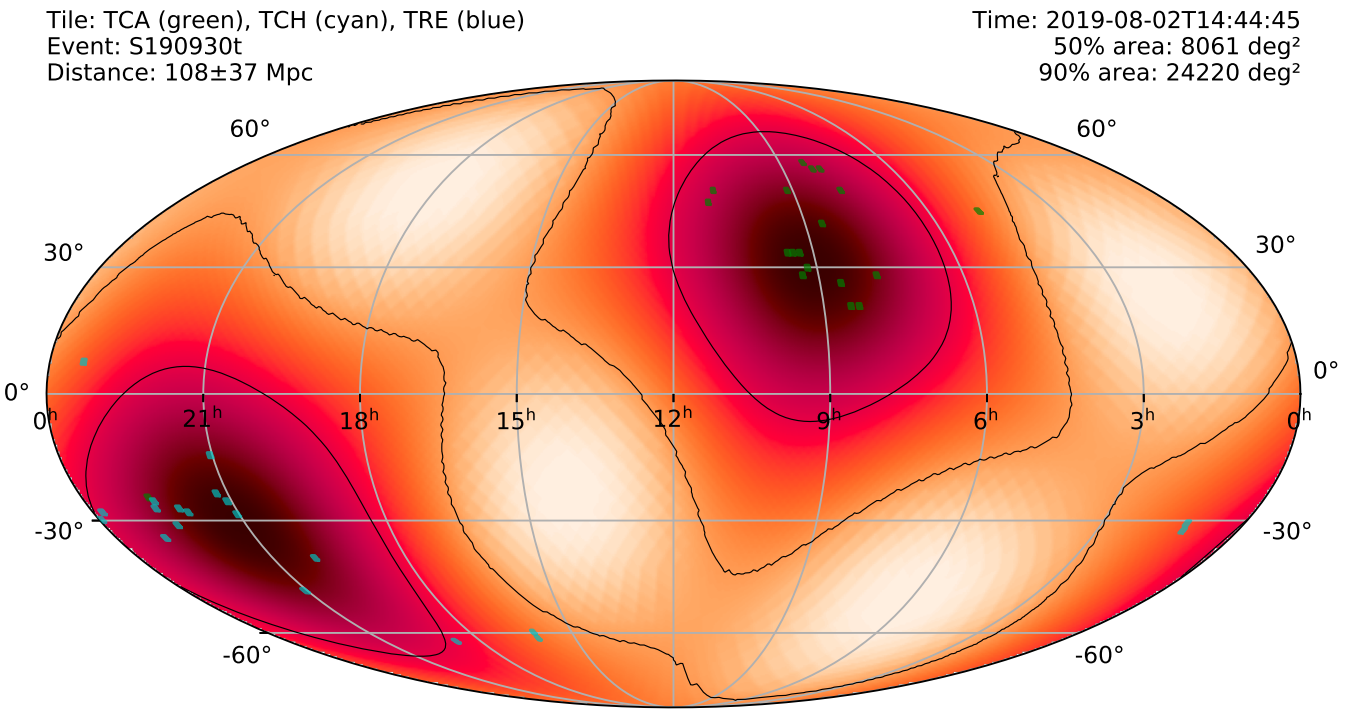

Figure A.30: TAROT tiles are displayed over the contours of the localization of S190930t.

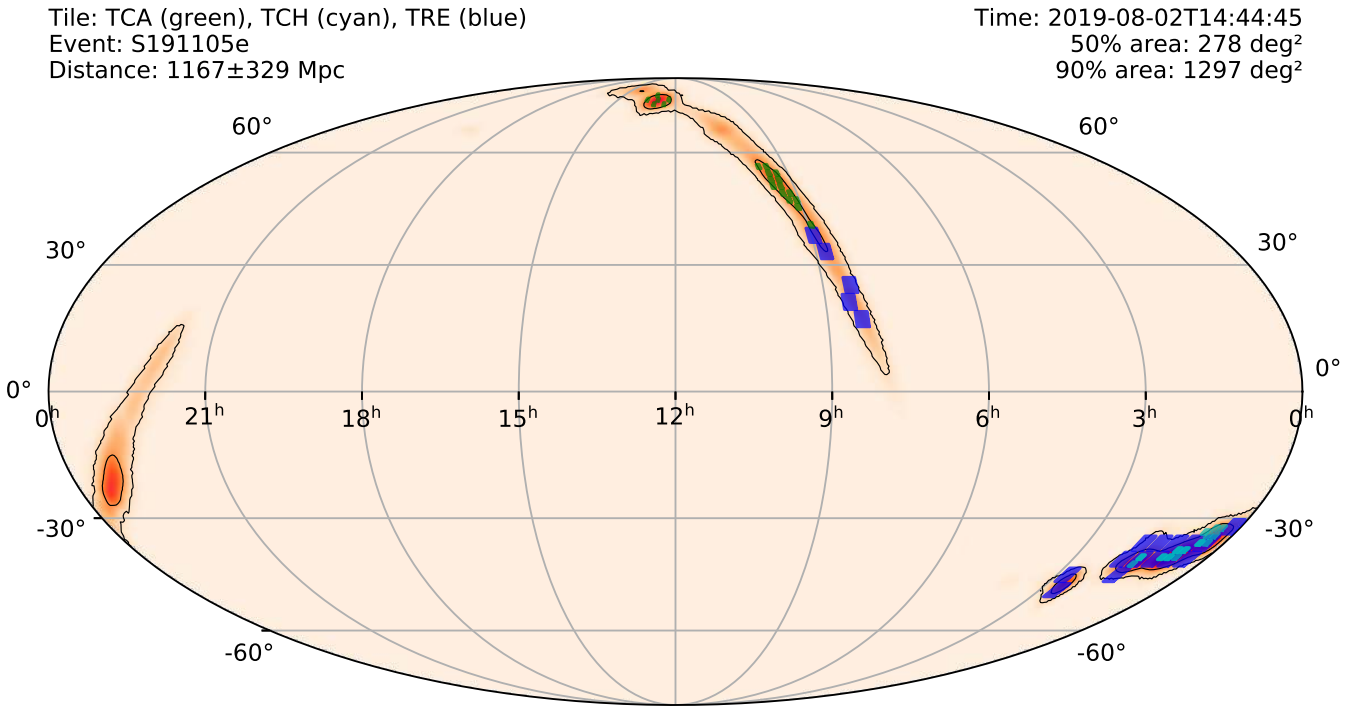

Figure A.31: TAROT tiles are displayed over the contours of the localization of S191105e. See the Circular report `https://gcn.gsfc.nasa.gov/gcn3/26215.gcn3`.

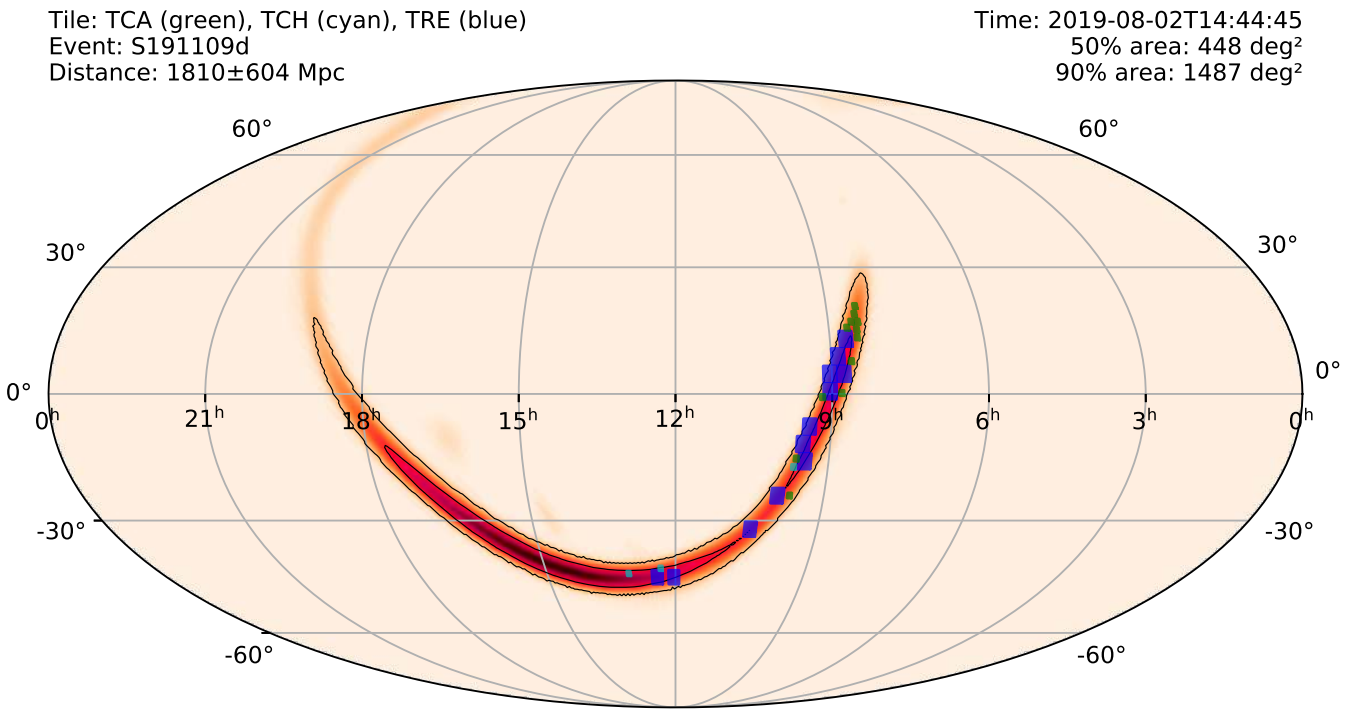

Figure A.32: TAROT tiles are displayed over the contours of the localization of S191109d. See the Circular report `https://gcn.gsfc.nasa.gov/gcn3/26219.gcn3`.

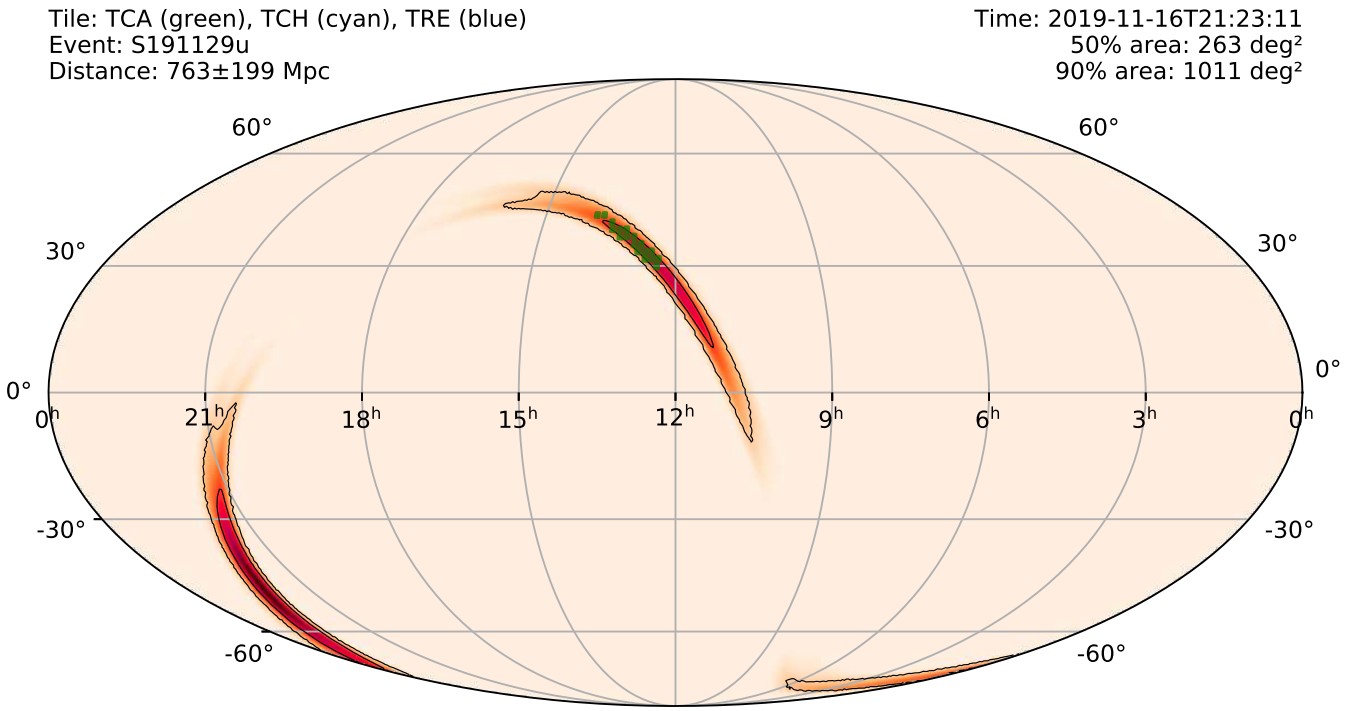

Figure A.33: TAROT tiles are displayed over the contours of the localization of S191129u. See the Circular report `https://gcn.gsfc.nasa.gov/gcn3/26362.gcn3`.

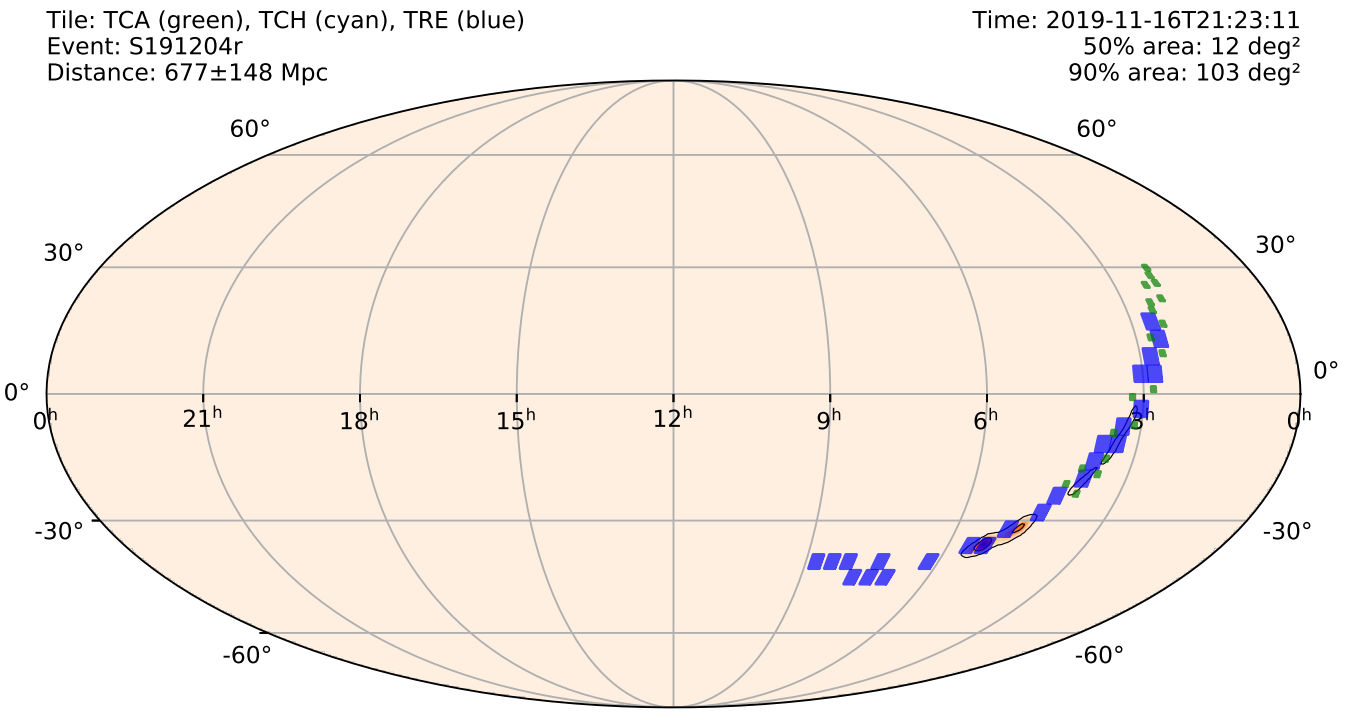

Figure A.34: TAROT tiles are displayed over the contours of the localization of S191204r.

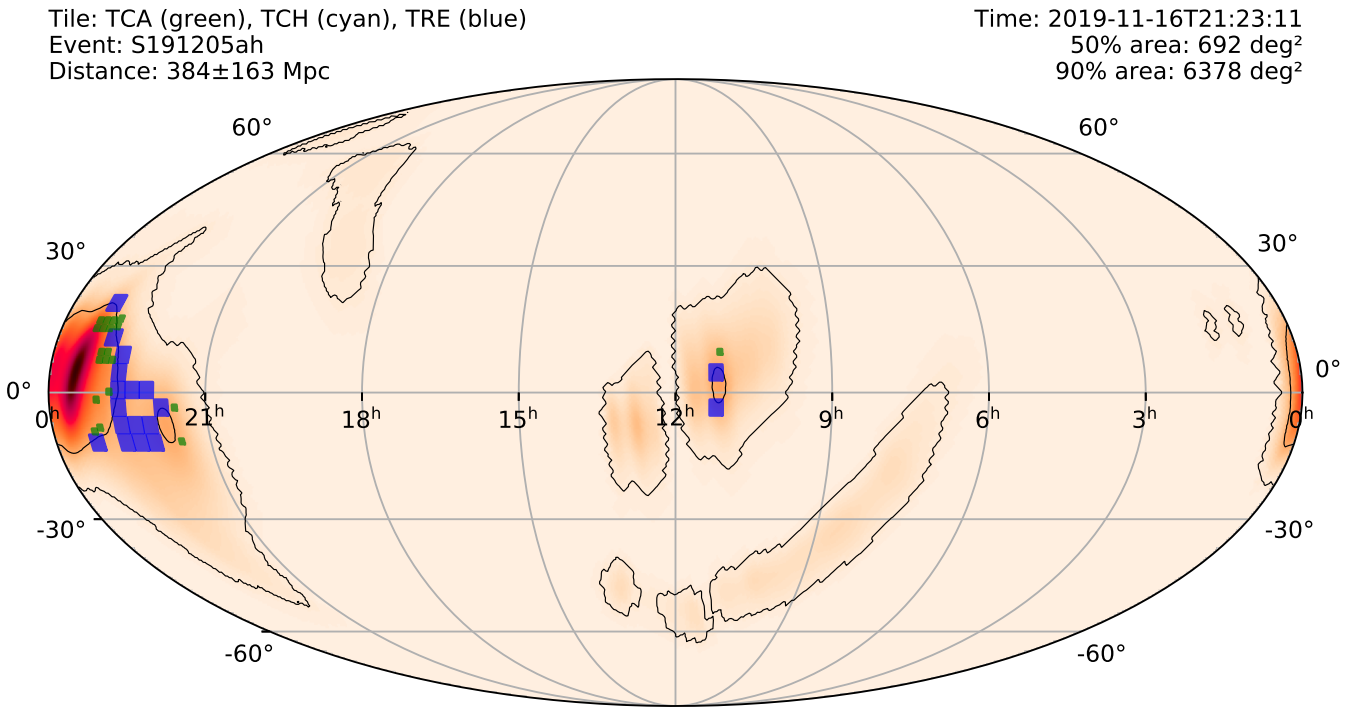

Figure A.35: TAROT tiles are displayed over the contours of the localization of S191205ah. See the Circular report `https://gcn.gsfc.nasa.gov/gcn3/26384.gcn3`.

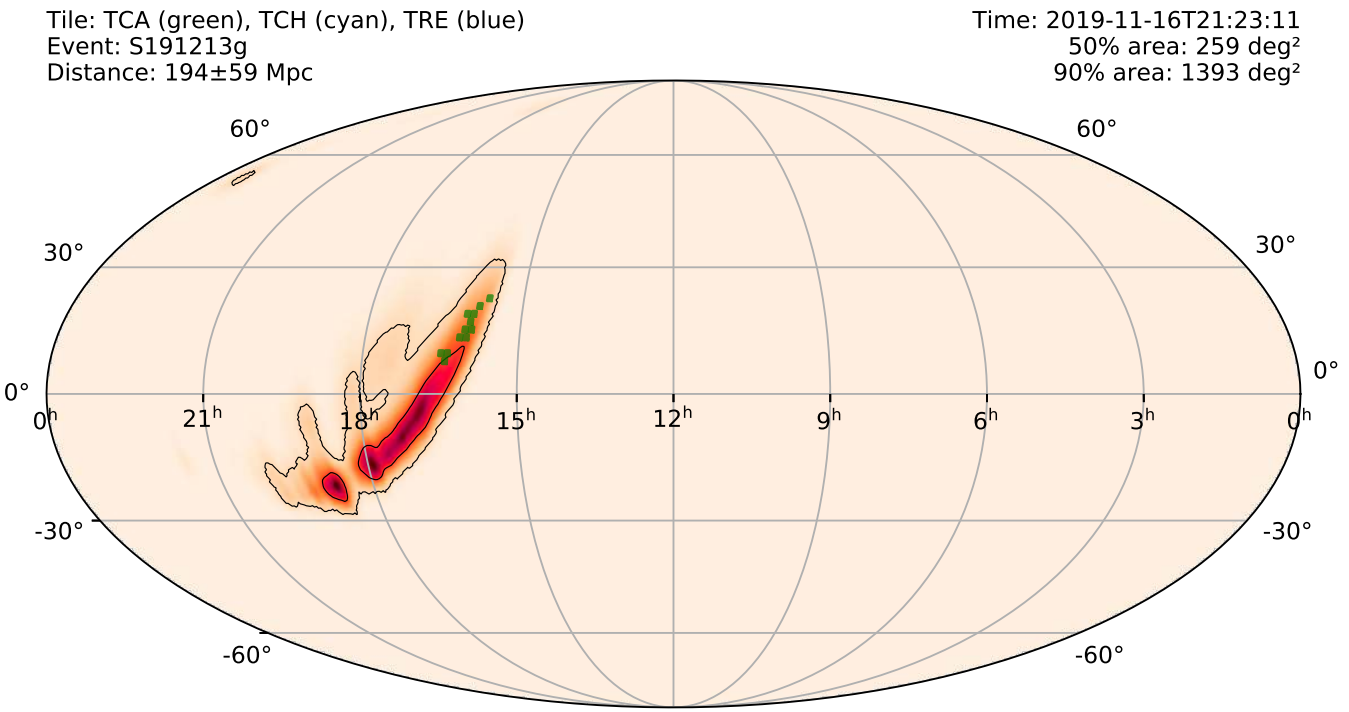

Figure A.36: TAROT tiles are displayed over the contours of the localization of S191213g. See the Circular report `https://gcn.gsfc.nasa.gov/gcn3/26558.gcn3`.

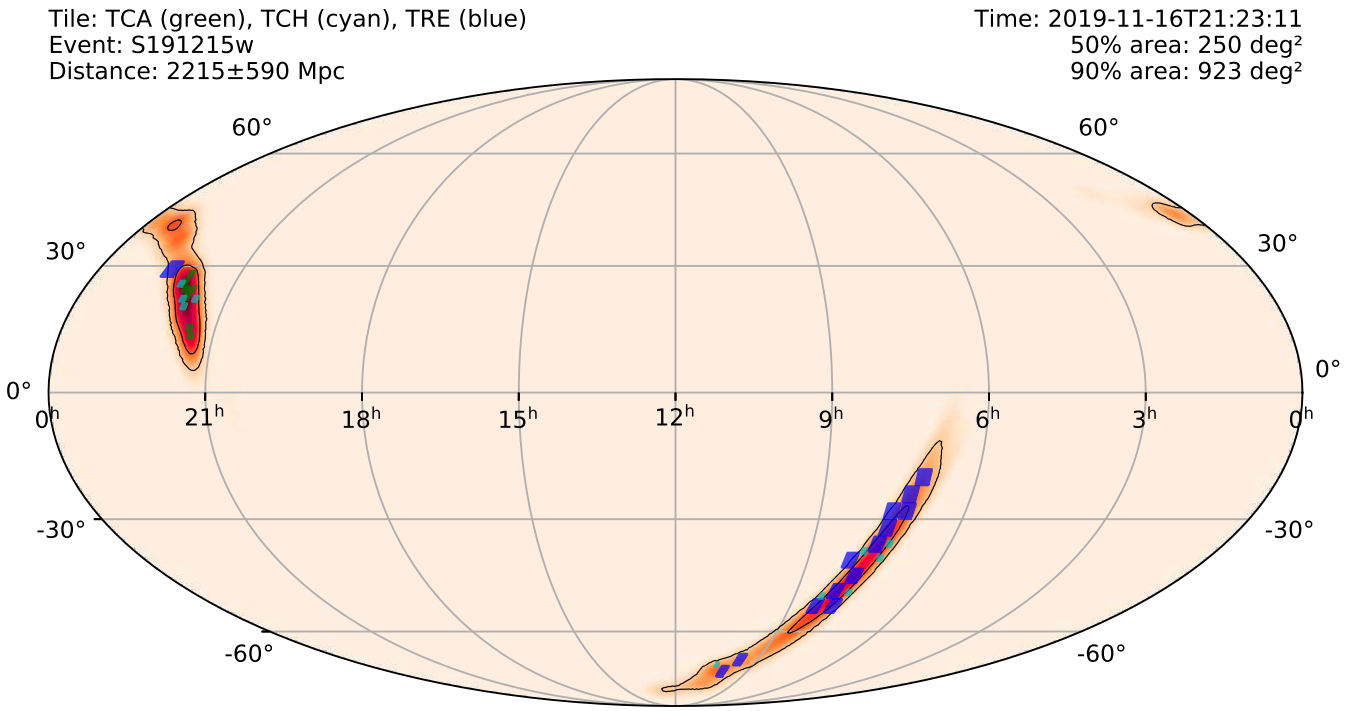

Figure A.37: TAROT tiles are displayed over the contours of the localization of S191215w. See the Circular report `https://gcn.gsfc.nasa.gov/gcn3/26469.gcn3`.

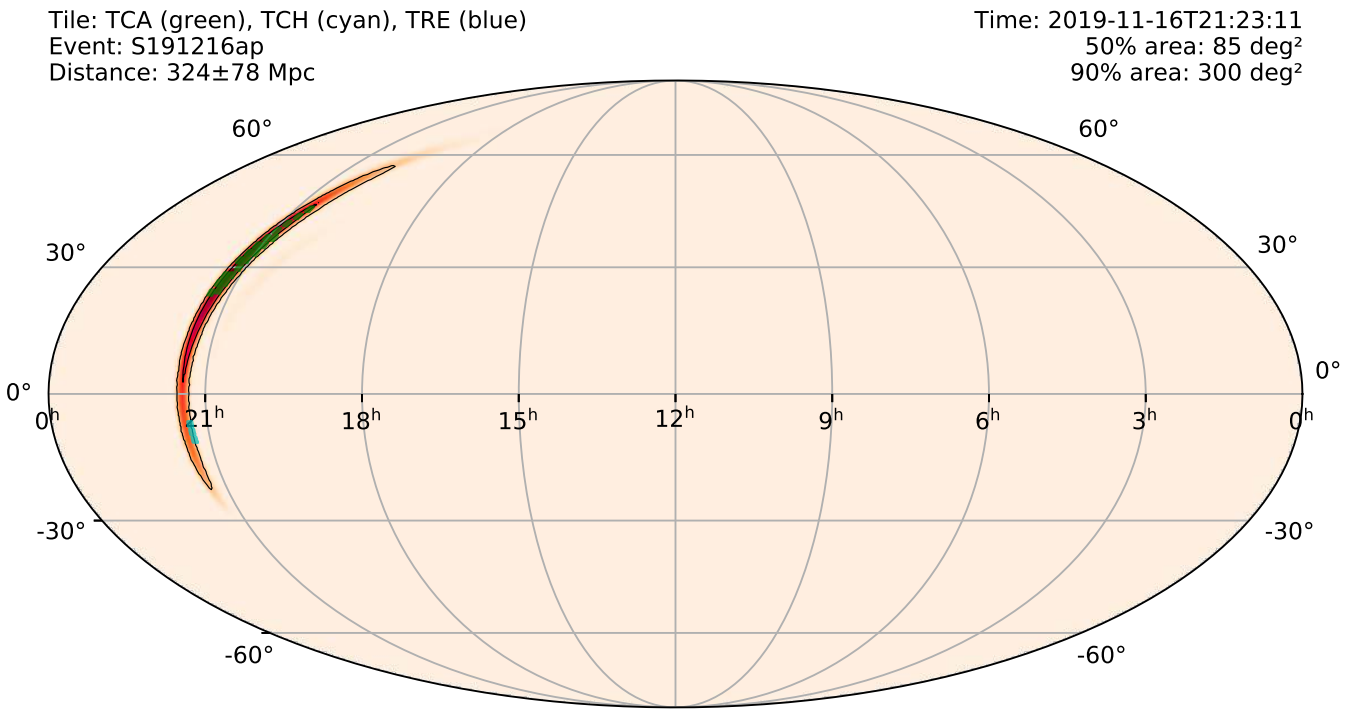

Figure A.38: TAROT tiles are displayed over the contours of the localization of S191216ap. See the Circular report `https://gcn.gsfc.nasa.gov/gcn3/26528.gcn3`.

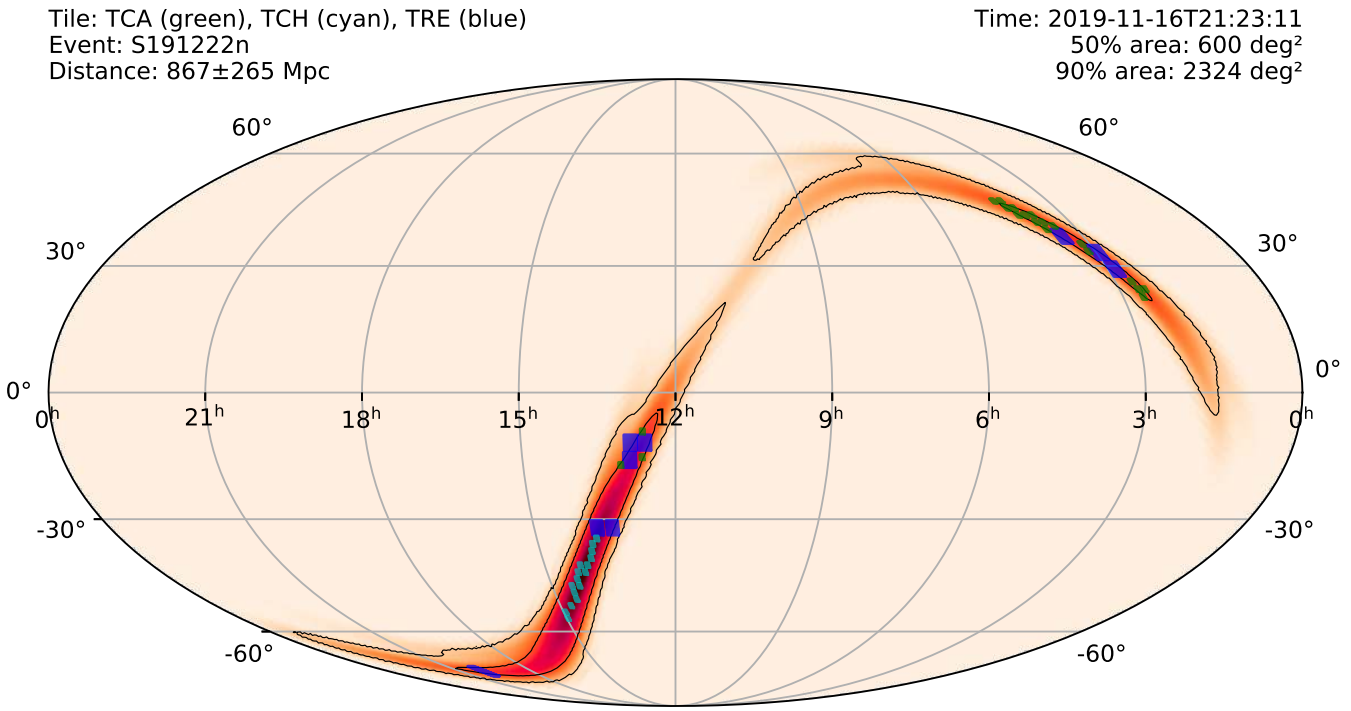

Figure A.39: TAROT tiles are displayed over the contours of the localization of S191222n. See the Circular report `https://gcn.gsfc.nasa.gov/gcn3/26575.gcn3`.

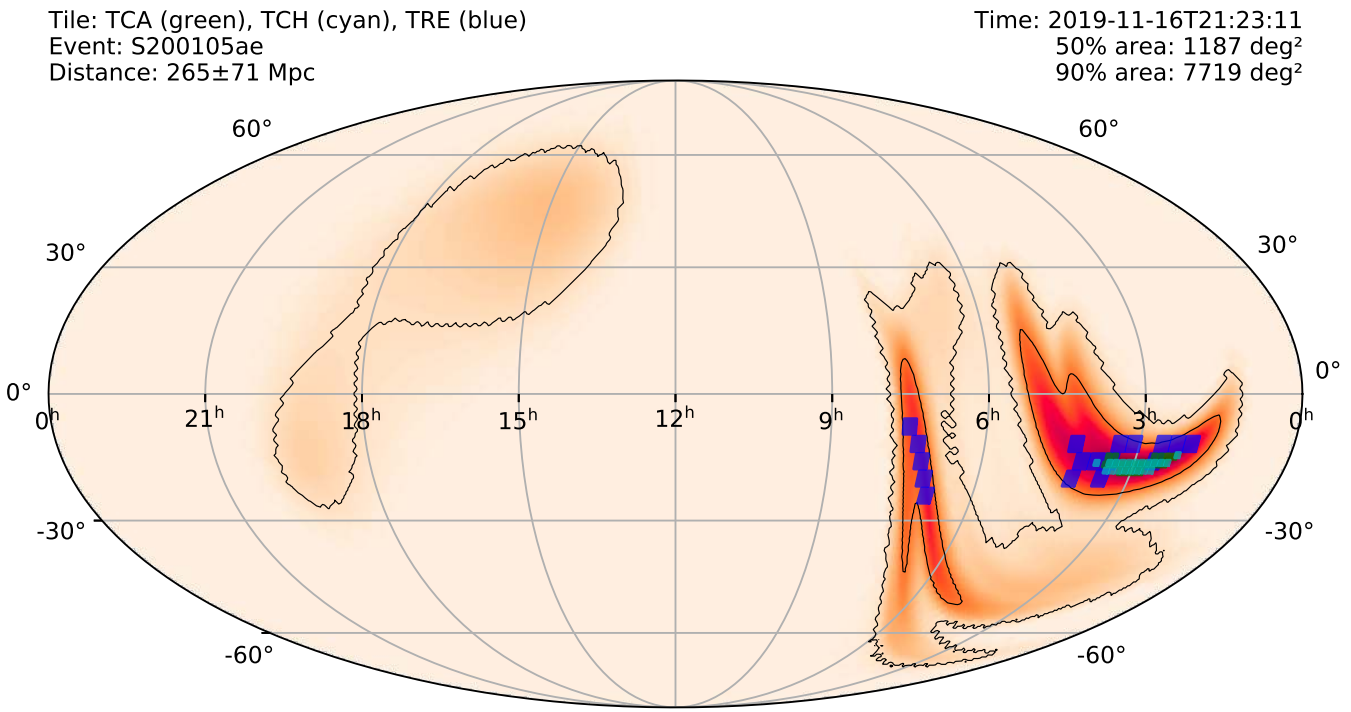

Figure A.40: TAROT tiles are displayed over the contours of the localization of S200105ae. See the Circular report `https://gcn.gsfc.nasa.gov/gcn3/26687.gcn3`.

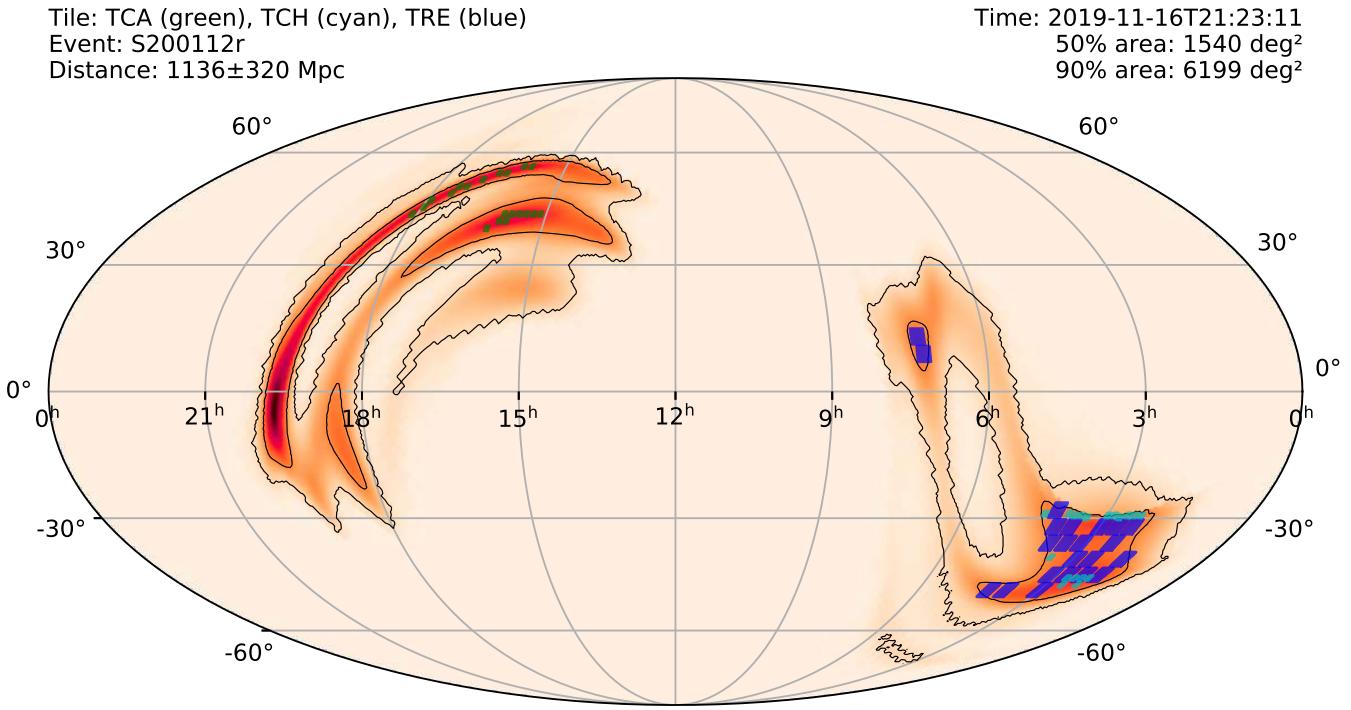

Figure A.41: TAROT tiles are displayed over the contours of the localization of S200112r. See the Circular report `https://gcn.gsfc.nasa.gov/gcn3/26789.gcn3`.

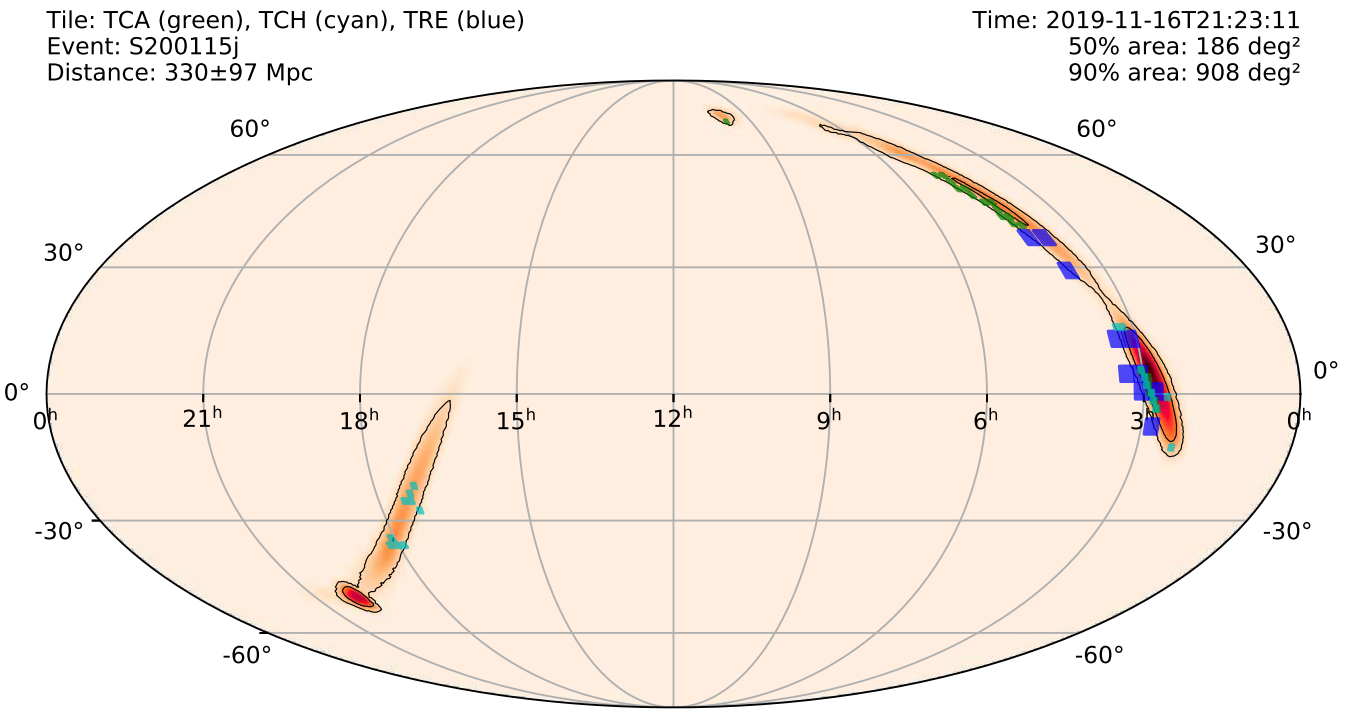

Figure A.42: TAROT tiles are displayed over the contours of the localization of S200115j. See the Circular report `https://gcn.gsfc.nasa.gov/gcn3/26820.gcn3`.

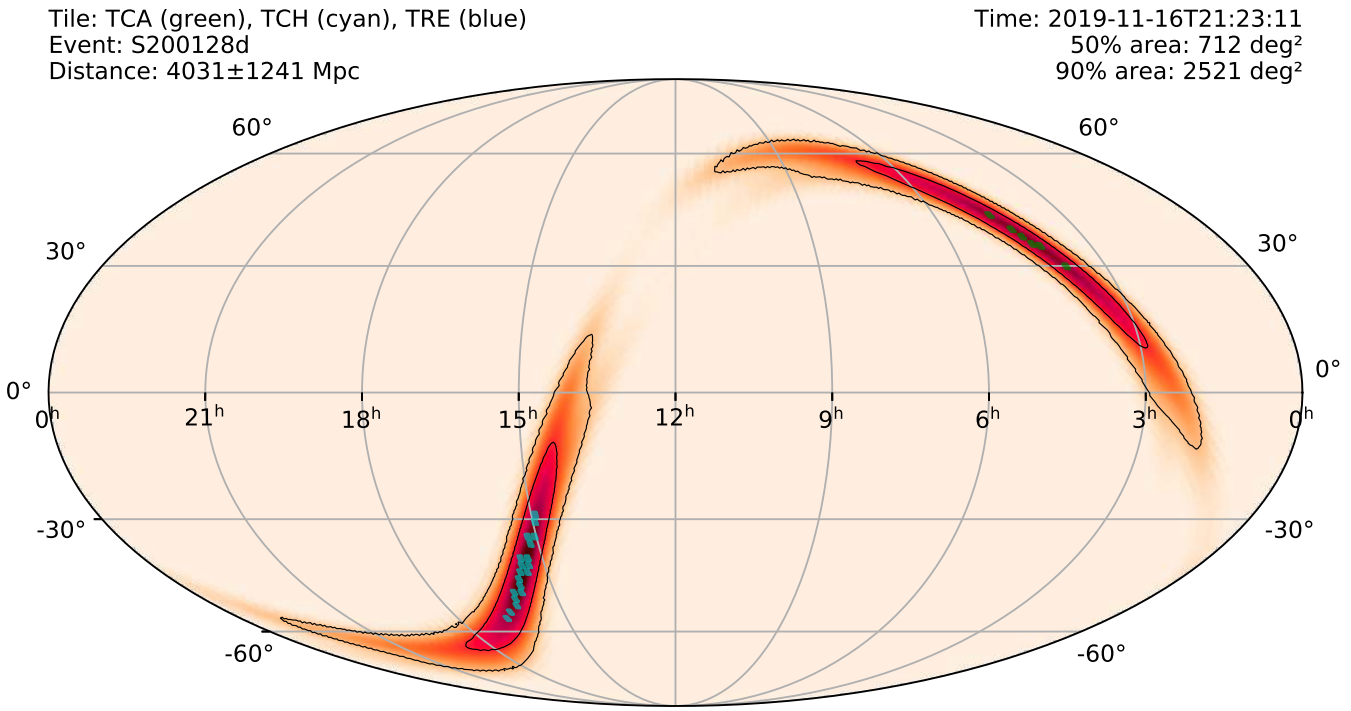

Figure A.43: TAROT tiles are displayed over the contours of the localization of S200128d. See the Circular report `https://gcn.gsfc.nasa.gov/gcn3/26947.gcn3`.

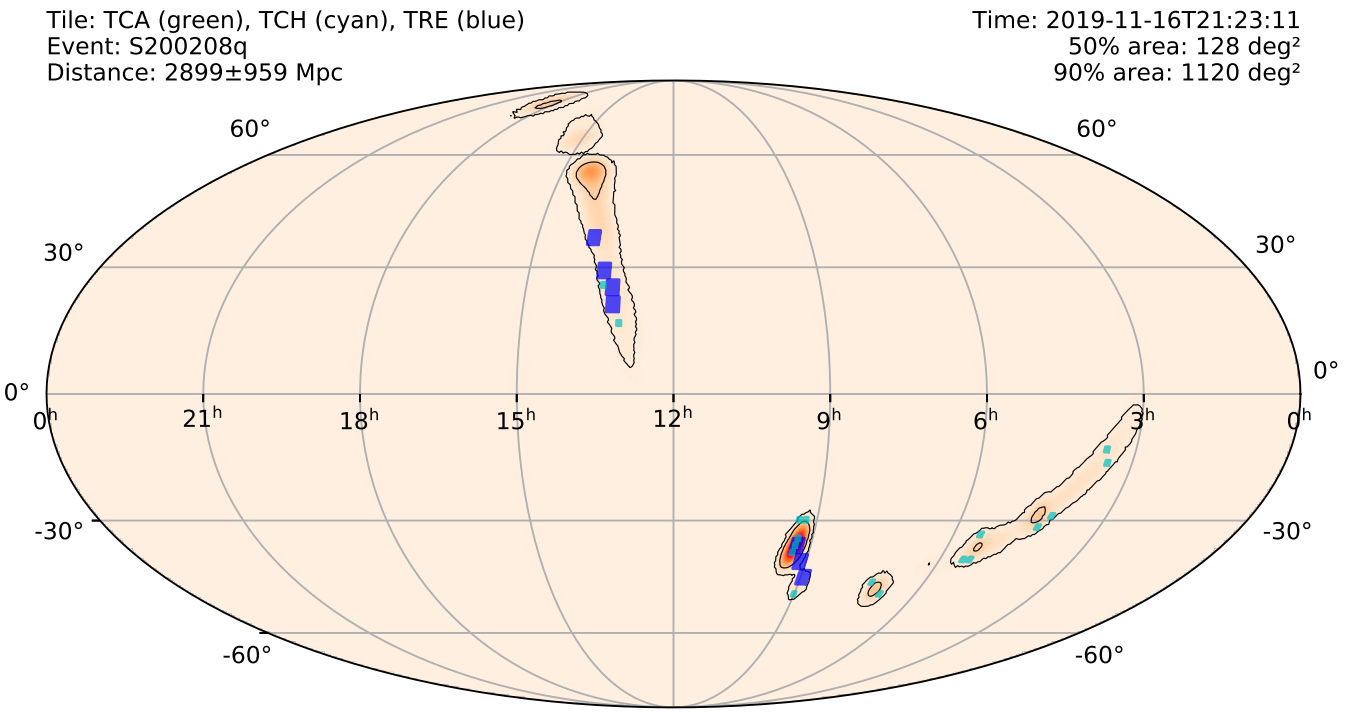

Figure A.44: TAROT tiles are displayed over the contours of the localization of S200208q. See the Circular report `https://gcn.gsfc.nasa.gov/gcn3/27054.gcn3`.

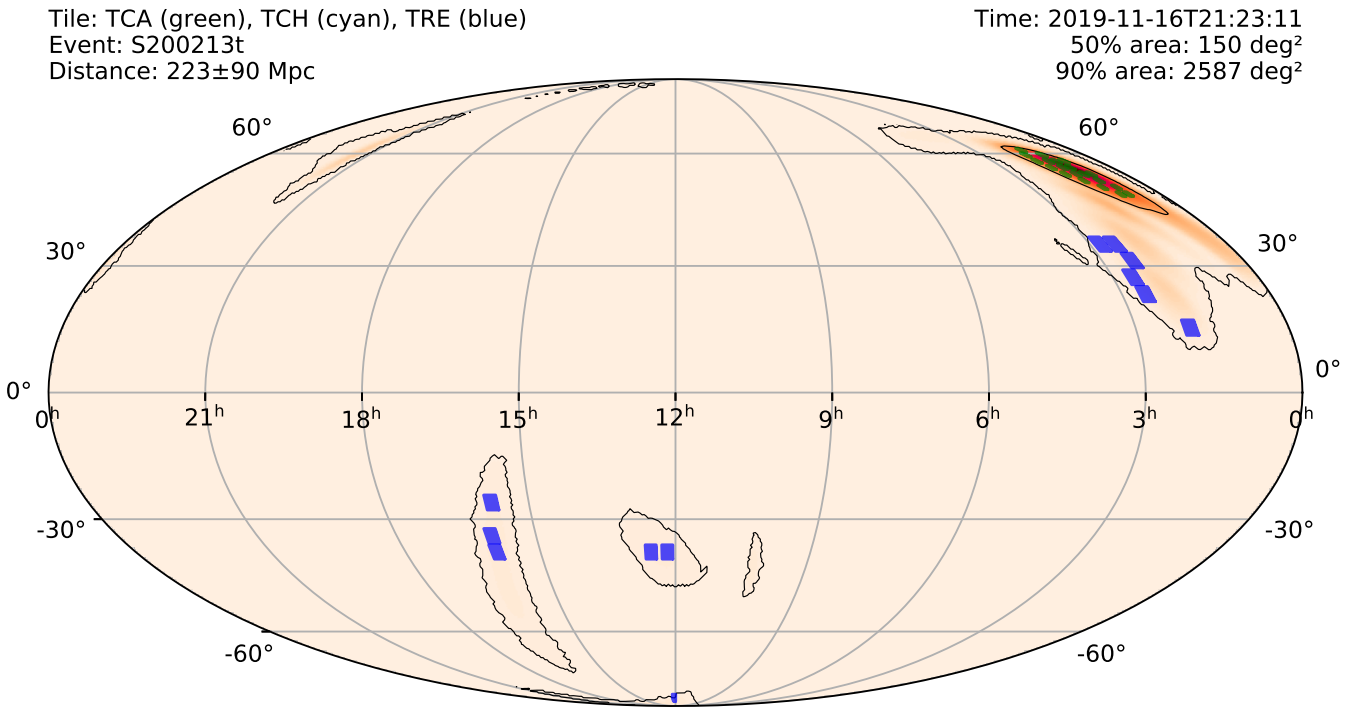

Figure A.45: TAROT tiles are displayed over the contours of the localization of S200213t. See the Circular report `https://gcn.gsfc.nasa.gov/gcn3/27116.gcn3`.

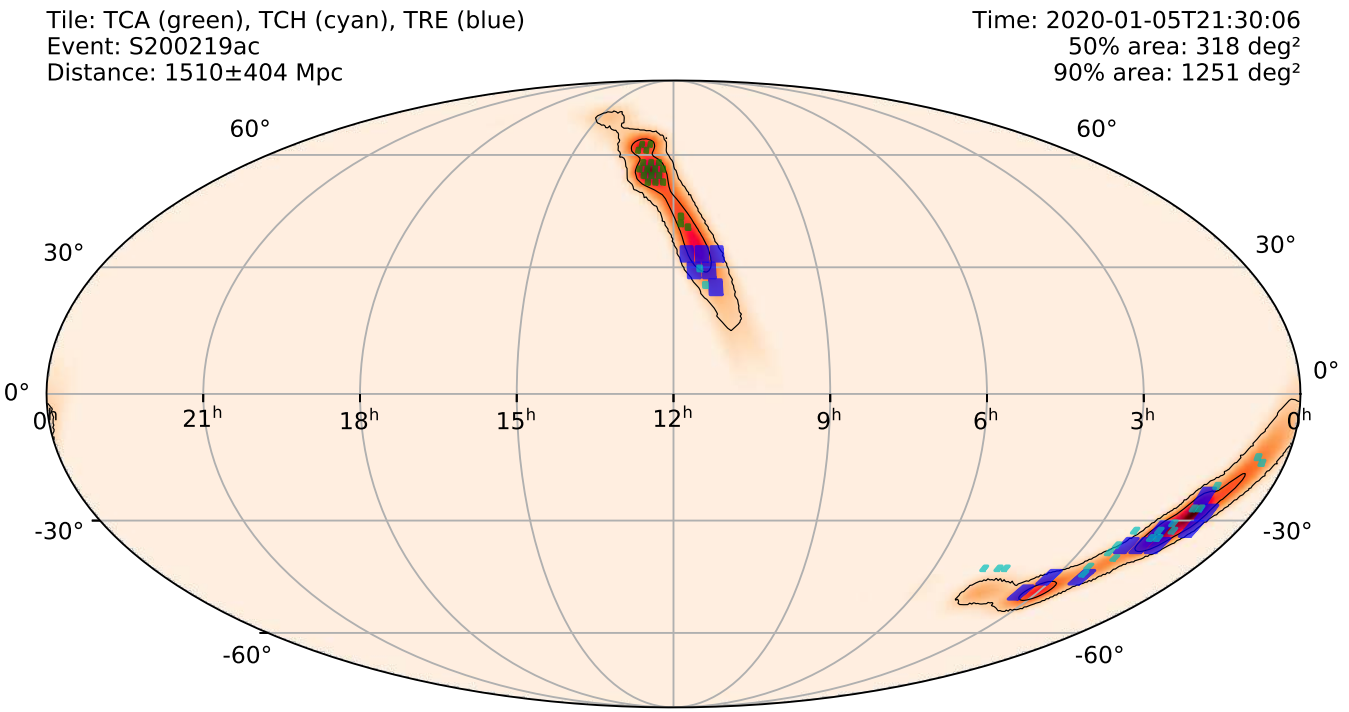

Figure A.46: TAROT tiles are displayed over the contours of the localization of S200219ac. See the Circular report `https://gcn.gsfc.nasa.gov/gcn3/27168.gcn3`.

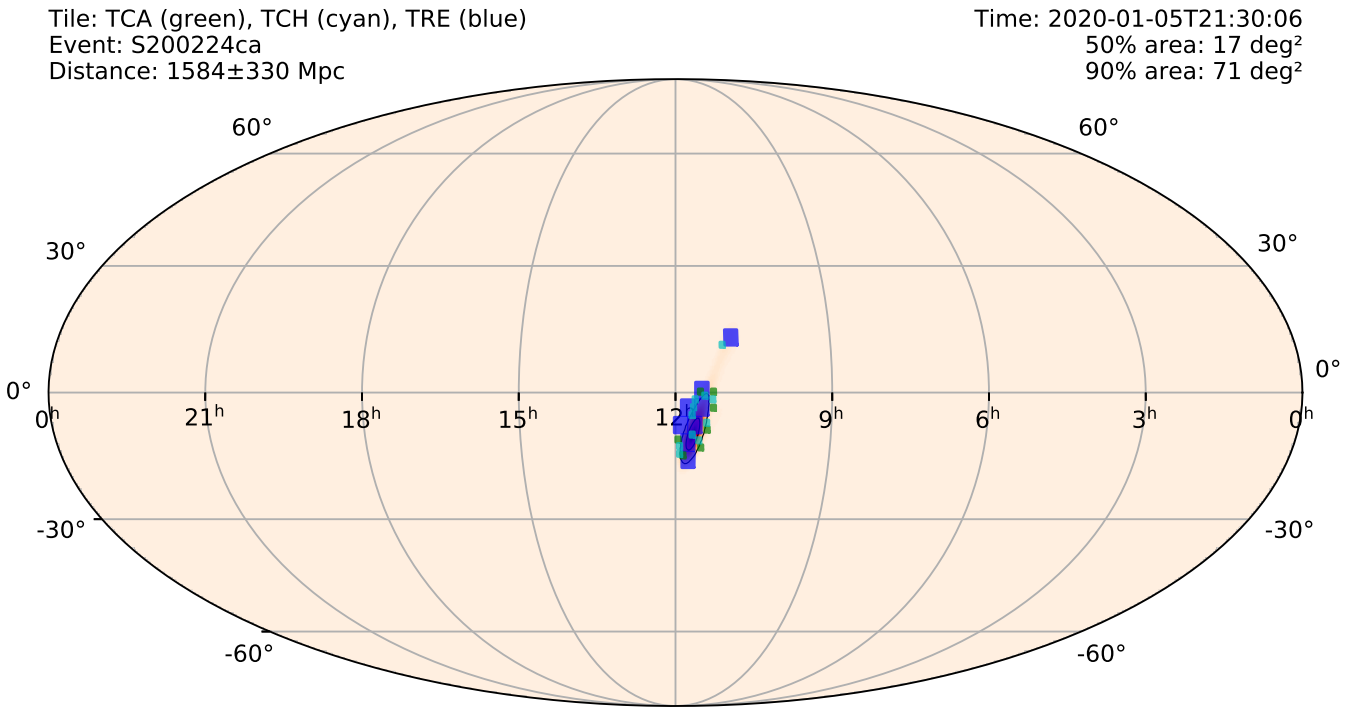

Figure A.47: TAROT tiles are displayed over the contours of the localization of S200224ca. See the Circular report `https://gcn.gsfc.nasa.gov/gcn3/27238.gcn3`.

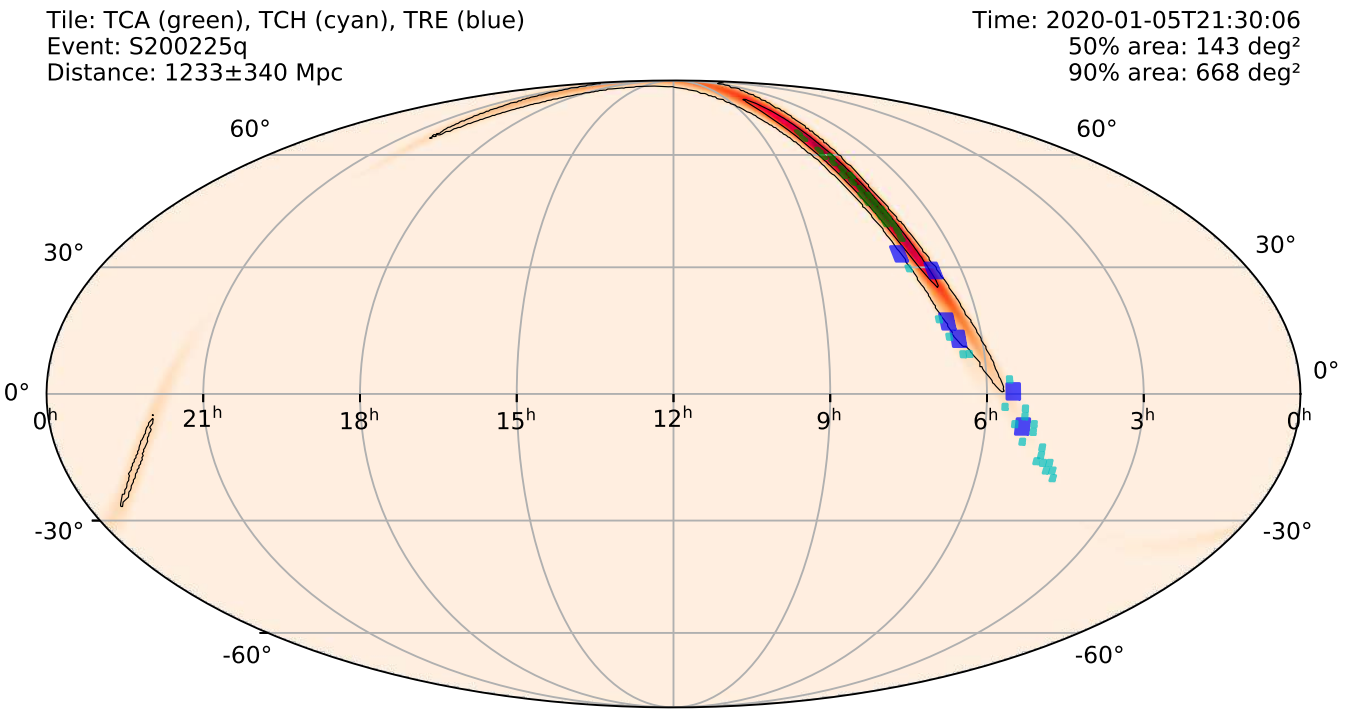

Figure A.48: TAROT tiles are displayed over the contours of the localization of S200225q. See the Circular report `https://gcn.gsfc.nasa.gov/gcn3/27275.gcn3`.

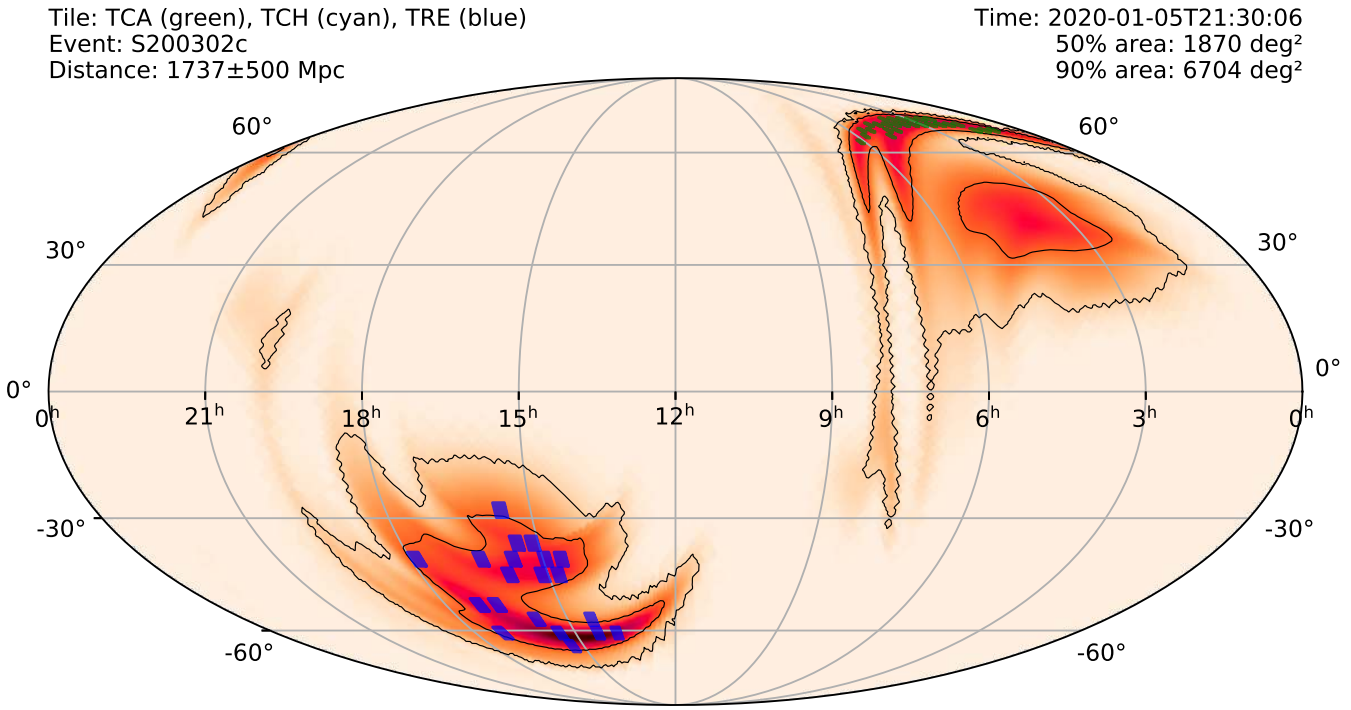

Figure A.49: TAROT tiles are displayed over the contours of the localization of S200302c. See the Circular report `https://gcn.gsfc.nasa.gov/gcn3/27322.gcn3`.

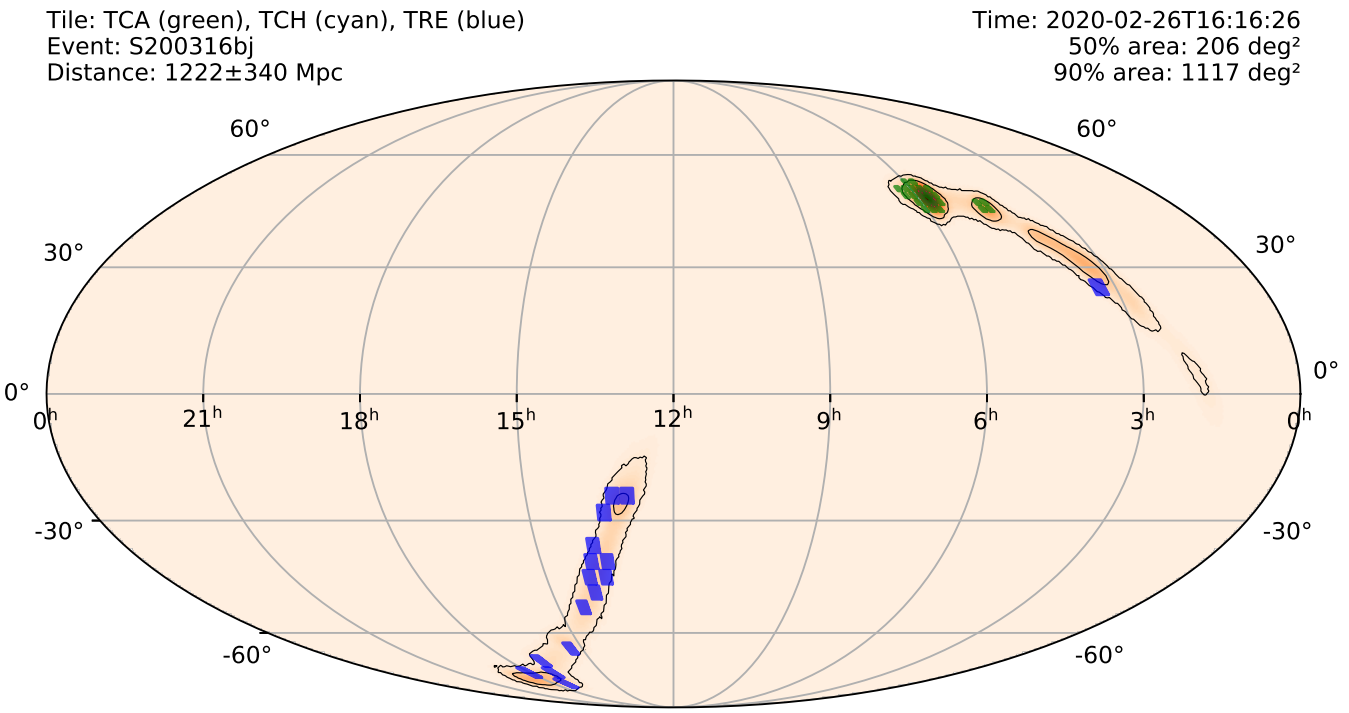

Figure A.50: TAROT tiles are displayed over the contours of the localization of S200316bj. See the Circular report `https://gcn.gsfc.nasa.gov/gcn3/27409.gcn3`.

Appendix B

Transient search algorithm

```
/* RA1,Dec1 = Data coordinates                          */
/* RA2,Dec2 = Catalog coordinates                       */
/* MATCH = math_coordinates_sky                         */
/* AngSep = Angular separation                          */
/* <A>, <B> are median of angular separation            */
```
initialization;
Data: Data[RA1, Dec1], Catalog[RA2, Dec2]
Result: Possible transient source
repeat
  Index, AngSep = MATCH(Data, Catalog);
  $< A >$ = median(AngSep);
  Match = catalog[index];
  δRA = Data[RA1] - Match[RA];
  δDec = Data[Dec1] - Match[Dec];
  Data = Data[RA1+δRA, Dec1+δDec];
  Index, AngSep = MATCH(Data, Catalog);
  $< B >$ = median(AngSep);
until $(< A > - < B >) \sim 0$;
foreach *Souce status* $\longleftarrow$ *AngSep* **do**
  if *Souce status less than* $(< B > + 3\sigma)$ **then**
    Souce status = existent souce
  else
    if *Souce status in VizieR database* **then**
      Souce status= existent in USNOB1.0 catalogs
    else
      Souce status = possible transient source
    end
  end
end

Algorithm 1: Transient search algorithm

Appendix C

Candidate detection rate

Table C.1: The detection rate of unknown source and pre-candidate.

	Coverage Area (deg^2)			No. Unknown Source (deg^{-2})			Pre-candidate (deg^{-2})		
Event	TCA	TCH	TRE	TCA	TCH	TRE	TCA	TCH	TRE
S200316bj	69		244	20.90		0.00	1.13		0.00
S200302c	92		349	28.12		0.23	1.02		0.08
S200225q	81	74	106	9.85	0.00	3.25	2.10	0.00	0.29
S200224ca	26	32	139	22.77	26.91	31.78	2.46	5.41	0.60
S200219ac	70	63	277	16.70	0.00	14.41	1.40	0.00	0.00
S200213t	70	4	193	65.81	22.75	12.18	4.17	4.00	0.02
S200208q	69	69	364	0.00	39.14	0.00	0.00	3.71	0.00
S200128d	22	67		5.45	14.37		1.55	5.27	
S200115j	71	68	174	480.86	74.94	14.88	0.41	0.99	0.39
S200112r	71	63	379	6.99	3.81	27.25	0.27	0.65	0.05
S200105ae	70	70	295	5.04	0.37	12.23	2.87	0.00	0.01
S191222n	71	56	157	1.14	0.77	20.52	0.23	0.18	0.72
S191216ap	67	11		0.22	65.73		0.01	0.55	
S191215w	25	36	226	0.00	110.08	4.47	0.00	7.39	1.62
S191213g	42			0.29			0.17		
S191205ah	71	68		4.59	4.94		0.96	0.26	
S191204r	68	68	417	2.13	69.47	22.37	0.44	3.07	0.26
S191129u	63	63		0.60	30.43		0.05	1.44	
S191109d	43	11	191	0.67	4.64	10.16	0.26	0.00	0.00
S191105e	25	46	242	89.96	84.28	33.34	0.00	0.00	0.00
S190930t	135	110	94	3.30	90.97		0.54	0.55	0.00
S190930s	68	38	242	0.75	50.87	8.26	0.03	9.58	0.03
S190923y	64	64	312	4.64	126.25	0.00	0.03	1.08	0.00
S190915ak	80			2.69			0.79		
S190910h	175	161		1.94	10.35		0.57	0.04	
S190910d	103	158	360	1.51	87.35	0.86	1.18	0.31	0.00
S190901ap	100	112	279	4.22	70.55	1.46	0.78	2.40	0.13
S190828l	67	69	157	0.57	43.94	21.31	0.07	9.17	0.13
S190828j	67	21	122	19.78	103.67	3.98	0.01	14.10	0.03
S190814bv	32		139	3.59		78.50	2.63		0.00
S190728q	26	56	121	0.46	212.64	70.86	0.12	1.91	0.54
S190727h		68	70		47.99	0.73		1.16	0.00
S190720a	60	50	71	1.55	44.24	17.89	0.63	0.00	0.52
S190718y			120			2.24			0.00
S190707q	21	25	88	0.48	34.24	2.39	0.05	3.44	0.32
S190706ai	22	24	121	2.59	145.29	75.53	1.09	4.00	0.02
S190701ah			71			29.82			0.18
S190630ag	21		71	24.38		0.85	0.00		0.00
S190517h		11			0.55			0.36	
S190513bm	24	21		0.25	73.24		0.08	1.95	
S190512at	22	24		2.09	34.29		0.82	5.83	
S190510g	24	31		10.08	170.16		3.92	0.19	
S190503bf		24			79.50			0.96	
S190426c	23	25	105	3.52	330.60	0.56	0.39	19.32	0.00
S190425z	18	25	124	2.67	270.60	0.71	1.06	2.96	0.00
S190421ar			124			1.11			0.67
S190412m	24		123	29.54		6.38	14.50		4.03

The first column is the GW event; column 2 is the coverage area by the telescopes; and column 3 is the average of detection rate for unknown source per square degree; column 4 is the average of detection rate for pre-candidate per square degree.

Bibliography

Abbott, B. P. et al.
2016a. Binary black hole mergers in the first advanced ligo observing run. *Phys. Rev. X*, 6:041015.

Abbott, B. P. et al.
2016b. Gw151226: Observation of gravitational waves from a 22-solar-mass binary black hole coalescence. *Phys. Rev. Lett.*, 116:241103.

Abbott, B. P. et al.
2016c. Localization and broadband follow-up of the gravitational-wave transient gw150914. *The Astrophysical Journal Letters*, 826(1):L13.

Abbott, B. P. et al.
2016d. Observation of gravitational waves from a binary black hole merger. *Phys. Rev. Lett.*, 116:061102.

Abbott, B. P. et al.
2016e. Observation of gravitational waves from a binary black hole merger. *Phys. Rev. Lett.*, 116(6):061102.

Abbott, B. P. et al.
2016f. Sensitivity of the Advanced LIGO detectors at the beginning of gravitational wave astronomy. *Phys. Rev.*, D93(11):112004. [Addendum: Phys. Rev.D97,no.5,059901(2018)].

Abbott, B. P. et al.
2017a. Gravitational waves and gamma-rays from a binary neutron star merger: GW170817 and GRB 170817a. *The Astrophysical Journal*, 848(2):L13.

Abbott, B. P. et al.
2017b. Gw170104: Observation of a 50-solar-mass binary black hole coalescence at redshift 0.2. *Phys. Rev. Lett.*, 118:221101.

Abbott, B. P. et al.
2017c. Gw170817: Observation of gravitational waves from a binary neutron star inspiral. *Phys. Rev. Lett.*, 119:161101.

Abbott, B. P. et al.
2019. GWTC-1: A Gravitational-Wave Transient Catalog of Compact Binary Mergers Observed by LIGO and Virgo during the First and Second Observing Runs. *Phys. Rev.*, X9(3):031040.

Adrián-Martínez, S. et al.
2016. Optical and X-ray early follow-up of ANTARES neutrino alerts. , 2016(2):062.

Andreoni, I. et al.
2017. Follow up of GW170817 and its electromagnetic counterpart by Australian-led observing programs. *Publ. Astron. Soc. Austral.*, 34:e069.

Antier, S. et al.
2019. The first six months of the Advanced LIGO's and Advanced Virgo's third observing run with GRANDMA. *Monthly Notices of the Royal Astronomical Society*, 492(3):3904–3927.

Antier, S. et al.
2019. The first six months of the Advanced LIGO's and Advanced Virgo's third observing run with GRANDMA.

Antier, S. et al.
2020. GRANDMA Observations of Advanced LIGO's and Advanced Virgo's Third Observational Campaign. *arXiv e-prints*, P. arXiv:2004.04277.

Astropy Collaboration, T. Robitaille, E. Tollerud, et al.
2013. Astropy: A community Python package for astronomy. *Astronomy and Astrophysics*, 558:A33.

Barthelmy, S. D. et al.
1995. BACODINE, the Real-Time BATSE Gamma-Ray Burst Coordinates Distribution Network. , 231(1-2):235–238.

Becerra, R. L. et al.
2019. Reverse Shock Emission Revealed in Early Photometry in the Candidate Short GRB 180418A. , 881(1):12.

Belczynski, K., D. E. Holz, T. Bulik, and R. O'Shaughnessy
2016. The first gravitational-wave source from the isolated evolution of two 40-100 Msun stars. *Nature*, 534:512.

Bentley, J. L.
1975. Multidimensional binary search trees used for associative searching. *Commun. ACM*, 18(9):509–517.

Berthier, J. et al.
2006. SkyBoT, a new VO service to identify Solar System objects. In *Astronomical Data Analysis Software and Systems XV*, C. Gabriel, C. Arviset, D. Ponz, and S. Enrique, eds., volume 351 of *Astronomical Society of the Pacific Conference Series*, Pp. 367–+.

Bertin, E. and S. Arnouts
1996. SExtractor: Software for source extraction. *Astronomy and Astrophysics, Supplement*, 117:393–404.

Bhat, P. N. et al.
2016. The Third Fermi gbm Gamma-ray Burst Catalog: the First six Years. *Astrophys. J. Suppl.*, 223(2):28.

Boër, M., M. Bringer, A. Klotz, et al.
1999. TAROT: Observing gamma-ray bursts "in progress". , 138:579–580.

Boër, M. et al.
2001. Limits on the early afterglow phase of gamma-ray burst sources from TAROT-1. , 378:76–81.

Boër, M. et al.
2006. Detection of a Very Bright Optical Flare from the Gamma-Ray Burst GRB 050904 at Redshift 6.29. , 638(2):L71–L74.

Boër, M., A. Klotz, R. Laugier, et al.
2017. TAROT: a network for space surveillance and tracking operations. In *7th European Conference on Space Debris ESA/ESOC, Darmstadt/Germany*, Darmstadt, Germany. ESA.

Braga-Ribas, F. et al.
2013. The Size, Shape, Albedo, Density, and Atmospheric Limit of Transneptunian Object (50000) Quaoar from Multi-chord Stellar Occultations. , 773(1):26.

Briggs, M. S. et al.
1996. BATSE Observations of the Large-Scale Isotropy of Gamma-Ray Bursts. , 459:40.

Brocato, E. et al.
2018. GRAWITA: VLT Survey Telescope observations of the gravitational wave sources GW150914 and GW151226. *Mon. Not. Roy. Astron. Soc.*, 474(1):411–426.

Budavári, T. and S. H. Lubow
2012. Catalog matching with astrometric correction and its application to the hubble legacy archive. , 761:188.

Burns, E. et al.
2019. A Fermi Gamma-ray Burst Monitor Search for Electromagnetic Signals Coincident with Gravitational-Wave Candidates in Advanced LIGO's First Observing Run. , 871(1):90.

Calabretta, M., F. Valdes, E. Greisen, et al.
2004. Representations of distortions in FITS world coordinate systems. In *Astronomical Data Analysis Software and Systems (ADASS) XIII*, F. Ochsenbein, M. G. Allen, and D. Egret, eds., volume 314 of *Astronomical Society of the Pacific Conference Series*, P. 551.

Cervantes-Cota, J. L., S. Galindo-Uribarri, and G.-F. Smoot
2016. A Brief History of Gravitational Waves. *Universe*, 2(3):22.

Cline, T. L., U. D. Desai, R. W. Klebesadel, and I. B. Strong
1973. Energy Spectra of Cosmic Gamma-Ray Bursts. , 185:L1.

Contreras, C. et al.
2018. SN 2012fr: Ultraviolet, Optical, and Near-infrared Light Curves of a Type Ia Supernova Observed within a Day of Explosion. , 859(1):24.

Costa, E. et al.
1997. Discovery of an X-ray afterglow associated with the γ-ray burst of 28 February 1997. , 387(6635):783–785.

Coughlin, M. W., S. Antier, D. Corre, et al.
2019. Optimizing multitelescope observations of gravitational-wave counterparts. *Monthly Notices of the Royal Astronomical Society*, 489(4):5775–5783.

Coulter, D. et al.
2017a. Swope Supernova Survey 2017a (SSS17a), the Optical Counterpart to a Gravitational Wave Source. *Science*, 358:1556.

Coulter, D. A. et al.
2017b. Swope supernova survey 2017a (sss17a), the optical counterpart to a gravitational wave source. *Science*, 358(6370):1556–1558.

Damerdji, Y., A. Klotz, and M. Boër
2007. The TAROT Suspected Variable Star Catalog. , 133(4):1470–1477.

Della Valle, M. et al.
2006. Hypernova Signatures in the Late Rebrightening of GRB 050525A. , 642(2):L103–L106.

Doctor, Z. et al.
2019. A Search for Optical Emission from Binary-Black-Hole Merger GW170814 with the Dark Energy Camera. *Astrophys. J.*, 873(2):L24.

Drout, M. R. et al.
2017. Light curves of the neutron star merger gw170817/sss17a: Implications for r-process nucleosynthesis. *Science*, 358(6370):1570–1574.

Díaz, M. C. et al.
2016. GW150914: First search for the electromagnetic counterpart of a gravitational-wave event by the TOROS collaboration. *Astrophys. J.*, 828(2):L16.

Egret, D., P. Didelon, B. J. McLean, et al.
1992. The tycho input catalogue - cross-matching the guide star catalog with the hipparcos inca data base. , 258:217–222.

Einstein, A.
1915a. Die Feldgleichungen der Gravitation. *Sitzungsberichte der Königlich Preußischen Akademie der Wissenschaften (Berlin*, Pp. 844–847.

Einstein, A.
1915b. Zur allgemeinen Relativitätstheorie. *Sitzungsberichte der Königlich Preußischen Akademie der Wissenschaften (Berlin*, Pp. 778–786.

ESA
2020. ABOUT INTEGRAL. `https://www.cosmos.esa.int/web/integral/mission-overview`. Accessed: 30-07-2020.

Fishman, G. J., C. A. Meegan, T. A. Parnell, and R. B. Wilson
1982. The burst and transient source experiment for the gamma-ray observatory. *AIP Conference Proceedings*, 77(1):443–451.

Frail, D. A. et al.
2001. Beaming in gamma-ray bursts: Evidence for a standard energy reservoir. *The Astrophysical Journal*, 562(1):L55–L58.

Gendre, B. et al.
2012. GRB 110205A: Anatomy of a Long Gamma-Ray Burst. , 748(1):59.

Gendre, B. et al.
2013. The Ultra-long Gamma-Ray Burst 111209A: The Collapse of a Blue Supergiant? , 766(1):30.

Goodman, J.
1986. Are gamma-ray bursts optically thick? , 308:L47–L50.

Gretz, D. J.
2018. Early history of gravitational wave astronomy: The weber bar antenna development. *History of Physics Newsletter*, 13:5–16.

Hewish, A. et al.
1968. Observation of a rapidly pulsating radio source. *Nature*, 217:709–713.

Hjorth, J. et al.
2005. The optical afterglow of the short γ-ray burst GRB 050709. , 437(7060):859–861.

Kann, D. A. et al.
2018. The optical/NIR afterglow of GRB 111209A: Complex yet not unprecedented. , 617:A122.

Kasliwal, M. M. et al.
2016. iPTF Search for an Optical Counterpart to Gravitational Wave Trigger GW150914. *Astrophys. J.*, 824(2):L24.

Klebesadel, R. W., I. B. Strong, and R. A. Olson
1973. Observations of Gamma-Ray Bursts of Cosmic Origin. , 182:L85.

Klotz, A., M. Boër, J. L. Atteia, et al.
2005. Early re-brightening of the afterglow of GRB 050525a. , 439(3):L35–L38.

Klotz, A., M. Boër, J. L. Atteia, et al.
2009. Early optical observations of gamma-ray bursts by the tarot telescopes: Period 2001-2008. *The Astronomical Journal*, 137(5):4100.

Klotz, A., M. Boër, J. Eysseric, et al.
2008. Robotic observations of the sky with tarot: 2004–2007. *Publications of the Astronomical Society of the Pacific*, 120(874):1298.

Klotz, A., R. Delmas, D. Marchais, et al.
2012. The AudeLA software. In *Astronomical Society of India Conference Series*, volume 7, P. 15.

Klotz, A. et al.
2006. Continuous optical monitoring during the prompt emission of GRB 060111B. , 451(3):L39–L42.

Klotz, A. and P. Thierry
2019. TAROT Reunion a telescope based on the Rapido design for reliable optical observations of fast transients. *Experimental Astronomy*, P. 41.

Kouveliotou, C., , et al.
1993. Identification of two classes of gamma-ray bursts. *Astrophys. J. Lett.*, 413:L101–104.

Kouveliotou, C. et al.
1993. Identification of Two Classes of Gamma-Ray Bursts. , 413:L101.

Lang, D., D. Hogg, K. Mierle, et al.
2010. Astrometry.net: Blind Astrometric Calibration of Arbitrary Astronomical Images. *Astronomical Journal*, 139:1782–1800.

Le Borgne, J. F. et al.
2012. The All-sky GEOS RR Lyr Survey with the TAROT Telescopes: Analysis of the Blazhko Effect. , 144(2):39.

LIGO Scientific Collaboration and Virgo Collaboration
2020. LIGO/Virgo S200114f: Identification of a GW unmodeled transient candidate. *GRB Coordinates Network*, 26734:1.

LIGO Scientific Collaboration, Virgo Collaboration, J. Abadie, et al.
2012. Implementation and testing of the first prompt search for gravitational wave transients with electromagnetic counterparts. , 539:A124.

Lindegren, L., U. Lammers, U. Bastian, et al.
2016. Gaia data release 1. astrometry: one billion positions, two million proper motions and parallaxes. , 595:A4.

Lipunov, V. M. et al.
2017. Master optical detection of the first ligo/virgo neutron star binary merger gw170817. *The Astrophysical Journal*, 850(1):L1.

Maneewongvatana, S. and D. M. Mount
1999. Analysis of approximate nearest neighbor searching with clustered point sets. *eprint arXiv:cs/9901013*.

Meszaros, P. and M. J. Rees
1993. Relativistic Fireballs and Their Impact on External Matter: Models for Cosmological Gamma-Ray Bursts. , 405:278.

Metzger, B. D.
2017. Kilonovae. *Living Reviews in Relativity*, 20(1).

Metzger, B. D. et al.
2010. Electromagnetic counterparts of compact object mergers powered by the radioactive decay of r-process nuclei. , 406(4):2650–2662.

Monet, D., S. Levine, B. Canzian, et al.
2003. The USNO-B Catalog. *Astronomical Journal*, 125:984–993.

Moriya, T. J., P. Marchant, and S. I. Blinnikov
2020. Luminous supernovae associated with ultra-long gamma-ray bursts from hydrogen-free progenitors extended by pulsational pair-instability. *arXiv e-prints*, P. arXiv:2007.06221.

NASA
2012. Swift's Burst Alert Telescope (BAT). `https://swift.gsfc.nasa.gov/about_swift/bat_desc.html`. Accessed: 30-07-2020.

NASA
2020. The HETE-2 Satellite. `https://heasarc.gsfc.nasa.gov/docs/hete2/hete2.html`. Accessed: 30-07-2020.

Noysena, K., A. Klotz, M. Boër, et al.
2019. Limits on the Electromagnetic Counterpart of Binary Black Hole Coalescence at Visible Wavelengths. , 886(1):73.

Ochsenbein, F., P. Bauer, and J. Marcout
2000. The VizieR database of astronomical catalogues. *Astronomy and Astrophysics, Supplement*, 143:23–32.

Paczynski, B. and J. E. Rhoads
1993. Radio Transients from Gamma-Ray Bursters. , 418:L5.

Paczyński, B.
1991. Extragalactic scenarios for gamma-ray bursts. *AIP Conference Proceedings*, 265(1):144–148.

Piran, T.
1999. Gamma-ray bursts and the fireball model. , 314(6):575–667.

Piran, T.
1999. Gamma-ray bursts and the fireball model. *Physics Reports*, 314(6):575–667.

Piran, T. and J. Granot
2001. Theory of grb afterglow. Pp. 300–305.

Poincaré, H.
1905. Sur la dynamique de l' électron. `https://www.academie-sciences.fr/pdf/dossiers/Poincare/Poincare_pdf/Poincare_CR1905.pdf`. Accessed: 10-09-2018.

Proga, D., A. I. MacFadyen, P. J. Armitage, et al.
2003. Axisymmetric Magnetohydrodynamic Simulations of the Collapsar Model for Gamma-Ray Bursts. , 599(1):L5–L8.

Rodriguez, C. L., C.-J. Haster, S. Chatterjee, et al.
2016. Dynamical Formation of the GW150914 Binary Black Hole. , 824:L8.

Scarsi, L.
1984. The SAX mission. *Advances in Space Research*, 3(10-12):491–500.

Shupe, D., M. Moshir, J. Li, et al.
2005. The SIP Convention for Representing Distortion in FITS Image Headers. In *Astronomical Data Analysis Software and Systems XIV*, P. Shopbell, M. Britton, and R. Ebert, eds., volume 347 of *Astronomical Society of the Pacific Conference Series*, P. 491.

Soares-Santos, M. et al.
2016. A Dark Energy Camera Search for an Optical Counterpart to the

First Advanced LIGO Gravitational Wave Event GW150914. *Astrophys. J.*, 823(2):L33.

Stalder, B. et al.
2017. Observations of the GRB afterglow ATLAS17aeu and its possible association with GW170104. *Astrophys. J.*, 850(2):149.

Stanek, K. Z. et al.
2003. Spectroscopic discovery of the supernova 2003dh associated with GRB 030329. *The Astrophysical Journal*, 591(1):L17–L20.

Stone, N. C., B. D. Metzger, and Z. Haiman
2017. Assisted inspirals of stellar mass black holes embedded in AGN discs: solving the 'final au problem'. *Mon. Not. Roy. Astron. Soc.*, 464(1):946–954.

Stratta, G. et al.
2013. The Ultra-long GRB 111209A. II. Prompt to Afterglow and Afterglow Properties. , 779(1):66.

Tanvir, N. et al.
2013. A "kilonova" associated with short-duration gamma-ray burst 130603b.

Tanvir, N. R. et al.
2017. The emergence of a lanthanide-rich kilonova following the merger of two neutron stars. *The Astrophysical Journal*, 848(2):L27.

Taris, F. et al.
2018. Variability of extragalactic sources: its contribution to the link between ICRF and the future Gaia Celestial Reference Frame. , 611:A52.

Taylor, J. H. and J. M. Weisberg
1982. A new test of general relativity - Gravitational radiation and the binary pulsar PSR 1913+16. , 253:908–920.

The LIGO Scientific collaboration
2019. Gravitational wave astronomy with ligo and similar detectors in the next decade. *eprint arXiv:abs/1904.03187*.

The LIGO Scientific Collaboration, the Virgo Collaboration, B. P. Abbott, , et al.
2019. Gwtc-1: A gravitational-wave transient catalog of compact binary mergers observed by ligo and virgo during the first and second observing runs. *Physical Review X*, 9(3).

The LIGO Scientific Collaboration, the Virgo Collaboration, the KAGRA Collaboration, et al.
2013. Prospects for observing and localizing gravitational-wave transients with advanced ligo, advanced virgo and kagra. *eprint arXiv:abs/1304.0670*.

Turpin, D.
2016. *Study of the high-energy transient objects in the Universe in the era of the multimessenger observations*. Theses, Universite Toulouse 3 Paul Sabatier (UT3 Paul Sabatier).

Turpin, D. et al.
2019. The mini-GWAC optical follow-up of the gravitational wave alerts: results from the O2 campaign and prospects for the upcoming O3 run. *eprint arXiv:abs/1902.08476*.

Weisberg, J. M., D. J. Nice, and J. H. Taylor
2010. Timing Measurements of the Relativistic Binary Pulsar PSR B1913+16. *Astrophys. J.*, 722:1030–1034.

Woosley, S. E., R. G. Eastman, and B. P. Schmidt
1999. Gamma-ray bursts and type ic supernova sn 1998bw. *The Astrophysical Journal*, 516(2):788–796.

Zevin, M. et al.
2017. Constraining Formation Models of Binary Black Holes with Gravitational-wave Observations. , 846(1):82.

Zhang, B.
2016. Mergers of Charged Black Holes: Gravitational Wave Events, Short Gamma-Ray Bursts, and Fast Radio Bursts. *Astrophys. J.*, 827(2):L31.

Zhang, S.-N., Y. Liu, S. Yi, et al.
2016. Do we expect to detect electromagnetic radiation from merging stellar mass black binaries like gw150914? no.

Abstract

The detection of gravitational waves (GWs) from LIGO and Virgo interferometers opened a new era for multimessenger observations especially with the coincident detection between GW events and gamma-ray burst (GRB) detection. The first GW event detected by LIGO on the 14^{th} September 2015 (Abbott et al., 2016d) was a binary black hole merger (BBH). Until August 2017 nine other mergers of black holes were detected during runs O1 and O2. But the most interesting object for multimessenger astronomy was the merger of two neutron stars (BNS) detected on 17^{th} August 2017 (Andreoni et al., 2017). This merger was detected in various electromagnetic waves and allowed to confirm the kilonova model.

This research started with the analysis of images recorded by the TAROT telescopes during runs O1, O2 to detect new optical sources associated to black hole mergers. The analysis pipeline was developed to process images and none of optical transient detected but the limiting magnitude of the particular BBH event of 14^{th} August 2017 gave new constraints about the hypothetical link with gamma ray bursts (Noysena et al., 2019). Three GW events; GW150914, GW170104 and GW170814 were observed with TAROT allowing us to constrain $\alpha < 10^{-5}$, the fraction of energy emitted by gravitational waves converted into optical light. An approximately 100% coverage of localization of GW170814 was observed at 0.6 days after GW triggering with no evidence of optical transient and 65% of 147 optical light curves of GRBs known redshift were excluded.

The chance to observe optical transient began when GW interferometers started the run O3 on 1^{st} April 2019 and the campaign ended on 27^{th} March 2020. At the end of run O3, 55 events were detected by LIGO and Virgo and 47 GW events were followed-up by TAROT, thousands of images were searched and analyzed for transient by pipeline using processing techniques described in this manuscript. No new credible optical source associated to GW events was found and 34 GCN circulars reporting optical observations were published to GCN network. The conversion efficiency α for BNS, BBH, and NSBH is at 2×10^{-6}, 3×10^{-7} and 2×10^{-8} respectively. The limiting magnitude and the short delay to start optical observations allow us to reduce severely the hypothesis of the association between GWs and GRBs in case of BBH mergers. However, we have not enough number of cases to exclude definitively the association.

Five binary neutron star mergers were detected before the end of GW observation but none of them was closer than 100 Mpc which is beyond limiting distance where TAROT could detect the associated kilonova. As a consequence, no conclusion to derive any relevant with BNS optical observations.

The optical follow up by TAROT was a pioneering experience with a lot of exciting jobs to adjust event after event to increase the efficiency of the detection pipeline. Joining the GRANDMA group brought more opportunity to detect optical transient during run O3 and result in scientific papers published by Antier et al. (2019, 2020). More GW counterparts and optical observations are needed and we are ready to participate to the optical follow-up of the next GW runs.

Resumé

La détection des ondes gravitationnelles (GWs) par les interféromètres LIGO et Virgo a ouvert une nouvelle ère pour les observations multimessagers, en particulier la détection simultanée d'événements GW et de sursauts gamma (GRB). Le premier événement GW détecté par LIGO le 14 septembre 2015 (Abbott et al., 2016d) était une fusion de trous noirs binaires (BBH). Jusqu'en août 2017, neuf autres fusions de trous noirs ont été détectées lors des campagnes d'observation O1 et O2. Mais l'objet le plus intéressant pour l'astronomie multi messager a été la fusion de deux étoiles à neutrons (BNS) détectée le 17 août 2017 (Andreoni et al., 2017). Cette fusion a été détectée par divers détecteurs d'ondes électromagnétiques et a permis de confirmer l'existence du modèle kilonova.

Mon travail de thèse a commencé par l'analyse d'images enregistrées par les télescopes TAROT lors des campagnes O1, O2 pour essayer de détecter de nouvelles sources optiques associées aux fusions de trous noirs (BBH). J'ai développé la chaîne d'analyse pour traiter les images TAROT. Aucun transitoire optique n'a été détecté, mais la magnitude limite de l'événement BBH du 14 août 2017 a apporté de nouvelles contraintes concernant le lien hypothétique avec les sursauts gamma et a donné lieu à une publication (Noysena et al., 2019). Les trois événements GW150914, GW170104 et GW170814 observés par TAROT nous ont permis de contraindre la valeur $\alpha < 10^{-5}$ de la fraction d'énergie émise par les ondes gravitationnelles convertie en lumière optique. Une couverture d'environ 100% de la localisation de GW170814 a été observée 0,6 jour après l'émission des ondes gravitationnelles sans signe de transitoire optique. Cette limite, comparée à 147 courbes de lumière optiques de GRB de redshift connus, a permis de conclure que 65% des GRBs connus auraient été détectés si GW170814 avait été associé à un GRB.

La possibilité de détecter un transitoire optique a repris lorsque les interféro-mètres GW ont effectué la campagne O3 entre le 1er avril 2019 et le 27 mars 2020. À la fin de la campagne O3, 55 événements ont été détectées par LIGO et Virgo et 47 événements GW ont été suivi par TAROT. Des milliers d'images ont été enregistrées et analysées pour rechercher les transitoires optiques avec une chaîne logicielle utilisant des techniques de traitement décrites en détail dans ce manuscrit. Aucune nouvelle source optique crédible associée aux événements GW n'a été trouvée. 34 circulaires GCN rapportant les limites de détection des observations optiques ont été publiées dans les circulaires GCN. L'efficacité de conversion α pour BNS, BBH et NSBH est respectivement de 2×10^{-6}, 3×10^{-7} et 2×10^{-8}. La limite de détection et le court délai pour commencer les observations optiques avec TAROT nous ont permis de réduire fortement l'hypothèse de l'association entre GWs et GRBs en cas de fusion BBH. Cependant, nous n'avons pas suffisamment de cas pour exclure définitivement l'association.

Cinq fusions d'étoiles à neutrons binaires ont été détectées pendant la campagne O3 mais aucune d'entre elles n'était plus proche que 100 Mpc, ce qui est au-delà de la distance limite où TAROT pouvait détecter la kilonova associée. En conséquence, nous ne tirons pas de conclusion sur les observations optiques de BNS.

Le suivi optique par TAROT a été une expérience pionnière, passionnante, et nous avons ajusté la méthodologie événement après événement afin d'augme-nter l'efficacité de la chaîne de détection. Le fait d'avoir rejoind le groupe GRANDMA nous a apporté plus d'opportunités pour détecter les transitoires optiques pendant la campagne O3 et a donné lieu à deux articles scientifiques publiés en collaboration (Antier et al., 2019, 2020). Un plus grand nombre de détection d'ondes gravitationnelles et d'observations optiques seront nécessaires dans le futur et nous sommes prêts à participer au suivi optique des prochaines campagnes GW.